Development and Characterization of Light Weight High Entropy Alloys

Ph.D. Thesis

Ornov Maulik
(2013RMT9040)

June 2017

Department of Metallurgical and Materials Engineering
MALAVIYA NATIONAL INSTITUTE OF TECHNOLOGY
JAIPUR
JAIPUR-302017

Development and Characterization of Light Weight High Entropy Alloys

This thesis is submitted as a partial fulfillment of
Ph.D. Program in Engineering

Ornov Maulik
(2013RMT9040)

June 2017

Department of Metallurgical and Materials Engineering
MALAVIYA NATIONAL INSTITUTE OF TECHNOLOGY
JAIPUR
JAIPUR-302017

Malaviya National Institute of Technology, Jaipur
DEPARTMENT OF METALLURGICAL AND MATERIALS ENGINEERING

CERTIFICATE

This is to certify that the thesis, entitled "**Development and Characterization of Light Weight High Entropy Alloy**" is being submitted by me to the for the award of **Doctor of Philosophy** in *Metallurgical and Materials Engineering, Malaviya National Institute of Technology Jaipur,* is an original research work carried out by me. The content of the thesis has been checked using Plagiarism Detector software.

I have incorporated all the suggestion/queries/changes raised by the Examiner in the Thesis Evaluation Report.

(Ornov Maulik)

This is to certify that the above statement made by the candidate is true to my knowledge.

(Vinod Kumar)
Supervisor

Ph.D. viva-voce examination of Mr. Ornov Maulik, Research Scholar, was held on 09-06-2017 in the seminar hall of department of Metallurgical and Materials Engineering, MNIT, Jaipur. The candidate defended the viva-voce successfully to the satisfaction of Oral Defense Committee. The Committee recommends for the award of Ph.D. Degree.

(Signature of Supervisor) **(Signature of External Examiner)**

ACKNOWLEDGEMENTS

First and foremost, I am really indebted to my thesis supervisor **Dr. Vinod Kumar** who provided me precious opportunity to pursue research under his guidance. His guidance put me on a new platform of wonderful and challenging materials world. His unique guiding quality, interest, working enthusiasm and analytical approach towards the experimental results impressed me so much. It is great honour for me to work with him. I would like to express my sincere thanks to **Prof. A.K. Bhargava**, **Prof. M. K. Banerjee, Dr. Rahul Singhal, and Dr. S. K. Gupta** for being in my DREC committee as well as for their encouragement, analytical insights and recommendations. I further extend my thanks to all the staff members of **Materials Research Center (MNIT Jaipur), ACMS (IIT Kanpur)and RRCAT (Indore)**for providing characterization facilities. Thanks are also due to the **CGCRI (Kolkata) and M/s TechnoS Instruments (Jaipur)** for providing materials processing facility and **DST-SERB** for the financial support. I express my deep appreciation to my friends and co-workers **Dr. Pramod Kumar Sain, Mr. Devesh Kumar**, **Mr. Robin Gupta, Mr. Ankit Goyal**, **Mr. Arun Kumar, Mr. Anil Kumar, Mr. Saurav Kumar, Mr. Sachin Rathi, Mr. Vijay Prakash Sharma, Mr. Akshay Kumar** and all the post graduate students of the department of Metallurgical and Materials Engineering, MNIT Jaipur for their moral support and help. I would like to extend my sincere thanks to all the faculty and staff members of MNIT, Jaipur for their support during my Ph.D. I would like to thank **my parents, sister, brother in law and other family members** for their unconditional support. Without them, this thesis would not be possible.

(Ornov Maulik)

Abstract

Novel $AlFeCuCrMg_x$ (x = 0, 0.5, 1, 1.7 mol) high-entropy alloys (HEAs) were synthesized by mechanical alloying and spark plasma sintering/conventional sintering. The effect of Mg content on the phase evolution of as milled and bulk HEAs was investigated using X-Ray diffractometry (XRD), transmission electron microscopy (TEM) and selected area electron diffraction (SAED) pattern analysis. The particle morphology and composition of HEAs were investigated by scanning electron microscopy (SEM). The phase stability with respect to temperature has been determined by differential scanning calorimetry (DSC)/Differential Thermal Analysis (DTA). Local atomic structure of as milled $AlFeCuCrMg_x$ (x= 0.5, 1, 1.7) high entropy alloys (HEAs) was studied by Fe, Cr and Cu K-edge X-ray absorption near edge spectroscopy(XANES) and extended X-Ray absorption fine structure (EXAFS) spectroscopy. Thermodynamic parameters for $AlFeCuCrMg_x$ alloy is calculated and analyzed to explain the formation of a solid solution. Further, based on the present study material-structure-processing-property correlation has been established in the $AlFeCuCrMg_x$ (x = 0, 0.5, 1, 1.7 mol) HEAs. Also, a mathematical model has been proposed by utilizing conventional strengthening mechanisms. Phase analysis of as milled $AlFeCuCrMg_x$ alloy powders revealed formation of dual phase solid solution. Phase evolved after mechanical alloying has been conferred with calculated thermodynamic parameters. XRD of the bulk alloys revealed the formation of AlFe type, BCC, and Cu_2Mg type phases. TEM bright field image and selected area diffraction pattern (SAED) revealed the formation of tetragonal Cr precipitates within the Cu_2Mg phase of $AlFeCuCrMg_x$ alloys (x = 0.5, 1, 1.7).In addition to these studies possibilities for other light weight Mg-Ca containing HEAs is also being searched upon. The Mg content in $AlFeCuCrMg_x$ (x= 0, 0.5, 1, 1.7 mol) HEAs has a significant effect on hardness, increasing to a peak hardness of 853 HVN for $AlFeCuCrMg_{0.5}$ alloy of spark plasma sintered alloys. On the other hand, conventionally sintered bulk $AlFeCuCrMg_x$ (x = 0, 0.5, 1, 1.7) HEAs show peak hardness of 678 HVN for $AlFeCuCrMg_{1.7}$ alloy. A heat treatment of spark plasma sintered alloys was performed at 470^{o}C, 600^{o}C and 820^{o}C and the structure-property relationship has been proposed.

Table of Content

List of Figures

List of Table

List of abbreviations

HEA	High Entropy Alloy
MA	Mechanical Alloying
SPS	Spark Plasma Sintering
XRD	X-Ray Diffraction
SEM	Scanning Electron Microscopy
BSE	Back Scattered Electron
EDS	Energy Dispersive X-Ray Spectroscopy
TEM	Transmission Electron Microscopy
STEM	Scanning Transmission Electron Microscopy
DSC	Differential Scanning Calorimetry

Chapter 1: Introduction

1.1 Background

Lightweight materials are the primary focus area for research in the 21st century [1]. Lower density of these materials makes them a suitable candidate for the applications involving energy efficiency like transport and aerospace industries [2, 3]. In the recent times lot of research work on the varieties of lightweight materials with the densities from as low as 0.80 g/cm^3 of the polymers to around 5 g/cm^3 for titanium alloys have been carried out [1]. Aluminium (Al) alloys (density ~ 2.7 g/cm^3) are most widely used engineering material in automobile and aerospace applications due to their superior specific strength, good corrosion/oxidation resistance, high ductility and cost efficient [1,4]. Although Al alloys are also associated with some limitations like lower strength and moderate modulus of elasticity.

Magnesium alloys (density ~ 1.74 g/cm^3) generally compete with the Al alloys for the lightweight applications. Advantages of magnesium alloys are low in density, comparable specific strength and very good damping capacity [5]. Although with these advantages there are large number of limitations associated with these alloys like low tensile strength, limited formability at room temperature, very poor corrosion resistance and high costs compared to Al alloys [5, 6]. There have been lot of research undergoing for improving the limitations associated with these category of lightweight alloys yet other alloy systems can also be designed and looked upon for filling the gap for the energy efficient materials. Similarly, titanium and beryllium alloys are also used in light weight applications such as aircraft body due to better specific strength but has a major disadvantage of being expensive [1].

High entropy alloys (HEAs) or multi component alloys are the new breed of alloys first reported by J.W. Yeh in 2004 [7]. Initially, Yeh defined HEAs as the alloy consisting of five or more than five principal alloying elements of concentration 5-35 at. % [7, 8]. Advantage of using HEAs as an engineering material is their properties which are independent of constituent elements and dependent upon the microstructure. It has been

reported that HEA shows remarkable properties such as high specific strength, good thermal stability, high oxidation resistance and better wear resistance having a potential application in automobile and structural applications [9, 10]. Also, some HEAs have excellent thermal stability and resistance to softening at high temperature making them uniquely useful for applications such as turbine blades, and refractory materials.

In the recent years ongoing effort are being made by researchers to design a lower density (light weight) HEA with a desired microstructure and superior properties for the potential applications in automotive and aerospace industries. Some of the efforts have been made to design alloys based on lower density elements such as aluminium (Al), magnesium (Mg), beryllium (Be) and titanium (Ti). The major difficulties in order to synthesize HEAs containing lower density elements is there higher reactivity with an environment, comparably lower melting point and cost efficiency.

Numerous techniques have been used to synthesize HEAs so far such as arc melting, induction melting, solid state processing technique and direct laser fabrication methods [9-11]. Most of the work reported suggests that melting and casting methods are widely used for the synthesis of HEAs. Major advantage of melting and casting method is reduced synthesis time, cost efficient, and energy saving. Although in case of light weight HEAs difference between the melting point of low density elements and other transition elements makes it difficult to synthesize light weight HEAs by this method. Mechanical alloying (MA) is solid state processing technique which comprises of synthesis of alloy systems from the blend of elemental powders. MA involves repeated cold welding and fracturing of the elemental powders by the impact of balls and vials during milling action resulting in the formation of equilibrium or non-equilibrium phases of alloy. Thus, MA is the only techniques by which alloys can be synthesized even when there is high positive enthalpy of mixing between the individual elements [12]. Further, as milled alloy powders after MA can be consolidated by compaction and sintering operation to form the bulk alloys. There are various techniques for the synthesis of bulk alloys from the as milled powders such as conventional pressure less sintering, hot isostatic pressing, and spark plasma sintering (SPS). It can be pointed out that SPS is the most cost effective and energy saving consolidation technique compared to all other techniques. SPS comprises

of pulsed DC current passing through a powder compact and graphite dies which results in compaction and densification through internal heating in order to approach the theoretical density value. The advantages of SPS include retention of nanostructured materials due to very short heating times, the low pressure required for compaction and better grain to grain contacts.

1.2 Goals of the Research Project

The demand of lightweight materials is increasingly becoming a necessary requirement for better energy efficiency in transport sector such as automotive and aerospace applications. As mentioned above the conventional light weight alloys like Al-based alloys and Mg-based alloys have poor mechanical properties compared to steel and also not suitable for high temperature applications. Light weight alloys such as Ti based alloys are not cost effective. The above shortcomings and requirements motivated the investigator to undertake the research to synthesize a light weight HEAs. Lightweight HEAs can have outstanding properties such as higher strength to weight ratio, and better mechanical property such as hardness.

Still there are major complications in designing of lightweight HEAs as most of the elements in periodic table possessing lower density are having very poor corrosion/oxidation resistance, lower strength, and lower hardness. Also, most of these elements are immiscible with transition group of elements in periodic table due to their varying atomic radius and high positive enthalpy which leads them to form intermetallic phases rather than solid solution. Magnesium (Mg) being the lightest structural metal elements in the periodic table can be incorporated in the HEAs to achieve low density and cost effectiveness with good mechanical properties.

Lot of research has been going on in the recent days to design new alloy systems with improved properties and low density which could be suitable for different engineering applications. Also, an on-going effort is focused on empirically correlating the phase evolution and thermodynamic parameters of the HEAs and understanding the structure-

property relation. Therefore, the present research work focuses on the designing of alloy by introducing varying concentration of lower density elements with the transition elements to synthesize HEA which are lighter in weight along with cost effectiveness.

1.3 Outline of the Thesis

The present research work is split into 8 chapters including an introduction to the high entropy alloys. In Chapter 2 contains a review of thermodynamic parameters proposed and some previous work on the phase formation, stability, properties of light weight HEAs. The methodology for the alloy preparation, phase characterization and properties has been described in Chapter 3. In Chapter 4 the novel $AlFeCuCrMg_x$ (x = 0, 0.5, 1, 1.7 mol) HEAs were synthesized by mechanical alloying. The effect of Mg content on the phase evolution of HEAs was investigated. Also, phase formation of the present HEAs has been correlated with calculated thermodynamic parameters. Further, the spark plasma sintering of as-milled $AlFeCuCrMg_x$ alloys and the study of phase evolved after sintering are studied in Chapter 5. The phase evolved after sintering in these alloys has been considered using thermodynamic parameters and the structure-property relationship has also been proposed by conventional strengthening mechanism. Chapter 6 discusses an attempt to synthesize Mg-Ca-Al based light weight HEAs, such as AlMgCaNiCu, $(AlMgCa)_{1.33}(NiCu)_{0.5}$ and AlMgCaFeCr alloys, by mechanical alloying and spark plasma sintering. Chapter 7 and Chapter 8 discuss about the conventional sintering and heat treatment of spark plasma sintered $AlFeCuCrMg_x$ (x = 0, 0.5, 1, 1.7 mol) alloys respectively.

Chapter 2

Literature Review

2.1 Background

Materials are the basic building block for the development of human civilization. From the Bronze Age to the modern age, man has seen much of groundbreaking developments in the field of materials science and metallurgical engineering. Ever increasing demands on the engineering materials in the applications like transportation and building materials have opened doors to alloying pure metals with some other elements. In contrast, thefirst alloy discovered around 2500 BCE were those of copper-arsenic and copper-tin [13]. First industrial revolution in the 18^{th} century led to innovation and development of new alloy systems which had enhanced the knowledge and expertise of humanity in the field of material science and technology. Moreover, these alloys showed superior mechanical properties than the pure metals and are used in major part of engineering applications even today. Majorly steel, an alloy of iron and carbon has been widely usedfrom ages due to its superior properties like good strength, better oxidation/corrosion resistance, and superior wear resistance. Although first successful synthesis of aluminum alloys and magnesium alloys in the 1900s led to bring the concept of energy efficiency in different applications such as transportation, aerospace, etc. In the later years many improved alloy systems like nickel alloys, titanium alloys had been synthesized for high-temperature applications like in turbine, etc.

Although the concept of multi principle alloys had not been explored in the first half of 20^{th} century [8, 9, 14]. In 1970s Prof. Brain Cantor first thought of multicomponent alloys but he was unable to perform work due to lack of funding. Moreover he was also unable to persuade other people in this field. First work on multicomponent alloys was in 1981 by his undergraduate student. Surprisingly, he found single phase FCC microstructure with excellent mechanical properties in $Fe_{20}Cr_{20}Ni_{20}Mn_{20}Co_{20}$ multicomponent system but this work was not published. Much later his undergraduate

student Peter Knight and Isaac Chang repeated the work and found the same result and the results was published in 2004 [15]. Independently Prof. J.W. Yeh also reconnoitered the concept of multicomponent alloys since 1995. First paper on concept of HEA was published in Advanced Engineering Materials in 2004 [7]. This paper had reported the formation of single phase solid solution in the multicomponent alloy system and explained the related theory accompanying the solid solution formation. Moreover he also used for the first time term HEA to designate multicomponent alloy systems.

Prof. S. Ranganathan independently explored the concept of multicomponent alloys and bulk metallic glasses and published a paper on the principle of multi-metallic cocktails in 2003 which primarily became one of the core effects in the stabilization of solid solution in the HEAs.

2.2 Concept of High Entropy Alloys

High-entropy alloys constitute of multi-principal elements ($\geq$ 5) with each element having an atomic percentage of 5 to 35 [16-21]. Some studies suggest the definition must include that HEA must be single-phase solid solution [22] and in others the definition is widened to include 4 component systems. There is no right or wrong answer, and the appropriate approach will depend on the intent of the work being performed. Thus it can be said that there are multiple definition of high entropy alloy based on composition, phase etc. so as to allow researchers to explore the field with flexibility [23].

Microstructure and exceptional properties of high-entropy alloys are explained to be due to four core effects [9, 10, 24]. These four effects are high entropy, severe lattice distortion, sluggish diffusion and cocktail effect which will be discussed in this section.

2.2.1 High Entropy

Entropy is the thermodynamic properties which deal with the measure of the disorderness of the system given by Eq. 2.1 [9,10,14]

$$S = k\ln W \qquad (2.1)$$

where k = 1.38 X 10^{-23} J/K is Boltzmann's constant and W is the no. of possible microstates in a macroscopic state.

Thermodynamically every alloy system is in an equilibrium state when its Gibbs free energy of mixing ($\Delta G_{mix,}$ Eq. 2.2) is minimum.

$$\Delta G_{mix} = \Delta H_{mix} - T\Delta S_{mix} \qquad (2.2)$$

Eq. 2.2 suggests that the minimization that ΔG_{mix} always depends on enthalpy of mixing (ΔH_{mix}) and entropy of the mixing (ΔS_{mix}). In the case of HEAs ΔS_{mix} becomes large which tends to reduce ΔG_{mix} which will be more negative making the system more stable. Thus, for a random alloy system with N no. ofelements, ΔS_{mix} is given by Eq. 2.3

$$\Delta S_{mix} = -R\sum_i c_i ln c_i \qquad (2.3)$$

where c_i is the molar content of i^{th} element, R (8.31 J/K mol) is the universal gas constant. It is to be noted that here that we are only considering the configurational entropies of the system as it is assumed that in random solid solution alloy systems containing N elements the configurational entropy plays a major part for stabilization [7]. Configurational entropy of mixing becomes maximum for equiatomic compositions and is given by Eq. 2.4

$$\Delta S_{mix} = R\ln N \qquad (2.4)$$

For ternary and quaternary equiatomic alloy systems, the configurational mixing of entropy is 1.1R and 1.3R and are sometimes classified as medium entropy alloys [25, 26]. It was suggested by Yeh [27] that the system can be only called as high entropy alloy when its configurational mixing of entropy is equivalent or greater than 1.6R. However, for a real alloy system other entropy terms like magnetic, electronic and vibrational

entropies also play there part thus making overall entropy much more complicated to explain the phase stabilization in the alloy.

2.2.2 Lattice Distortion Effect

The multi-element matrix in the solid solution for the HEAs leads to high lattice strain and stress mainly due to the different atomic radius associated with the individual elements. In addition to the atomic size difference other factors such as bonding energy and crystal structure also have a significant contribution for the higher lattice distortion. Overall lattice distortion in HEAs is more severe compared to conventional alloy systems [28]. Fig 2.1 shows the distorted lattice due to atomic size difference in case of HEAs.

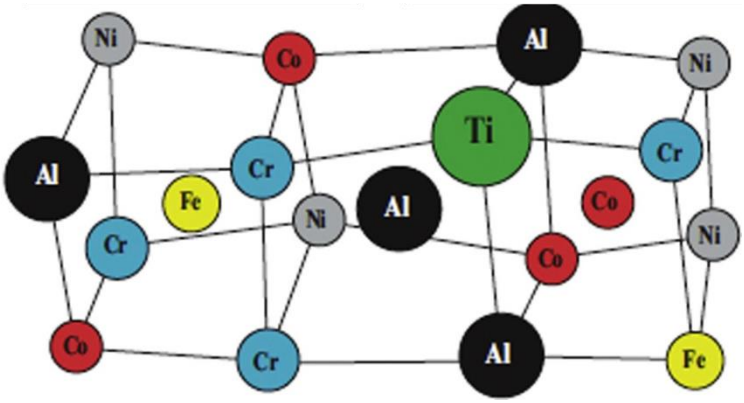

Figure 2.1 Schematic illustrations of crystalline structures of a solid solutions composed of multi-principal elements [10].

X-Ray diffraction (XRD) studies suggested that due to the effect of severe lattice distortion in case of HEA, the intensity of the peaks is smaller than the perfect lattice [29]. The severe lattice distortion in HEAs greatly influences the mechanical properties and the thermal resistance. For example, the hardness of BCC structured $Al_3CoCrCuFeNi$ alloy is found to be 655 HV, and that of FCC structured $Al_{0.5}CoCrCuFeNi$ alloy is 200 HV. Murty et al. [9] has suggested the lower hardness in the case of FCC structured alloy is due to the smaller fraction of unlikely atoms in the nearest neighbor which results in smaller distortion thus lower hardness. Moreover, the large phonon scattering causes low thermal conductivity in the HEAs. Electric resistance also increases because of the distortion [10].

2.2.3 Sluggish Diffusion Effect

Diffusion kinetics is an important phenomenon for the formation of a new phase in any alloy system. It had been proposed that the sluggish diffusion in HEAs lowers the diffusion rate of atoms which in turn slows the phase transformation rate in the multi-element matrix of a phase. The formation of new phases from the old phase requires cooperative diffusion of many different kinds of atoms to accomplish the partitioning of the composition. Tsai et al. [30] had made the first study on the diffusion kinetics CoCrFeMnNi HEAs. The study concluded that the sequence in the order of decreasing diffusion rate is Mn, Cr, Fe, Co, and Ni. Also, the diffusion coefficients were found to be smaller than the pure FCC metals and Fe–Cr–Ni (– Si) alloys.

However, the normalized activation energies Q/T_m in the present HEA (Fig 2.2) were higher for the CoCrFeMnNi alloys than other references. It has been found that as a number of constituent elements in the matrix increase the degree of sluggish diffusion increases. Thus, these results concluded that sluggish diffusion effect exists in HEAs. It has also been suggested that slower diffusion rate exists due to the abundant low lattice potential energy (LPE) sites that serve as a trap and hinder atomic diffusion. Therefore, larger LPE fluctuation in HEA leads to higher normalized activation energies and a lower diffusion rate leading to slower diffusion in HEAs. Further Kulkarni and Chauhan [31] also studied interdiffusion coefficients of Fe-Co-Ni-Cr system. Study concluded that the value of interdiffusion coefficients shows sluggish diffusion kinetics having an order of 10^{-16} m^2/s. Also, it was suggested that in case of HEAs, single atoms will only jump towards the another atoms if there is relatively higher negative heat of mixing and jump away if there is having relatively higher positive heat of mixing. Thus, the diffusion of atoms in HEAs essentially depends upon relative thermodynamic parameters of other components. Moreover, it is usual that sluggish diffusion effect in alloy system tends to form fine precipitates and controlled grain structure which in turn improve the overall strength of HEAs.

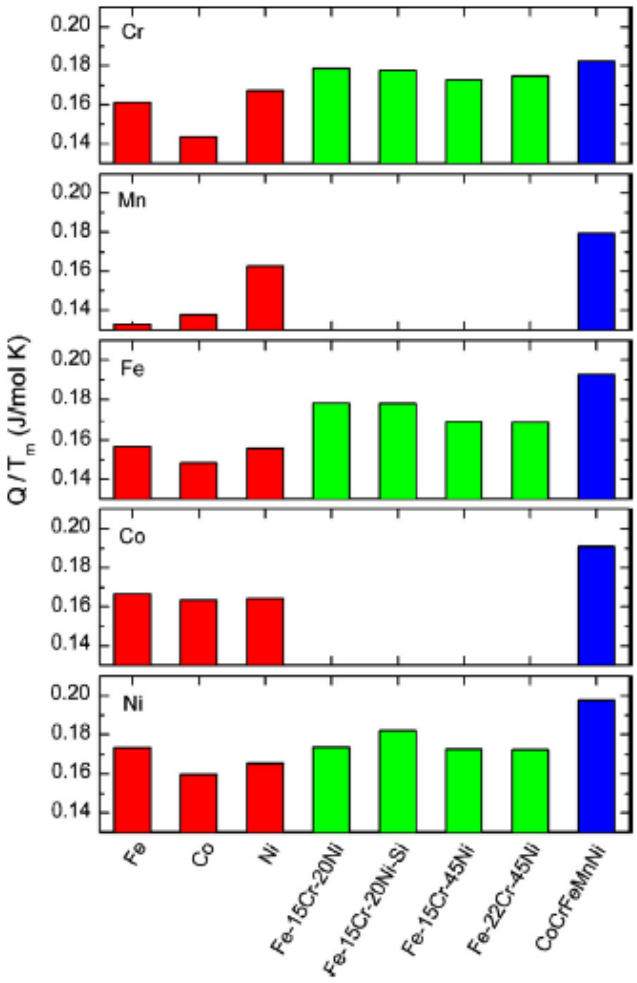

Figure 2.2 Comparison among the melting point normalized activation energy of diffusion for Cr, Mn, Fe, Co, and Ni in different matrices: pure metals, stainless steels, and high-entropy alloy CoCrFeMnNi [30].

2.2.4 Cocktail Effect

Cocktail effect was first given by Prof. Ranganathan [32]. It was suggested that there could be unexpected properties obtained after mixing many elements in an alloy system, which could not be obtained from any independent element. It implies that alloy can be adjusted by finely adjusting the number and composition of the individual elements. The 'cocktail' effect allows researchers to remain open for unexpected results that may come due to larger possibilities of the combination of different elements in case of HEAs [23].

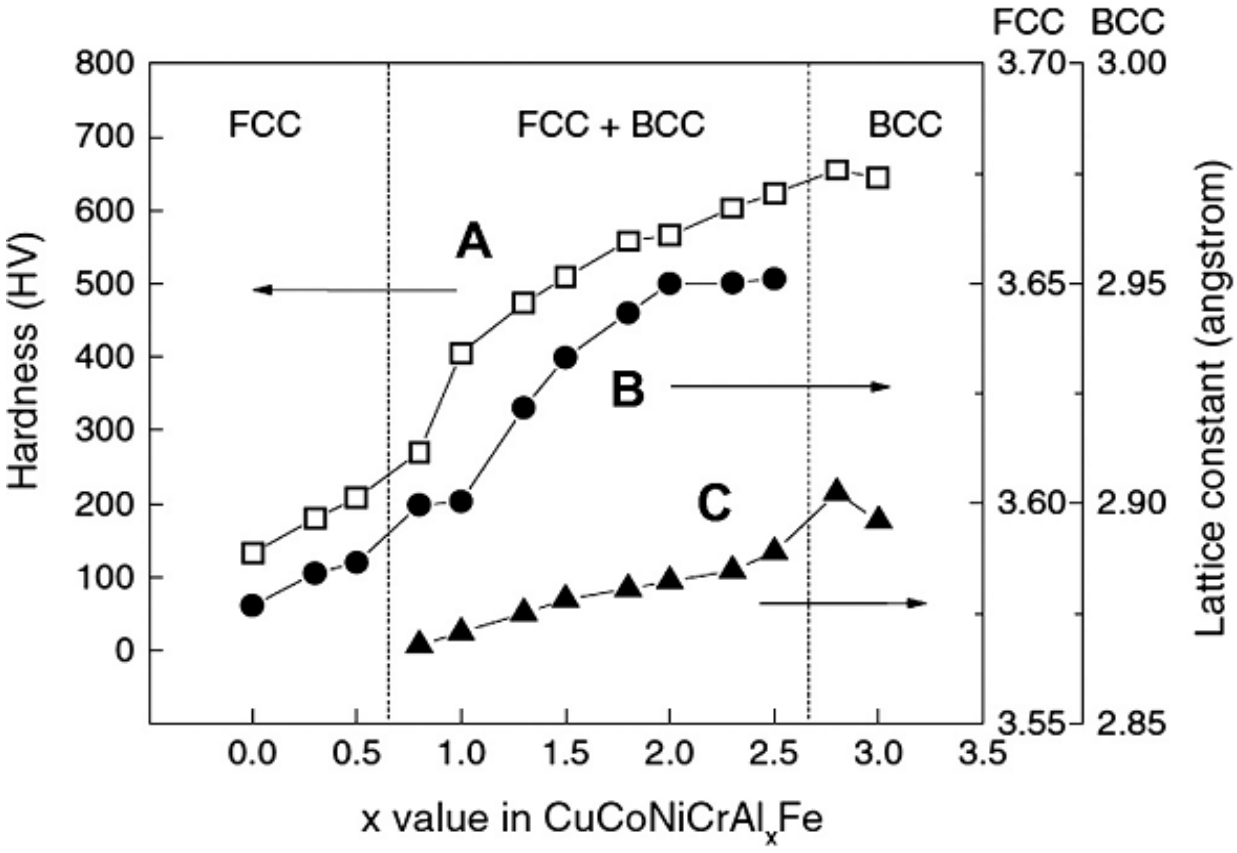

Figure 2.3 Hardness and lattice constants of a $Al_xFeCuCrCoNi$ alloy system with different x values: (A) hardness of $Al_xFeCuCrCoNi$ alloys, (B) lattice constants of an FCC phase, (C) lattice constants of a BCC phase [36]

The cocktail effect in HEAs can be understood by two examples first, $Al_xFeCuCrCoNi$ [17, 33] HEA (Fig 2.3) prepared by casting route shows variation from complete FCC microstructure at Al content x = 0.5 with hardness value 133 HV to complete BCC microstructure at Al content x = 3 and hardness 653 HV. Secondly, change in the microstructure and properties as function of Al element content in $CoCrFeNiAl_x$ HEAs (Fig 2.4) [34].

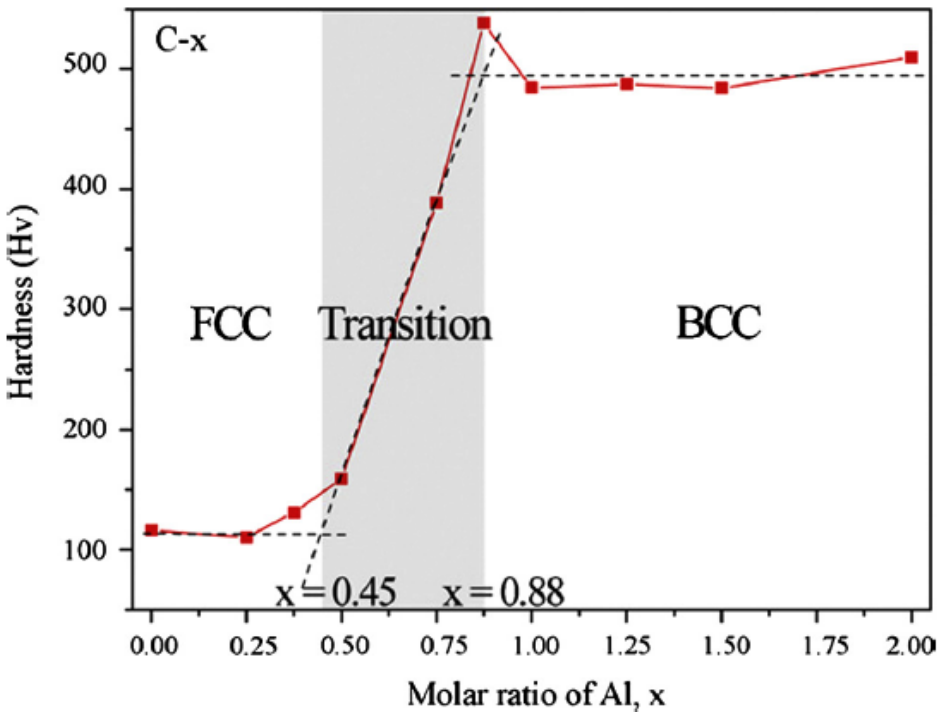

Figure 2.4 Hardness of a CoNiCrFeAl$_x$ alloy system with different x values, the Cu-free alloy has lower hardness than that of the CoCrFeNiAl$_x$ alloy [37].

The hardness of the FCC phase does not vary too much with changing the Al content from 0 to 0.45, while the hardness of the BCC phase decreases from about HV 538 to HV 480 as the Al content increases from 0.88 to 2.0. It can also be suggested from these two examples that addition of single Cu element plays an important role in the stabilization of FCC phase for Al$_x$CoCrCuFeNi HEAs and absence of Cu causes BCC + FCC phase region narrower in case of CoCrFeNiAl$_x$ HEAs.

2.3 Alloy designing through thermodynamic parameters for HEAs

Earlier it was believed that the addition of 5 or more elements in equal composition will lead to the formation of intermetallic phase rather than a solid solution due to the different heat of formation and atomic size difference between binary elements. On the other hand, Cantor and Yeh [15, 7] have found that some multi component alloy systems form random solid solution phases which can be explainedon the basis ofthermodynamic parameters between elements supports the formation of solid solution. Formation of solid

solution in conventional binary alloys follows the condition called as Hume-Rothery rules which are being developed to understand the conditions by which one element is soluble into another. Hume-Rothery rules suggested that the solid solubility majorly depends upon the atomic size, crystal structure, electronegativity and valence.

The Hume Rothery rules are stated as follows:

1. The atomic size of the solute and solvent may not differ more than 15%.
2. The crystal structure of the two elements should be same.
3. Electronegativity of the two elements should be same.
4. Valency of solute and solvent should be same.

In the case of HEAs, earlier studies on the microstructure evolution by J.W. Yeh discussed mainlyatomic size difference, crystal structure, enthalpy of mixing, electronegativity. In addition to these effects Tong et al. [33] concluded that high mixing entropy also leads to the formation of the solid solution rather than the formation of intermetallic compounds. However, Otto et al. [22] studied the effects of entropy and enthalpy on the phase stability in HEAs and suggested that phase evolution in HEAs is associated with a minimization of Gibbs free energy, including both enthalpy and entropy contributions. Further, it was concluded that high configurational entropy might rarely form a single phase solid solution. It was also suggested that highest entropy values are obtained in a single phase solid solution and should be called as real HEAs while alloys that consist of multiple phases can be referred to as multicomponent alloys. Therefore, to design and define the formation of solid solution in HEAs different criterions based on the basic thermodynamic parameter such as mixing enthalpy, atomic size misfit, electronegativity, mixing entropy have been defined. In case of HEAs the mixing of enthalpy (ΔH_{mix}) and atomic radii mismatches (δ) was given by Eq. 2.5 and Eq. 2.6 respectively

$$\Delta H_{mix} = \sum_{i=1,i\neq j}^{N} 4\,\Delta H_{AB}^{mix} c_i c_j \qquad (2.5)$$

$$\delta = \sqrt{\sum_{i=1}^{N} c_i(1 - r_i/(\sum_{i=1}^{N} c_i r_i))^2} \qquad (2.6)$$

where $\Delta H_{AB}^{mix}$is the enthalpy of mixing between binary A and B elements, c_i, c_j are the molar content of i^{th} and j^{th} element, r_i atomic radii of ith component. Zhang et al. [35] predicted that simple solid solution may be formed when -15kJ/mol < ΔH_{mix}< 5kJ/mol, and δ < 5% and a 2D plot in support for the criterion is shown in Fig 2.5.

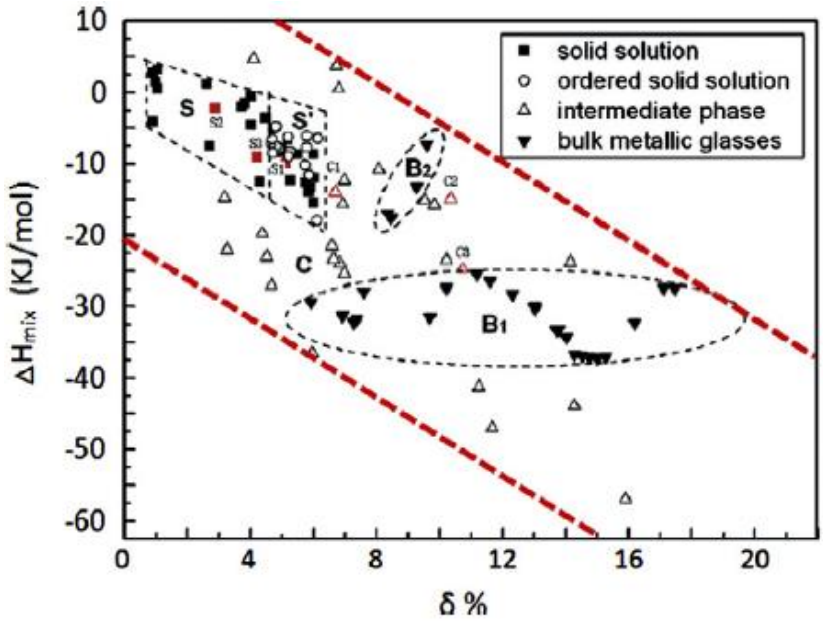

Figure2.5 A phase formation map based on the enthalpy of mixing ΔH_{mix} and the atomic size differenceδ, for the formation of solid solution, ordered solid solution, intermediate phase and bulk metallic glasses.[35]

Similarly, Guo et al. [36] predicted that formation of simple solid solution microstructure is related to ΔH_{mix}, ΔS_{mix} and δ as $11 \leq \Delta S_{mix} \leq 19.5$ J/Kmol, $-11.6 \leq \Delta H_{mix} \leq 3.2$kJ/mol and $\delta \leq 6.6$. Zhang et al. [37] has also defined the criterion for the formation of simple solid solution in case of HEAs as ΔS_{conf} > 13.38J/K mol, -10kJ/mol < ΔH_{mix}< 5kJ/mol, and δ < 4%.

Later other parameters (Ω) for the formation of the solid solution was defined as Eq. 2.7 [38, 39]

$$\Omega = \frac{T_m \Delta S_{mix}}{|\Delta H_{mix}|} \qquad (2.7)$$

Theoretical melting temperature, T_m, of an alloy containing N elements is calculated by relation as given in Eq. 2.8

$$T_m = \sum_{i=1}^{N} c_i \, (T_m)_i \qquad (2.8)$$

It has been proposed that if $\Omega > 1$, then the contribution of $T\Delta S_{mix}$ will exceed that of ΔH_{mix} and HEAs will form a solid solution and in case when $\Omega < 1$, then ΔH_{mix} will be a predominant part, thus resulting in formation of intermetallic compounds in HEAs system. This relationship has been shown by Yang et al. [38] in 2D maps between Ω and δ (Fig 2.6).

Electronegativity also plays an important role in stabilization of solid solution in HEAs. Electronegativity is a tendency of an atom to attract an electron and according to the Hume-Rothery rules high electronegativity of a solute tends to form intermetallic compounds. In, HEAs the electronegativity difference is calculated by the composition of the HEA and not by lattice type, and is given by Eq. 2.9

$$\Delta X = \sqrt{\sum_{i=1}^{N} c_i \, (X_i - X_{avg})^2} \qquad (2.9)$$

Where, X_i is the Pauling electronegativity for the ith element and $X_{avg} = \sum_{i=1}^{N} c_i \, X_i$.

The role of electronegativity on the phase stability of HEAs was described by Dong et al. [40] showing that a topologically closed packed (TCP) structure is stable in HEAs where $\Delta X > 0.133$ (Fig 2.7).

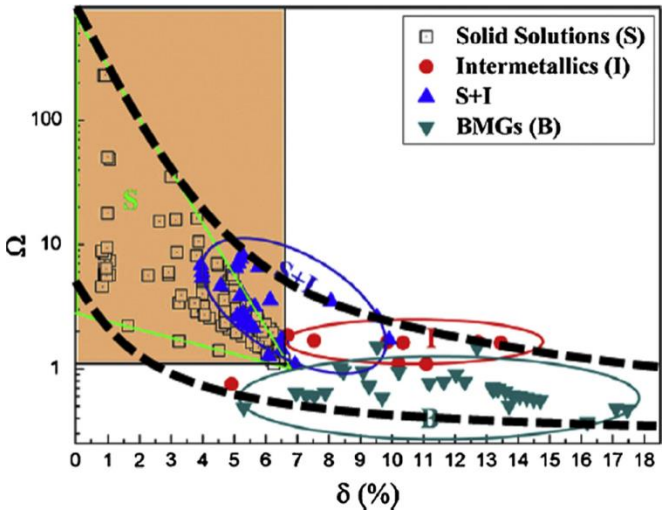

Figure 2.6 Phase-formation map based on the Ωand δ for the multi-component alloys. For the formation of solid-solutions, Ω > 1.1 and δ < 6.6% [381]

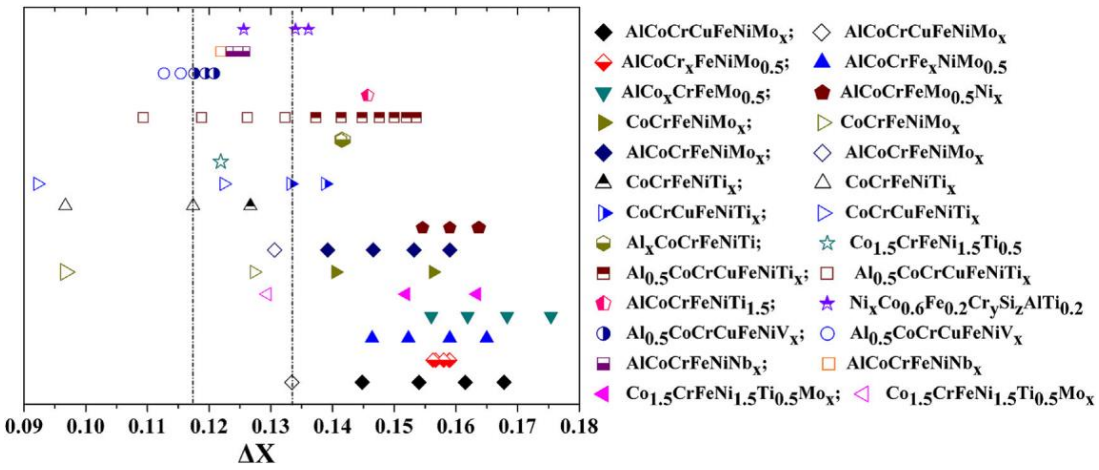

Figure 2.7 Relationship between the DX and the TCP phase stability for the HEA systems containing Mo, Si, Ti, V, and Nb elements. Note on the legend: fully closed symbols and top-half closed symbols for solid solution phase plus TCP phase; fully open symbols for sole solid solution phases [40].

Lu et al. [41] further proposed new parameter based on average value of d orbital energy level ($\overline{Md}$) for HEAs showing that TCP is most stable when value of $\overline{Md} > 1.09$. This method reported in [42] can be estimated by Eq. 2.10

$$\overline{MD} = \sum_{i=1}^{n} C_i \, (Md)_i \qquad (2.10)$$

where C_i is the atomic fraction of component *i* in the alloy, and'Md' is the d-orbital energy level of element *i* in the *M*-element centered cluster in the *i-M* binary solid solution alloy, in which *i* is a solvent and *M* is a solute. The value of $(Md)_i$ of the elements are determined based on the FCC Ni_3Al structure [42].

More recently, Wang et al. [43] proposed α_1 and $\alpha_2$parameters based on multiple alloy systems from literature in which the effect of atomic size and lattice distortion on the ability of HEAs to form solid solution phases were considered. Parameter α_1 is defined by assuming dimensionless displacement of an atom from an ideal atom and hence given by Eq. 2.11 and parameter α_2 is defined by the dimensionless displacement between an atomic pair and its counter pair. α_1 and α_2 are calculated using Eq. 2.11 and 2.12 respectively,

$$\alpha_1 = \sum_{i}^{n} \frac{c_i |r_i - \bar{r}|}{\bar{r}} \qquad (2.11)$$

$$\alpha_2 = \sum_{j \geq i}^{n} \frac{c_i \; c_j \; |r_i + r_j - 2\bar{r}|}{2\bar{r}} \qquad (2.12)$$

Where, c_i and c_j are the molar content of i^{th} and j^{th} component, r_i and r_j are the atomic radii of ith and jth element and $\bar{r}=\sum_{i=1}^{N} c_i \, r_i$.

Recently, Senkov et al. [44] proposed a new parameter for the phase formation in the HEAs assuming linear relationships between enthalpy of formation for intermetallic (IM) phase (ΔH_{IM}) , ΔH_{mix}, and entropy of formation of IM phases (ΔS_{IM}) , ΔS_{mix} for HEAs. It had been concluded that for the formation of solid solution the critical value $\kappa_1^{cr}(T)$given by Eq. 2.13

$$\kappa_1^{cr}(T) = -\frac{T\Delta S_{mix}}{\Delta H_{mix}}(1-\kappa_2)+1 \qquad (2.13)$$

where $0 \leq \kappa_2 < 1$.

should be greater than$\Delta H_{IM}/\Delta H_{mix}$ i.e.

$$\kappa_1^{cr} > \Delta H_{IM}/\Delta H_{mix} \qquad (2.14)$$

The dotted line in Fig 2.8 clearly shows the separation of solid solution alloys from IM-containing alloys. Almost all SS alloys, except two with a BCC structure, fall above the dashed line and almost all IM-containing HEAs fall below this line. Thus it had been predicted that κ_1^{cr}(T) parameter has an improved ability to predict the SS, SS+IM phase formation in the HEAs.

Ye et al. [45] has proposed a parameter which suggests total configurational entropy of mixing S_T for an alloy can be expressed as $S_T = S_C + S_E$, where S_c is the configurational entropy of mixing and S_E is excessive entropy of mixing as a function of atomic packing and their sizes. Further, authors suggested a single dimensionless thermodynamic parameter Ø for the design of HEAs given by Eq. 2.15

$$\emptyset = \frac{S_C - S_H}{|S_E|} \qquad (2.15)$$

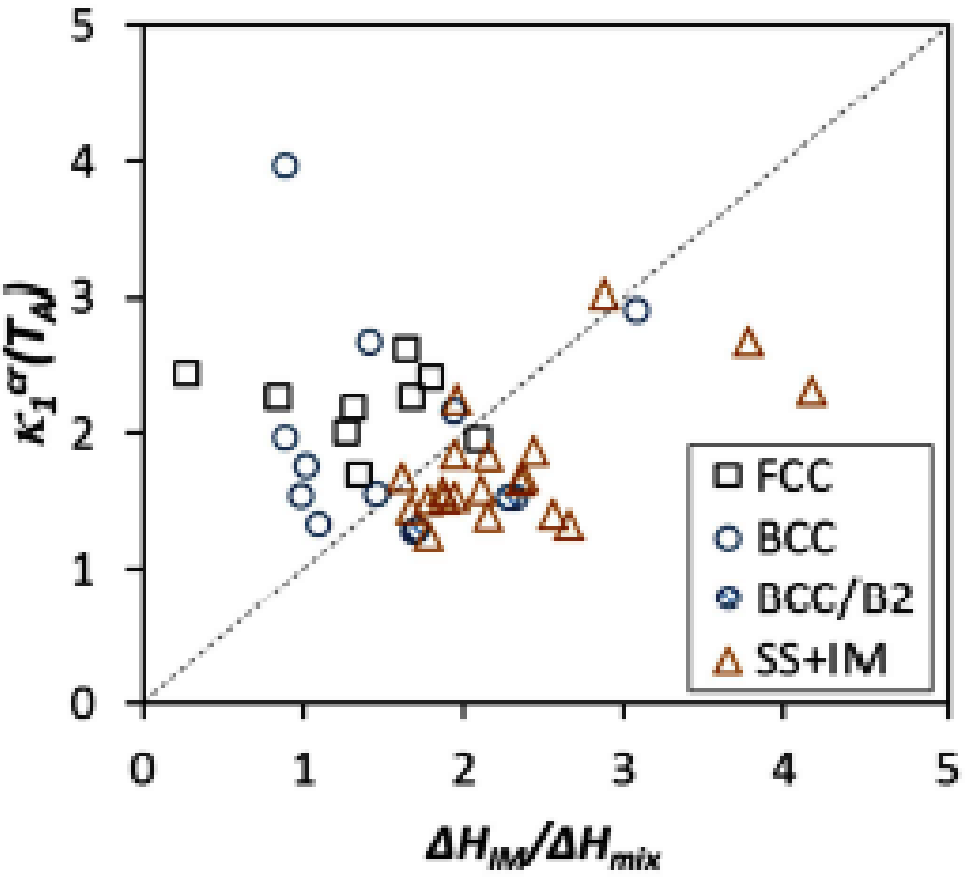

Figure 2.8 $\kappa_1^{cr}(T_A)$- $\Delta H_{IM}/\Delta H_{mix}$ plots for annealed HEAs with different phase contents after annealing [44].

where $S_H = |H_{mix}|/T_m$ is defined as the complementary entropy derived from the enthalpy $|H_{mix}|$.It was observed that HEA tends to display a multi-phase structure when $Ø<Ø_C$ while a single-phase solid solution when $Ø > Ø_C$ where $Ø_C$ is critical value ~ 20.

Caraballo et al. [46, 47] also discussed the formation of solid solution microstructure based on the lattice distortion and introduced two new parameters i.e. interatomic spacing mismatch (s_m), and the bulk modulus mismatch (K_m). s_m and K_m describe separate regions displaying solid solutions, intermetallic, and bulk metallic glasses (Fig 2.9) .

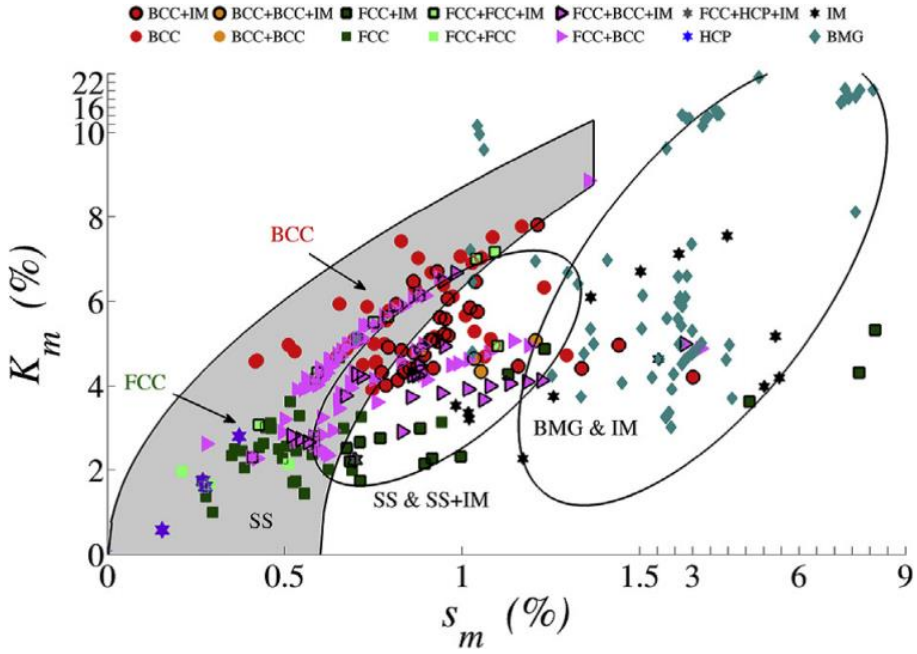

Figure 2.9 Interatomic spacing mismatch s_m vs. bulk modulus mismatch K_m [47].

All the above discussed parameters are effective in predicting the formation of solid solution. However, these parameters generally do not give a general idea about the type of the crystal structure obtained. To predict the crystal structure of HEAs Guo et al. [48] suggested that valence electron concentration (VEC) is an important parameter for deciding the formation of FCC, BCC or mixed phases. It was reported that only BCC phase will form when VEC < 6.87, both BCC and FCC will form when 6.87 < VEC < 8 and only FCC phase will form when VEC > 8. Later Tsai et al. [49] also used VEC to demarcate the σ phase formation in HEAs (Fig 2.10).

The stabilization of solid solution is also dependent on the number of the itinerant s and p and total number of valence electrons (e/a) [50]. Also, it was observed that BCC solid solution only forms for 1.8 < e/a < 2.3 and FCC microstructure forms for 1.6 < e/a < 1.8. Further, a criterion for the designing a new HEA is by selecting the multi elements with $\delta < 6\%$, $\Delta X < 6\%$.

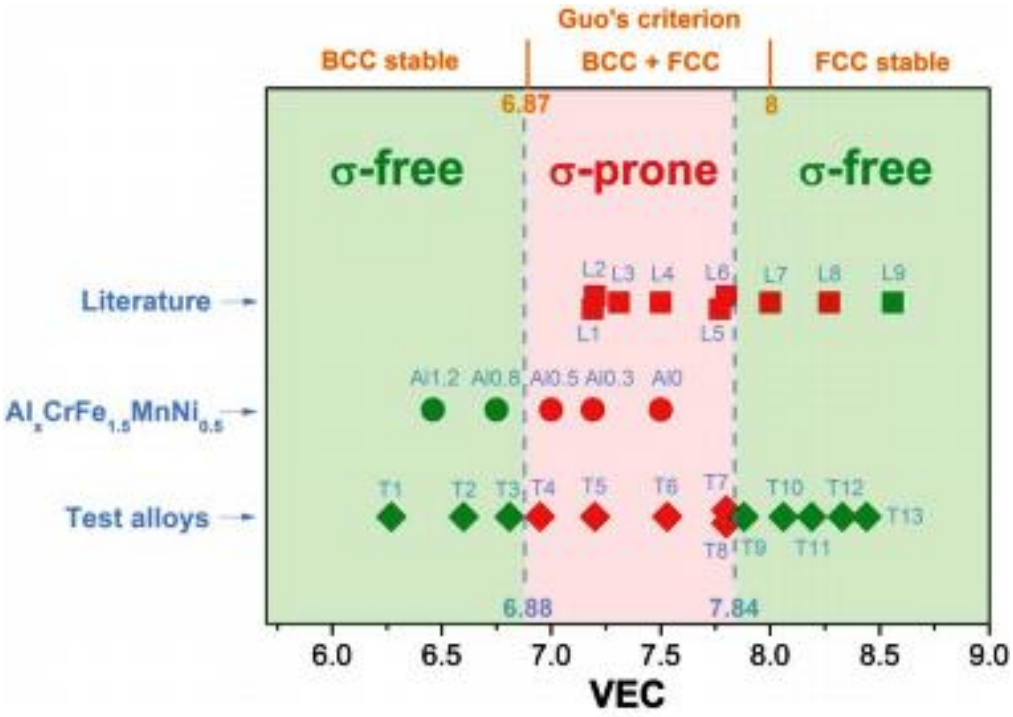

Figure 2.10 Conditions for the phase formation in HEAs [51].

Apart from all these models recently, Laurent-Brocq et al. [51] suggested that higher value of configurational entropy is not sufficient to form a simple solid-solution in HEAs. Further, it had been concluded that all the existing thermodynamic models, poorly predict the range of formation of a solid-solution. Moreover, it was suggested that the current definition of high entropy alloys is not appropriate as it does not provide distinction between multi-component alloys i.e. the alloy having the multiphase microstructure and HEAs. Thus, a new definition, based on structural, physical, chemical or mechanical parameters, is required.

Recently a new alloy designing based on Pettifor map for AB compounds with 1:1 stoichiometry was developed for HEAs. The Pettifor map is tabulated according to the Mendeleev number for the elements. Tackeuchi et al. [52] utilized Pettifor map for the information about the structure of binary $A_{50}B_{50}$ alloys and has been shown in accordance with the mixing enthalpy (ΔH_{mix}) on the basis of Miedema's model.

2.4 Synthesis of HEAs

Several different methods have been adopted for the synthesis of HEAs such as casting route, powder metallurgical route, coating and spraying. Mostly all the methods are being discussed in detail in this section.

2.4.1 Casting Route

Melting and casting route has been widely used for the synthesis of conventional alloys and HEAs. Up till now the maximum number of HEAs reported is synthesized by melting and casting route. Melting and casting route has advantages such as reduced synthesis time, cost efficient, and energy saving which gives it an edge over other alloy synthesis techniques. Although the major limitation of this technique is that high temperature leads to the evaporation of low melting point elements like Mg, Zn and Mn which leads to change in the stoichiometry of the alloy during synthesis. Arc melting is most commonly used for the synthesis of HEAs [17, 18, 20, 21]. Moreover, the advantage of using an arc melting method is its ability to attain high temperature (~ 3000^{o}C) which enables it to melt most of the elements in periodic table. Basic limitations involved in the synthesis of HEAs through this route is that at low cooling rates typically dendritic and interdendritic microstructures are formed in HEAs due to elemental segregation. Singh et al. [54] reported decomposition in multi-component AlCoCrCuFeNi HEAs which showed formation of interdendritic region as well as dendritic region. Similarly, Senkov et al. [55] while studying microstructure of WNbMoTa and WNbMoTaV HEAs reported that the dendritic structures are enriched with heavier elements than interdendritic regions. A rapid cooling of HEAs generally favors the formation of single phase solid solution [56]. These results employed that stabilization of the solid solution microstructure is more dependent upon cooling kinetics rather than thermodynamics of the system in case of HEAs synthesized by melting and casting route. Some of the rapid cooling synthesis techniques in HEAs are splat quenching, melt spinning, injection casting, suction casting, and drop casting.

Another technique that involved melting and casting is the Bridgman solidification (Fig 2.11) for synthesis of HEAs. This method was mainly used for growing single crystalline materials. This technique involved heating of the polycrystalline material above melting

point and slowly cooling it from the end where a seed material is located. A single crystal of the same crystallographic orientation as the seed is grown, and gradually formed along the length of the container.

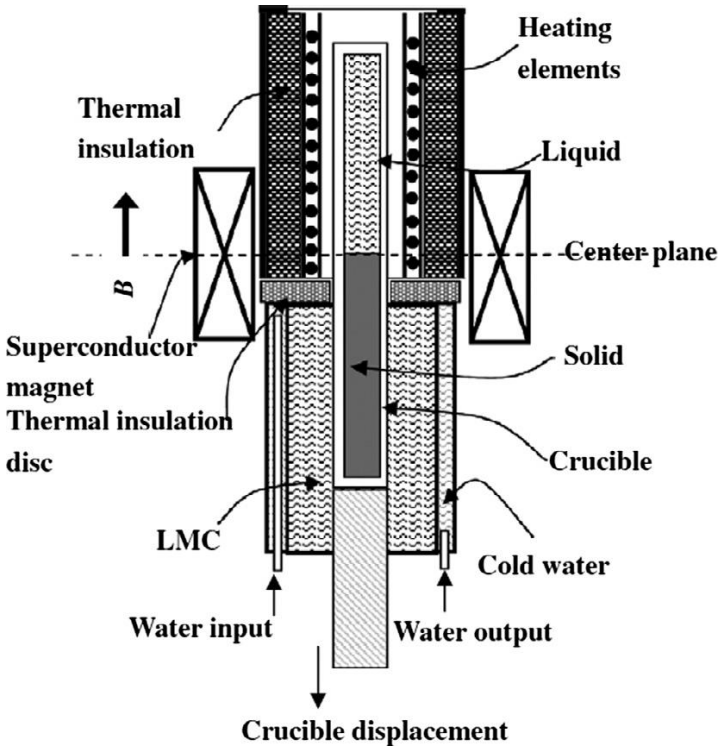

Figure 2.11 Schematic diagram of the Bridgman solidification [57]

Cui et al. [57] reported AlCoCrFeNi alloys, by Bridgman solidification and results indicate that the microstructure constitutes of the finer dendritic region and decreased the concentration difference between the dendritic and interdendritic regions due to rapid growth rate and high temperature gradients. Ma et al. [58] reported low withdrawal velocity of 5 μm/s to synthesize single crystal of FCC $CoCrFeNiAl_{0.3}$ using a Bridgman solidification technique.

2.4.2 Laser Fabrication Method

Direct laser fabrication technique is also used for synthesis of HEA [59, 60, 61]. The procedure for synthesis includes two hopper system used to prevent powder segregation. By varying the flow-rate of elemental powder to the melt region the various alloy

compositions were manufactured. To reduce oxide formation high purity argon gas was continuously purged in the sealed melt deposition region. Thus, maintaining an atmospheric oxygen concentration of 10 ppm or less. The depositions were performed on a 15 mm thick stainless steel plate which was locally preheated via laser scanning in the deposition region in order to reduce thermal stress between interface of the deposited material and the plate. Joseph et al. [11] synthesized $Al_xCoCrFeNi$ HEAs using direct laser fabrication, and the resulting microstructure consists of FCC, BCC+FCC and BCC for $Al_{0.3}CoCrFeNi$, $Al_{0.6}CoCrFeNi$ and $Al_{0.85}CoCrFeNi$ HEAs respectively. Also, the microstructure of $Al_{0.6}CoCrFeNi$ resembles widmanstätten structure which is mainly observed in steels.

2.4.2 Solid State Processing Route

Mechanical alloying (MA) is a solid state synthesis technique that allows synthesis of both miscible and immiscible alloy materials starting from elemental powder blends. MA was first developed in 1966 by John Benjamin and his colleagues at the International Nickel Company (INCO). This process uses a high-energy ball mill to favor plastic deformation required for cold welding and reduce the process times.

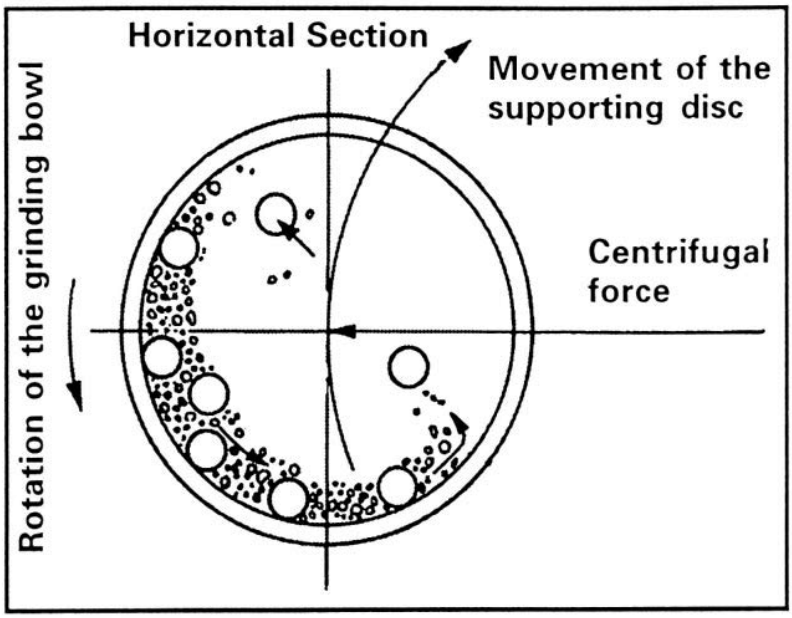

Figure 2.12 Schematic diagram for MA [62].

In the process of ball milling, different elemental powder particles are mixed in a vial containing the ball. The basic mechanism while MA is governed by the cold welded, fractured and again welded during milling action (Fig 2.12). Generally, when two balls while milling collide, some elemental powders are stuck between them,which in turn deforms the elementparticles leading to cold welding and fracture. In the initial hours of milling, the tendency of cold welding of different particles is predominant due to softer nature of particles. The increase in the milling causes particle deformation, which results in increased work hardening thus increasing the brittleness of powder particle causing it to fracture into smaller flakes leading to a reduction of the particle size [9, 10].Further milling tends inter-layer spacing of different elements to decrease and the number of different elemental layers in a particle to increase. Prolonged hours of milling during MA causes heavy deformation into the particles which in turn increasing various crystal defects such as vacancies, dislocations, and stacking faults. The presence of these defect enhances the diffusivity in such a way that an atom of one element is diffused into the lattice of another. There are three different combinations of interactions between particles while MA. These are ductile-ductile interaction, ductile-brittle interaction, and brittle-brittle interaction [62]. Also, MA operation takes place at room or slightly higher temperature and may take prolonged hours of milling for alloying which also causes the refinement of the crystallite size up to the nanometer level. Thus, MA is also the technique which can be used for the synthesis of nanocrystalline materials. Synthesis of high entropy alloys (HEAs) by MA technique was first reported by Varalakshmi et al. [63] and the resulting microstructure consisted of a BCC solid solution.

Compaction and sintering of the as milled powder to produce bulk alloys in solid state processing has mostly been done by conventional method which leads to coarse grains microstructure due to long period of heating. For the synthesis of nanocrystalline microstructure HEAs spark plasma sintering (SPS) technique is generally used for the as-milled alloy powders [64, 65]. SPS technique was first discovered in 1960 although this technique gained its usage much later after 1990s for the producing bulk alloys [66]. SPS finds applications to synthesize wide variety of the bulk metallic, ceramic and nanostructured materials.

The SPS uses DC pulse voltage and current to as milled powder particles. High temperature is generated by spark plasma and spark impact pressure between the surfaces of the powder particles. In this technique the spark discharge between the particles causes the melting of the surface of the particles during the sintering process. Thus “necks” are developed around the contact area between the particles. These necks gradually grow while sintering, resulting in a bulk compact of over 99% density. The action causes high-speed diffusion between the particles due to the high-speed migration of atoms leading to completion of sintering within a short period of time. Thus, it can be suggested that mechanism of sintering of a bulk alloy in the SPS follow four steps namely, generation of plasma, heating, vaporization and melting action on the particle surface, sputtering of the molten particles, neck growth [67]. SPS techniques have many advantages over other conventional sintering techniques such as fast sintering process, energy efficient easy control of sintering parameters like density and porosity, nanocrystalline microstructure etc. However, major limitation associated with this technique is difficulty to fabricate of bigger size sample due to different temperature gradient.

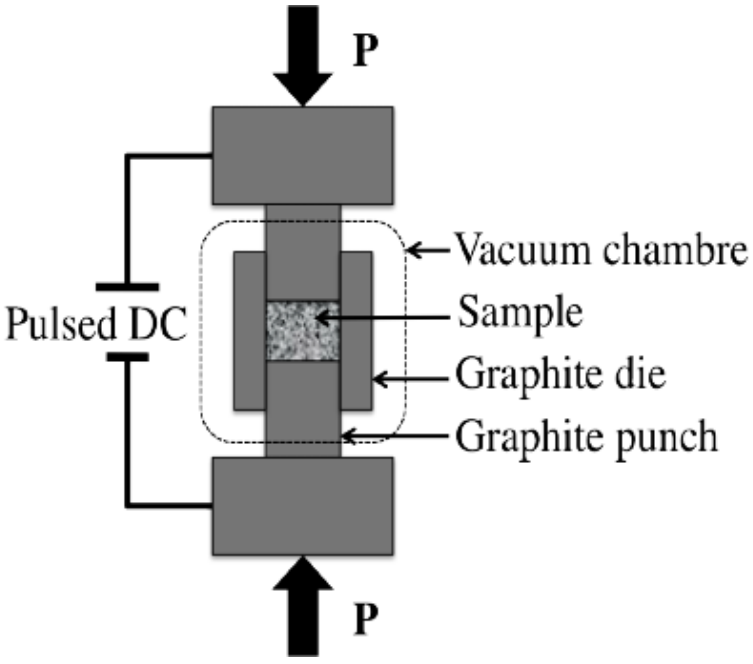

Figure 2.13 Schematic representation of Spark Plasma Sintering [67].

2.4.3 Sputtering

Sputtering techniques are also used for preparation of HEA thin films from the gaseous state. The sputtering is a technique in which thin films are synthesized onto the substrate by atoms as the target is deposited on the substrate by the bombardment of charged gas ions. The sputtering can be divided between DC sputtering, RF sputtering (radio frequency) and magnetron sputtering [68]. Difference between the DC and RF sputtering techniques is that in case of DC sputtering the deposition is mainly governed by the higher values of voltage and argon pressure compared to RF sputtering. As a result the RF sputtering technique is suitable for the deposition of insulating materials. In case of magnetron sputtering, both electric as well as magnetic fields are used to increase the ions path length leading to higher deposition rates (Fig 2.14). Magnetron sputtering is widely used for coating of HEAs. An et al. [69] synthesized a single phase CrCoCuFeNi thin films by RF sputtering route. It was observed that the elements distribution in the thin film is much more uniformly distributed.

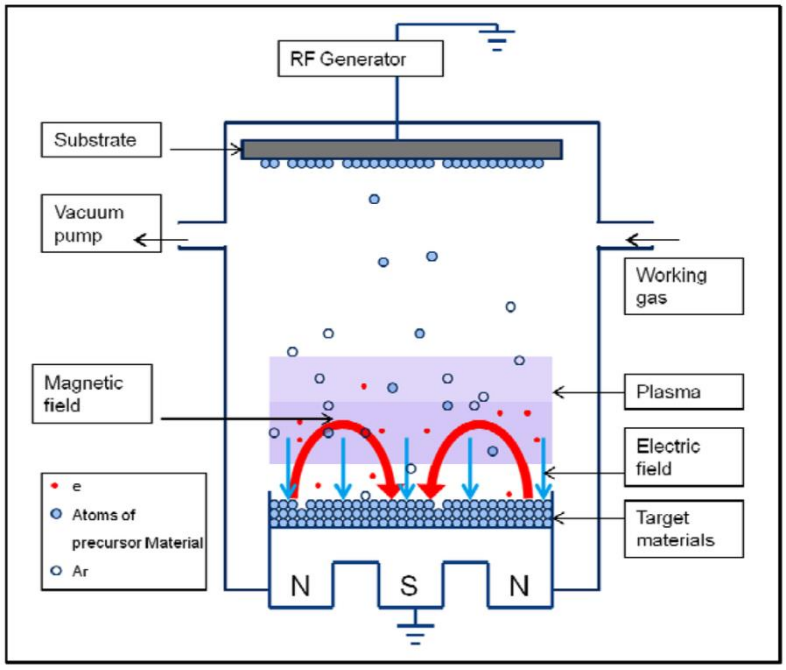

Figure 2.14 Schematic diagram of Magnetron Sputtering[70].

Other techniques such as plasma spray techniques, thermal spray techniques and plasma nitriding are also some of the efficient methods for the synthesis of HEA coatings on the substrate.

2.5 Some unique structures and properties of HEA

In HEAs, different parameters like atomic size effect, enthalpy of mixture and high configurational entropy leads to the formation of simple disordered solid solution. Generally these disordered solid solution phases are having FCC, BCC, or HCP structures leading to some unique properties. Structure and the properties of the HEAs can be varied by changing the content of the elements from equiatomic to near equiatomic compositions. The effect of Al on the microstructure and the properties of $Al_xCoCrFeNi$ alloys have been studied by Yang et al. [70]. XRD studies showed that the $Al_{0.1}CoCrFeNi$ alloys (Fig 2.15(a)) show single phase FCC structure.

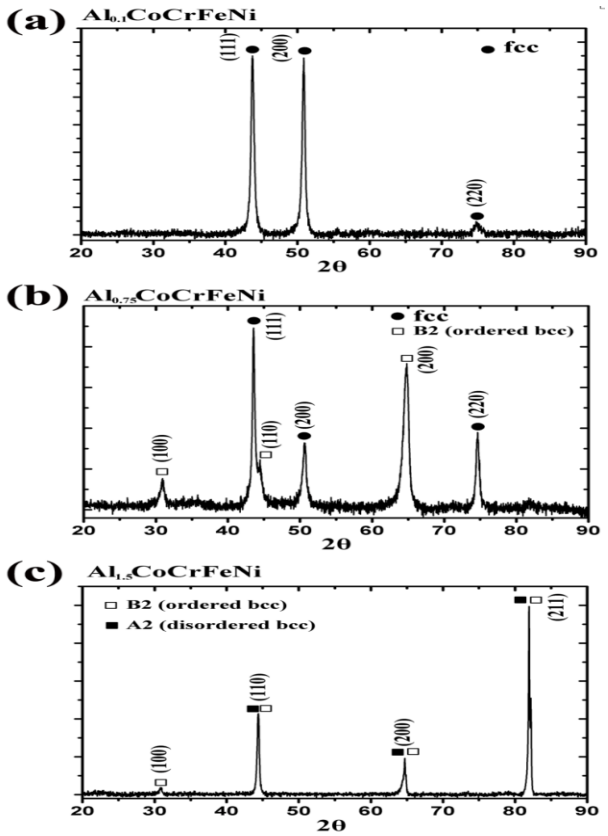

Figure 2.15 XRD Pattern for $Al_xCoCrFeNi$ (x = 0.1, 0.75, 1.5) [67]

With the increase in the Al content upto x = 0.75 (Fig 2.15(b)), some fraction of B2 structure also forms along with the FCC phase. Further it was observed that increase in the Al content upto x = 1.5 cause microstructure transformation from the FCC phase (x = 0.1, 0.75) to the BCC phase and ordered B2 structures. The mechanical property studies on $Al_xCoCrFeNi$ alloys suggested that hardness increases from 1.85 GPa in case of x = 0.1 alloy to 5.60 GPa for x = 1.5 alloy. This variation in the hardness value was found to be due to the formation of B2 and BCC phases in case of x = 1.5 alloy which are having poor ductility in comparison to FCC phase. Thus, structural transformations from FCC to BCC with increasing Al content results in higher hardness.

Heat treatment behavior of equi-atomic AlCoCrFeNi alloy was studied by Munitz et al. [71]. Heat treatment of these alloys was performed at different temperatures i.e. 850^{o}C, 975^{o}C, 1100^{o}C and 1200^{o}C in air atmosphere for 3 hrs. An XRD result (Fig 2.16) showed that as-cast alloy consisted majorly of BCC phase with a minor B2 phase. On heat treating these alloys at 850^{o}C, FCC and σ phases are evolved with BCC phase. It was interesting to note that σ phase disappears when the heat treatment was performed at 975^{o}C, 1100^{o}C and rest of the phases like BCC, FCC and B2 mainly constitute the microstructure of the alloy.

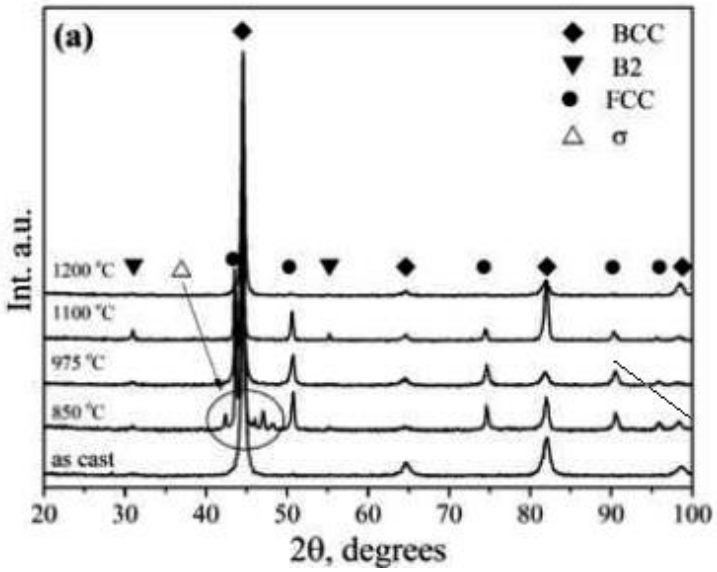

Figure 2.16 XRD patterns from the AlCoCrFeNi alloy in as-cast condition and after different heat treatments [68]

Heat treatment at 1200^{o}C causes FCC phase to disappear and primarily BCC phase becomes the major phase with very small fraction of B2 phase. Microstructural studies suggested that the AlCoCrFeNi constitute of mainly two types of regions Al rich dendrite core (DC) and Fe and Cr rich inter dendritic (ID) regions. Micro hardness of these DC and ID regions are shown in Table 2.1

Table. 2.1 Micro hardness value of DC and ID phases in AlCoCrFeNi [68]

Alloy condition	Dendrite core(DC) [GPa]	Inter dendrite(ID) [GPa]
As-cast	4.6	5.1
850^{o}C	4.5	6.0
975^{o}C	4.3	4.4
1100^{o}C	4.4	4.5
1200^{o}C	5.4	5.5

Zhang et al. [72] have synthesized equi-atomic AlCoCrFeNi alloy using the elemental mixture in SPS. The elemental powder mixture sintered at 1200°C for 20 min under a pressure of 30 MPa. The phase evolution studies had shown the formation of FCC, BCC and small fraction of B2 type structures. The micro hardness was found to be 518 HVN. These alloys also possess high strength and ductility which is because of the combined FCC+BCC phase.

Sriharitha et al. [73] synthesized $Al_xCoCuCrFeNi$ (x = 0.45, 1, 2.5, 5) by MA and detailed XRD studies on $Al_{0.45}CoCuCrFeNi$ and AlCoCuCrFeNi revealed the formation of a three phase microstructure consisting of two FCC and one BCC phases (Fig 2.17).

However, with increase in Al content, a single B2 phase was observed in $Al_{2.5}$CoCuCrFeNi and Al_5CoCuCrFeNi alloys. Calorimetric studies till 1480^{o}C revealed two melting peaks in the alloys containing 0.45 and 1 mol of Al. A detailed analysis based on thermo-physical properties together with DSC and XRD analysis suggest that these two endothermic peaks correspond to that of Cu-Ni and Fe-Ni FCC solid solutions. Similarly, the BCC phase present in these alloys has been analyzed as Fe-Cr type solid solution, which disappears at high temperatures in DSC. $Al_{2.5}$CoCrCuFeNi forms two phase microstructure when heated in DSC while Al_5CoCrCuFeNi retains its B2 structure. The phases retain their nanocrystallinity even after heating to 1480^{o}C in DSC. The results of Al_5CoCrCuFeNi illustrated that the composition limit (up to 35 at. %) for components of high entropy alloys proposed need not be a necessary condition. The results also suggested that the range of δ parameter to form ordered solid solutions proposed by Zhang et al. [35] can be extended to higher values.

Further phase evolved in Al_xCoCuCrFeNi alloy after SPS [74] (Fig. 2.18) suggests that for $Al_{0.45}$CoCrCuFeNi and AlCoCrCuFeNi alloys majorly two FCC type phases (F_1, F_2) and BCC phase are formed. In the case of $Al_{2.5}$CoCrCuFeNi alloy forms, two phases consisting of B2 as a major phase and minor FCC phase were observed while in Al_5CoCrCuFeNi alloys single phase B2 structure was found. Micro hardness measurements of Al_xCoCrCuFeNi HEAs indicate high hardness values ranging from

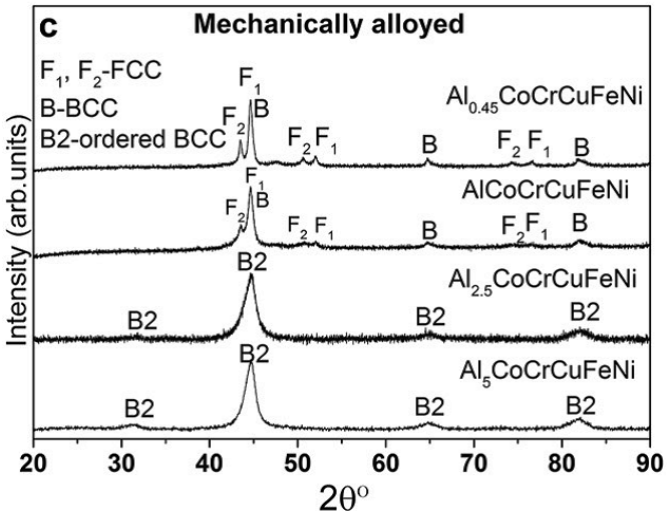

Figure 2.17 XRD Pattern of as milled Al_xCoCuCrFeNi alloys [73]

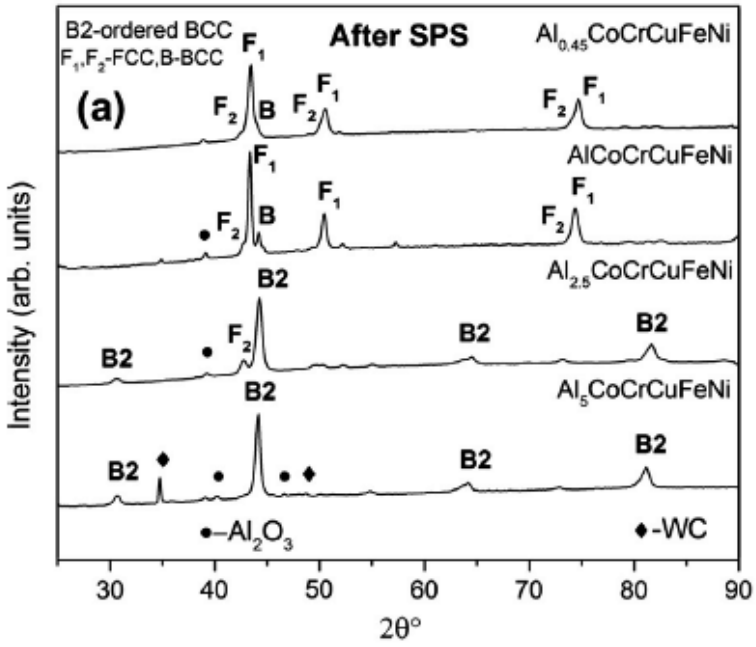

Figure 2.18 XRD Pattern of spark plasma sintered $Al_xCoCuCrFeNi$ alloys [74]

410–950 HVN. It was suggested that the higher value of hardness in these alloys are majorly due to solid solution strengthening and grain size strengthening and the order of the strengthening increases with increase in Al content. The effect of grain size strengthening was consider by the Eq. 2.16

$$\sigma_P = \sum_{i=1}^{5} \sigma_{0,i}\, C_{iP} + \sum_{i=1}^{5} k_i\, C_{iP} d^{-1/2} \qquad (2.16)$$

Where C_i is the composition of i^{th} element in a particular phase, σ_o and k are materials constant for friction stress for dislocation movement and strengthening coefficient respectively, σ_P is the yield strength of a particular phase, and d is the crystallite size.

Studies on the HEAs containing transition element has been carried out in detail. Praveen et al. [75] studied the synthesis of CoCrFeNi HEAs by MA and SPS. Fig 2.18 shows the XRD pattern of as-milled, sintered and heat treated (900^{o}C for 600 hours) CoCrFeNi alloys. Phase studies showed formation of major FCC phase with minor BCC phase after MA. XRD studies of sintered CoCrFeNi alloy suggested formation of major FCC phase with the formation of other phases like Cr_7C_3 and Cr_2O_3. Phase study of heat treated alloy

at 900^{o}C for 600 hours shows no phase change in comparison to the sintered alloy, indicating good thermal stability after SPS. TEM bright field image as shown in Fig 2.19mainly constitute of three types microstructure faceted grains (region A), faulted grains (region B), and fine precipitates (region C). The electron diffraction (ED) pattern from faceted grain found to have FCC structure, and ED pattern taken from faulted grain is having an orthorhombic structure (Cr_7C_3).

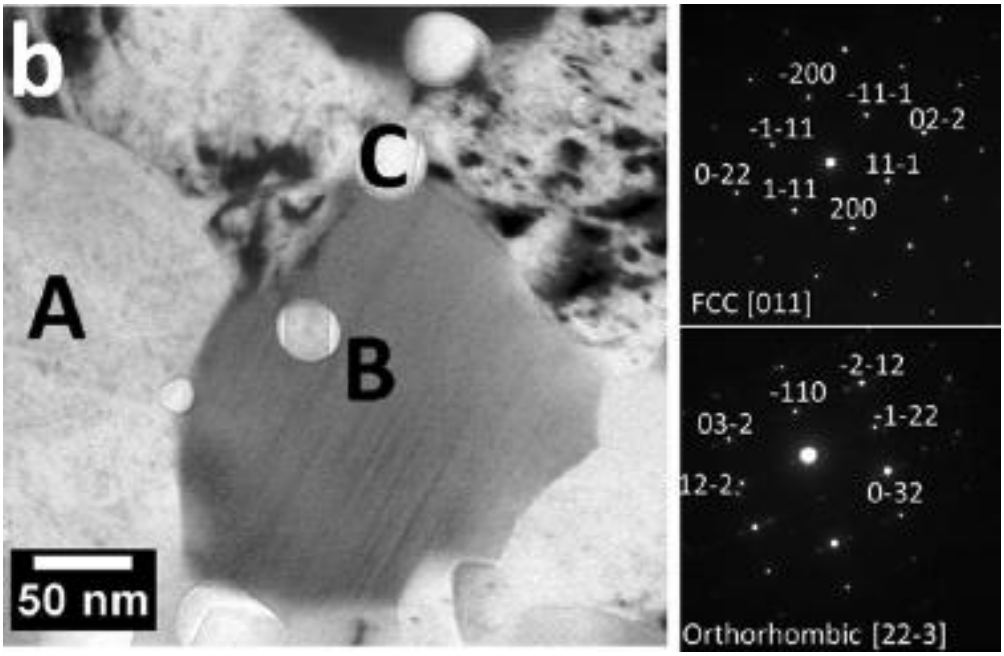

Figure 2.19 TEM image (left) showing three different grain morphology, and SAD patterns (right) corresponding to FCC phase (A) and orthorhombic phase (B) and Cr_2O_3 precipitate [72].

The elemental mapping of as-sintered alloys is shown in Fig 2.20. It can be observed that smaller precipitates present in the alloy are Cr-O rich, faceted grains are Fe-Co-Ni rich, and faulted grains are Cr-C rich.

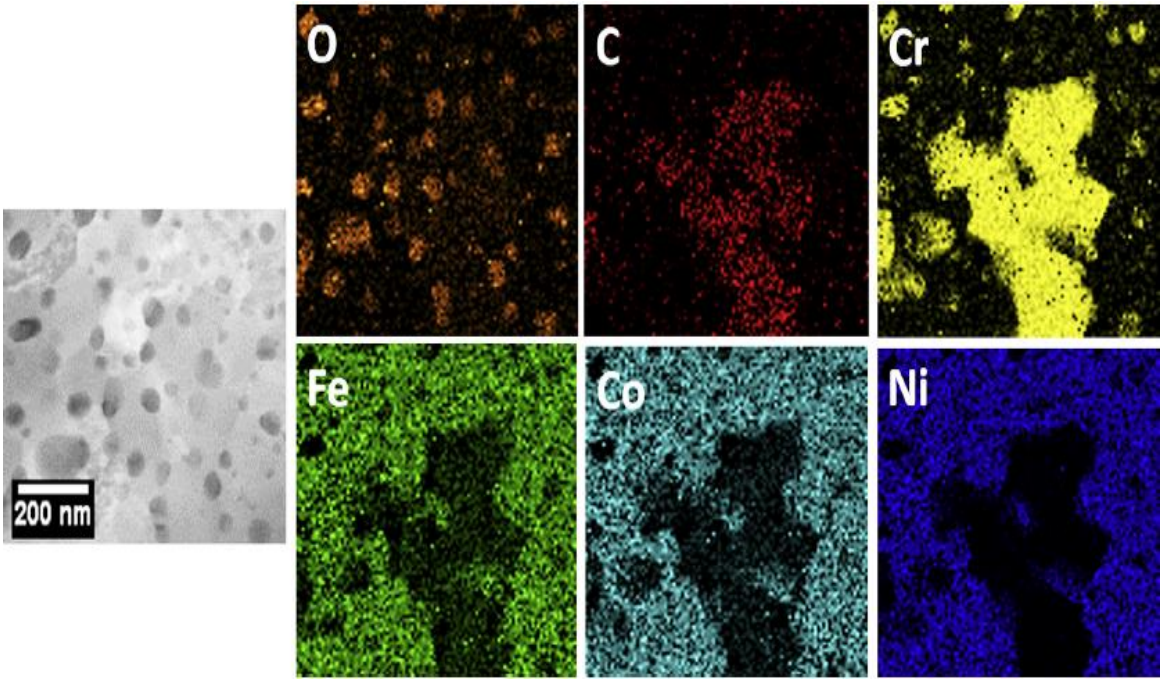

Figure 2.20 STEM image of as sintered compact and corresponding EDS mapping [72]

Studies showed that grain growth at high temperatures in nanocrystalline CoCrFeNi alloys is controlled by mainly three factors i.e. Zener pinning effect, long range diffusion of carbide phase, and cooperative diffusion of elements. Micro hardness test performed on CoCrFeNi alloy was determined to be 570 HVN. Liu et al. [76] synthesized equimolar FeCoCrNi alloy by powder extrusion method. Phase studies show formation of single phase solid solution having a FCC structure (Fig 2.21) peaks with lattice parameter of 359 pm. Yield strength of the FeCoCrNi alloy was revealed to be 359 MPa. The improvement in the mechanical properties is found to be due to combined effect of solid solution strengthening and grain boundary strengthening.

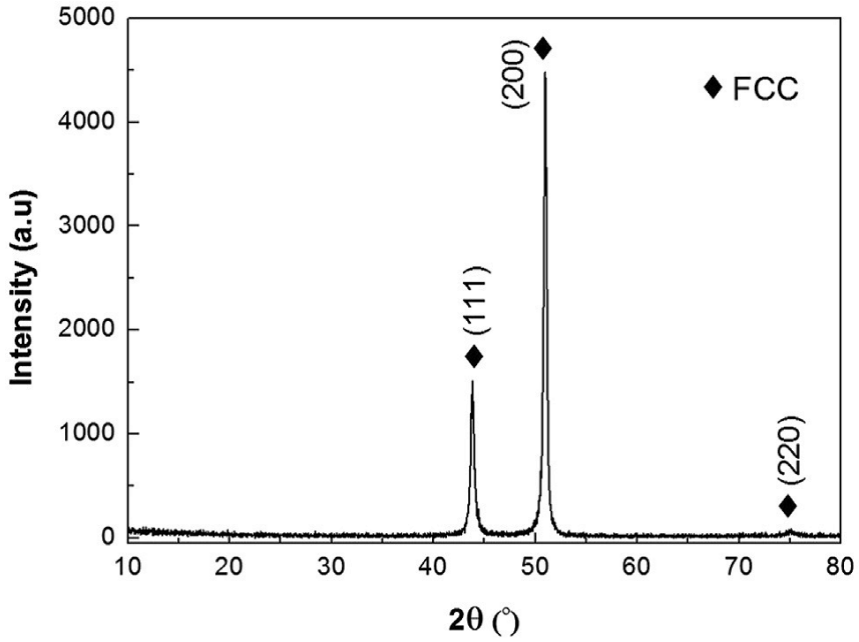

Figure 2.21 XRD pattern of FeCoCrNi alloy [76].

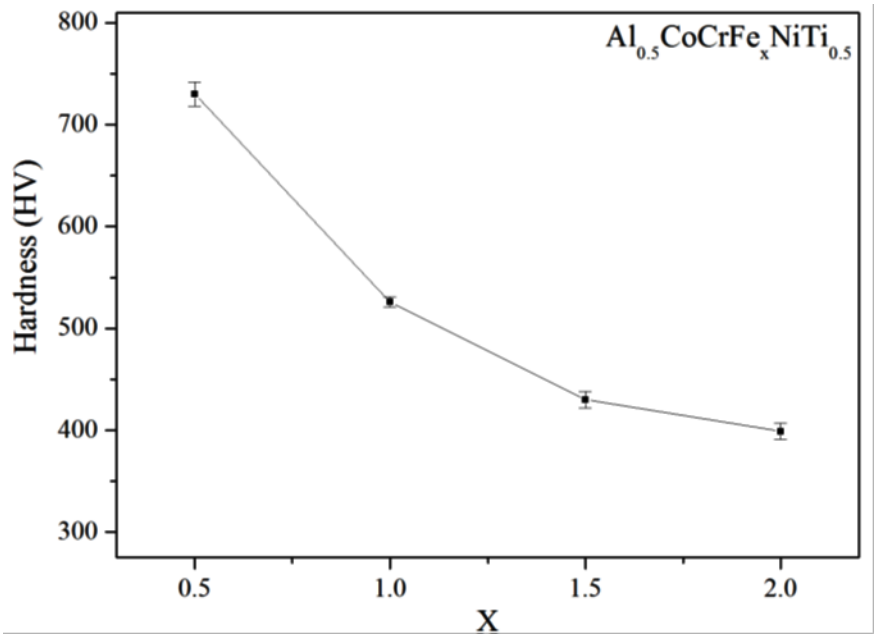

Figure 2.22 Hardness of $Al_{0.5}CoCrFe_xNiTi_{0.5}$ (x = 0.5, 1.0, 1.5, 2.0) high-entropy alloys [77].

Effect of Fe on near equiatomic $Al_{0.5}CoCrFe_xNiTi_{0.5}$ (x = 0.5, 1, 1.5, 2) [77] synthesized by vacuum arc melting has been studied. The resulting microstructure for

$Al_{0.5}CoCrFe_{0.5}NiTi_{0.5}$ and $Al_{0.5}CoCrFe_1NiTi_{0.5}$ shows the formation of BCC, FCC, σ phase, and ordered BCC phases. For $Al_{0.5}CoCrFe_{1.5}NiTi_{0.5}$ and $Al_{0.5}CoCrFe_2NiTi_{0.5}$ alloys, the microstructure consists of the FCC, BCC, and ordered phases. Fig 2.22 shows the hardness of the $Al_{0.5}CoCrFe_xNiTi_{0.5}$ (x = 0.5, 1, 1.5, 2) alloys. It was observed that hardness decreases from 748 HVN to 399 HVN with increasing Fe content. It can be suggested from these results that Fe element addition hinders the formation of σ phase and Fe elements act as a FCC stabilizer in case of these alloys.

Effect of Cr addition in $AlCoCr_xFeMo_{0.5}Ni$ (x = 0, 0.5, 1, 1.5, 2) alloys have been studied by Hsu et al. [78]. Phase evolution studies suggested the formation of majorly ordered B2 phase and tetragonal σ phase. It was observed that phase fraction of σ phase increases with the increase in Cr concentration for $AlCoCr_xFeMo_{0.5}Ni$ (x = 0, 0.5, 1, 1.5, 2) alloys. Further, this σ phase mainly constitutes of multi-element such as Co-Cr, Fe-Cr, Ni-Mo, and Fe-Mo phases. The hardness values showed increase the hardness with the increase in the Cr concentration from 601 HVN (x = 0) to 867 HVN (x = 2). Thus, it can be concluded from the result that Cr concentration enhances the probability for the formation of σ phase in HEAs. Also, high Cr content had good softening resistance at elevated temperatures.

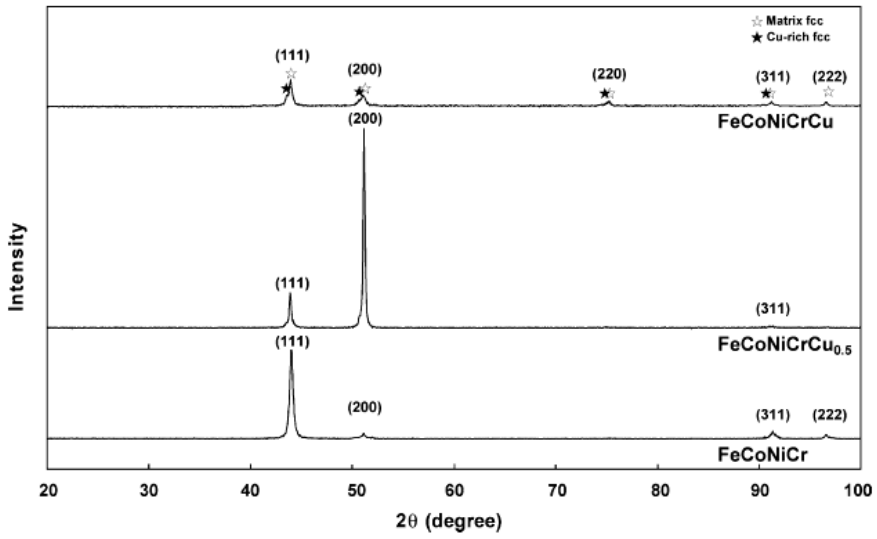

Figure 2.23 Phase evolution in $FeCoNiCrCu_x$ (x = 0, 0.5, 1) HEAs [79]

Effect of Cu addition in the $FeCoNiCrCu_x$ (x = 0, 0.5, 1) HEAs was carried out by Hsu et al. [79]. Phase studies (Fig. 2.23) showed the formation of majorly FCC phase. Although with an increase in the Cu content segregation of Cu rich interdendrites was being observed. The results conclude that the addition of the Cu in the HEAs mostly enhances the Cu segregation in HEAs . Some other studies on the effect of Cu addition has also showed similar results [80].

Recently, HEAs with HCP structure had been successfully synthesized. First successful synthesis of HCP structured HEAs has made by Takeuchi et al. [81] in 2014. The alloy design was done considering the structures of each constituent elements and their phase diagrams. Thermodynamic parameter ΔH_{mix}, δ and VEC are also calculated for the alloy design of HEAs. Out of all the possible elements heavy lanthanides YGdTbDyLu and GdTbDyTmLu alloys have been synthesized by arc melting in argon atmosphere and repeatedly changing their tops and bottoms upside down, and eventually they were formed at approximately 12 mm Ø*5 mm height.

The phase evolution after casting shows the formation of HCP solid solution (Fig 2.24). Thermodynamic parameters calculated suggest that ΔH_{mix}= 0 kJ/mol which is due to the similarity between the elements among the heavy lanthanides. VEC of GdTbDyTmLu and YGdTbDyLu HEAs have been calculated to be 3, which opposes the criterion that VEC of the BCC, BCC + FCC, and FCC VEC < 6.87 (BCC), 6.87 < VEC < 8.0 (BCC + FCC), and FCC for VEC > 8. Thus, VEC = 3 for the HEAs having a HCP structure may give a lower limit value of VEC for HEAs with a BCC structure.

Similarly, equiatomic ScYLaTiZrHf HEAs was synthesized via arc melting [82]. The microstructure evolved was found to be (Sc,Y,La) type and (Sc,Ti,Zr,Hf) type dual HCP phase.

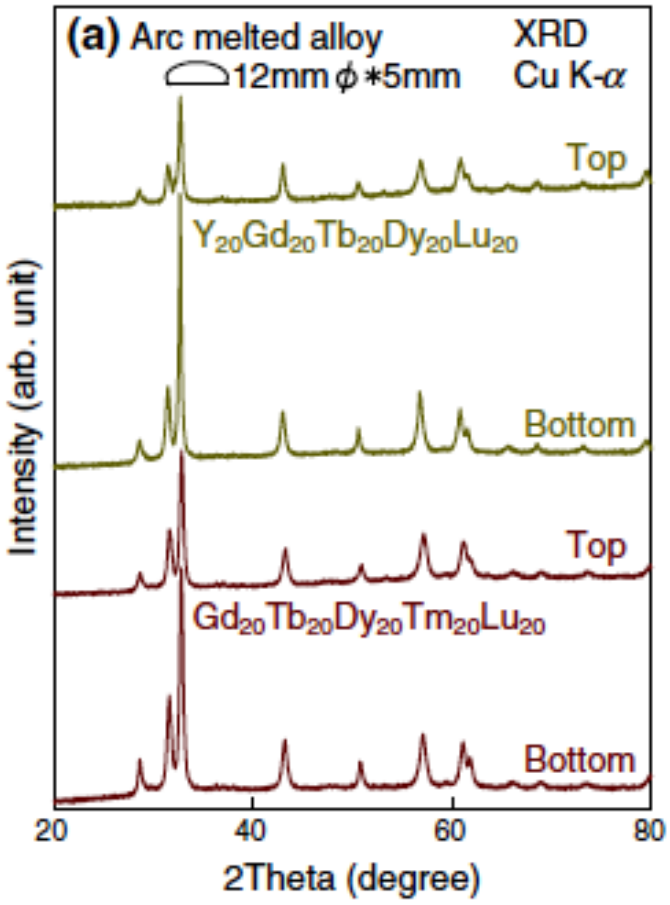

Figure 2.24 XRD profiles of (a) YGdTbDyLu and GdTbDyTmLu alloy ingots [81]

Thermodynamic parameter was calculated and the ΔH_{mix} was found to be 11.4 kJ/mol, δ = 8.3 and VEC = 3.5. EDS analysis (Fig 2.25) suggests that Sc element plays important role in the stabilization of HCP structure in ScYLaTiZrHf alloy; also Sc element is distributed homogeneously in both HCP phases. Segregation of elements is due to the positive mixing of enthalpy between the binary elements.

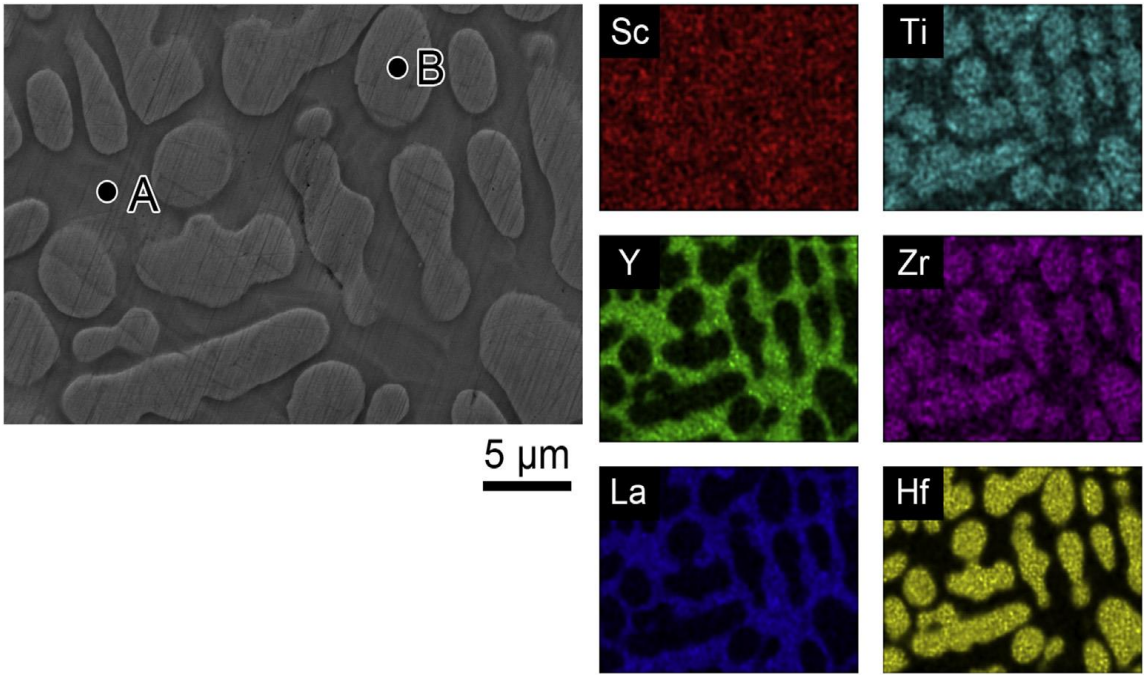

Figure 2.25 Typical SEM image and elemental-maps by EDS of the ScYLaTiZrHf alloy ingot (A) Yttrium (Y)-Lanthanum (La) rich phase, (B) Titanium (Ti)-Zirconium (Zr)- Hafnium (Hf) rich Phase [82]

It was suggested that due to this behavior the ScYLaTiZrHf alloy should be considered as multi principal elements alloys instead of a HEA, as S_{conf} is not maximized because of the presence of dual phases.

Further, GdHoLaTbY alloy was synthesized by Zhao et al. [83] by arc melting method. XRD indicates formation of single hcp phase (Fig. 2.26). The lattice constants (a and c) and the *c*/*a* ratios were found to be a = 0.3658 nm and c = 0.5812 nm, and the *c*/*a* ratio is 1.5888.

The hardness of GdHoLaTbY HEA was found to be 96 HVN. As in case of YGdTbDyLu and GdTbDyTmLu alloys these alloys shows ΔH_{mix} and VEC to be 0 kJ/mol and 3, respectively, suggesting that the lower limit of VEC is around 3 to stabilize HCP structure.

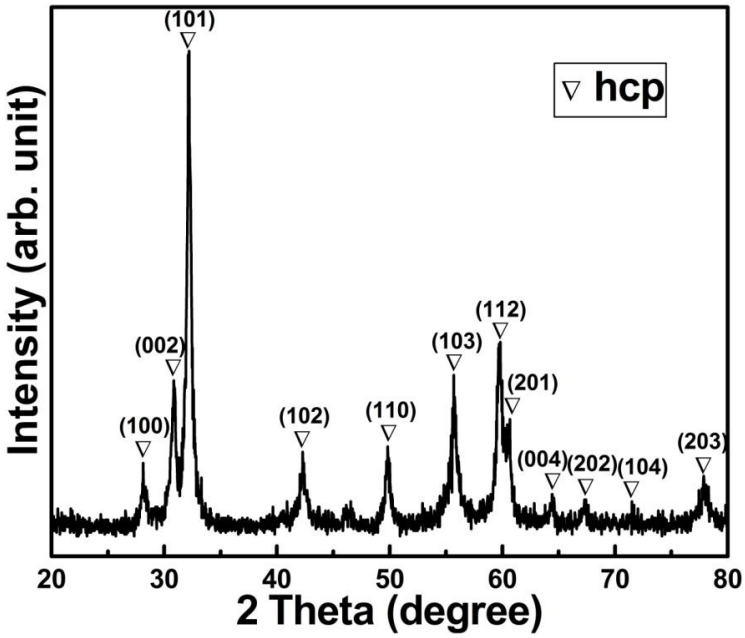

Figure 2.26 XRD pattern of GdHoLaTbY alloy [83]

2.6 Structure-Property of lightweight high entropy alloys

Lightweight high entropy alloys are also a potential candidate in the application involving energy efficiency like automobile, aerospace. Lower density can be achieved by alloy designing and selection of materials in such a way that the synthesized alloys are lower in density and having remarkable properties. Although there are only few works reported in the past for development of light weight high entropy alloy. Li et al. [84] synthesized light weight $Mg_x(MnAlZnCu)_{100-x}$ alloy by casting method. XRD revealed the formation of $Mg_{20}(MnAlZnCu)_{80}$ alloy (Fig 2.27) simple solid solution phases and complex intermetallic phases. Thus, only HCP and Al-Mn icosahedral quasicrystal phases were found in $Mg_{20}(MnAlZnCu)_{80}$ alloy. The high confusion of atoms in Al-Mn system was kept by the effect of high entropy of mixing, and the quasicrystal phases were formed in $Mg_{20}(MnAlZnCu)_{80}$ alloy with a moderate cooling speed. With decrease in the mixing of entropy, the phases in $Mg_x(MnAlZnCu)_{100-x}$ alloys were complex. The number of phases in the alloys except $Mg_{20}(MnAlZnCu)_{80}$ was increased to 4, which is HCP phase, icosahedral phase, Mg, and Mg_7Zn_3.

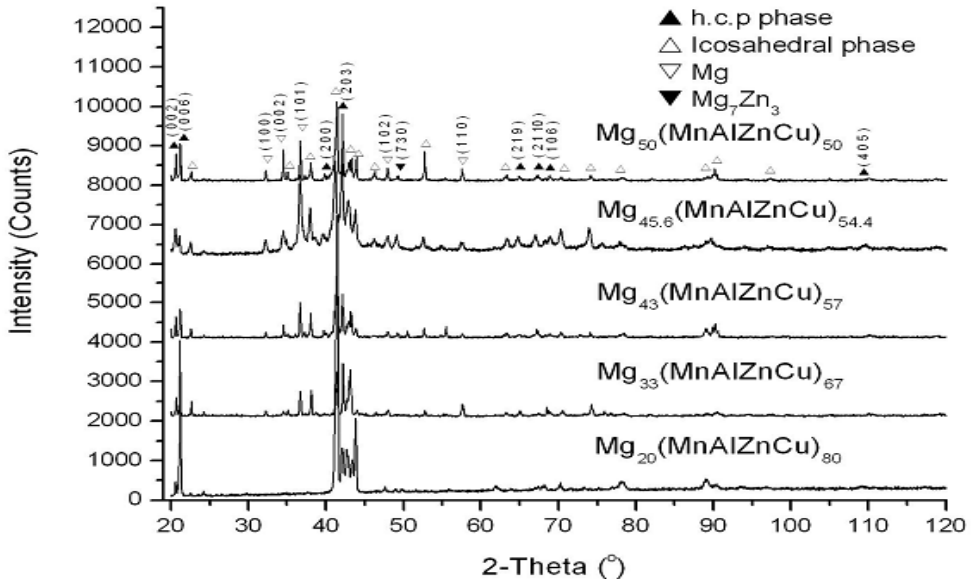

Figure 2.27 XRD pattern of $Mg_x(MnAlZnCu)_{100-x}$ alloy [84]

$Mg_x(MnAlZnCu)_{100-x}$ alloys exhibited high compressive strength (Fig 2.28), but the plasticity of alloys was bad. The alloys showed brittle behavior except $Mg_{50}(MnAlZnCu)_{50}$ alloy, which could be deformed 1.80% plastically. Solution strengthening and quasicrystal dispersion strengthening were the main strengthening mechanics of $Mg_x(MnAlZnCu)_{100-x}$ alloys. The effect of solution strengthening was most significant in $Mg_{20}(MnAlZnCu)_{80}$ alloy for the maximum entropy of mixing. High confusion atoms in the alloys were kept by effect of high entropy, and the alloys were formed as super solid solution. Due to the variation in the atomic radius of components, the lattice distortion energy is high. Generally HCP structure has few slip systems in the lattice which causes inferior plasticity in these alloys. As the mixing entropy decreases with the increase in atomic percentage of Mg, the effect of solution strengthening also decreases. This might cause improve in plasticity of $Mg_{50}(MnAlZnCu)_{50}$ alloy. The quasicrystal phases were hard and fine, they were distributed uniformly in base phases, and the compressive strength of alloys could be enhanced by quasicrystal dispersion strengthening. According to Fig 2.29, it could be deduced that the effect of quasicrystal dispersion strengthening was most significant in $Mg_{43}(MnAlZnCu)_{57}$ alloy.

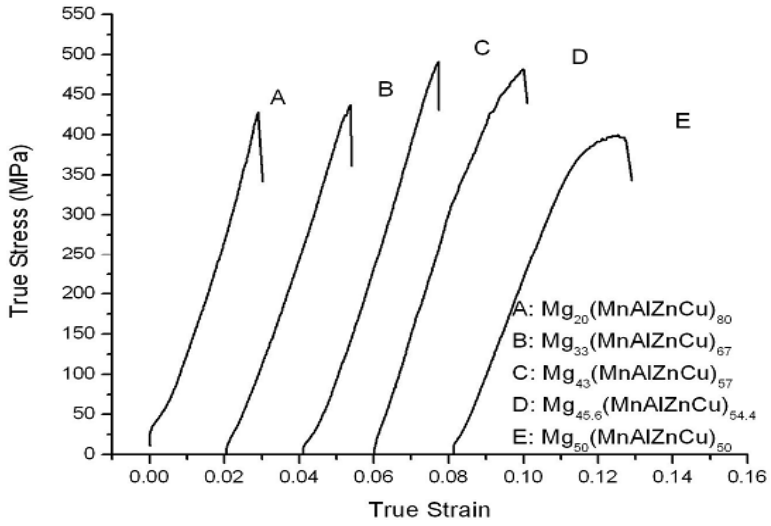

Figure 2.28 Compressive true stress-strain curves of $Mg_x(MnAlZnCu)_{100-x}$ alloys [84]

$Mg_x(MnAlZnCu)_{100-x}$ alloys exhibited moderate densities (4.29 g/cm^3 -2.20 g/cm^3, Fig 2.30) and high hardness (431 HV-178 HV, Fig 2.28). The high hardness might be caused by effect of rapid solution and quasicrystal phase.

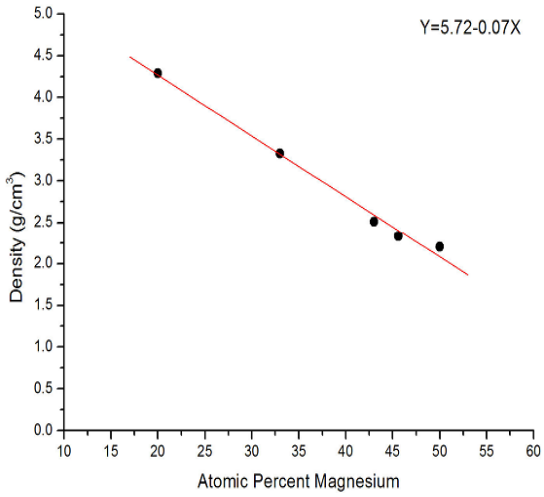

Figure 2.29 Densities of $Mg_x(MnAlZnCu)_{100-x}$ alloys[84]

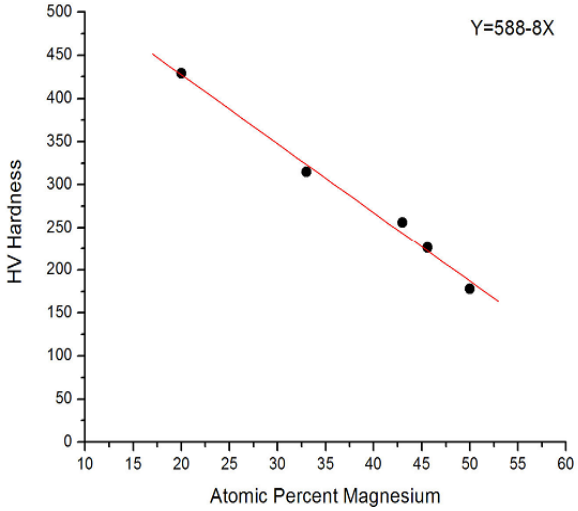

Figure 2.30 Hardness of $Mg_x(MnAlZnCu)_{100-x}$ alloys [84]

Li et al. [85] studied the MgMnAlZnCu HEA prepared by induction melting and then cast in copper molds in air, water and salt water respectively. The XRD results showed

that the alloy was composed mainly of HCP and Al-Mn quasicrystal phases. The alloy exhibits high hardness (431HV-467HV) and high compression strength (428MPa-450MPa) at room temperature. The alloy was fragile and the strains were from 3.29% to 5.53%.

Chen et al. [86] studied two equimolar alloys, entirely composed of HCP elements, BeCoMgTi and BeCoMgTiZn, from elemental powders by mechanical alloying. The as milled powder was characterized to be of amorphous phase (Fig 2.31). The amorphization processes in these two alloys conform to type II amorphization [86]. The inhibition of intermetallic compounds before amorphization is due to chemical compatibility among the constituent elements in company with high entropy effect and deformation effect which enhance the mutual solubility. Direct formation of the amorphous solid solution phase is basically due to the large atomic difference between the constituent atoms. This mechanism could be a guideline for type II amorphization of multi-component alloys.

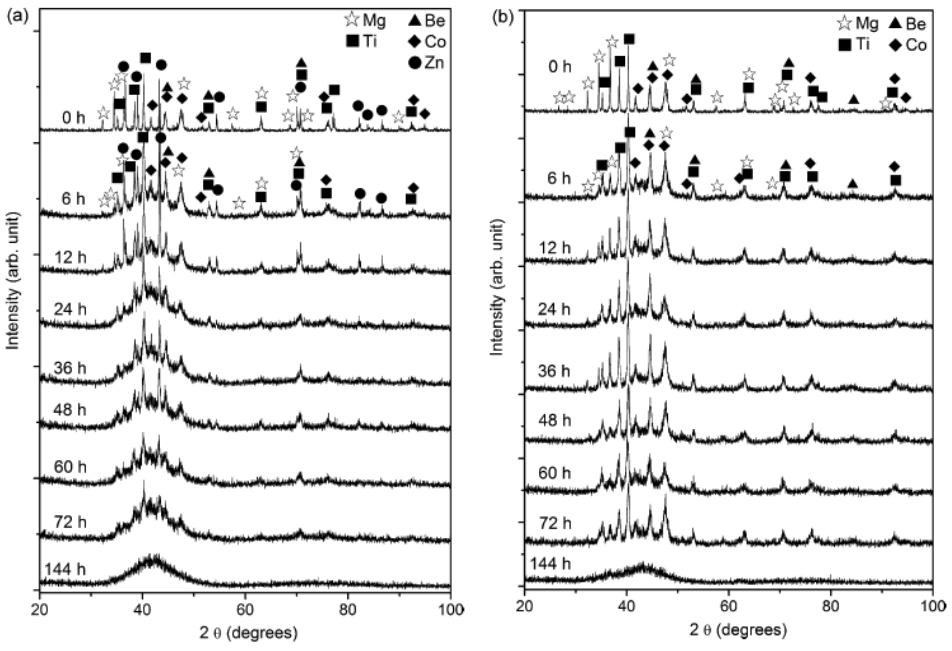

Figure 2.31 XRD patterns of alloy powders milled with different times (a) BeCoMgTi alloy and (b) BeCoMgTiZn alloy[86]

Mg containing $Sr_{20}Ca_{20}Yb_{20}Mg_{20}Zn_{20}$ high entropy bulk metallic glasses were also studied by Gao et al. [87] with high glass formation ability.

Yang et al. [88] studied low density alloys based on the Al-Li-Mg-(Zn, Cu, Sn) system by induction melting. Densities of these alloys are found to be below 4.23 g/cm^3. Phase study of these alloys (Fig 2.32) suggested the formation of complex microstructure containing ordered Mg_2Sn or Li_2MgSn phases in addition to the terminal α-Al, α-Zn, and α-Sn phases in these alloys. It was suggested that high configurational entropy may not be a necessary condition to stabilize a solid solution. Also, it was concluded that electronegativity difference ($\Delta X > 0.175$) parameter plays an important role in the formation of intermetallic phase.

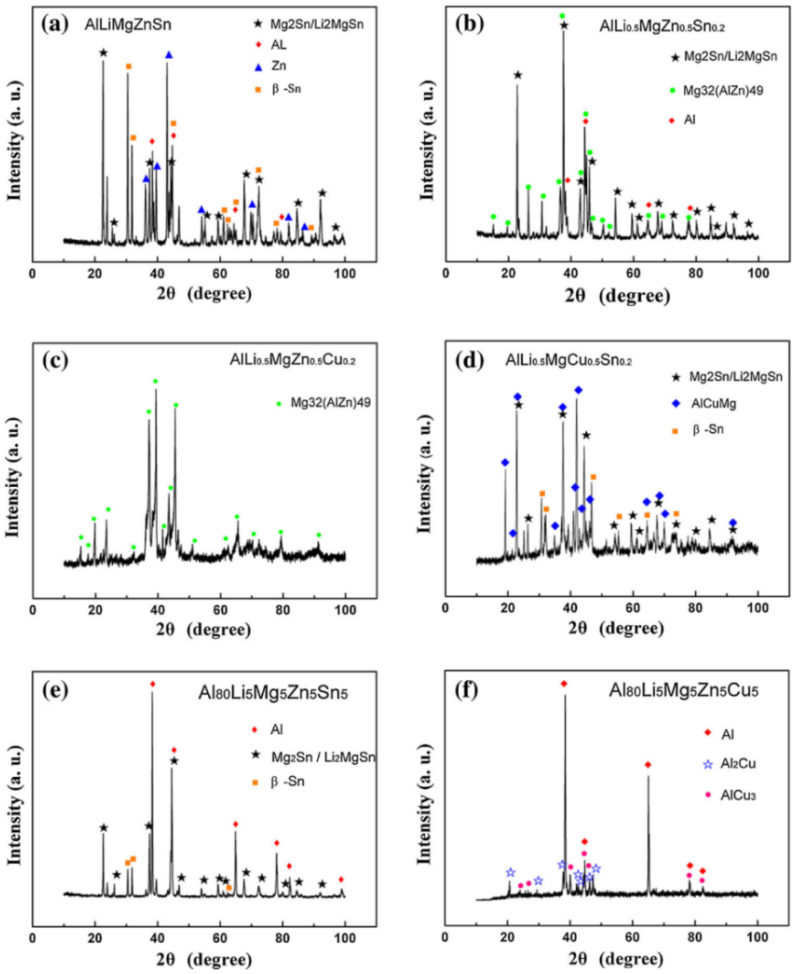

Figure 2.32 XRD patterns of low-density multicomponent alloys. (a) AlLiMgZnSn; (b) $AlLi_{0.5}MgZn_{0.5}Sn_{0.2}$ (c) $AlLi_{0.5}MgZn_{0.5}Cu_{0.2}$; (d) $AlLi_{0.5}MgCu_{0.5}Sn_{0.2}$; (e) $Al_{80}Li_5Mg_5Zn_5Sn_5$; and (f) $Al_{80}Li_5Mg_5Zn_5Cu_5$ alloys [88].

Youseff et al. [89] synthesized a low density (2.67 g/cm^3) $Al_{20}Li_{20}Mg_{10}Sc_{20}Ti_{30}$ alloys by cryomilling and conventional sintering. The phase evolution in low N, O contamination as milled powder was found to be FCC. After compaction and conventional sintering the microstructure transformed to HCP structure with the hardness of 4.9 GPa. For as milled powder having a higher N, O contamination the phase evolved after MA was found to have a FCC structure. Further, annealing at 500°C and 800°C revealed that FCC structure is retained. Hardness of the alloys annealed at 500^{o}C and 800^{o}C had been found to be 5.9 GPa and 5.75 GPa respectively.

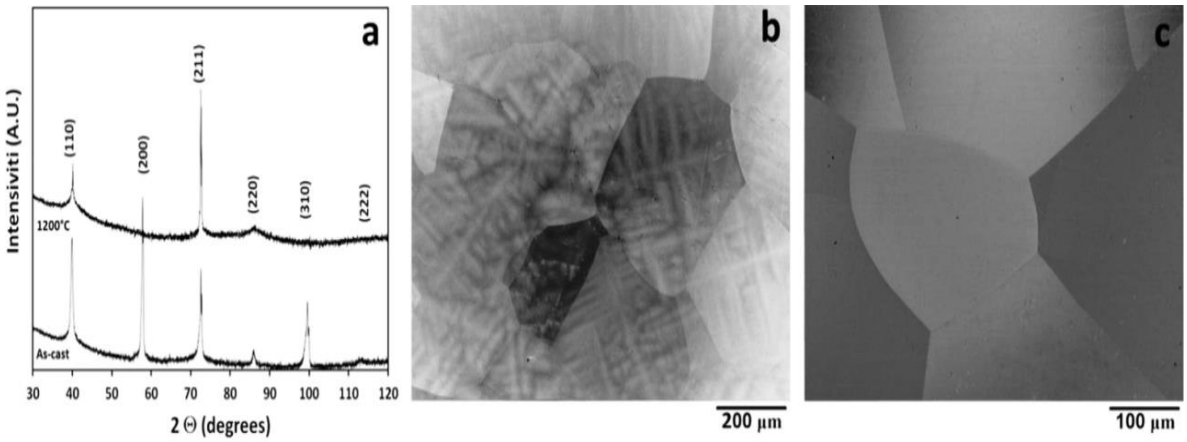

Figure 2.33 Structure of the AlNbTiV alloy in as-cast and homogenized conditions:(a) XRD pattern , SEM-BSE images (b)as-cast condition;(c) homogenized condition [90].

Typical light weight AlNbTiV alloys was synthesized by arc melting method in Ar atmosphere [90]. Density of the alloys was found out to be 5.59 g/cm^3. It was observed that the density in this case is higher than most of the conventional low density alloys. The structural and mechanical study of AlNbTiV alloys concluded that material can be considered to be light weight based on the application for which it has been proposed. Phase studies suggested the formation of single phase solid solution with a BCC microstructure. Microstructure of AlNbTiV alloys had shown that in as cast conditions both dendritic as well as interdendritic areas are present (Fig 2.33). Although dendritic structure was removed after the homogenization of alloy at 1200^{o}C for 24 hours in

vacuum though AlNbTiV alloys showed higher hardness of 4315 ± 98 MPa and 4394 ± 118 MPa in as cast and homogenized condition respectively.

Most recent work on light weight $Al_xCrFeMnTi_y$ alloys (x = 1, 1.5, 2, 3, and 4; and y = 0.25 and 1) prepared by arc-melting method is reported by Feng et al. [91]. The microstructure of the alloys (Fig 2.34) exhibits the presence of a BCC phase. Other phases formed in these alloys were found to be Fe_2AlTi-type $L2_1$ structure. In case of $Al_{1.5}CrFeMnTi$ and $Al_2CrFeMnTi$ alloys additional intermetallic phase (Laves Phase) had also been formed. In case of $Al_3CrFeMnTi_{0.25}$ and $Al_4CrFeMnTi_{0.25}$ alloys some complex phases evolved like Al_8Cr_5 type and $Al_{58.5}Cr_{10.3}Fe_{31.2}$ type in addition to BCC phase and laves phase.

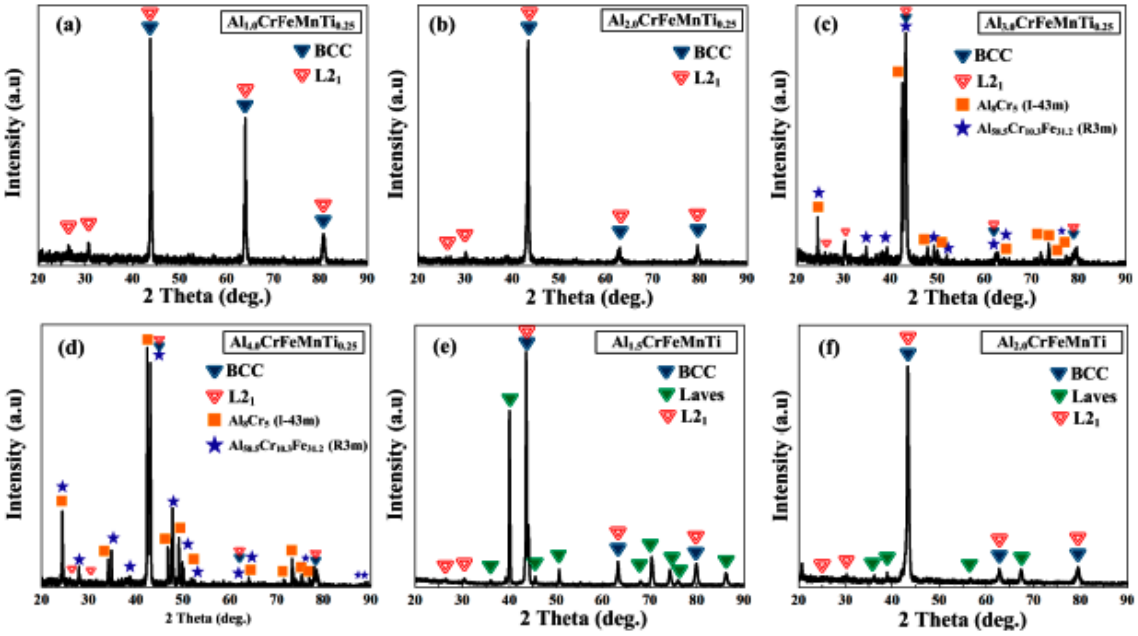

Figure 2.34 XRD patterns of a series of newly-designed light-weight HEAs: (a) $Al_{1.0}CrFeMnTi_{0.25}$ (b) $Al_{2.0}CrFeMnTi_{0.25}$ (c) $Al_{3.0}CrFeMnTi_{0.25}$; (d) $Al_{4.0}CrFeMnTi_{0.25}$ (e) $Al_{1.5}CrFeMnTi$ and (f) $Al_{2.0}CrFeMnTi$.

It was also reported that lower heat of formation between Al, Ti and transition metals causes formation of intermetallic compounds in an alloy system. Thus, it is difficult to synthesize a single phase HEAs containing Al and Ti.

Until now total number of single-phase light-weight HEAs are limited, having densities more than 5.5 g/cm^3. It was suggested that in coming years the design of light-weight HEAs can be performed on the basis of selecting the main alloying elements with the dominant light weight elements such as Ti, Al, or Mg etc. and using high entropy concept to alter the composition in such a way that strengthening can be maximized [91].

Table 2.2 summarizes the phase evolved, properties and density of different light weight HEAs synthesized by various methods.

Table 2.2 List of light weight HEAs with processing route, phase evolved, properties and density

Alloys	Synthesis Route	Phases	Hardness (HVN)	Yield strength (GPa)	Compressive strength (GPa)	Density (g/cm^3)	Ref.
NbVAlTi	AM	BCC	440		1.2	5.59	[92]
NbVZrTiAl	AM	BCC, Laves (C14)	540	1.08	1.21	5.76	[92]
$NbVZrTiAl_{1.5}$	AM	BCC, Laves (C14), AlZr2	620	-	1.31	5.50	[92]
AlLiMgZnSn	IM	Mg_2Sn/Li_2MgSn, Zn, Al, β-Sn	-	0.60	-	4.23	[88]
$AlLi_{0.5}MgZn_{0.5}Sn_{0.2}$	IM	Mg_2Sn/Li_2MgSn $Mg_{32}(AlZn)_{49}$, Al	-	-	-	3.22	[88]
$AlLi_{0.5}MgZn_{0.5}Cu_{0.2}$	IM	$Mg_{32}(AlZn)_{49}$	-	0.48	-	3.73	[88]
$AlLi_{0.5}MgCu_{0.5}Sn_{0.2}$	IM	Mg_2Sn/Li_2MgSn, AlCuMg, β-Sn	-	-	-	3.69	[88]
$Al_{80}Li_5Mg_5Zn_5Sn_5$	IM	Mg_2Sn/Li_2MgSn, Al, β-Sn	-	0.41	-	3.05	[88]
$Al_{80}Li_5Mg_5Zn_5Cu_5$	IM	Al, Al_2Cu, $AlCu_3$	-	0.48	-	3.08	[88]
$Mg_{50}(MnAlZnCu)_{50}$	IM	HCP, Icosahedral, Mg, Mg_7Zn_3	173	0.34	-	2.20	[84]
$Mg_{45.6}$(MnAl	IM	HCP,	-	0.48	-	2.50	[84]

$ZnCu)_{54.4}$		Icosahedral, Mg, Mg_7Zn_3					
$Mg_{43}(MnAlZnCu)_{57}$	IM		-	0.50	-	2.75	[84]
$Mg_{33}(MnAlZnCu)_{67}$	IM	HCP, Icosahedral, Mg, Mg_7Zn_3	-	0.43	-	3.50	[84]
HCP, Icosahedral, Mg, Mg_7Zn_3	IM	HCP, Icosahedral, Mg, Mg_7Zn_3	431	0.42	-	4.29	[84]
BeCoMgTi	MA	Amorphous	-	-	-	-	[86]
BeCoMgTiZn	MA	Amorphous	-	-	-	-	[86]
$Al_{20}Li_{20}Mg_{10}Sc_{20}Ti_{30}$	MA + Sintering	HCP	499	-	-	2.67	[89]
$Al_{20}Li_{20}Mg_{10}Sc_{20}Ti_{30}$ (N,O)	MA + Sintering (500^oC)	FCC	599	-	-	2.67	[89]
AlNbTiV	Casting	BCC	448	1.02	1.318	5.59	[90]
$Al_{20}Be_{20}Fe_{10}Si_{15}Ti_{35}$	Casting	One major and two minor phases	911	-	-	3.91	[93]
$Al_{1.0}CrFeMnTi_{0.25}$	AM	BCC, $L2_1$	-	-	-	5.87	[91]
$Al_{2.0}CrFeMnTi_{0.25}$	AM	BCC, $L2_1$	-	-	-	5.16	[91]
$Al_{3.0}CrFeMnTi_{0.25}$	AM	BCC, $L2_1$, Al_8Cr_5-type, $Al_{58.5}Cr_{10.3}Fe_{31.2}$-type	-	-	-	4.71	[91]
$Al_{4.0}CrFeMnTi_{0.25}$	AM	BCC, $L2_1$, Al_8Cr_5-type, $Al_{58.5}Cr_{10.3}Fe_{31.2}$-type	-	-	-	4.40	[91]
$Al_{1.5}CrFeMnTi$	AM	BCC, Laves, $L2_1$	-	-	-	5.31	[91]
$Al_{2.0}CrFeMnTi$	AM	BCC, Laves, $L2_1$	-	-	-	5.06	[91]

AM-Arc Melting, IM-Induction Melting, MA-Mechanical Alloying

Thus the literature review concludes that the HEAs are the promising new age material with exceptional properties and can be the potential candidate for different applications. Earlier it was supposed that the simple solid solution microstructure in the HEAs is generally due to the high configurational entropy. But recent work has shown that it is the enthalpy of mixing and atomic size mismatch rather than configurational entropy which decides the formation of simple microstructure. The matter of fact is that there is no single definition which has been decided by scientific community on HEA rather the definitions provided in the literature are mostly based on composition and microstructure that gives scientists the flexibility to work. Also, a large number of HEAs were synthesized by different methods including arc melting, spark plasma sintering and direct laser fabrication methods which have shown a simple solid solution microstructure and remarkable properties. Light weight HEAs is one of the most promising areas of research in energy efficiency. The HEAs can be considered as a light weight if its density is lower than that of an alloy used for that particular application [94]. Low density HEAs were synthesized using the elements like Al, Mg and Li. The effect of low density element like Al has been widely studied and the microstructure varies from solid solution to solid solution plus intermetallic. Some previous studies on the effect of Ti in HEAs have also been studied showing a multiphase micro structure. But the effect of varying concentration of low density Mg and Ca on HEAs has not been studied carefully to understand the phase evolution and phase transformation at different temperatures. Moreover the hardness and corrosion properties in Mg containing HEAs have not been studied in detail so far and structure–property correlation has not been established yet. Furthermore, the effect of heat treatment is also very much essential to study to establish materials-structure-process-properties correlation of light weight HEAs.

Thus, based on the literature review it is scientifically and technologically important to synthesize lightweight HEAs having simple microstructure with superior properties and cost effectiveness. Hence, the present research work focuses on attempt to synthesize bulk light weight HEA by choosing the lightest structural element i.e. Mg ($\rho \sim 1.74$ g/cc) along with other alloying elements such as Al ($\rho \sim 2.70$ g/cc), Fe ($\rho \sim 7.87$ g/cc), Cu ($\rho \sim 8.96$ g/cc), Cr ($\rho \sim 7.19$ g/cc), for the potential application in automobile and/or aerospace

industry. Moreover, the effect of variation in Mg content has been studied to establish the materials-structure-process–properties correlation in case of proposed light weight high entropy alloy system. The composition of Mg is selected on the basis of compositional definition of HEAs i.e. the constituent elements should be between 5 at. % to 35 at. %.

Furthermore, light weight Ca ($\rho \sim 1.54$ g/cc) containing HEAs has also been designed. Other alloying elements such as Ni ($\rho \sim 8.90$ g/cc), Al ($\rho \sim 2.70$ g/cc), Mg ($\rho \sim 1.74$ g/cc), Fe ($\rho \sim 7.87$ g/cc), Cu ($\rho \sim 8.96$ g/cc), and Cr ($\rho \sim 7.19$ g /cc) were selected on the basis of the binary enthalpy of mixing between Ca and other alloying elements. In this case the composition was selected in such a way to make the HEAs lighter.

Thus the **main objectives of this work can be outlined as follows:**

- Design and Development of light weight HEA powders via mechanical alloying.
- Synthesis of bulk HEA by conventional sintering or spark plasma sintering (SPS).
- Material-Structure-Process-Property correlation for proposed novel high entropy alloys.

In order to achieve the goals following methodology have been adopted (see Fig. 2.35)

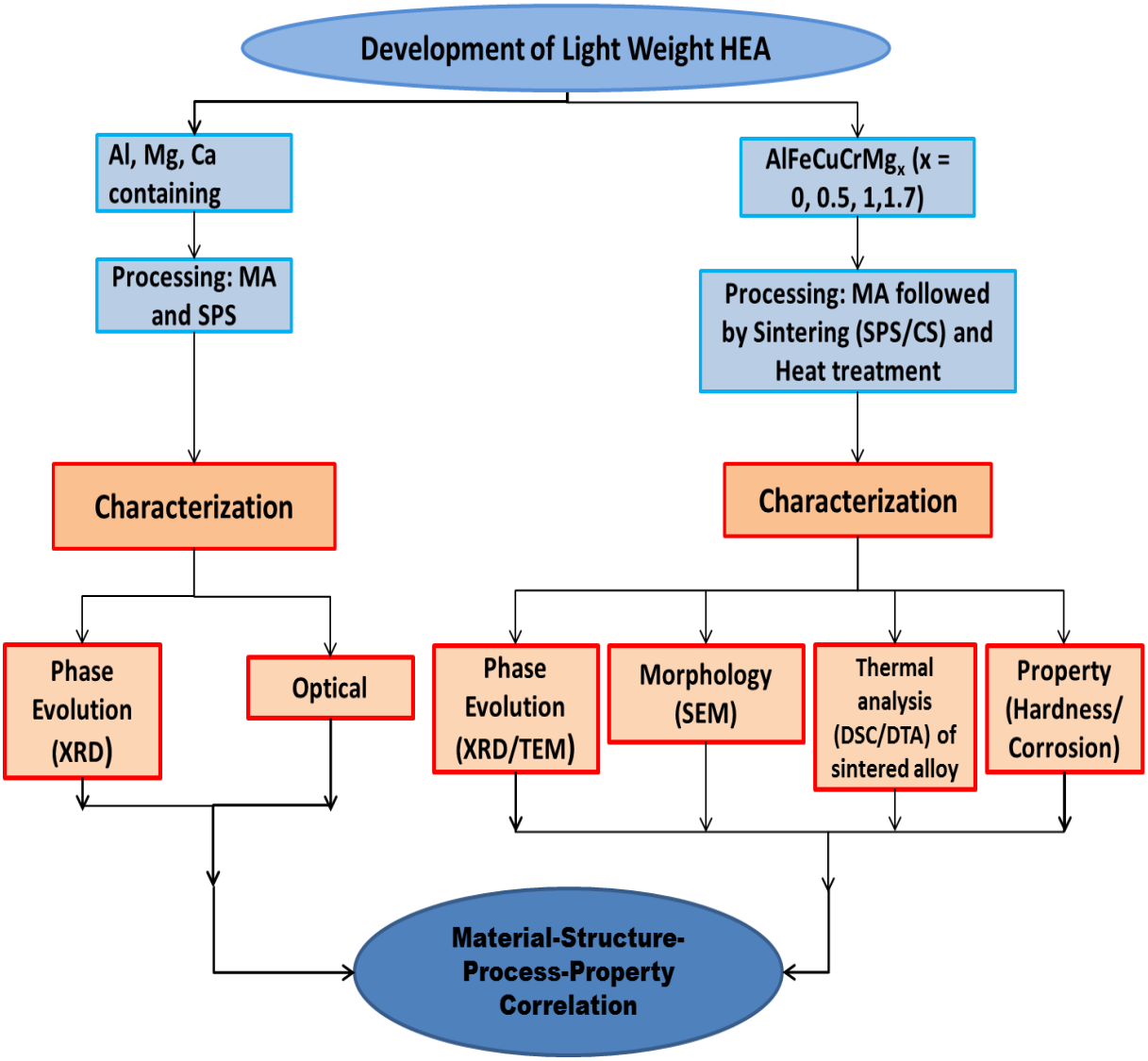

Figure 2.35 Flow diagram showing methodology for development and characterization of lightweight HEAs

Chapter 3

Materials and Methods

This chapter discusses about the materials and methods implemented for the preparation of light weight HEA.

3.1 Materials Preparation

3.1.1 Preparation of $AlFeCuCrMg_x$ (x = 0, 0.5, 1, 1.7 mol) HEA powders

The pure metal powders of Al, Mg, Fe, Cu, and Cr (Loba Chemie, India) of purity more than 99.5% were procured. The powders were mechanically alloyed utilizing Pulverisette-P6 high energy planetary ball mill (Fritsch, Germany) using a vial and balls of tungsten carbide. Ball to powder weight ratio was maintained to be around 10:1. Toluene was used as a process controlling agent (PCA) to prevent excessive cold welding on the surface of the ball and vial and also provide reducing media during the milling. The milling was carried out up to 20 hours in a planetary ball mill at 300 RPM. The as-milled powders were collected after 10 min and then after every 5 hours of milling to study the phase evolution, and dissolution sequence of each element with respect to the milling time. Furthermore, the morphology of the as milled alloys powders were discussed in details.

3.1.2 Spark Plasma Sintering of $AlFeCuCrMg_x$ (x = 0, 0.5, 1, 1.7 mol) alloys powders

As-milled powders of $AlFeCuCrMg_x$ (x = 0, 0.5, 1, 1.7) mechanically alloyed for 20 hours were spark plasma sintered using a FCT system GmbH (Model- HP D25-S1, CGCRI, Kolkata) using a graphite die. Graphite dies were purchased from Nikunj Eximp. Entp. P Ltd., Mumbai with the dimension Dia 50 mm X ID 20.4 mm X 40 mm long. Graphite pinches are had a dimension of Dia 20 mm X 20mm.

The as milled alloy powders were filled in a die cavity having diameter of 20 mm. Graphite foil was used to prevent the sticking of alloy powders from the die walls.

At first, as milled $AlFeCuCrMg_x$ (x = 0, 0.5, 1, 1.7 mol) alloys were SPSed at 500^{o}C. The holding time at sintering temperature, the heating rate and applied pressure were 10 min, 100^{o}C/min and 75 MPa, respectively. Lower temperature (500^{o}C) and higher pressure (75

MPa) was selected due to lower melting point of Mg and Al elements. The results showed large fraction of porosity in the microstructure for all the alloys.

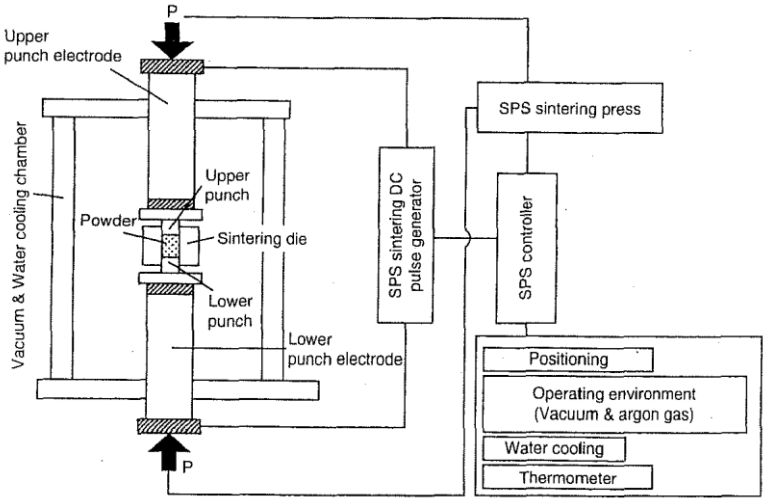

Figure 3.1 Schematic diagram of spark plasma sintering set up [67].

In general the literature defines sintering temperature to be around $0.7T_m$ to $0.9T_m$ where T_m is a melting temperature (given by Eq. 2.8) [95]. Thus, sintering temperature for AlFeCuCr was kept at 800^{o}C. It was interesting to note that for AlFeCuCrMg$_x$ (x = 0.5, 1, 1.7) alloy excessive melting was observed at a sintering temperature of 800^{o}C. Thus, sintering temperature was reduced to 700^{o}C for the magnesium-containing HEAs. Although for all the alloys the holding time at sintering temperature, the heating rate and applied pressure were kept to be 5 min, 100^{o}C/min and 50 MPa, respectively. It is to be noted that in this case the pressure is reduced to 50 MPa to prevent excess of melting at comparatively higher temperature.

Table 3.1 Theoretical melting temperature of AlFeCuCrMg$_x$ alloys

Alloys	AlFeCuCr	AlFeCuCrMg$_{0.5}$	AlFeCuCrMg	AlFeCuCrMg$_{1.7}$
T_m (^{o}C)	1570.53	1498.4	1441.0	1377.1

3.1.3 Synthesis of Al, Mg, Ca containing HEAs

Mg-Ca-Al containing HEAs, such as AlMgCaNiCu, (AlMgCa)$_{1.33}$(NiCu)$_{0.5}$, and AlMgCaFeCr have been synthesized by mechanical alloying and spark plasma sintering.

The powders of Al, Mg, Fe/Ni, Cr/Cu of purity 99.5% and Ca of purity 98% (Loba Chemie, India) are mechanically alloyed for 20 hrs using Pulverisette-P6 high energy planetary ball mill (Fritsch, Germany)to synthesize AlMgCaNiCu, $(AlMgCa)_{1.33}(NiCu)_{0.5}$, and AlMgCaFeCr alloys. Tungsten carbide balls and vials are used and ball to powder weight ratio was maintained to be around 10:1. Toluene was used as the process controlling agent (PCA) to prevent excessive cold welding on the surface of ball and vial. Mechanical alloying was performed at 300 RPM. Further, Spark Plasma Sintering of AlMgCaNiCu, $(AlMgCa)_{1.33}(NiCu)_{0.5}$, and AlMgCaFeCr alloys were carried out at the temperatures of 700^{o}C, 600^{o}C and 700^{o}C respectively, based on theoretical melting point assumptions [95] using a graphite die. The as milled alloy powders were filled in a die cavity having diameter of 20 mm. Graphite foil was used to prevent the sticking of alloy powders from the die walls. The holding time at sintering temperature, the heating rate and pressure were kept to be 5 min, 100^{o}C/min and 50 MPa, respectively.

Table 3.1 Theoretical melting temperature of AlMgCaNiCu, $(AlMgCa)_{1.33}(NiCu)_{0.5}$ and AlMgCaFeCr alloys

Alloys	AlMgCaNiCu	$(AlMgCa)_{1.33}(NiCu)_{0.5}$	AlMgCaFeCr
T_m (^{o}C)	1211.4	1081.1	1424.9

3.1.4 Conventional Sintering of $AlFeCuCrMg_x$ (x = 0, 0.5, 1, 1.7 mol) alloy powders

The as milled $AlFeCuCrMg_x$ (x = 0, 0.5, 1, 1.7) alloys are conventionally sintered by first hot compacting in hot press (Kimaya Enginners Pvt. Ltd.) using a tool steel die. The as milled alloy powders were filled in a die cavity having diameter of 10 mm. The filled-in die-assembly was placed in the hot press and subjected to heating with an average heating rate of 7^{o}C/min under a pressure of 100 MPa to a maximum temperature of 250 ^{o}C. After a soaking period of 30min under the constant pressure of 100 MPa, the sample was naturally cooled down to a temperature of approximately 50^{o}C. Finally the alloy sample was ejected out from the die and sintered in an electric resistance furnace (Varma Industrials, Trichur, India) for 4 hours at 900^{o}C in case of AlFeCuCr alloy and 800^{o}C for

$AlFeCuCrMg_x$ (x = 0.5, 1, 1.7) alloys. The temperature was selected considering the theoretical melting points assumptions and non isostatic nature of sintering.

3.2 Characterization of $AlFeCuCrMg_x$ (x = 0, 0.5, 1, 1.7 mol) HEAs

Different characterization techniques were used to analyze the phase evolution in $AlFeCuCrMg_x$ alloys. The methods were discussed in subsequent paragraphs.

3.2.1 Density Measurement

Theoretical density has been calculated by the rule of mixture given by Eq. 3.1.

$$\rho_{th} = \rho_m . (1-V_f) + \rho_f . V_f \qquad (3.1)$$

where ρ_m and ρ_f are the densities of matrix and filler respectively and V_f is the volume fraction.

The densities of sintered samples were determined by the Archimedes principle using a density measurement apparatus and precise weighing balance (Mettler Toledo) with the accuracy of 0.1mg. Ethanol as a media was used to determine the bulk density of the alloys. The density was calculated by Eq. 3.2

$$\rho_{exp} . = [W_{air}/(W_{air} - W_{med})] \text{ X } \rho_{med} \qquad (3.2)$$

where W_{air} and W_{med} are the weight of the sample in air and medium respectively. The ρ_{med} is the density of the medium

3.2.2 Phase Evolution Studies

Phase changes from the sintering process were characterized by X-Ray Diffraction **(**XRD) using an X'pert Pro (Panalytical, USA) X-ray diffractometer unit with a CuKα (λ = 0.1540598 nm) source. The scan step size and scan time was fixed to be 0.02^o and 0.7sec respectively. XRD has been performed to study the phase evolution both after MA and sintering. Also, lattice parameter, crystallite size and lattice strain were calculated by using the XRD data. The deconvolution of the overlapped peak is performed by the

Lorentzian function and instrumental broadening was corrected using single crystal Si wafer. The crystallite size was calculated by the Scherrer equation given by

$$D = \frac{K\lambda}{\beta cos\theta} \qquad (3.3)$$

where D is the crystallite size, K is the shape factor (~ 1), λ is the X-Ray wavelength, β is the line broadening, θ is the Bragg angle.

3.2.3 Microstructure by Scanning Electron Microscopy (SEM)

Microstructure of the as milled alloy powders and sintered alloys were characterized by using FE-SEM (Nova Nano 450SEM, FEI, North America) operated at 30 kV. The sample of as milled alloy powders was prepared by dispersing and sticking the powder on carbon tape and analyzed under SEM. The samples of sintered bulk alloys were prepared by grinding on a series of bonded abrasive paper (SiC) up to 1200 grit size. Mirror finish of the alloy surface was obtained by velvet cloth polishing using mixture of alumina powder (particle size, 1μm) and kerosene. Local phase composition was characterized by energy dispersive X-ray spectroscopy (EDS) detector (Bruker, Germany).The EDS data were obtained from at least 5 points, and the atomic percentage of each element has been averaged out.

In addition to above, microstructure of conventional sintered and heat treated alloys were characterized by W-SEM (Jeol, JSM-6060LA) at ACMS, IIT Kanpur.

3.2.4 Microstructure study by Transmission Electron Microscopy (TEM)

Investigation of the microstructure at the sub-micron scale was conducted by transmission electron microscopy (TECHNAI 20, FEI, North America) operated at 200 kV. High resolution-TEM, dark field TEM and selected area electron diffraction (SAED) patterns of as milled alloy powders were analyzed to confirm the crystallite size and phases present. TEM samples for as milled alloy powders were prepared by ultra sonicating the milled powders in ethanol for 30 min. Agglomerated particles were allowed to settle down for 10 min. Then the sample from upper part of the solution was collected using micropipette and spread onto the carbon coated copper grid. TEM samples for the bulk alloys were prepared by thinning by mechanical grinding up to 80

μm followed by dimpling and ion milling. Further Scanning Transmission Electron Microscopy (STEM) was performed and the phase composition at sub-micron level is investigated by EDS (Bruker, Germany) technique.

3.2.5Thermal Analysis

As-milled powder samples were analyzed up to 950^{o}C with the heating rate of 20^{o}C/min utilizing PerkinElmer Differential Thermal Analysis (DTA) (Model no.: STA 6000) to examine the phase stability of the HEAs with respect to temperature. High-temperature stability of spark plasma sintered samples were determined up to 1000^{o}C by Differential Scanning Calorimetry (DSC) (Netzsch Model no. DSC 404 F3) with a heating rate of 10^{o}C/minute. Baseline was corrected before acquiring the temperature curve for each alloy. For all the alloy samples the data were acquired repeatedly for 3 times to check the reproducibility of the results.

3.2.6 Local Atomic Environment Studies

X-ray Absorption Near Edge Structure (XANES) and Extended X-ray Absorption Fine Structure (EXAFS) measurements of the as milled alloy powders have been carried out at room temperature at the Energy Scanning EXAFS beamline (BL-9) in the transmission mode at the INDUS-2 Synchrotron source (2.5 GeV, 100 mA) at the Raja Ramanna Centre for Advanced Technology (RRCAT), Indore, India [96, 97]. The beam line operates in the photon energy range of 4-25 KeV. The beamline optics consists of a Rh/Pt coated collimating meridional cylindrical mirror used for the collimation of the beam. The collimated beam is monochromatized by a Si (111) based double crystal monochromator (DCM). This mirror is used prior to the DCM for the higher harmonic rejection. Second crystal of the DCM is a sagittal cylindrical crystal, which is used for horizontal focusing of the beam while another Rh/Pt coated bendable post mirror facing down is used for vertical focusing of the beam at the sample position. For the data collection in the transmission mode two ionization chambers of 30 cm length have been used with appropriate gas pressure. The first ionization chamber measures the incident flux (I_0) and the second ionization chamber is used for the measurement of the transmitted flux (I_t). In order to obtain a proper edge jump the samples were taken in

powder form of appropriate weight and were palletized to 15 mm diameter by mixing with 100 mg cellulose.

3.2.7 Contamination determination

O, N contamination has been determined by LECO TC436 Nitrogen/Oxygen analyzer and C contamination was determined by Horiba EMIA-8100 series combustion analyzer at M/s JLC Electromet Pvt. Ltd., Jaipur.

3.2.8 Hardness

Vickers hardness measurements were performed by UHL VMHT (Walteruhl GmBH, Germany) on bulk $AlFeCuCrMg_x$ (x=0, 0.5, 1, 1.7) HEAs. The load of 200 gf and dwell time of 15 sec were applied to take the hardness of the bulk alloys. The hardness is given by the Eq. 3.3.

$$HV = 0.1891 \ \frac{F}{d^2}\left[\frac{kgf}{mm^2}\right] \qquad (3.3)$$

where F is the load applied and d is the diagonal of the indentation

Hardness test was performed at 5 different positions in the same alloy to check the reproducibility.

3.2.9 Corrosion Study

Potentiodynamic polarization measurements of bulk $AlFeCuCrMg_x$ (x = 0, 0.5, 1, 1.7) alloys were carried out in a typical three-electrode cell setup with the specimen as a working electrode, a saturated calomel reference electrode (SCE), and a platinum counter electrode. The potential of the working electrode was measured through the Luggin probe with respect to the reference electrode which was placed as close as possible to the specimen. The electrochemical polarization measurements were conducted in aerated 3.5% NaCl solution at 25^oC under atmospheric pressure. The specimen was scanned potentiodynamically at a rate of 1mV s−1 from the initial potential of −250 mV versus open circuit potential to the final potential of 1.6VSCE. Calibration was conducted in accordance with ASTM standard.

3.2.10 Functional group analysis by Fourier Transform Infra-Red Spectroscopy (FTIR)

Infrared (IR) spectroscopy was employed to characterize the corrosion product after polarization measurement. FTIR spectrometer (Perkin Elmer, Spectrum Two, L160000A) was used for this purpose. The IR spectrum was acquired from the range of 400 cm^{-1} to 4000 cm^{-1}.

3.3 Heat Treatment of SPSed $AlFeCuCrMg_x$ (x = 0, 0.5, 1, 1.7 mol) alloys

Heat treatment of the SPSed $AlFeCuCrMg_x$ (x = 0, 0.5, 1, 1.7) was performed in an electric furnace (MTI OTF-1200X-UL, M/s TechnoS Instruments, Jaipur) in Ar atmosphere. All the alloys were heat treated in three temperature ranges i.e. 470^oC, 600^oC and 820^oC for 4 hours. These temperature ranges were chosen according to the result obtained from the thermal analysis and the binary phase diagram of Mg and other elements. The phase evolution, microstructure and hardness were studied in detail for heat treated $AlFeCuCrMg_x$ alloys.

Chapter 4

Synthesis and characterization of $AlFeCuCrMg_x$ HEAs by Mechanical Alloying

Novel $AlFeCuCrMg_x$ (x = 0, 0.5, 1, 1.7 mol) alloys were synthesized by mechanical alloying (MA). The effect of Mg content on the phase evolution of HEAs was investigated using X-Ray diffractometry (XRD), scanning electron microscopy (SEM), transmission electron microscopy (TEM) and selected area electron diffraction (SAED) pattern analysis.

4.1 Characterization of $AlFeCuCrMg_x$ (x = 0, 0.5, 1, 1.7) alloy powders

In this section phase evolution, particle morphology and composition of HEAs were thoroughly investigated Thermodynamic parameters were calculated and analyzed to explain the formation of a solid solution.

4.1.1 Phase Evolution

X-Ray Diffraction pattern of $AlFeCrCuMg_x$ (x = 0, 0.5, 1, 1.7 mol) HEA powder samples that were sequentially collected after predecided interval are shown in Fig 4.1.

Fig. 4.1(a) illustrates the phase evolution in the case of $AlFeCuCrMg_x$ (x = 0) i.e. AlFeCuCr HEA where magnesium content was nil. As the milling time a progress, Al dissolves first consequently peaks of Al completely disappear after 10 hours of milling. Cu starts to dissolve after 5 hours as indicated by a decrease in the relative intensity. Further upon milling up to 15 hrs all the elemental peaks vanish except for a small fraction of Cu. After 20 hours of milling, majorly BCC phase is formed with a small fraction of Cu (FCC) phase. Therefore, it can be concluded that microstructure of as-milled AlFeCuCr powder consists of BCC as main phase plus precipitates. Lattice parameter of BCC phase is determined to be 287.0 pm. Based on XRD pattern analysis (Fig. 4.1(a)) and the lattice parameter it can be predicted Al, Fe, and partial Cu dissolve

simultaneously in Cr. The alloying sequence of this quaternary compound during mechanical alloying is Al, Fe → Cr and Cu is partially dissolved in Cr.

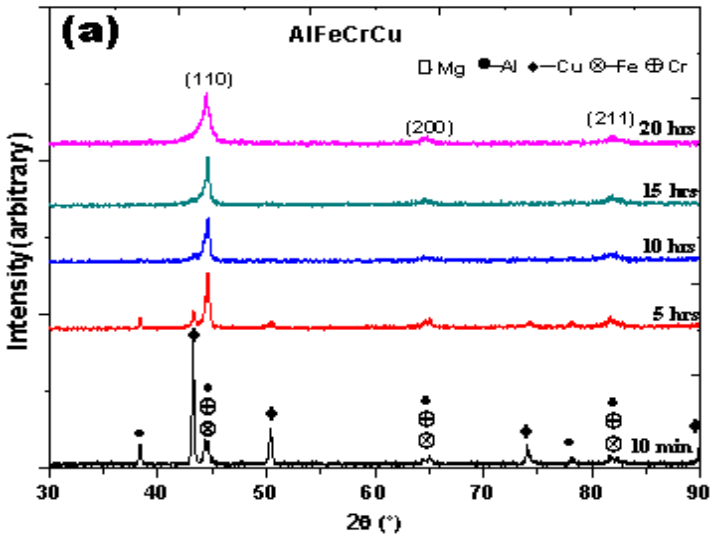

Figure4.1 (a) XRD pattern of as milled AlFeCuCr alloy as a function of milling time.

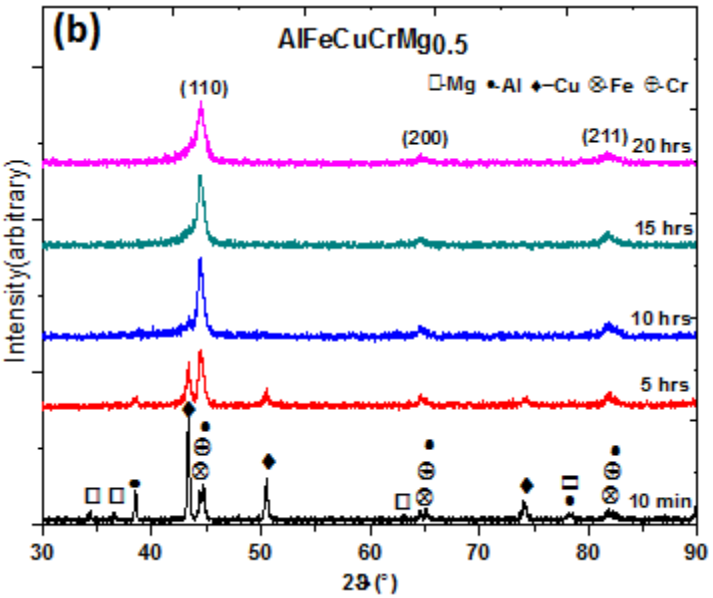

Figure4.1 (b) XRD pattern of as milled $AlFeCuCrMg_{0.5}$ alloy as a function of milling time.

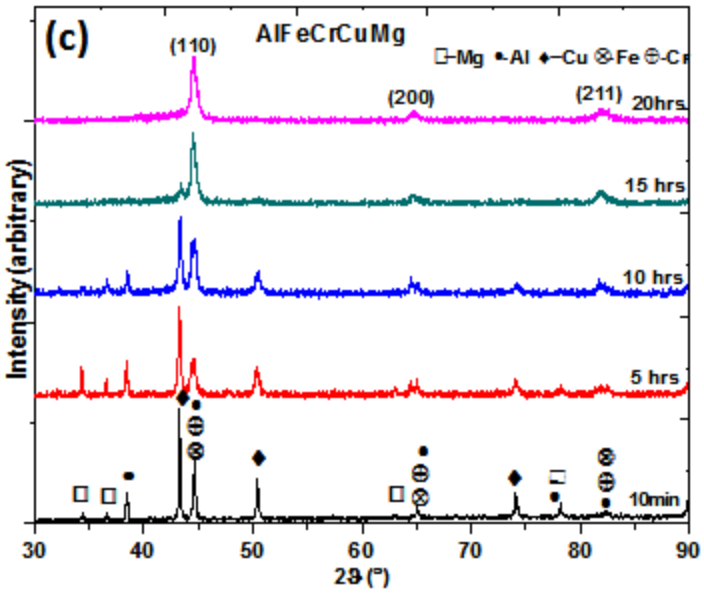

Figure4.1 (c) XRD pattern of as milled AlFeCuCrMg alloy as a function of milling time.

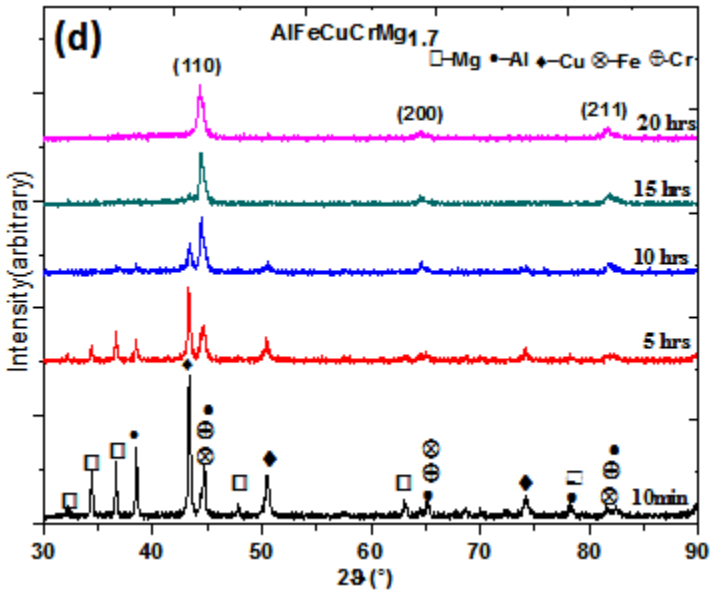

Figure4.1 (d) XRD pattern of as milled AlFeCuCrMg$_{1.7}$ alloy as a function of milling time.

Fig. 4.1(b) shows the phase evolution of AlFeCuCrMg$_{0.5}$ HEA with respect to milling time. With an increase in the milling time, peaks of Mg element completely disappear after 10 hours of milling. Further milling up to 15 hrs all the Al peaks disappeared. After 20 hours of milling time, BCC phase was observed as a major phase with the minor Cu

(FCC) phase. Lattice parameter of BCC phase was determined to be 288.2 pm. Based on the XRD pattern and study of lattice parameter it can be concluded that the alloying sequence of multicomponent $AlCuFeCrMg_{0.5}$ high entropy alloy follows Mg, Al, Fe → Cr and Cu is partially dissolved in Cr.

Fig. 4.1(c) shows the phase evolution with respect to the milling time in case of equiatomic AlFeCuCrMg HEA. It is interesting to note that most of the elemental peaks are present after 5hrs and 10 hrs of milling. As the milling process progresses, the Mg and Al peaks disappear after 15 hrs. It was observed that Cu peak completely disappears in an alloy having BCC phase after 20 hrs of milling. The alloying sequence for this equiatomic HEA can be predicted based on XRD pattern and physical properties of individual elements as Mg, Al, Cu → Cr or Fe. Also, there exist two BCC phases after 20 hours milling for AlFeCuCrMg HEA. XRD patterns of HEA having highest magnesium content i.e. $AlFeCuCrMg_{1.7}$, with varying milling time is shown in Fig. 4.1(d). It can be seen that $AlFeCuCrMg_{1.7}$ HEA has a similar pattern as AlFeCuCrMg HEA. Alloying sequence, based on lattice parameters for this alloy, can be suggested as Mg, Al, Cu → Cr or Fe, which is same as in AlFeCuCrMg HEA. Chen et al. [98] discussed the relationship between the alloying rate and the melting point of individual elements. It can be suggested that metal with higher melting point has high bonding strength and has lower self-diffusion coefficient which leads to the lower alloying rate. Altogether the alloying rate in the high entropy alloy might be dependent on various factors such as melting point, self-diffusion coefficient, and the atomic sizes of the individual elements. Table 4.1 shows the atomic size, melting point, crystal structure, self-diffusion coefficient and lattice parameter of individual elements that are present in HEAs. In cases of AlFeCuCr and $AlFeCuCrMg_{0.5}$ HEAs, all the elements are mostly dissolving in Cr matrix. Minor FCC phase in these two HEAs is due to the high positive enthalpy of mixing between Cu and other elements [99]. On the other hand, in the cases of higher Mg content HEAs such as AlFeCuCrMg and $AlFeCuCrMg_{1.7}$ it seems that all the elements are diffusing majorly in Cr lattice and minor in Fe lattice which can be explained due to high melting point of Cr (1857^{o}C) followed by Fe (1538^{o}C).

EDS spectra of the as-milled powder are shown in Fig. 4.2.

Table 4.1: Atomic size, Melting point, crystal structure, self-diffusion coefficient and Lattice parameter of individual elements

	Mg	Al	Cu	Fe	Cr
Metallic Atomic Size (pm)	160	143	128	127	128
Melting Point (^{o}C)	650	660	1083	1538	1857
Crystal Structure	HCP	FCC	FCC	BCC	BCC
Self-Diffusion Coefficient	$10^{-13}\perp$, $10^{-12}\parallel$	10^{-19}	10^{-27}	10^{-31}	10^{-41}
Standard Lattice Parameter, a (pm)	a =320.9 c = 521.1	404.94	361.5	286.6	288.3

Table 4.2: Experimentally, Vegard's law and N-R Method predicted Lattice parameter of as milled $AlFeCuCrMg_x$ (x = 0, 0.5, 1, 1.7).

Composition	Lattice Parameter, $a = d\sqrt{h^2+k^2+l^2}$(pm)	Lattice Parameter Vegard's Law (pm)	Lattice Parameter N-R method (pm)
AlFeCuCr	287.0	300.1	287.9
$AlMg_{0.5}$FeCuCr	288.2	306.4	288.2
AlMgFeCuCr	BCC 1= 288.4	311.5	BCC 1= 288.4
	BCC 2= 286.5		BCC 2= 286.6
$AlMg_{1.7}$FeCuCr	BCC 1= 288.5	317.0	BCC 1= 288.1
	BCC 2= 286.2		BCC2= 285.0

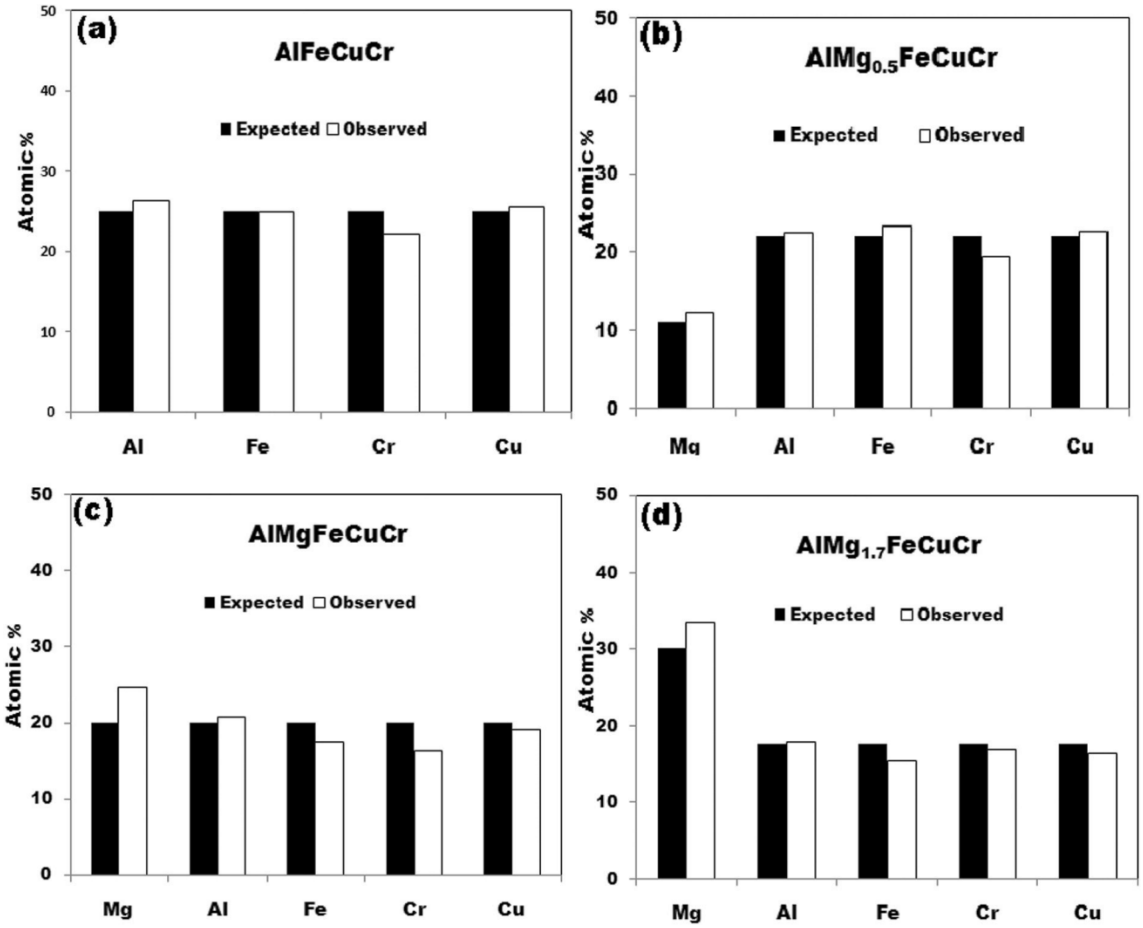

Figure4.2 Elemental composition of 20 hour as-milled powder (a) AlFeCuCr, (b) AlFeCuCrMg$_{0.5}$, (c) AlFeCuCrMg, and (d) AlFeCuCrMg$_{1.7}$.

It is clear from the EDS study that the composition of the as-milled powder is very close to the theoretically calculated composition, confirming good homogeneity even after MA.

4.1.2 Phases Determination and Lattice Parameter

Fig. 4.3 shows the detailed XRD analysis of AlFeCuCrMg$_x$ (x = 0, 0.5, 1, 1.7 moles) HEAs Fig. 4.3(a) and 4.3(b) show the deconvoluted peak of 20 hrs as-milled powders of AlFeCuCr and AlFeCuCrMg$_{0.5}$ HEAs respectively. The precise lattice parameter was calculated by Neilson-Riley method (N-R Method) and was found to be 287.989 pm and 288.226 pm for AlFeCuCr and AlFeCuCrMg$_{0.5}$, respectively (see Table. 4.2).

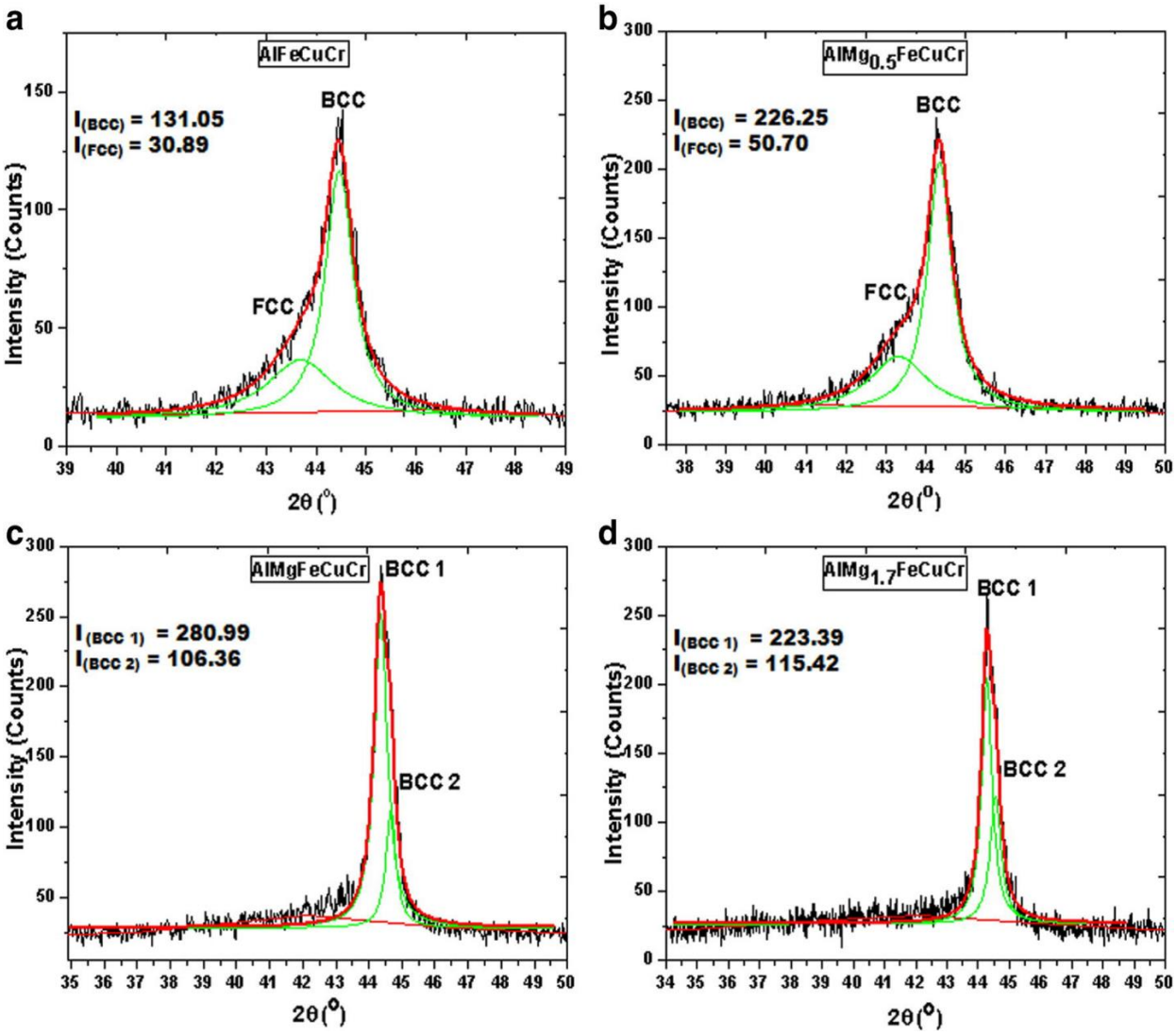

Figure4.3 (a) Deconvoluted XRD pattern of as milled AlFeCuCr. (b) Deconvoluted XRD pattern of as milled AlFeCuCrMg$_{0.5}$. (c) Deconvoluted XRD pattern of as milled AlFeCuCrMg. (d) Deconvoluted XRD pattern of as milled AlFeCuCrMg$_{1.7}$.

It can be seen that there is a little shift in the peak position towards lower 2θ for AlFeCuCrMg$_{0.5}$ HEA as compared to AlFeCuCr HEA. Thus, confirming the presence of tensile stresses in the lattice due to increasing lattice distortion as a result of Mg addition. In AlFeCuCr and AlFeCuCrMg$_{0.5}$ HEAs, BCC remains the major phase after 20 hrs of milling, which may be attributed to the large variation in atomic radius between the individual elements present in the HEA. Thus, making the BCC structure more favourable as it has a lower packing efficiency and can accommodate elements with

higher atomic volume without much distortion[100]. Fig. 4.3(a) and 4.3(b) show the overlapped peak corresponding to (111) plane, which cannot be indexed due to the absence of any other consecutive FCC peak.

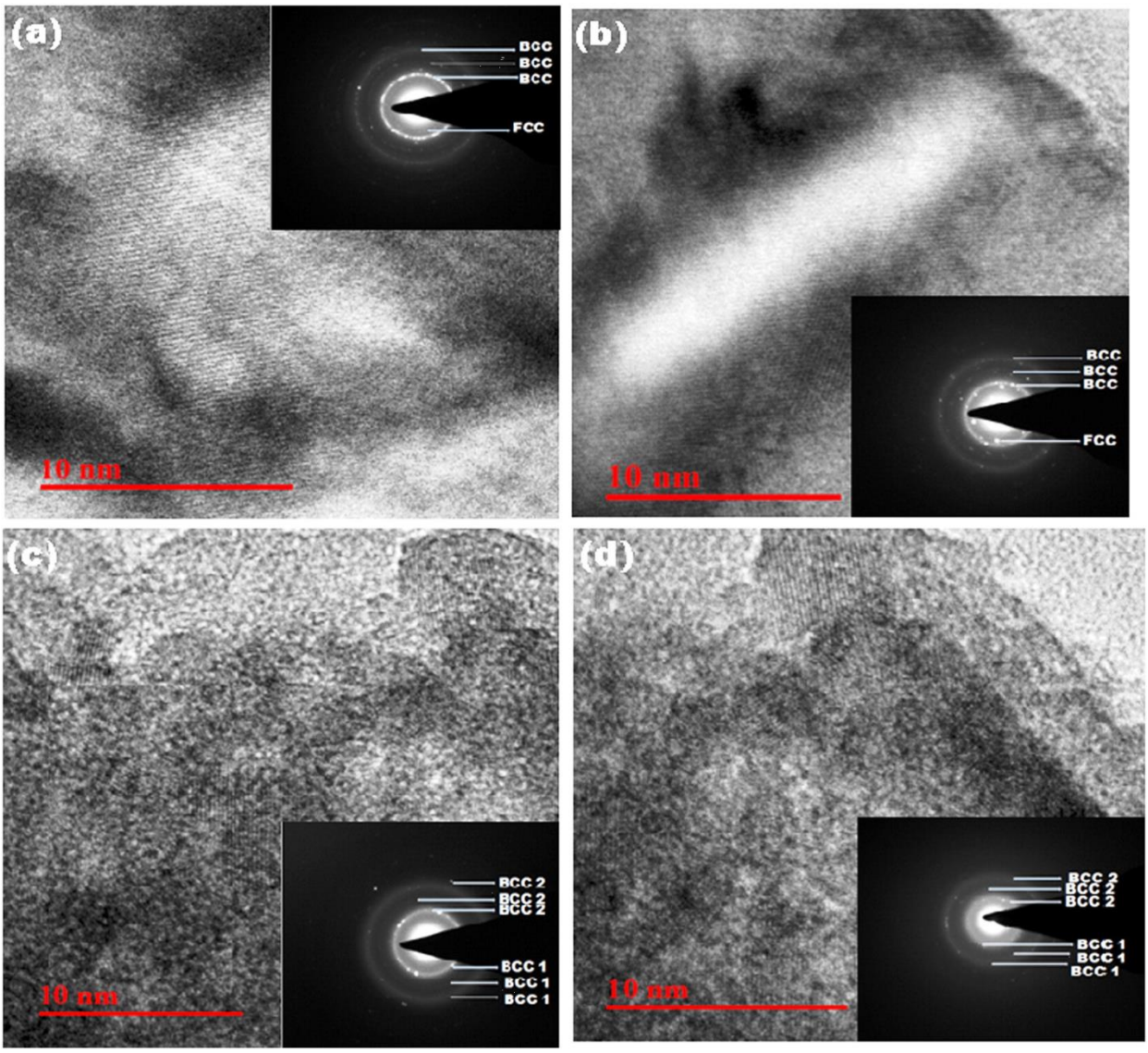

Figure 4.4 Typical HRTEM and SAED pattern of as milled (a) AlFeCuCr, (b) AlFeCuCrMg$_{0.5}$, (c) AlFeCuCrMg, and (d) AlFeCuCrMg$_{1.7}$ alloys.

Fig. 4.4(a) and 4.4(b) show the HR-TEM and SAED patterns for AlFeCuCr and AlFeCuCrMg$_{0.5}$ HEAs. The interplanar spacing was calculated with the help of HR-TEM

and SAED pattern which is in support with the XRD results. SAED also confirmed the formation of BCC as a major phase along with a small fraction of FCC phase (see Fig. 4.4).

Detailed XRD study of AlFeCuCrMg and $AlFeCuCrMg_{1.7}$ (Fig. 4.3) revealed that there are two BCC phases (BCC 1 and BCC 2) present as shown in Fig.4.3(c) and 4.3(d). The lattice parameter for AlFeCuCrMg HEA is determined to be 288.44 pm, 286. 83 pm for BCC 1 and BCC 2 respectively. For $AlFeCuCrMg_{1.7}$ alloy lattice parameter is 288.14 pm and 285.02 pm for BCC 1 and BCC 2 respectively (Table. 4.2). It is interesting to note that the lattice parameter obtained for both the phases formed in $AlFeCuCrMg_x$ (x = 1, 1.7) are closely matching to the lattice parameters of Cr (288.3 pm) and Fe (286.6 pm), which justifies the formation of Cr type and Fe type of BCC1 and BCC2 structures respectively in $AlFeCuCrMg_x$ (x = 1, 1.7). Also, it can be predicted that higher Mg content results in dissolution of complete FCC and decomposition of two BCC lattices [101].The dissolution of the FCC can be explained due to increase of potential sites for Cu to go inside the BCC lattice. Fig. 4.4(c) and 4.4(d) show SAED pattern of $AlFeCuCrMg_x$ (x = 1, 1.7) HEAs. SAED analysis confirmed the formation of two BCC phases. Interplanar spacing determined from XRD analysis is matched with interplanar spacing determined from HR-TEM and SAED patterns. Thus, it can be concluded that for $AlFeCuCrMg_x$ (x = 1, 1.7) Fe and Cr act as solvent elements whereas Mg, Al, and Cu behave like solute elements. The phase fractions of the BCC 2 phase in AlFeCuCrMg and $AlFeCuCrMg_{1.7}$alloy have been calculated by Eq. 4.1

$$\text{BCC 2 Phase Fraction} = \frac{I_{BCC\,2}}{I_{BCC\,1}+I_{BCC\,2}} \qquad (4.1)$$

where $I_{BCC\,2}$ is the peak intensity of the BCC 2 phase and $I_{BCC\,1}$ is the peak intensity of BCC 1 phase.

The amount of BCC 2 phase was determined to be 27.45% and 34.06% for AlFeCuCrMg and $AlFeCuCrMg_{1.7}$alloys respectively. Further, Fig. 4.5 shows the variation between experimentally calculated lattice parameter of major BCC phase and lattice parameter predicted by Vegard's law. For all the HEAs, the experimental value of lattice parameter deviates from the theoretically calculated lattice parameter in a negative direction. For

AlFeCuCr and $AlFeCuCrMg_{0.5}$ HEAs the deviations in the experimentally calculated lattice parameter are due to the presence of minor Cu (FCC) phase. However, in cases of AlFeCuCrMg and $AlFeCuCrMg_{1.7}$alloy the deviation is due to a decomposition of another BCC phase (BCC 2). As the concentration of Mg increases, lattice parameter increases in $AlFeCuCrMg_x$ (x = 0, 0.5, 1 mol) HEAs (Fig. 4.5). It decreases slightly in $AlFeCuCrMg_{1.7}$ HEA which may result from some relaxation in lattice parameter due to a higher percentage of BCC 2 phase.

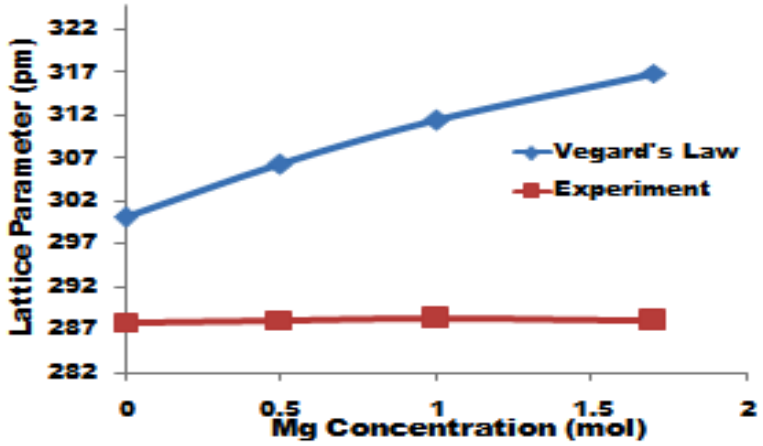

Figure4.5 Variation between experimentally calculate lattice parameter and lattice parameter predicted by Vegard's law.

Detailed XRD study and HR-TEM/SAED pattern (Fig. 4.3) of AlFeCuCrMg and $AlFeCuCrMg_{1.7}$ alloys revealed that there are two BCC phases (BCC 1 and BCC 2) present as shown in Fig. 4.3(c) and 4.3(d). The lattice parameter for AlFeCuCrMg HEA is determined to be 288.44 pm, 286.83 pm for BCC 1 and BCC 2 respectively. For $AlFeCuCrMg_{1.7}$ alloy, the lattice parameter is 288.14 pm and 285.02 pm for BCC 1 and BCC 2 respectively. The amount of BCC 2 phase was determined to be 27.45% and 34.06% for AlFeCuCrMg and $AlFeCuCrMg_{1.7}$ respectively.

4.1.3 Crystallite Size and Lattice Strain

Table 4.3 shows the comparison between the crystallite size of $AlFeCuCrMg_x$ (x = 0, 0.5, 1, 1.7 moles) obtained from Debye-Scherrer formula, Williamson Hall Method (W-H method) and TEM dark field images. Dark field TEM image (Fig. 4.6) was obtained by moving the aperture to the selected portion of (110) diffraction ring. For AlFeCuCrMg and $AlFeCuCrMg_{1.7}$ HEA crystallite size of BCC 2 was obtained by moving the aperture on the (110) plane of BCC2 phase. The bright region in the dark field TEM image shows the (110) planes oriented normal to the diffraction vector and parallel to the optical axis. Fig. 4.6 (inset) shows the respective distribution of crystallite size of $AlFeCuCrMg_x$ (x = 0, 0.5, 1, 1.7 moles) HEAs, which have been determined by image j software. It can be clearly seen that for $AlFeCuCrMg_x$(x = 0, 0.5, 1, 1.7 mol) HEAs, the crystallite size obtained by Willamson Hall (W-H) method is greater than the crystalline size obtained by TEM dark field image (Table 4.3). The higher value of crystallite size by these methods is due to the existence of anisotropic variation in the residual strain [102]. The strain anisotropy effect has been ignored while calculating the crystallite size and strain which may be the probable reason for the error in the prediction by W-H method. Fig. 4.8 shows the variation in the microstrain in $AlFeCuCrMg_x$ (x = 0, 0.5, 1, 1.7 moles) HEAs calculated by the following formula.

$$\varepsilon = \beta_{hkl}/4\tan\theta \qquad (4.2)$$

where β_{hkl} is the full-width half maximum (FWHM)

It is evident that microstrain initially increases with increase in Mg content and then decreases for AlFeCuCrMg and again increase slightly for $AlFeCuCrMg_{1.7}$ alloy. It was interesting to note that while milling of AlFeCuCrMg and $AlFeCuCrMg_{1.7}$ HEAs, the temperature rise was much more than that in cases of AlFeCuCr and $AlFeCuCrMg_{0.5}$alloys which may be due to the exothermic reaction while milling of higher Mg content HEAs. This increase in temperature tends to relax microstrain (see Fig. 4.7) [62].

Thus, AlFeCuCrMg and $AlFeCuCrMg_{1.7}$HEA have a much lower value of micro strain than AlFeCuCr and $AlFeCuCrMg_{0.5}$. Slight increase in the lattice strain (0.335%) in $AlFeCuCrMg_{1.7}$ compared to AlFeCuCrMg is due to the Mg-super saturation and increase in lattice distortion in the lattice of Cr and Fe.

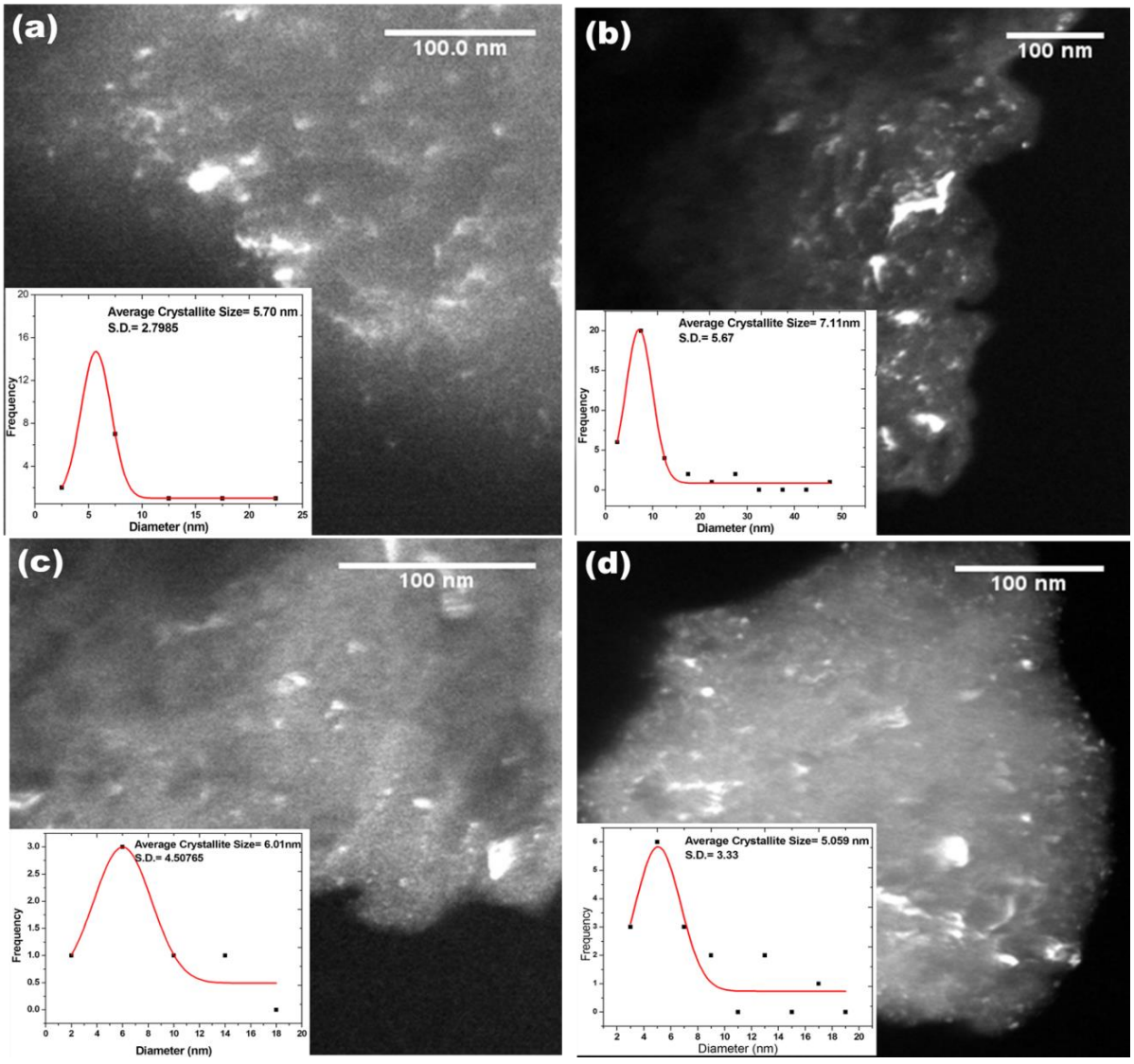

Figure 4.6 TEM dark field image of as milled (a) AlFeCuCr, (b) $AlFeCuCrMg_{0.5}$, (c) AlFeCuCrMg, and (d) $AlFeCuCrMg_{1.7}$ HEAs (inset: respective crystallite size distribution).

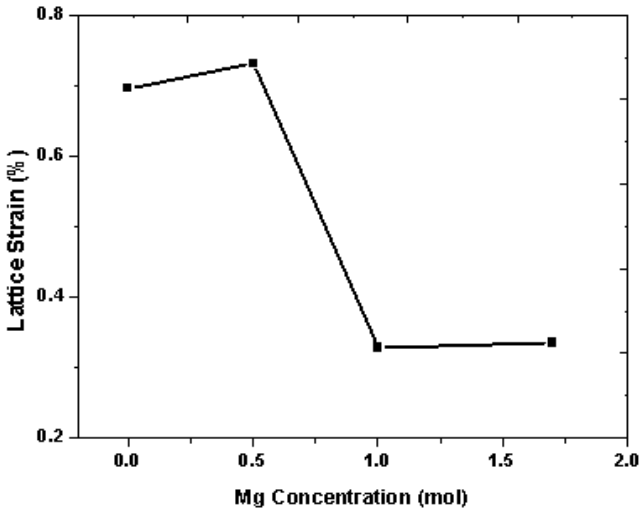

Figure 4.7Variation of micro-strain in AlFeCuCrMg$_x$ (x = 0, 0.5, 1, 1.7 mole) HEAs.

Table 4.3 Crystalline size by Scherer method and Williamson Hall method dark field TEM image and the lattice strain of as milled AlFeCuCrMg$_x$ (x = 0, 0.5, 1, 1.7).

Composition	Crystallite size, Scherrer Formula, D (nm)	Crystallite size, W-H method, D (nm)	Average Crystallite size, TEM, D (nm)	Strain $\varepsilon = \beta_{hkl}/4\tan\theta$ (%)	Strain, W-H method (%)
AlFeCuCr	12.12	99.0	5.70	0.696	0.633
AlFeCuCrMg$_{0.5}$	10.95	86.6	7.11	0.731	0.678
AlFeCuCrMg	BCC 1: 23.1	BCC 1: 35.1	BCC 1: 6.01	BCC 1: 0.328	BCC 1: 0.169
	BCC 2: 17.0	BCC 2: 628.0	BCC 2: 2.60	BCC 2: 0.341	BCC 2: 0.343
AlFeCuCrMg$_{1.7}$	BCC 1: 29.30	BCC 1: 81.5	BCC 1: 5.05	BCC 1: 0.335	BCC 1: 0.280
	BCC 2: 38.10	BCC 2: 33.7	BCC 2: 3.33	BCC 2: 0.353	BCC 2: 0.185

4.1.4 Morphology of Alloy Formation

Fig. 4.8(a), 4.8(b), 4.8(c) and 4.8(d) show morphology of the 20 hrs milled powder of AlFeCuCr, AlFeCuCr$Mg_{0.5}$, AlFeCuCrMg, and AlFeCuCr$Mg_{1.7}$alloys respectively. It can be clearly seen that as the Mg concentration increases the excessive amount of cold welding is increased as compared to fracturing. Also, the morphology of as-milled HEA suggests the formation of a layered structure that results from cold welding and fracturing [103].

Mechanism of formation of solid solution in case of AlFeCuCr and AlFeCuCr$Mg_{0.5}$ alloys can be explained in two steps (1) repetitive cold welding and fracturing, (2) diffusion. It is to be noted that the rate of flattening of Al, Mg and Cu is more than that in Fe, and Cr. In the initial hours of milling all the elements are combined by the cold welding and interlamellar spacings of resultant crystal are decreased. As the milling continues increase in the work hardening of the elements increases the brittleness and initiates fracturing. Prolonged milling tends to reduce crystallite size which further reduces interlamellar spacing between the elements up to a level from where diffusion of the individual atoms starts. Atoms diffuse into the lattice defects of other elements which are created due to severe plastic deformation resulting in an increase in micro strain (see Table 4.3) [62, 12]. Although in the cases of AlFeCuCrMg and AlFeCuCr$Mg_{1.7}$HEAs higher content of larger atomic size element (Mg) results in an increase in the microscopic temperature during milling. Thereby, increasing the number of slip planes in Mg, which in turn increases the ductility of Mg. As a result overall alloying is delayed (see Fig. 4.1(c), 4.1(d)) because of excessive cold welding in the initial hours of milling. Fracturing of the powder particles takes place at much later stages.

Further, higher Mg content results in the formation of supersaturated solid solution by the

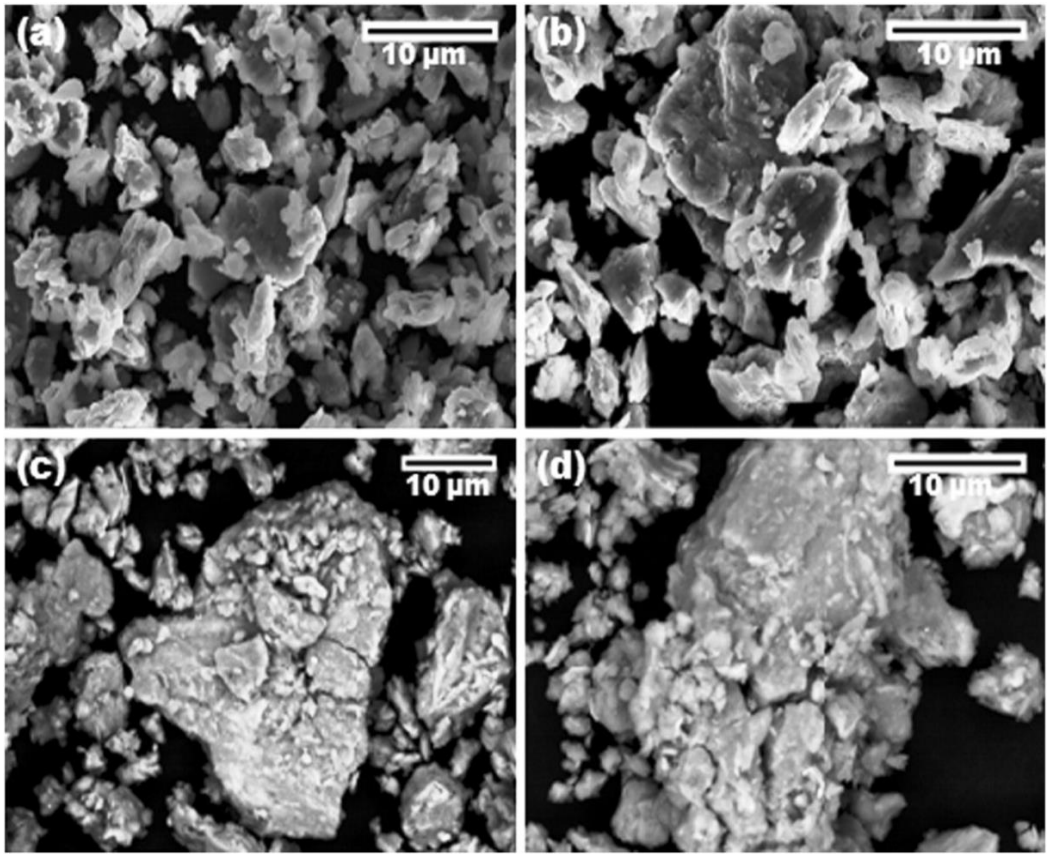

Figure 4.8 Morphology of 20 hour milled (a) AlFeCuCr, (b) $AlFeCuCrMg_{0.5}$, (c) AlFeCuCrMg, (d) $AlFeCuCrMg_{1.7}$ HEAs.

diffusion of Mg, Al, and Cu in Cr and/or Fe crystal structure thereby forming two BCC phases.

4.1.5 Thermodynamic parameters for formation of solid solution

Table 4.4 shows the calculated values of ΔH_{mix}, δ, and ΔS_{conf} for $AlFeCuCrMg_x$ (x = 0, 0.5, 1, 1.7 mol) HEAs.

Table 4.4 Thermodynamic Parameters of $AlFeCuCrMg_x$ (x = 0, 0.5, 1, 1.7) alloys.

Composition	ΔS_{config} (J/mol.K)	Delta (δ)	ΔH_{mix} (kJ/mol)	VEC	ΔX	T_m (K)	Ω	e/a
AlFeCuCr	11.52	5.05	0.50	7.0	0.1189	1570.53	36.18	2.25
$AlMg_{0.5}FeCuCr$	13.14	8.05	4.04	6.4	0.1779	1498.42	4.87	2.22
AlMgFeCuCr	13.38	9.37	6.24	6.0	0.2056	1441.03	3.08	2.2
$AlMg_{1.7}FeCuCr$	13.15	10.12	7.99	5.5	0.2247	1377.11	2.26	2.17

Fig 4.9 shows the variation of enthalpy of mixing (ΔH_{mix}), atomic radii mismatch (δ) and configurational entropy of mixing (ΔS_{conf}). It can be seen that the enthalpy of mixing (ΔH_{mix}) and atomic radii mismatch (δ) increase with an increase in the Mg concentration because of high positive enthalpies between Mg-Cr, Mg-Fe, Cu-Fe and Cu-Cr [104]. ΔS_{conf} increases with an increase in Mg content and is maximum for the equiatomic AlFeCuCrMg HEA. Although it decreases for $AlFeCuCrMg_{1.7}$ HEA which is because of higher Mg concentration that reduces the elemental disorderness. ΔS_{conf} for all synthesized HEAs by mechanical alloying have the values greater than 11.5 J/mol.K.

It is interesting to note that thermodynamic parameters in $AlFeCuCrMg_x$ (x = 0.5,1, 1.7 mol) do not favour the criterion i.e. ΔS_{conf} > 13.38J/K mol, -10kJ/mol < ΔH_{mix}< 5kJ/mol, and δ < 4% for formation of solid solution. Still, in the present case a simple solid solution is found in all $AlFeCuCrMg_x$ HEAs. The criterion Ω>1 which shows the dependency of configurational entropy and enthalpy of mixing in the formation of solid solution is very much applicable for $AlFeCuCrMg_x$ (x = 0, 0.5, 1, 1.7 mol) high entropy alloys (see Table. 4.4).

Although, present HEAs are synthesized by MA and the macro level temperature while MA do not rise to the melting temperature, T_m, it can be explained while the MA processing the local microscopic temperature, required for crystal structure change might have increased due to exothermic reaction occurring during the milling process. Thus reducing the dominance of high mixing enthalpy helps forming a solid solution to remain intact at room temperature due to the effect of severe lattice distortion. Thus showing the dependence of the Ω parameter in the formation of a solid solution even when the synthesis route is MA.

Electronegativity of the $AlFeCuCrMg_x$ (x = 0, 0.5, 1, 1.7 mol) HEAs is tabulated in Table. 4.4. The criterion ΔX > 0.133 is fulfilled by $AlFeCuCrMg_x$ (x=0, 0.5, 1, 1.7 mol) HEAs.

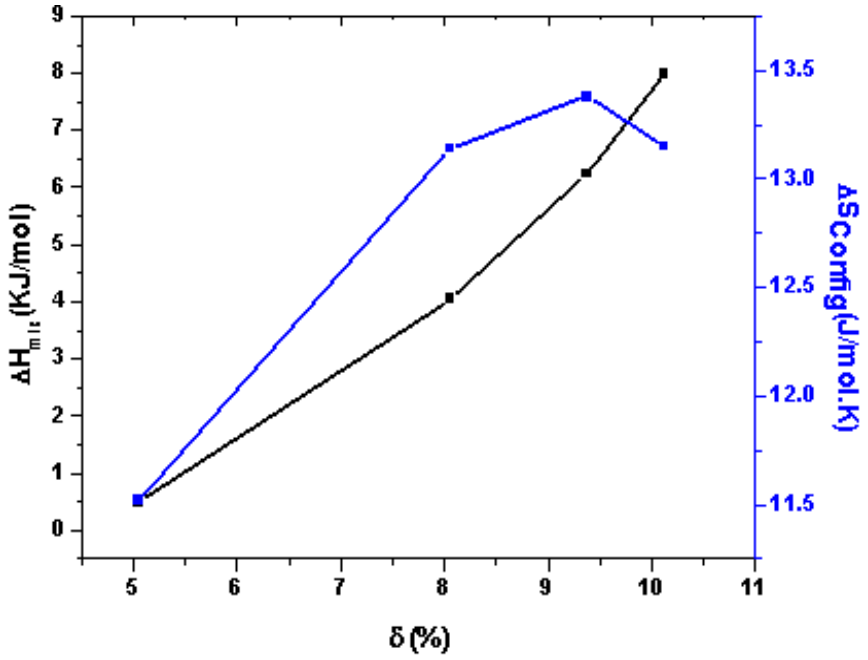

Figure 4.9 Plot showing variation between ΔH_{mix}, ΔS_{config} with δ (%).

Although the XRD patterns (see Fig. 4.1) do not show any topologically close packed phase, it proves that the role of electronegativity for the formation of solid solution is not vital in MAed alloys.

Fig. 4.10 shows the variation between Mg content and VEC for $AlFeCuCrMg_x$ (x = 0, 0.5, 1, 1.7 mol) HEAs. It is clear from Fig. 4.10 that as the Mg concentration in $AlFeCuCrMg_x$ HEAs is increasing the valence electron concentration is decreasing from 7 to 5.5. Number of itinerant electrons (e/a) is also calculated and found out to be decreasing from 2.25 to 2.17 as the Mg concentration is increasing from 0 to 1.7 at.% (see Table.4.4). Poletti et al. [50] suggested that stabilization of solid solution is dependent on the number of the itinerant electron (e/a). Further, the BCC solid solution only forms for $1.8 < e/a < 2.3$ [50].

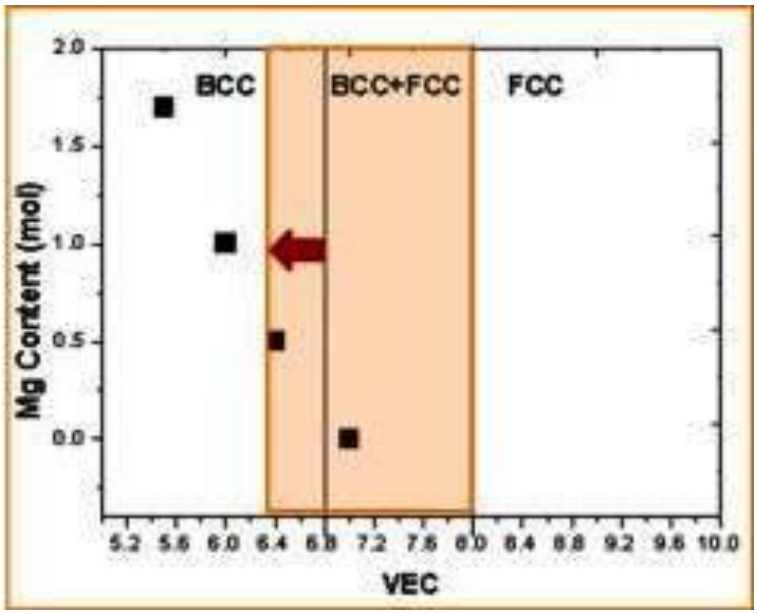

Figure 4.10 Variation between Mg content and VEC.

As the Mg content increases, the e/a value is lowered (see Table 4.4) promoting the formation of BCC phase. Hence, it can be concluded that Mg is a strong BCC former. Also, VEC of $AlFeCuCrMg_x$ HEAs supports the ranges predicted by Guo [48] for the formation BCC, BCC + FCC and FCC (Fig. 4.10). It can also be observed that minor FCC phase present in AlFeCuCr and $AlFeCuCrMg_{0.5}$ is due to the fact that VEC of these HEAs are close to the boundary wall, i.e. VEC = 6.87. It can be concluded that the boundary wall has shifted toward left at least up to 6.4 mainly because of the presence of Mg. For AlFeCuCrMg and $AlFeCuCrMg_{1.7}$, the value of VEC is much lower than the boundary wall for the formation of FCC system hence minor FCC system vanishes.

4.1.6 Phase transformation of $AlFeCuCrMg_x$ alloys

Fig. 4.11 shows the DTA curves for four $AlFeCuCrMg_x$ (x = 0, 0.5, 1, 1.7 mol) HEAs. It can be clearly seen that chosen HEAs are thermally stable up to 500^o C, and there is no substantial phase transformation in this range.

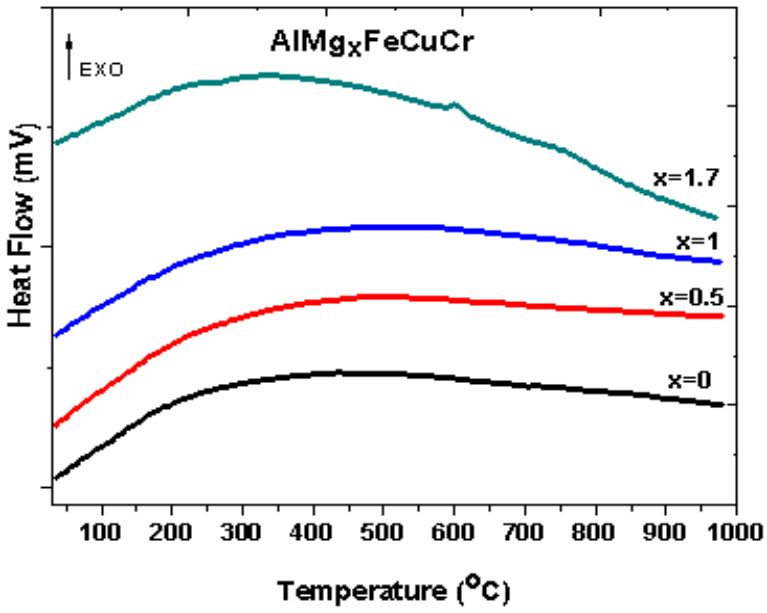

Figure 4.11 DTA scan of as milled AlFeCuCrMg$_x$ (x = 0, 0.5, 1, 1.7 mol) HEAs.

DTA curve shows a broad exothermic curve in the range of 25^o C to 450^{o}C for AlFeCuCr, AlFeCuCrMg$_{0.5}$ and AlFeCuCrMg HEAs, which is associated with the release of internal stress introduced by structural deformation and lattice strain. For AlFeCuCrMg$_{1.7}$ HEAs, there is a presence of an exothermic peak at 602.6^{o}C which is due to the formation of more stable phase resulting in the release of energy.

4.2 Local atomic structure investigation of AlFeCuCrMg$_x$ (x = 0.5, 1, 1.7 mol) HEAs

In this section local atomic structure of novel AlFeCuCrMg$_x$ (x = 0.5, 1, 1.7) high entropy alloys (HEAs) produced by mechanical alloying and aged for one year in desiccator was studied by Fe, Cr and Cu K-edge X-ray absorption near edge spectroscopy(XANES) and extended x-ray absorption fine structure (EXAFS) spectroscopy.

4.2.1 Fe, Cr and Cu K-edge XANES

Figs. 4.12 (a),(b), and (c) show the normalized XANES spectra of the HEA samples along with that of standard metal foils measured at the Fe, Cr and Cu K-edges

respectively. Fig. 4.12 indicates that the edge energies in the sample match with that of the respective metal foils confirming the elemental (0 oxidation) state of the metals in these alloy samples.

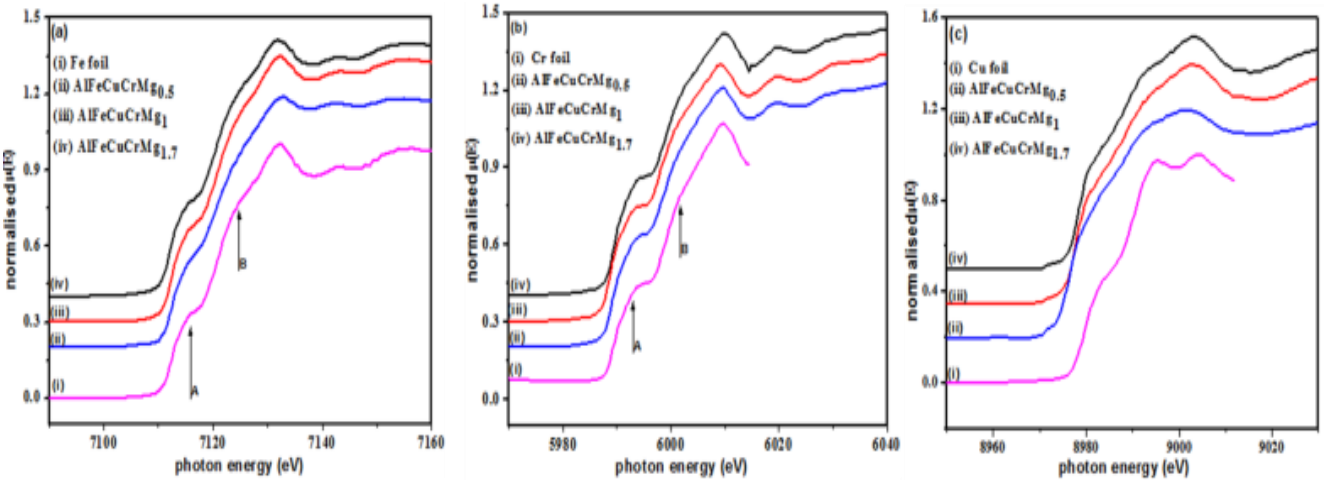

Figure 4.12 Normalized XANES spectra of the as milled HEAs at (a) Fe K-edge (b) Cr K-edge and (c) Cu K edge

Furthermore, the XANES spectra of the alloys at the Fe and Cr K-edges resemble that of the respective metal foils with two bumps in the edge energy region [105]. However, Cu K-edge XANES spectrum (Fig. 4.12(c)) of the samples, particularly of the low Mg alloy ($AlFeCuCrMg_{0.5}$), does not resemble with metallic Cu sample completely indicating the presence of some other phase in this sample.

4.2.2 Fe, Cr and Cu K-edge EXAFS

Figures 4.13(a), (b) & (c) show the normalized EXAFS ($\mu(E)$ versus E) spectra of the HEA samples measured at Fe and Cr and Cu K-edges respectively. The analyses of the EXAFS data have been carried out following the standard procedure[106, 107] using the IFEFFIT software package[108].

This includes data reduction and Fourier transform to derive the $\chi(R)$ versus R plots from the absorption ($\mu(E)$ versus E) spectra, generation of the theoretical EXAFS spectra starting from an assumed crystallographic structure and finally fitting of the experimental $\chi(R)$ versus R data with the theoretical ones using the FEFF 6.0 code.

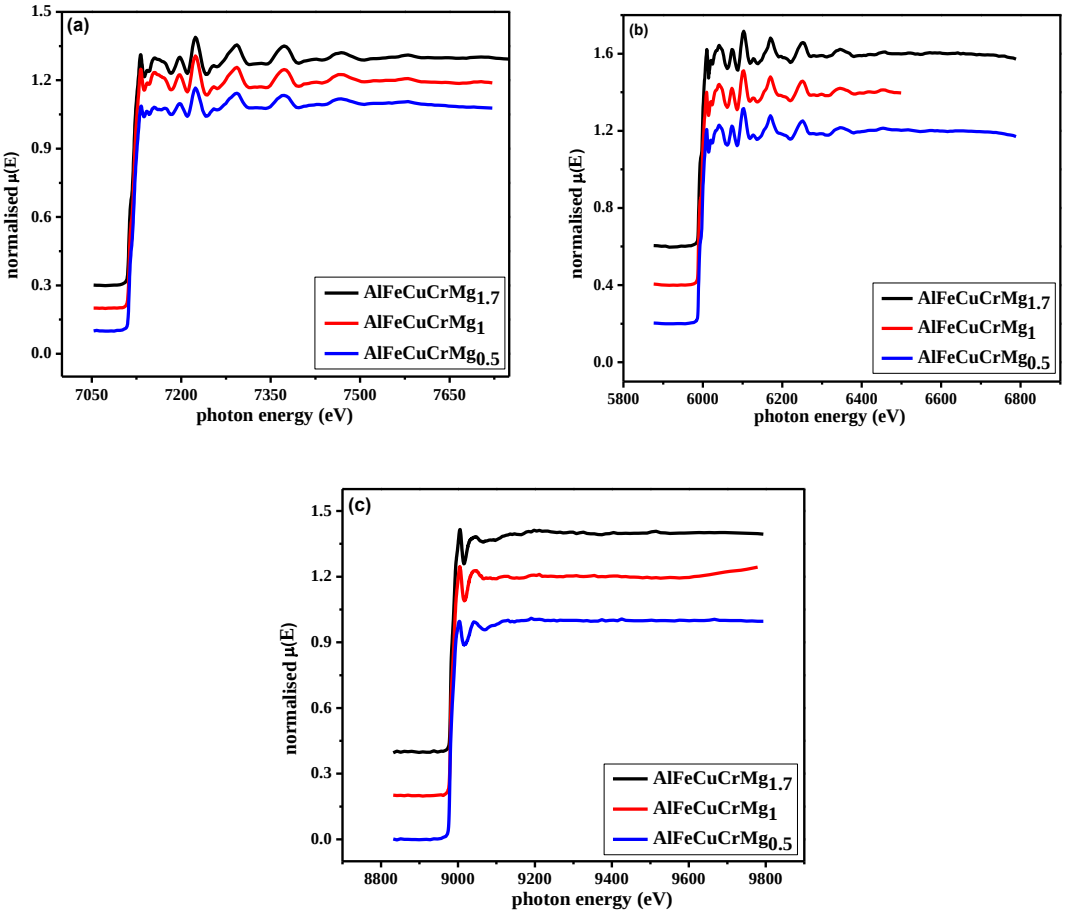

Figure 4.13 Normalized EXAFS spectra of the as milled HEAs at (a) Fe K-edge, (b) Cr K-edge and (c) Cu K-edge.

The experimental phase uncorrected $\chi(R)$ versus R plots of the samples at Fe, Cr and Cu K-edges have been shown in Figs. 4.14(a), (b) & (c). The $\chi(R)$ versus R data for the respective metal foils are also shown in the above figures. Fig. 4.14(a) & (b) reveal that the $\chi(R)$ versus R .plots of the samples at both the Fe and Cr K-edges are identical to each other due to their nearby atomic numbers and similar crystal structure. It can also be seen that the plots at Fe and Cr K edges are identical to that of Fe and Cr metals. This further suggests that both Fe and Cr have the same kind of local structures as their metallic state and do not change significantly with a change in Mg concentration in the HEAs. These results justify the formation of major BCC structures in the as-milled HEAs. The Fourier transformation of the EXAFS spectra to obtain the $\chi(R)$ versus R

plots has been carried out using a window function in the k -range of 3-11 Å^{-1} and the experimental spectra have been fitted with theoretically generated data in the R range of 1-5 Å for both Fe and Cr K-edge data.

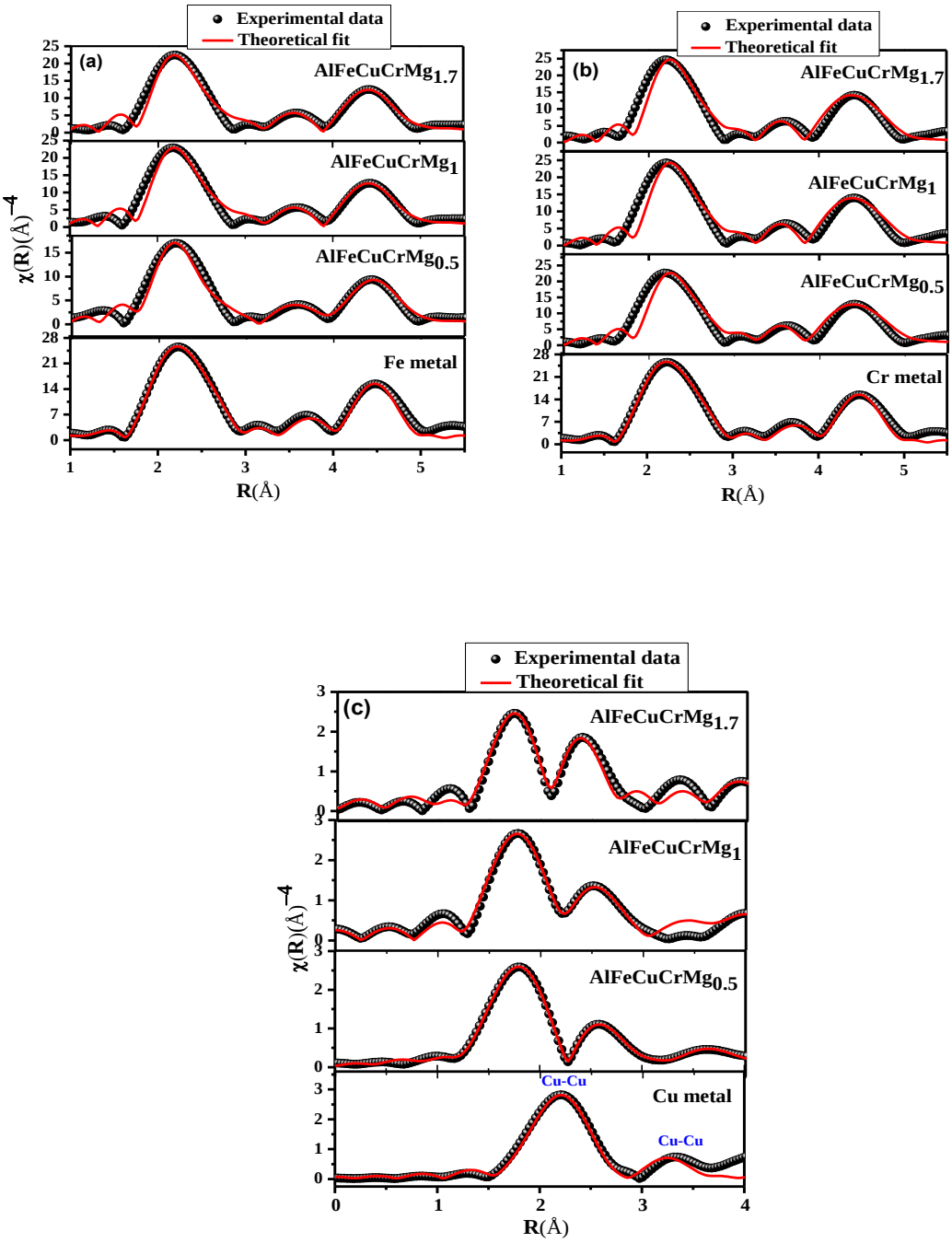

Figure 4.14 Experimental $\chi(R)$ versus R plots along with the theoretical fitted plot of the as milled HEAs samples at (a) Fe K-edge, (b) Cr K-edge and (c) Cu K-edge

XRD results of the samples show the presence BCC as a major phase in these HEAs (Fig. 4.1). Thus, in order to generate the theoretical $\chi(R)$ versus R plots BCC structure has been taken as input structure and various structural parameters have been obtained from ICSD database [109]. Though it is well known that for such high entropy alloy samples, each element has the same possibility to occupy the different lattice sites [10], to generate the theoretical EXAFS spectra we have assumed the BCC structure of 5-prinicipal element HEA systems (of the type ABCDE) as shown in Fig. 4.15, where the body center position is occupied by Mg and all the remaining atoms are situated at the corner positions [10]. In this configuration, Mg atoms form the 1st co-ordination shell of the core absorbing atom (Fe or Cr) while the atoms sitting at corner positions form the 2nd and 3rd coordination spheres.

For fitting of the spectra, amplitudes of the scattering (NS_0^2) have been kept fixed for the different coordination shells for all the samples at a particular edge, while the bond distances and disorder (Debye-Waller) factors (σ^2), which give the mean-square fluctuations in the distances, have been varied during fitting. The goodness of the fit in the above process is generally expressed by the R_{factor} which is defined as:

$$R_{factor} = \sum \frac{[\mathrm{Im}(\chi_{dat}(r_i) - \chi_{th}(r_i)]^2 + [\mathrm{Re}(\chi_{dat}(r_i) - \chi_{th}(r_i)]^2}{[\mathrm{Im}(\chi_{dat}(r_i)]^2 + [\mathrm{Re}(\chi_{dat}(r_i)]^2} \quad (4.3)$$

where, χ_{dat} and χ_{th} refer to the experimental and theoretical $\chi(R)$ values respectively and Im and Re refer to the imaginary and real parts of the respective quantities.

The best fit theoretical $\chi(R)$ versus R spectra of the samples are also shown in Fig.4.14 (a) & (b) along with the experimental data measured at Fe and Cr K edges and the values of the best fit parameters have been shown in Table 4.5 & 4.6 respectively. Fe K-edge (Fig 4.14(a)) data show three significant peaks in the $\chi(R)$ versus R plots , the 1st peak at ~2.2Å appears little broader which is due to the contributions of 8 nearby Mg atoms at 2.48 Å in the 1st co-ordination shell and 2 Al, Cr and Cu atoms each at 2.87 Å in the 2nd

co-ordination shell. The 2nd peak ~ 3.7 Å is due to the scattering from 12 Fe atoms at 4.06 Å in the 3rd co-ordination shell and the 3rd peak at ~4.5Å appears due scattering from the 24 Fe and 8 Fe atoms at 4.76 Å and 4.97 Å respectively. Similar peaks appear also in the Cr K-edge $\chi(R)$ versus R plots (Fig. 4.14(b)) and the contributions of the different scattering paths in the respective peaks are also similar.

The 1st peak is due to the mixed contributions of the nearby 8 Mg atoms at 2.49 Å and 2 Al, Fe and Cu atoms each at 2.88 Å. The2nd peak arises due to scattering from 12 Cr atoms at 4.07 Å and the 3rd peak is due to 24 Cr and 8 Cr atoms at 4.78 Å and 4.99 Å respectively surrounding the core Cr atom. Fitting of the sample data suggests that the disorder in the structure increases with an increase in the Mg concentration in the samples which, however, also increases their entropy and stability. The overall structure of the sample however remains same over the whole concentration range of Mg.

Tables 4.5 and 4.6 reveal that for the alloy without Mg, the bond distance of the 1st co-ordination shell is very much close to the theoretical value. However, subsequent to inclusion of Mg to the lattice, the bond distance of the 1st coordination shell (viz., Fe-Mg or Cr-Mg) increases and remains almost same over the whole composition range. This may be due to the smaller atomic radii of Mg (145 pm) than Fe (156 pm) and Cr (166 pm) [110]. This also causes the contraction of other coordination shells (Fe-Fe and Cr-Cr etc.) which is evident from Table 1. The above results justify the assumed models shown in Fig.4.15.

4.2.3 Other phases in HEAs

Cu K-edge EXAFS (Fig. 4.14(c)) shows different results from the other two sets of data which reveals that the local structure around Cu atom is quite different from the Fe and Cr atoms in the high entropy alloy samples. As can be seen from fig. 4.14(c), the phase uncorrected Cu K-edge spectrum shows a prominent peak around 1.7 Å which is not present in the metallic Cu and hence has been attributed to some oxide phase present in the samples.

Table 4.5 Structural parameters Fe K-edge

Scattering Paths	**Parameters**	**Alloys**		
		$AlFeCuCrMg_{0.5}$	**$AlFeCuCrMg_{1}$**	**$AlFeCuCrMg_{1.7}$**
Fe-Mg1(Fe)	R (Å) (2.485)	2.68 ± 0.01	2.67 ± 0.01	2.67 ± 0.01
	σ^2	0.004 ± 0.001	0.002 ± 0.001	0.002 ± 0.002
Fe-Al1	R (Å) (2.87)	2.71 ± 0.01	2.704 ± 001	2.703 ± 0.01
	σ^2	0.005 ± 0.004	0.004 ± 0.006	0.003 ± 0.003
Fe-Cr1	R (Å) (2.87)	2.71 ± 0.01	2.704 ± 0.01	2.703 ± 0.01
	σ^2	0.001 ± 0.001	0.001 ± 0.001	0.001 ± 0.001
Fe-Cu1	R (Å) (2.87)	2.71 ± 0.01	2.704 ± 0.01	2.703 ± 0.01
	σ^2	0.006 ± 0.006	0.002 ± 0.002	0.002 ± 0.002
Fe-Fe1	R (Å) (4.058)	3.96 ± 0.04	3.89 ± 0.04	3.89 ± 0.03
	σ^2	0.014 ± 0.023	0.011 ± 0.01	0.011 ± 0.01
Fe-Fe2	R (Å) (4.759)	4.95 ± 0.04	4.95 ± 0.04	4.95 ± 0.04
	σ^2	0.016 ± 0.008	0.015 ± 0.01	0.014 ± 0.01
Fe-Fe3	R (Å) (4.971)	4.96 ± 0.05	4.95 ± 0.02	4.95 ± 0.02
	σ^2	0.004 ± 0.003	0.002 ± 0.002	0.002 ± 0.003
	R_{factor}	0.009	0.006	0.004

Table 4.6 Structural parameters Cr K-edge

Scattering Paths	**Parameters**	**Alloys**		
		$AlFeCuCrMg_{0.5}$	**$AlFeCuCrMg_{1}$**	**$AlFeCuCrMg_{1.7}$**
Cr-Mg1(Cr)	R (Å) (2.494)	2.69 ± 0.01	2.69 ± 0.01	2.69 ± 0.01
	σ^2	0.007 ± 0.002	0.006 ± 0.002	0.006 ± 0.002
Cr-Al1	R (Å) (2.88)	2.74 ± 0.01	2.74 ± 0.01	2.74 ± 0.01
	σ^2	0.001 ± 0.004	0.002 ± 0.006	0.002 ± 0.007
Cr-Fe1	R (Å) (2.88)	2.74 ± 0.01	2.74 ± 0.01	2.74 ± 0.01
	σ^2	0.001 ± 0.001	0.001 ± 0.001	0.001 ± 0.002
Cr-Cu1	R (Å) (2.88)	2.74 ± 0.01	2.74 ± 0.01	2.74 ± 0.01
	σ^2	0.003 ± 0.002	0.002 ± 0.002	0.002 ± 0.002
Cr-Cr1	R (Å) (4.072)	3.99 ± 0.02	3.98 ± 0.011	4.01 ± 0.010
	σ^2	0.014 ± 0.015	0.014 ± 0.019	0.015 ± 0.011
Cr-Cr2	R (Å) (4.775)	4.69 ± 0.03	4.68 ± 0.03	4.69 ± 0.02
	σ^2	0.006 ± 0.004	0.005 ± 0.004	0.005 ± 0.004
Cr-Cr3	R (Å) (4.988)	5.07 ± 0.04	5.07 ± 0.04	5.04 ± 0.04
	σ^2	0.002 ± 0.006	0.002 ± 0.006	0.002 ± 0.006
	R_{factor}	0.025	0.019	0.015

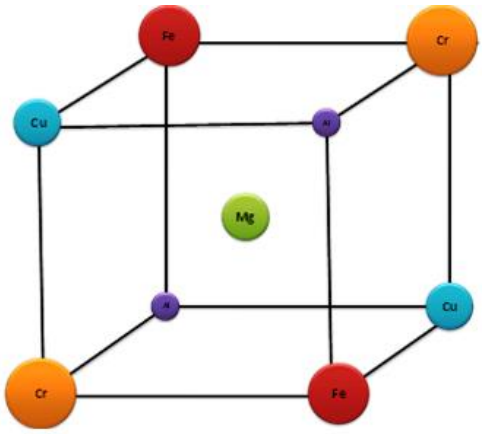

Figure 4.15 Major BCC structure of the as milled HEAs

Thus, to generate the theoretical $\chi(R)$ versus R spectra for the Cu K-edge data a mixed phase of metallic Cu with the structure shown in Fig. 4.15 and CuO structure have been taken by giving them a weight factor of x % and (1- x) % respectively. In this case, the parameter x has also been varied along with bond length (R) and the Debye-Waller factor (σ^2) to fit the spectra.

The Cu K-edge spectra are also characterized by the presence of three peaks. The 1st peak has mixed contributions of the Cu-O (coordination no., CN = 2) and Cu-Mg (CN = 8) scattering paths at 1.95 Å and 2.49 Å respectively. The 2nd peak is due to scattering paths of Cu-Al, Cu-Cr and Cu-Fe (CN = 2 each) at 2.88 Å and the 3rd peak arises due to the Cu-Cu scattering paths (CN = 12) at 4.07 Å. The best fit theoretical plots for the Cu K-edge have been shown in Fig. 4.14(c) along with the experimental data while the values of the best fit parameters have been given in Table 4.7.

In this case, the Cu-Mg bond length in the 1st co-ordination shell decreases with an increase in Mg concentration in the samples, whereas the Cu-O bond length increases. The variation of the Cu-Mg distance is found to be opposite to the variation of Fe-Mg and Cr-Mg distances with the increase in Mg concentration in the samples. This may be due to the fact that the calculated atomic radius of Mg is same as that of Cu (145 pm) and less than that of Fe and Cr [110]. However, the bond lengths of the 2nd and 3rd co-ordination shells do not show any regular variation with change in Mg concentration. It was observed that $AlFeCuCrMg_{0.5}$alloy contains some fraction of Cu type FCC phase (see Fig. 4.1(b)) which might have been oxidized to form CuO.

Table 4.7 Structural parameters Cu K-edge

Scattering paths	**Parameters**	**Alloys**		
		$AlFeCuCrMg_{0.5}$	**$AlFeCuCrMg_{1}$**	**$AlFeCuCrMg_{1.7}$**
Cu	x %	30.88	93.17	81.12
CuO	$(1-x)$%	69.12	6.83	18.88
Cu-O1	R (Å) (1.951)	2.05 ± 0.01	2.16 ± 0.01	2.16 ±0.01
	σ^2	0.005 ± 0.005	0.006 ± 0.002	0.003 ± 0.001
Cu-Mg1	R (Å) (2.494)	2.47 ± 0.01	2.35 ± 0.03	2.38 ±0.01
	σ^2	0.028 ± 0.007	0.007 ± 0.004	0.013 ±0.002
Cu-Al1	R (Å) (2.88)	2.97 ± 0.01	2.67 ± 0.05	2.95 ± 0.05
	σ^2	0.03 ± 0.001	0.03	0.001 ±0.004
Cu-Cr1	R (Å) (2.88)	2.97 ± 0.01	2.67 ±0.05	2.95 ± 0.05
	σ^2	0.019 ± 0.0003	0.001	0.028 ± 0.034
Cu-Fe1	R (Å) (2.88)	2.97 ± 0.01	2.67 ± 0.05	2.95 ± 0.05
	σ^2	0.021 ± 0.0003	0.001	0.023 ± 0.023
Cu-Cu1	R (Å) (4.07)	4.13 ± 0.01	3.94 ± 0.05	4.07 ±0.04
	σ^2	0.03 ± 0.004	0.005 ± 0.006	0.016 ±0.015
	R_{factor}	0.0001	0.006	0.008

Also, addition of higher amount of Mg increases the probability of formation of BCC structure and $AlFeCuCrMg_x$ (x = 1, 1.7) HEAs thus lower fraction of CuO phase forms in

these alloys. These results are also evident from XANES spectrum as shown in fig. 4.12(c).

Novel $AlFeCuCrMg_x$ (x = 0, 0.5, 1, 1.7 moles) HEAs prepared by mechanical alloying. XRD analysis indicates the formation major BCC phase with minor FCC fraction in AlFeCuCr and $AlFeCuCrMg_{0.5}$ HEAs. Although AlFeCuCrMg and $AlFeCuCrMg_{1.7}$ have two BCC phases i.e. BCC 1and BCC 2 as confirmed by XRD, phase fraction of BCC 2 is found out to be 27.45% and 34.06% for AlFeCuCrMg and $AlFeCuCrMg_{1.7}$ respectively. Moreover, calculated thermodynamic parameters suggest that present HEAs do not follow criterion given for the formation of a single phase solid solution. Moreover, phase evolution results show that the addition of Mg enhances the probability of formation of BCC structure. XANES and EXAFS measurements at Fe, Cu and Cr K edges have been used to study the local atomic structure of $AlFeCuCrMg_x$ (x = 0.5, 1, 1.7) HEAs synthesized by MA. The bond length distribution determined from Fe and Cr K-edge EXAFS measurements can be interpreted in favor of the formation of majorly BCC phase however; Cu K-edge data have shown formation of some copper oxide phases in the alloys. The fraction of oxide phase is maximum in $AlFeCuCrMg_{0.5}$ alloy and substantially decreases for $AlFeCuCrMg_x$ (x = 1, 1.7) HEAs.

Further studies on the bulk HEAs has been performed to understand the phase formation and the properties of the sintered $AlFeCuCrMg_x$ (x = 0, 0.5, 1, 1.7) alloy.

Chapter 5

Spark Plasma Sintering of as milled AlFeCuCrMg$_x$ (x = 0, 0.5, 1, 1.7 mol) HEAs

The as milled AlFeCuCrMg$_x$ alloys were spark plasma sintered. AlFeCuCr was sintered at 800^{o}C and the temperature was reduced to 700^{o}C for the magnesium-containing alloys AlFeCuCrMg$_x$ (x = 0.5, 1, 1.7 mol) as excessive melting was observed at a sintering temperature of 800^{o}C. The structure-property relationship has also been proposed by conventional strengthening mechanisms.

5.1 Structural Evolution of AlFeCuCrMg$_x$ HEAs after SPS

In this section phase evolution, microstructure and phase transformation study of the sintered AlFeCuCrMg$_x$ alloy were investigated by X-ray diffraction (XRD), scanning electron microscopy (SEM), transmission electron microscopy (TEM) and differential scanning calorimetry (DSC).

5.1.1 Bulk density measurements

In general the sintering temperature may be defined as to be around 0.7T$_m$ where T$_m$ is a melting temperature [95]. Although due to an absence of melting point of these HEAs initially 800^{o}C was chosen to be the sintering temperature. For AlFeCuCrMg$_x$ (x = 0.5, 1, 1.7) some excessive melting was being observed at 800^{o}C so sintering temperature was reduced to 700^{o}C.

Table. 5.1 shows the experimental bulk density determined by Archimedes principle and relative density calculated by image analysis of the sintered alloys.

Table 5.1 Experimental bulk density and calculated relative density of SPSed $AlFeCuCrMg_x$ (x = 0, 0.5, 1, 1.7) HEAs.

Composition	Sintering Temp. (^oC)	Experimental Bulk Density (g/cm^3)	Relative Density (%)
AlFeCuCr	800	6.091	99.6
$AlFeCuCrMg_{0.5}$	700	5.790	96.9
AlFeCuCrMg	700	5.367	95.0
$AlFeCuCrMg_{1.7}$	700	4.910	95.8

5.1.2 Phase Analysis of $AlFeCuCrMg_x$ HEAs

Fig 5.1 compares the XRD spectra of sintered $AlFeCuCrMg_x$ (x = 0, 0.5, 1, 1.7) HEAs. The XRD pattern of $AlFeCuCrMg_x$ HEA (x = 0, Fig. 5.1) sintered at 800^{o}C shows the formation of BCC phase with a lattice parameter of 290.14 pm and several minor peaks indicative of σ phase (JCPDS: 01-071-7530) having a tetragonal structure and lattice parameters such as a = 879.66 pm and c = 455.82 pm.The major peak at 44.08^o (see Fig.5.2 (a)) displayed asymmetry and upon deconvolution revealed a second BCC phase (BCC 2) having a lattice parameter 291.34 pm and phase fraction calculated from relative intensity was found to be 0.331.

The XRD spectra of $AlFeCuCrMg_{0.5}$ HEA sintered at 700^{o}C (Fig. 5.1) shows the formation of an ordered AlFe-type phase (JCPDS: 00-033-0020, lattice parameter, 290.37 pm), Cu_2Mg type intermetallic (JCPDS: 00-058-0360, lattice parameter 710.52 pm) and σ phase. Detailed analysis and deconvolution of the major peak of $AlFeCuCrMg_{0.5}$ HEA revealed the formation of disordered BCC phase (Fig. 5.2(b)) along with the ordered phase. The disordered BCC phase is having a lattice parameter of 292.07 pm and a phase fraction of 0.441.

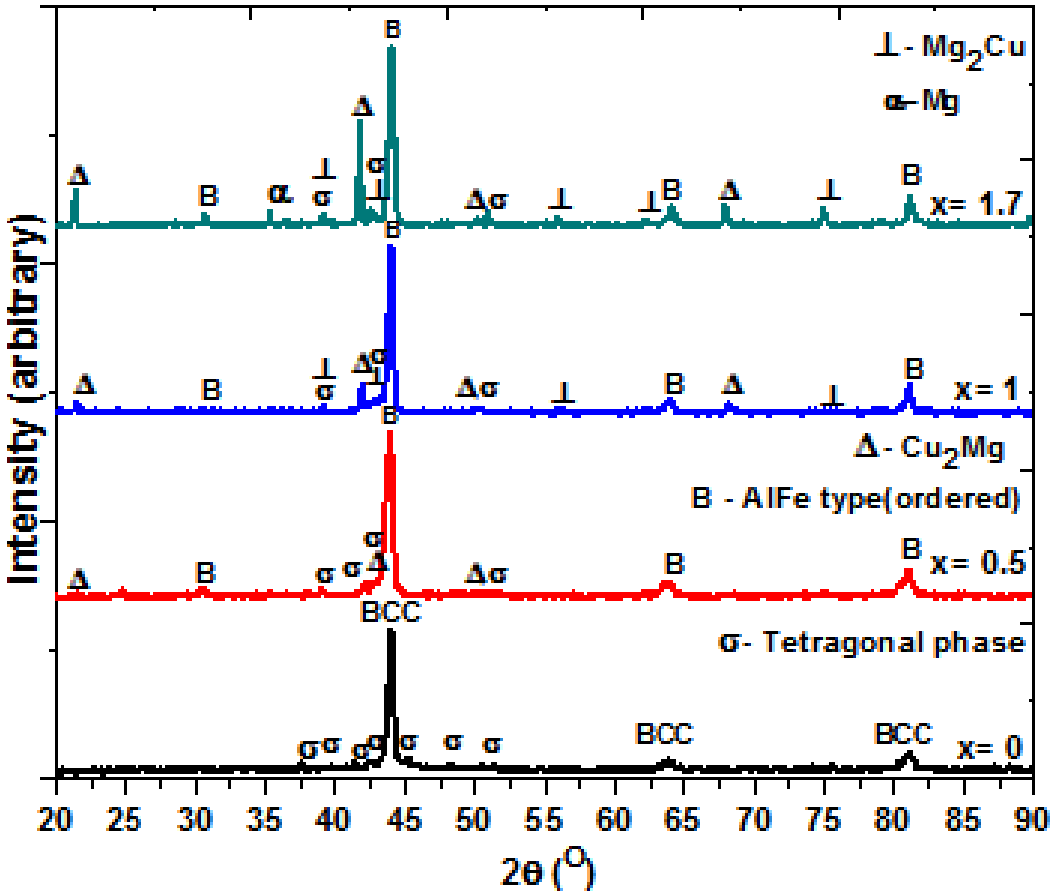

Figure 5.1 XRD patterns of SPSed AlFeCuCrMg$_x$ (x = 0, 0.5, 1, 1.7) HEAs.

XRD pattern of AlFeCuCrMg HEA sintered at 700^{o}C (Fig. 5.1) indicates a multi-phase material consisting of ordered AlFe type phase as the major phase, and Cu_2Mg type, Mg_2Cu and σ phase as minor constituents. The ordered phase and Cu_2Mg have a lattice parameter of 290. 05 pm and 712.86 pm respectively. Detailed analysis of the major peak in the XRD spectrum (Fig. 5.2(c)) indicates the presence of a disordered BCC phase (lattice parameter 290.74 pm, approximate phase fraction 0.503) and Mg_2Cu (JCPDS: 01-078-5939) coinciding with the ordered phase.

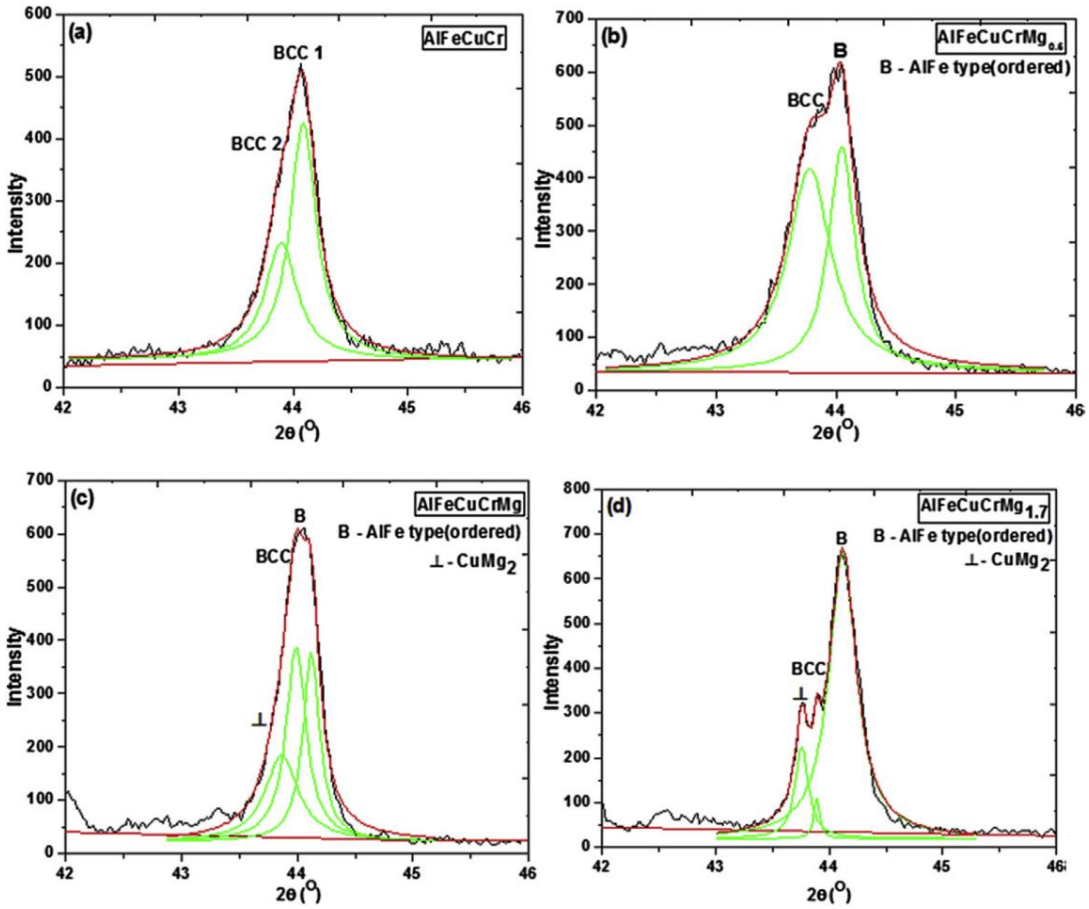

Figure 5.2 Deconvoluted XRD pattern of SPSed (a) AlFeCuCr, (b) AlFeCuCrMg$_{0.5}$ (x = 0.5), (c) AlFeCuCrMg (x = 1), (d) AlFeCuCrMg$_{1.7}$ (x = 1.7) HEAs.

Up to a molar Mg fraction of 1, an apparent relationship between increasing Mg content and increasing phase fraction of the disordered BCC phase may be the result of enhanced randomisation of atomic sites in the lattice favouring the formation of disordered structure. A further increase in Mg content (x = 1.7) produced a structure composed of an ordered AlFe phase (289.94 pm), Cu_2Mg type phase (715.70 pm), Mg_2Cu, σ phase and small amount of undissolved Mg (Fig 5.1). Deconvolution (Fig 5.2(d)) revealed that the disordered BCC phase (291.37 pm) is of low fraction (0.100) relative to ordered BCC and Cu_2Mg. This low fraction of disordered BCC phase may be explained due to a higher concentration of Mg phase fraction of intermediate phases which increases (Table. 5.2)

Table 5.2: Phase fraction, Lattice parameter, Crystalline size and lattice strain of SPSed $AlFeCuCrMg_x$ (x = 0, 0.5, 1, 1.7) HEAs.

Composition	Phases	Phase Fraction	Lattice parameter (pm)	Crystallite Size (nm)	Lattice Strain
AlFeCuCr	BCC 2	0.331	291.34	38.4	0.346
	BCC 1	0.669	290.14	53.9	0.270
$AlFeCuCrMg_{0.5}$	BCC	0.441	292.07	26.8	0.458
	Ordered phase	0.527	290.51	37.1	0.260
	Cu_2Mg	0.031	710.52	-	-
AlFeCuCrMg	BCC	0.503	290.74	93.1	0.188
	Ordered phase	0.391	289.92	150.4	0.139
	Cu_2Mg	0.104	712.86	-	-
$AlFeCuCrMg_{1.7}$	BCC	0.100	291.37	-	-
	Ordered phase	0.584	289.94	49.8	0.285
	Cu_2Mg	0.315	715.40	-	-

Table 5.2 summarizes XRD analysis conducted including the lattice parameter and phase fraction of constituent phases, crystallite size and lattice strain in the sintered $AlFeCuCrMg_x$ (x = 0, 0.5, 1, 1.7) HEAs. Instrumental broadening was corrected using a single crystalline Si substrate. Lattice strain, ε, was determined by the Eq. 4.2

Lattice parameter (Table 5.2) of AlFeCuCr HEA suggests that the two BCC phases have lattice parameters close to Fe and Cr, suggesting that these phases have Fe and Cr type lattices. Table 5.2 depicts that there is a constant relationship between the Mg content and lattice parameter of Cu_2Mg type phase in $AlFeCuCrMg_x$ (x = 0.5, 1, 1.7) HEAs. As the Mg content increases the lattice parameter continuously shifts towards a higher value which suggests the presence of sufficient amount of dissolved Mg in Cu_2Mg type phase. Although, for ordered and BCC phases the effect of an increase in the Mg is not evident as there is no relationship between lattice parameter of these phases with variation in Mg content, suggesting that these two phases present in $AlFeCuCrMg_x$ (x = 0.5, 1, 1.7) alloys are same [74].

5.1.7 Microstructure Characterization of AlFeCuCrMg$_x$ HEAs

Fig. 5.3(a) shows the back scattered electron (BSE) image and chemical composition (inset) of AlFeCuCr HEA. Despite the close atomic number of constituent elements, BSE image revealed the presence of two phases. At lower magnification, white particles were dispersed uniformly in AlFeCuCr HEA. EDS results show that these white particles are WC, which results from the contamination from ball mill. Other contaminations such as O, C and N due to milling media were estimated by oxygen/carbon analyzer was 0.43 wt. %, 0.67 wt. % and 53 ppm resp. High contamination of carbon is due to the combination of WC in the microstructure.

The BSE image and chemical composition (inset) of AlFeCuCrMg$_{0.5}$ HEA (Fig. 5.3(b)) shows a microstructure consisting of three regions. Based on compositional analysis the coarse grains observed (‘2’) may correspond to AlFe-type ordered BCC phase, the Cu_2Mg phase (‘3’) appears to be a distributed network surrounding the ordered phase, and Cr-rich grains (‘1’) are possibly disordered BCC phase with small amount of σ phase. A white particle dispersion was found to be WC contamination from the ball mill vials. O, C and N contamination is expected to be 0.32 wt. %, 0.68 wt. % and 201 ppm resp. A similar microstructure and phase composition was determined for the equimolar alloy AlFeCuCrMg (Fig. 5.3(c)).

The morphology and distribution of the Mg_2Cu phase revealed by XRD in this high-Mg alloy was not distinguishable in the BSE image. O, C and N contamination is expected to be 0.25 wt.%, 0.36 wt. % and 255 ppm resp. Increasing the Mg content (AlFeCuCrMg$_{1.7}$) produced a microstructure consisting of coarse grains AlFe-type BCC ordered phase (‘1’) surrounded by a network of Cu_2Mg phase, with a distribution of Mg_2Cu and coarse Cr-rich BCC phase (Fig. 5.3(d)). O, C and N contamination is expected to be 0.014 wt. %, 0.19 wt. % and 174 ppm respectively. It is to be noted that the carbon detection in all the HEAs is majorly due to the presence of WC contamination in the as milled alloy powder.

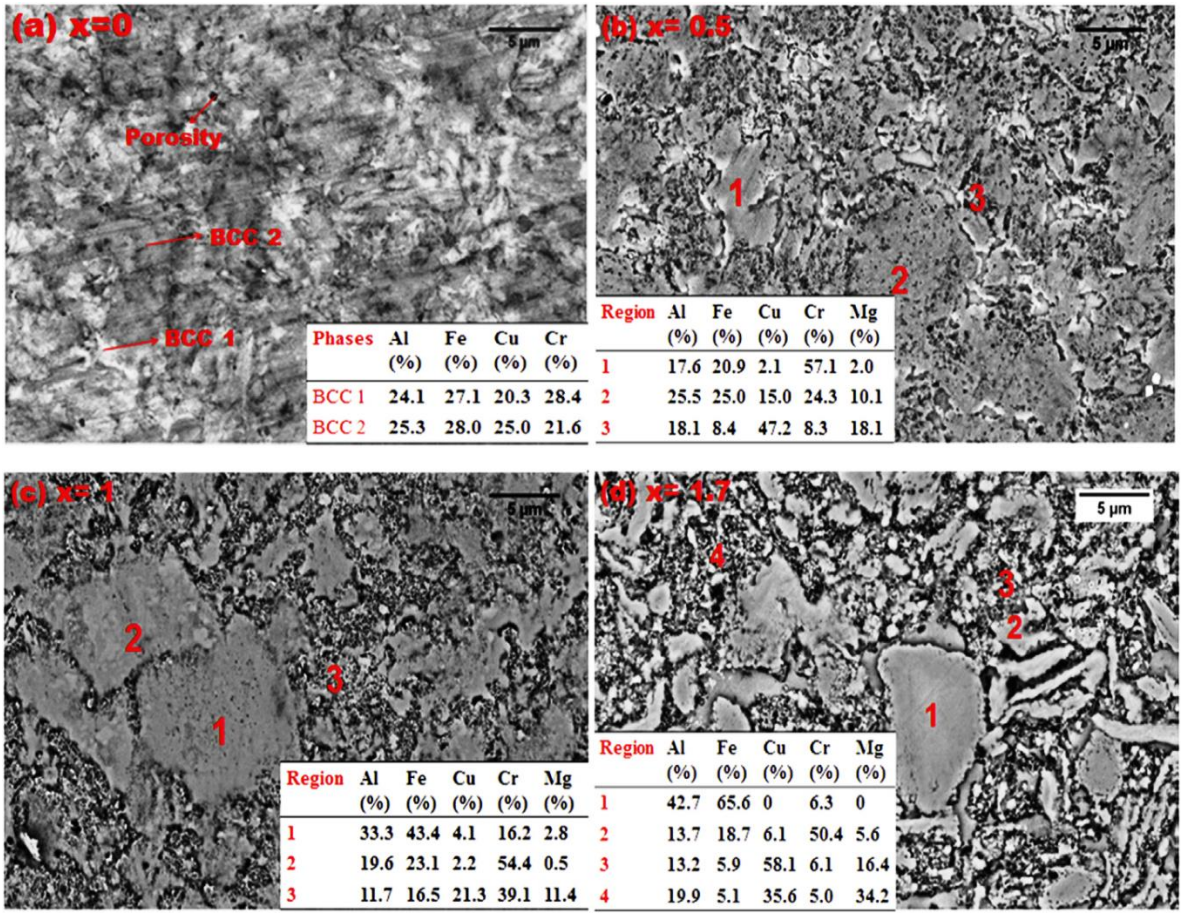

Figure 5.3 BSE micrograph and EDS analysis (inset) of SPSed (a) AlFeCuCr (x=0), (b) $AlFeCuCrMg_{0.5}$ (x = 0.5), (c) AlFeCuCrMg (x = 1), (d) $AlFeCuCrMg_{1.7}$ (x = 1.7) HEAs.

5.1.8 Transmission Electron Microscopy

Fig. 5.4(a) shows bright field micrograph of AlFeCuCr sintered at 800^{o}C and associated SAED pattern is shown in Fig. 5.4(b), which indicate the formation of nanocrystalline grains of BCC 1, BCC 2 and σ phase. A dark field image (Fig. 5.4(c)) was obtained by moving the aperture to selected portions of the BCC 1 and BCC 2 i.e. (110) diffraction ring. The distribution of grain size processed from the dark field image by the use of Image J software is shown in the inset of Fig. 4(c). Crystallite size is determined to be in the range of 20 nm to 170 nm, and average crystallite size is 32 nm, which is comparable to that obtained by the Scherrer formula (Table 2). Determining the discrete crystallite sizes of the BCC 1, BCC 2 and σ phases from the dark field image were not possible due

to the close proximity of the diffraction rings of these phases. Multipoint EDS analysis on the bright field image performed by exporting in STEM mode indicates the presence of the three phases (See Fig. 5.5).

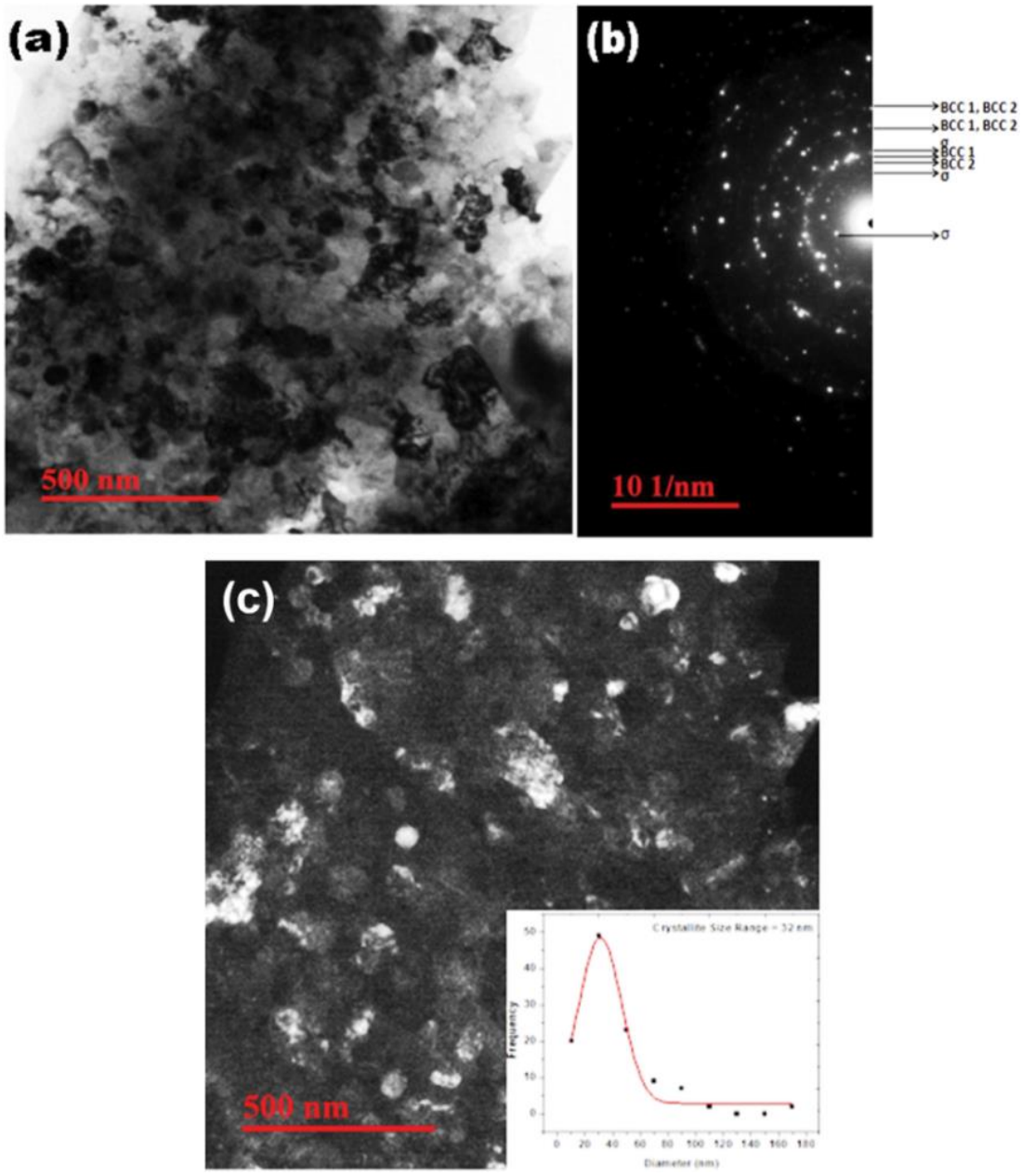

Figure 5.4 (a) TEM bright field image of SPSed AlFeCuCr (x = 0) HEA, (b) SAED pattern corresponding to the bright field image ,(c) TEM dark field image of AlFeCuCr (x = 0) HEA

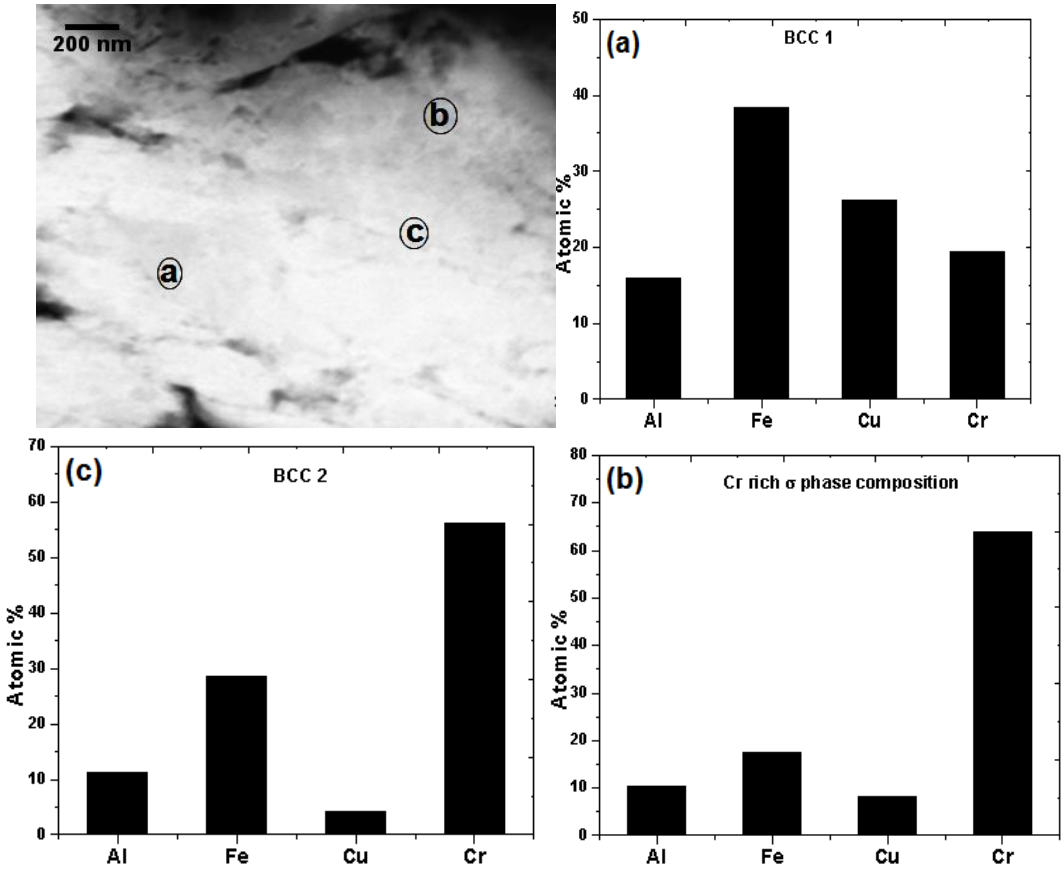

Figure 5.5 STEM image and multipoint EDS analysis of sintered AlFeCuCr (x = 0) HEA.

Fig. 5.6(a), 5.6(b), and 5.6(c) show the TEM bright field, SAED pattern and dark field image for $AlFeCuCrMg_{0.5}$ HEA respectively. The bright field image reveals the formation of nanocrystalline microstructure in addition to small tetragonal (σ) phase precipitates. SAED pattern (Fig 5.6(b)) reveals the formation of ordered AlFe type structure, disordered BCC phase, Cu_2Mg phase, and σ phase. Dark field image (Fig 5.6(c)) was obtained by moving the aperture to the σ phase ring and the crystallite size distribution was determined to be approx. 11 nm. Multipoint EDS analysis (See Fig. 5.7) revealed the composition of different phases present in $AlFeCuCrMg_{0.5}$ alloy which is consistent with the SEM-EDS analysis.

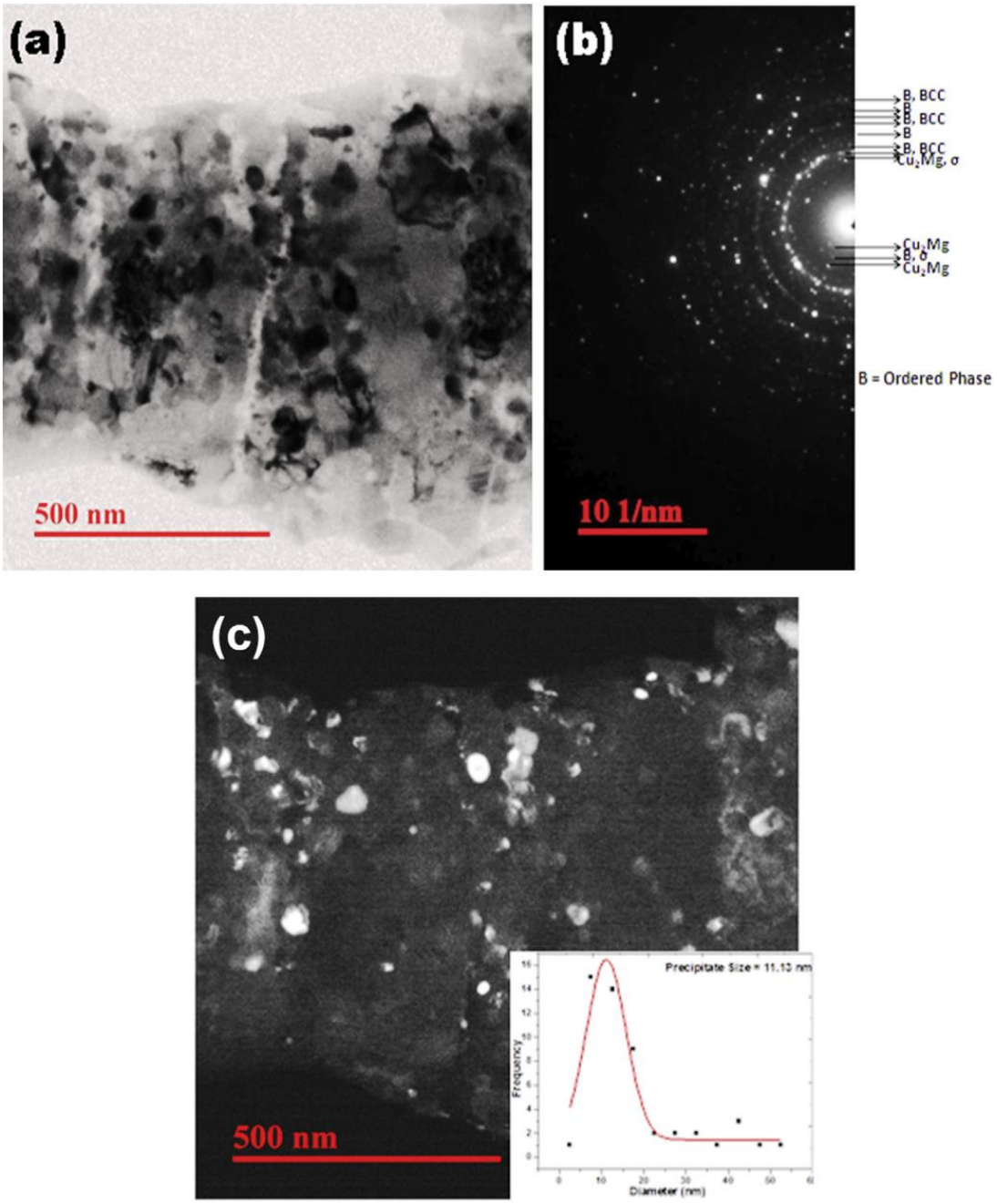

Figure 5.6 (a) TEM bright field Image of SPSed AlFeCuCrMg$_{0.5}$ (x = 0.5) HEA, (b) SAED pattern corresponding to the bright field image ,(c) TEM dark field image of AlFeCuCrMg$_{0.5}$ (x = 0.5) HEA.

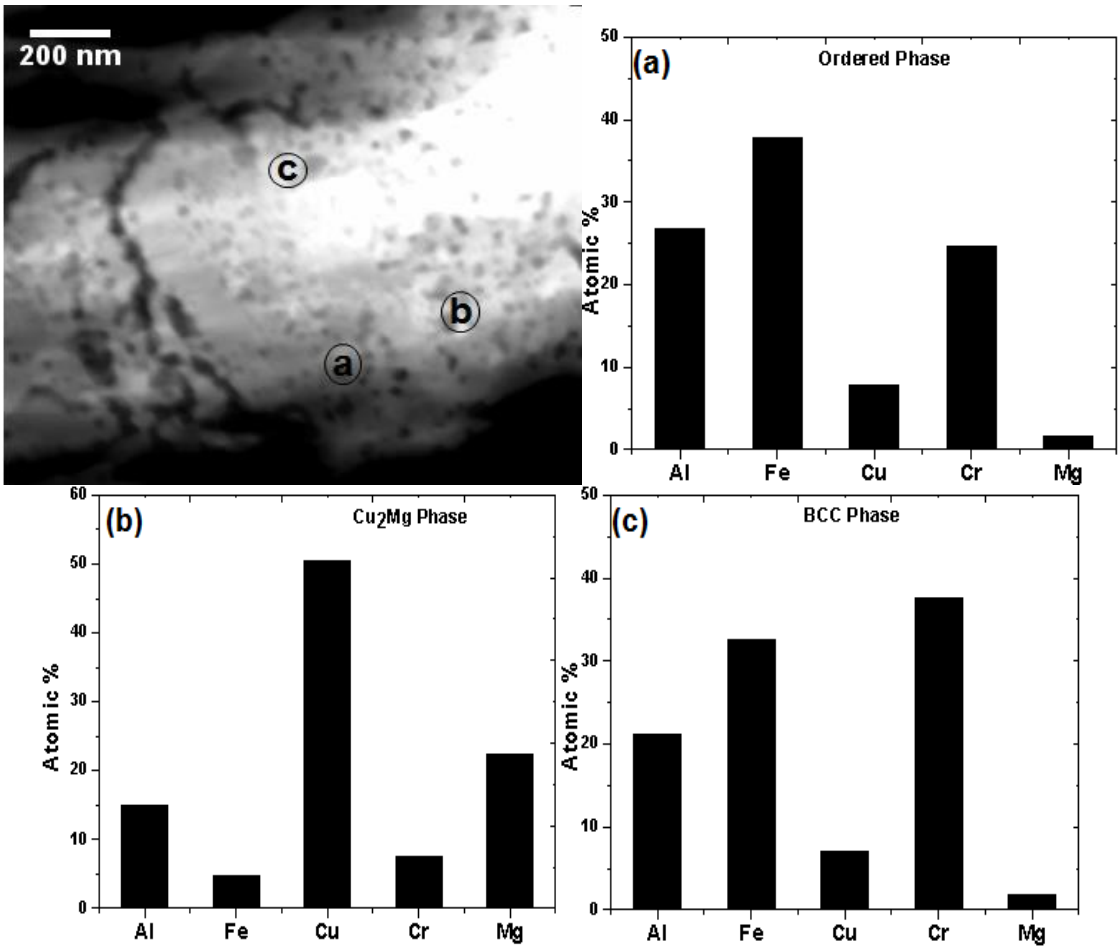

Figure 5.7 STEM image and multipoint EDS analysis of SPSed AlFeCuCrMg$_{0.5}$ (x = 0.5) HEA

Fig. 5.8(A) shows the bright field image and SAED patterns for AlFeCuCrMg HEA which are characterized by irregularly shaped tetragonal phase precipitates, in a cubic Cu_2Mg type phase (SAED, Fig. 5.8(B-C)). An absence of an orientational relationship between the Cu_2Mg phase and precipitates indicates that the precipitates are incoherent in nature. Fig. 5.8(D) shows the dark field image of the precipitate phase, which suggests a size of 20 nm to 150 nm and average precipitate size of 25 nm.

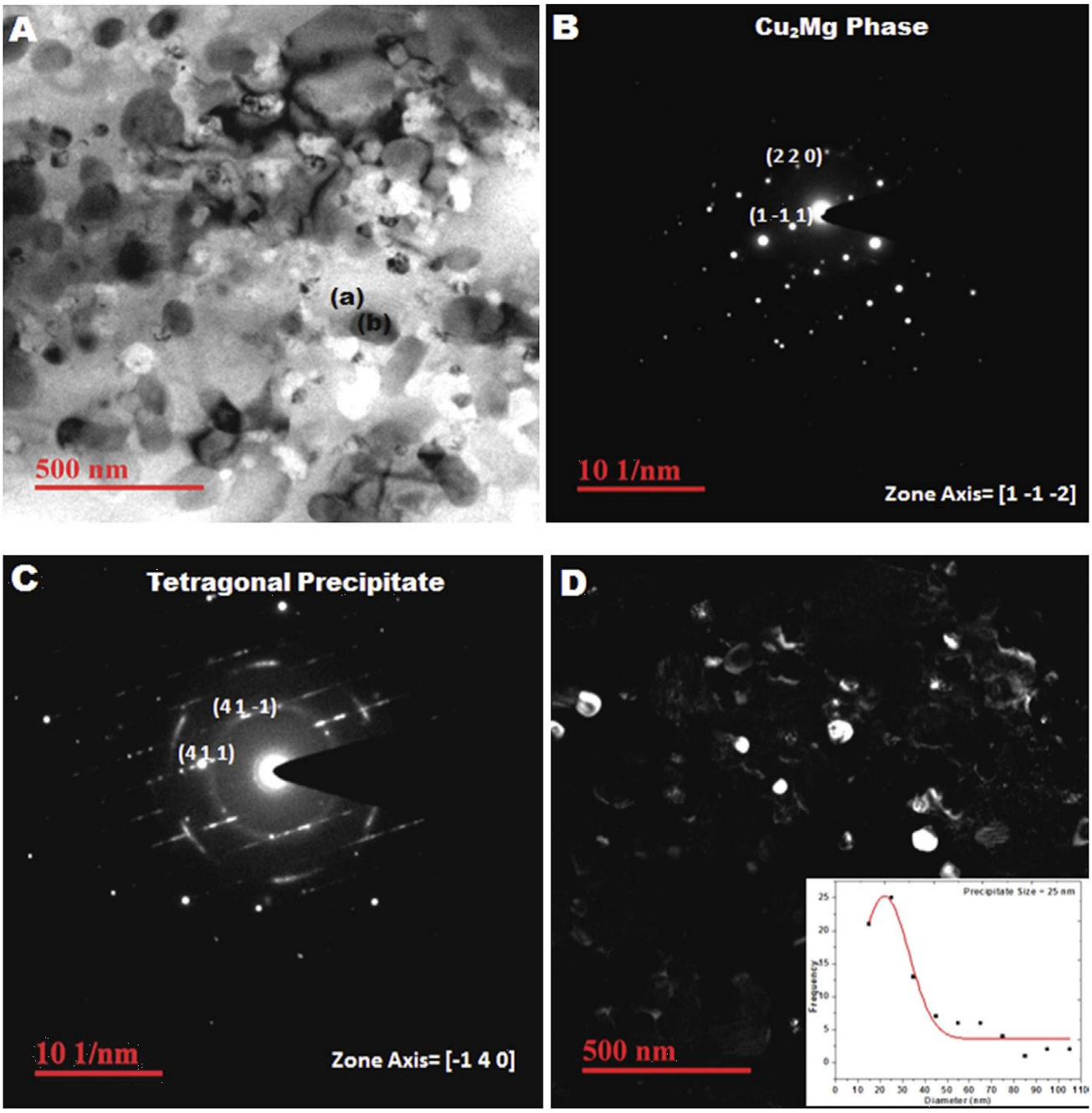

Figure 5.8 (A) TEM bright field image showing different morphology (B) SAED pattern corresponding to regiona in TEM image (C) SAED pattern corresponding to region b in TEM image, (D) TEM dark field image of SPSed AlFeCuCrMg (x = 1) HEA.

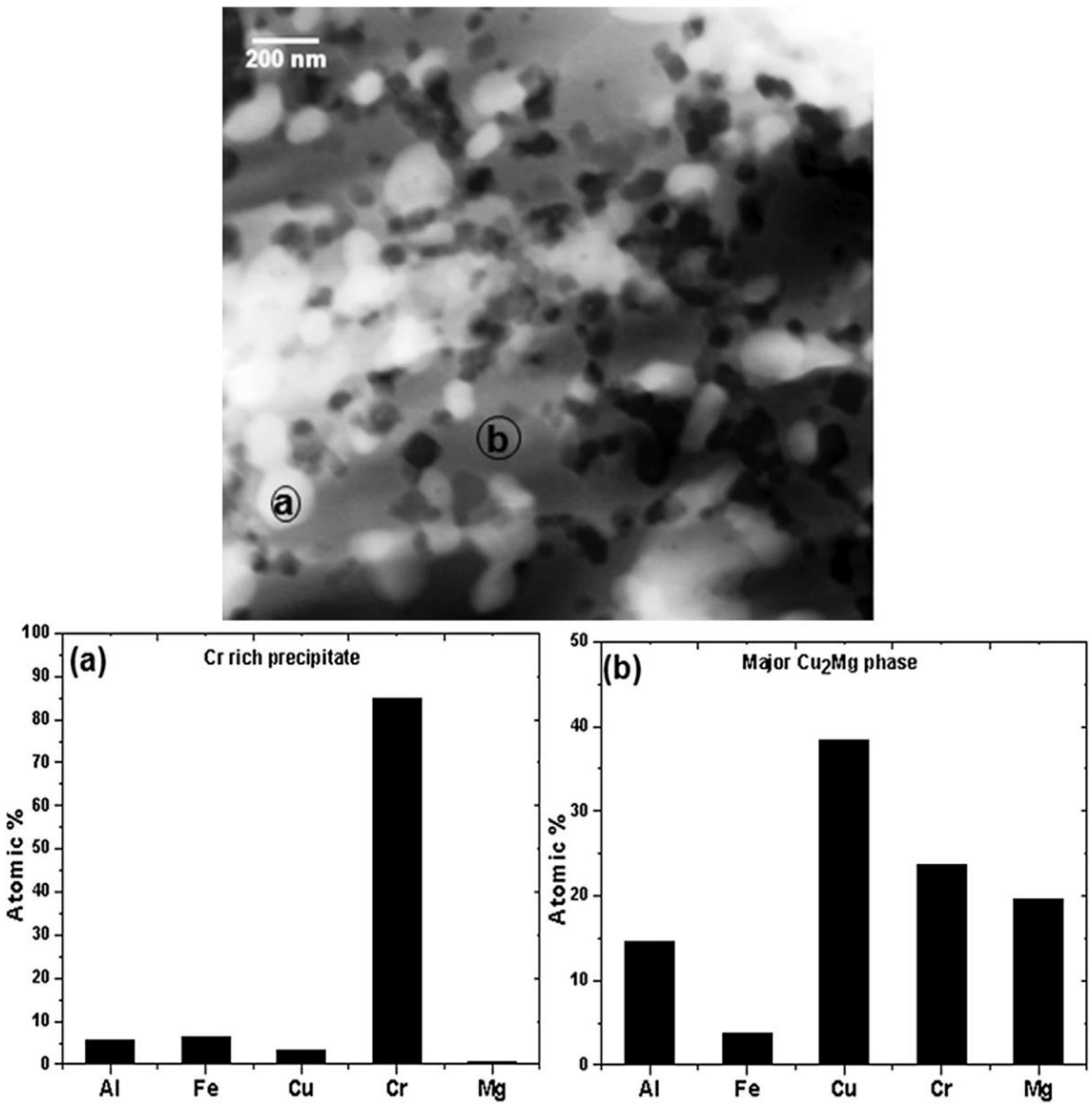

Figure 5.9 STEM image and multipoint EDS analysis of SPSed AlFeCuCrMg (x = 1) HEA.

Fig. 5.9 shows the STEM image and multipoint EDS analysis of AlFeCuCrMg alloy, which confirm the formation of tetragonal σ type precipitates having high Cr content and Cu_2Mg type phase.

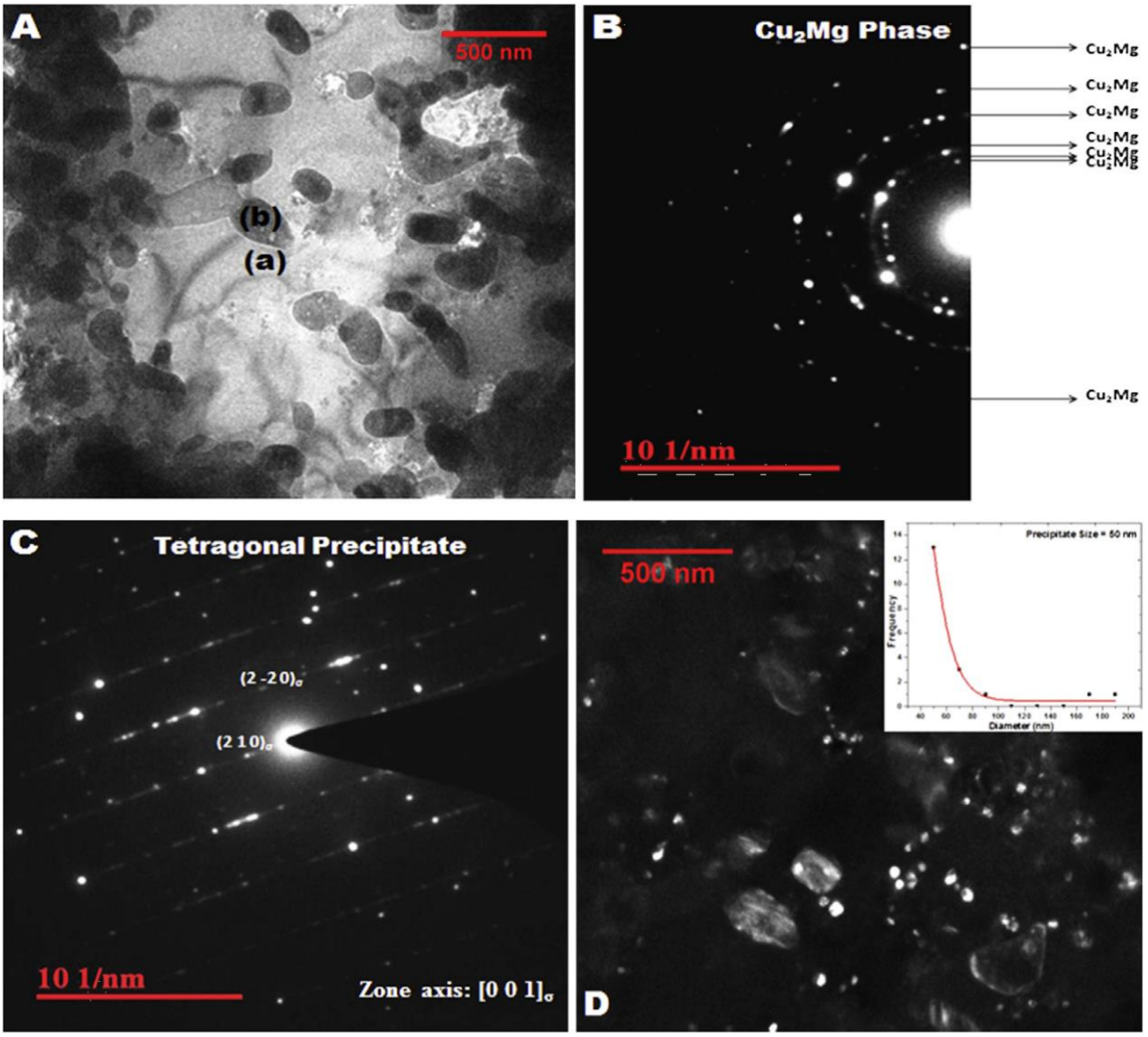

Figure 5.10 (A) TEM bright field image showing different morphology (B) SAED pattern corresponding to region 'a' in TEM image (C) SAED pattern corresponding to region 'b' in TEM image, (D) TEM dark field image of SPSed AlFeCuCrMg (x = 1.7) HEA.

$AlFeCuCrMg_{1.7}$ HEA had a similar microstructure having larger (50 nm to 250 nm, Fig. 5.10(A-D)) tetragonal Cr-rich incoherent precipitates of similar composition to those in AlFeCuCrMg in a cubic Cu_2Mg laves phase(Fig. 5.11).

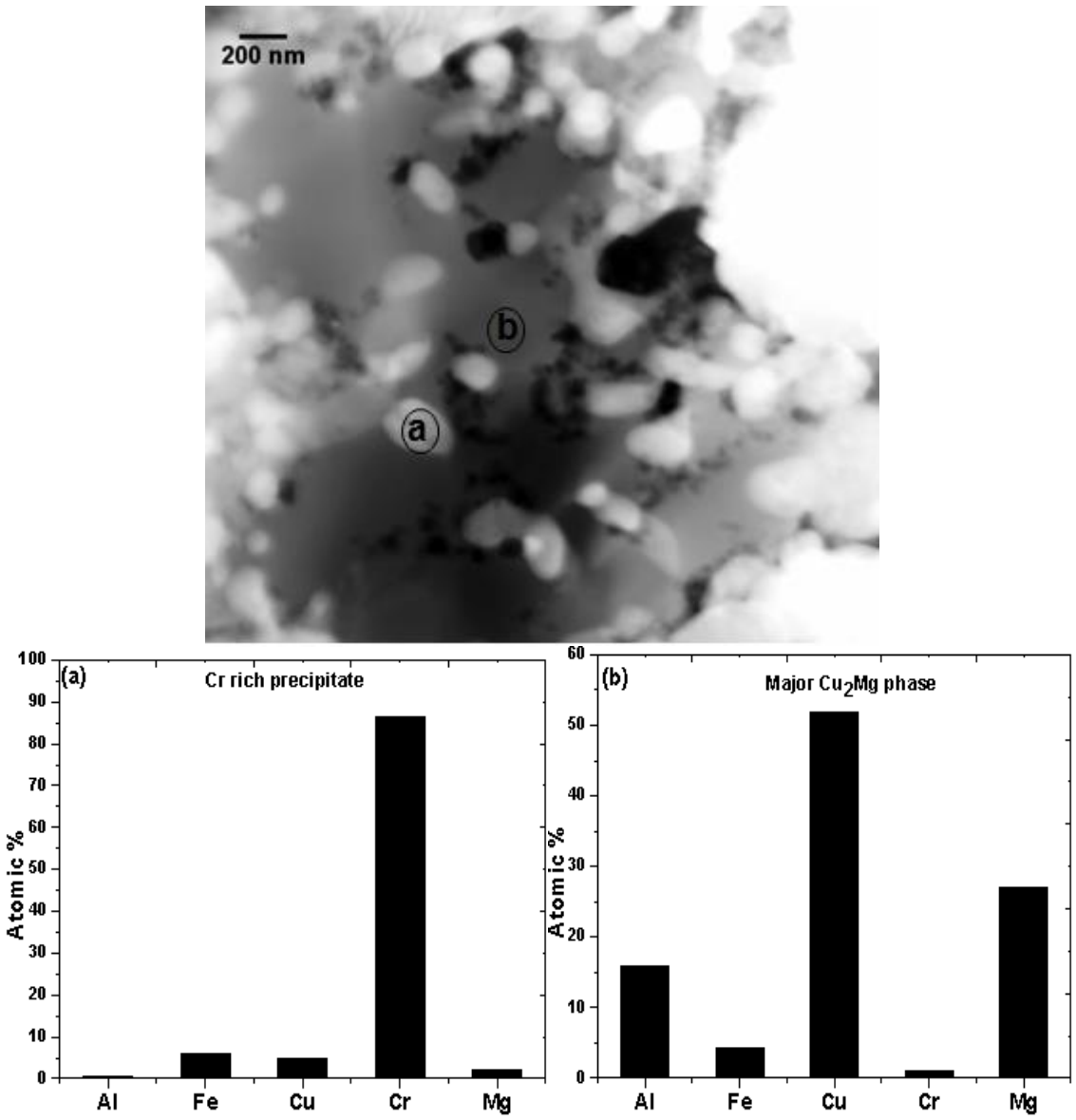

Figure 5.11 STEM image and multipoint EDS analysis of sintered SPSed AlFeCuCrMg$_{1.7}$ (x = 1.7) HEA.

5.1.5 Thermal Analysis

Fig 5.12 shows the heat flux curves over a temperature range of ambient to 1000^{o}C for the HEAs AlFeCuCrMg$_x$ (x = 0, 0.5, 1, 1.7). An absence of endothermic or exothermic peaks was observed for AlFeCuCr, suggesting that there is no phase transformation up to 1000^{o}C. AlFeCuCrMg (x = 0.5, 1) HEAs appears to be having endothermic peaks at 818^{o}C and 885^{o}C respectively. In contrast, the high Mg-containing HEA (AlFeCuCrMg$_{1.7}$) shows to be having two endothermic peaks at 483^{o}C and 888^{o}C.

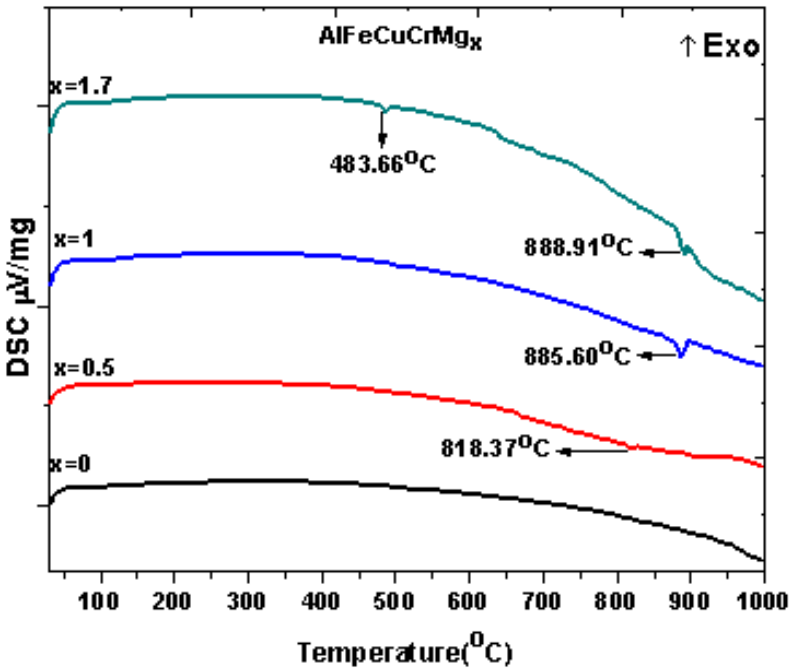

Fig 5.12 DSC scan of SPSed AlFeCuCrMg$_x$ (x = 0, 0.5, 1, 1.7) HEAs.

With reference to the binary phase diagrams for Cu-Mg and Fe-Cr [111], it is noted that Cu_2Mg intermetallic phase has a congruent melting point at 797^{o}C and the σ phase decomposes at 830^{o}C. It is likely that the endothermic peaks in the heat flow curves for AlFeCuCrMg$_x$ (x = 0.5, 1) HEAs is a combined effect of the melting of Cu_2Mg and decomposition of σ phase. For the AlFeCuCrMg$_{1.7}$HEA, the first endothermic peak appears to correspond to the melting of a mixture of two phases i.e. α+Mg_2Cu phase (480^{o}C) and the second peak correspond to the melting of Cu_2Mg phase. The area under the endothermic peak suggests that the fraction of Cu_2Mg phase increases as the Mg content increases. The shift in the endothermic peaks in AlFeCuCrMg$_x$ (x = 0.5,1, 1.7) HEAs can be explainedon the basis of EDS analysis which reveals that other elements are also present in Cu_2Mg type phase thus altering the melting point.

5.1.6 Hardness measurement

Vickers hardness measurements were performed on AlFeCuCrMg$_x$ (x = 0, 0.5, 1, 1.7) HEAs with load of 200 gf and dwell time as 15 sec. The results are plotted against Mg-content in Fig 5.13.

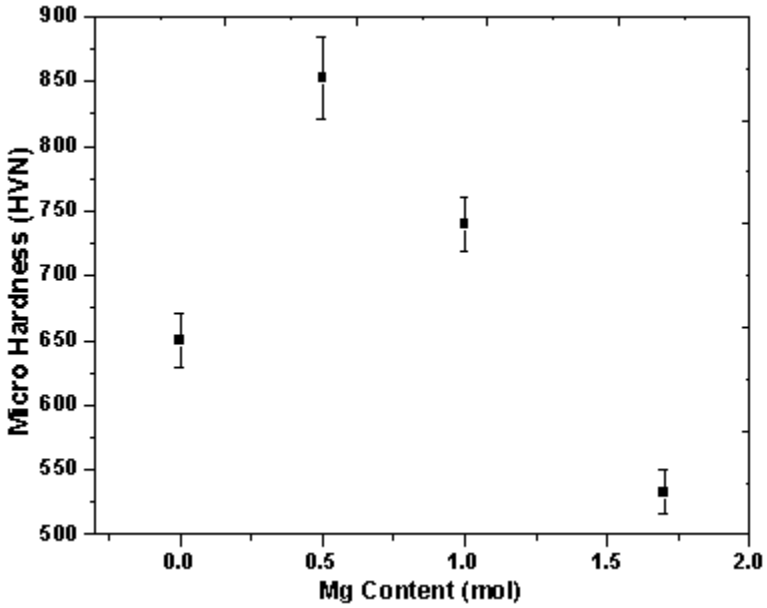

Fig 5.13 Hardness of SPSed AlFeCuCrMgx (x= 0, 0.5, 1, 1.7) HEAs.

A maximum hardness of 853 HVN ± 31.5 was attained by $AlFeCuCrMg_{0.5}$ followed by the decrease in the hardness value. x = 1.7 HEA had the lowest hardness value of 533 ± 17.4 HVN. An empirical relationship between the yield strength (σ_{YS}) and hardness value is given by Eq. 5.1[112].

$$\sigma_Y\ (MPa) = 3\ X\ H_V(HVN) \qquad (5.1)$$

The yield strength from the above Eq. 5.1 is determined to be 1950 MPa, 2559MPa, 2220 MPa and 1599 MPa for AlFeCuCr, $AlFeCuCrMg_{0.5,}$ AlFeCuCrMg, $AlFeCuCrMg_{1.7}$respectively.

5.1.7 Corrosion properties of $AlFeCuCrMg_x$ alloys

The potentiodynamic polarization curves of sintered $AlFeCuCrMg_x$ (x = 0, 0.5, 1, 1.7) alloys in 3.5% NaCl (pH = 8) solution are shown in Fig 5.14.

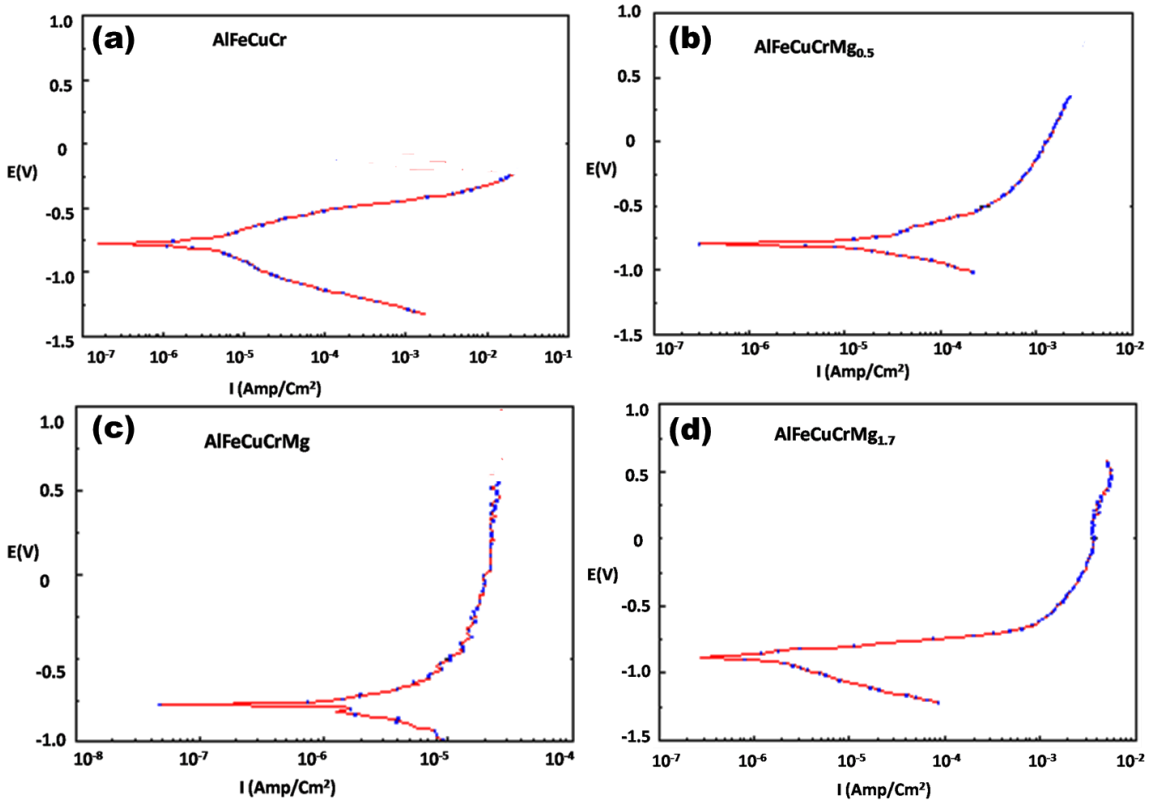

Figure 5.14 Potentiodynamic curves for SPSed (a) AlFeCuCr, (b) AlFeCuCrMg$_{0.5}$, (c) AlFeCuCrMg and (d) AlFeCuCrMg$_{1.7}$HEAs in 3.5% NaCl solution at 25^{o}C.

The average corrosion rates obtained from electrochemical polarization measurements can be calculated from Eq 5.2 [113]:

$$\text{Corrosion rate (mm year}^{-1}) = \frac{3.27 \times 10-3 \times I_{corr} \times EW}{D} \qquad (5.2)$$

where EW is the equivalent weight of the alloy, D is the density of alloy (in g/cm^3), and i_{corr} (μA/cm^2) is the corrosion current density of the specimen. Tafel fitting in the polarization curve was used to determine the value of E_{corr} and I_{corr}. The EW values of AlFeCuCr, AlFeCuCrMg$_{0.5}$, AlFeCuCrMg and AlFeCuCrMg$_{1.7}$ alloys are 53.30, 51.67, 50.06and 48.17 respectively. The electrochemical parameters and corrosion rates for sintered AlFeCuCrMg$_x$ (x = 0, 0.5, 1, 1.7) alloys and conventional alloys in 3.5% NaCl solution are presented in Table 5.3.

Table 5.3 Dynamic parameters derived from potentiodynamic polarization curves by tafel fit and corresponding corrosion rate

Composition	E_{corr} (V)	I_{corr} (A/cm^2)	E_{pit}	Corrosion rate (mm/year)	Reference
AlFeCuCr	-0.774	0.69 X 10^{-5}	-0.233	0.101	Present Study
$AlFeCuCrMg_{0.5}$	-0.791	0.71 X 10^{-5}	-0.499	0.112	Present Study
AlFeCuCrMg	-0.812	0.73 X 10^{-5}	-0.523	0.118	Present Study
$AlFeCuCrMg_{1.7}$	-0.872	0.76 X 10^{-5}	-0.610	0.123	Present Study
AZ91D	-1.51	0.8 X 10^{-6}	-	0.754	[117]
Al6061 alloy	-0.639	5.9 X 10^{-6}	-	0.647	[118]

It can be observed that the corrosion potentials (E_{corr}) for $AlFeCuCrMg_x$ alloys vary from −0.774V to −0.872V, and the pitting potentials vary from -0.233V to -0.610V. AlFeCuCr alloy has higher corrosion potential and pitting potential among all specimens. The corrosion experiments results (Table. 5.3) indicate that the corrosion rate in $AlFeCuCrMg_x$ alloys has a following order $AlFeCuCrMg_{1.7}$ > AlFeCuCrMg > $AlFeCuCrMg_{0.5}$ > AlFeCuCr alloy. Thus, AlFeCuCr alloy shows much easier passivation, and it is more corrosion-resistant in 3.5% NaCl solution. It can be observed from Table 5.3 that $AlFeCuCrMg_x$ alloys showbetter corrosion resistance than conventional Mg and Al alloys.

Surface examination (Fig 5.15) of the corroded specimen after cleaning with distilled water shows that all the alloys are having mainly non-uniform corrosion and pitting corrosion.

The micrographs (Fig 5.15) suggest that in $AlFeCuCrMg_x$ (x = 0, 0.5, 1, 1.7) alloys the corrosion is not uniform rather it is localized, and the corrosion product is scattered over the surface of the alloys [79, 114]. It can be suggested that this corrosion is a form of crevice corrosion which results from the formation of concentration cell between the

electrolyte in the oxygen depleted region and electrolyte in oxygen rich region [115]. Also, some micro pits are being observed which shows the presence of pitting corrosion in AlFeCuCrMg$_x$ (x = 0, 0.5, 1, 1.7) alloys.

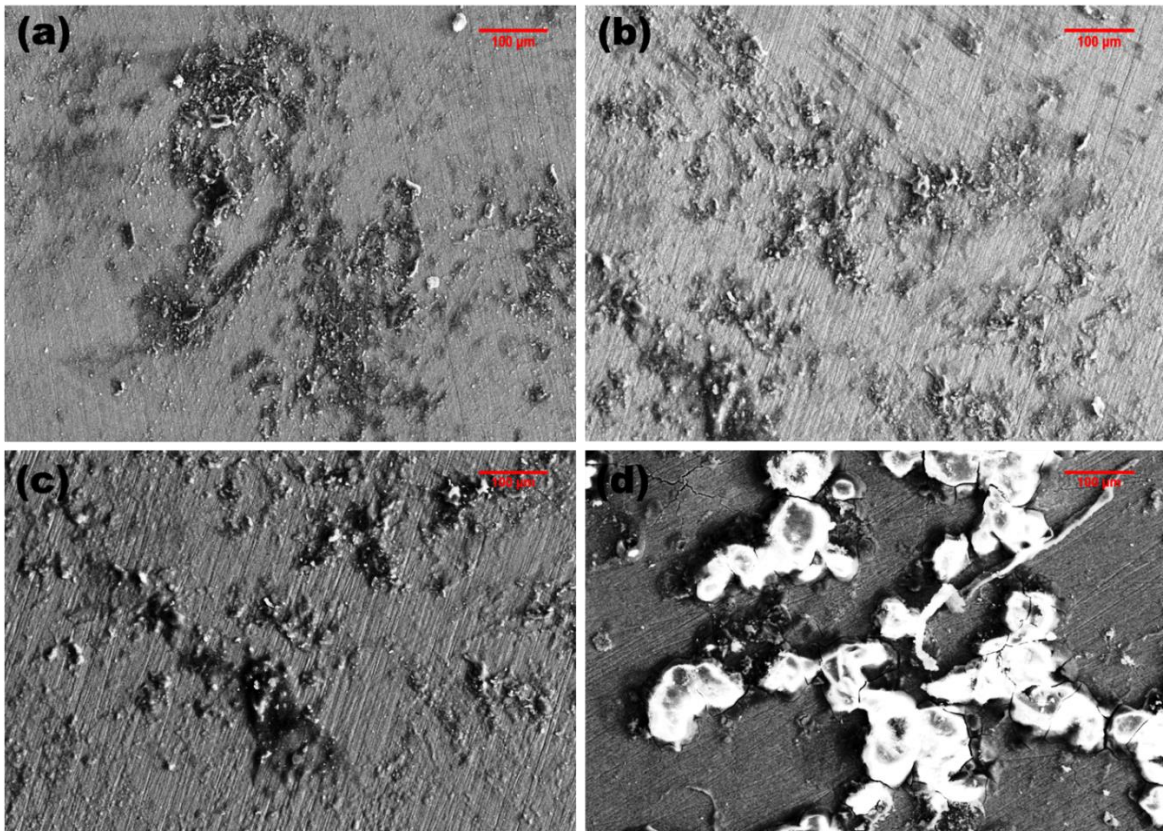

Figure 5.15 Surface appearances of SPSed (a) AlFeCuCr (x = 0), (b) AlFeCuCrMg$_{0.5}$ (x = 0.5), (c) AlFeCuCrMg (x = 1), (d) AlFeCuCrMg$_{1.7}$ (x = 1.7) HEAs after corrosion study

Further, FTIR was performed to determine the functional groups present on the surface after polarization experiment. The FTIR spectrum of the AlFeCuCrMg$_x$ alloys after polarization measurement is shown in Fig 5.16. In case of AlFeCuCr (x = 0) alloy bands from 450 cm^{-1} to 750 cm^{-1} corresponds to the M-X stretching: M (metal), X (halogen) (like CuCl). The frequencies at 797 cm^{-1} and 1016 cm^{-1}correspond to M-H stretching and M = O stretching respectively. It is to be noted that bands from the range 1259 cm^{-1} to 1597 cm^{-1}correspond to the stretching in linear as well as bent triatomic molecules (like $CuCl_2$). Similarly, for AlFeCuCrMg$_{0.5}$ (x = 0.5)alloy absorption bands of M-X stretching,

M-H stretching and stretching in linear (MgH_2, and FeH_2) as well as bent triatomic molecules (like AlH_2 and $Mg(OH)_2$) were observed in IR spectrum.

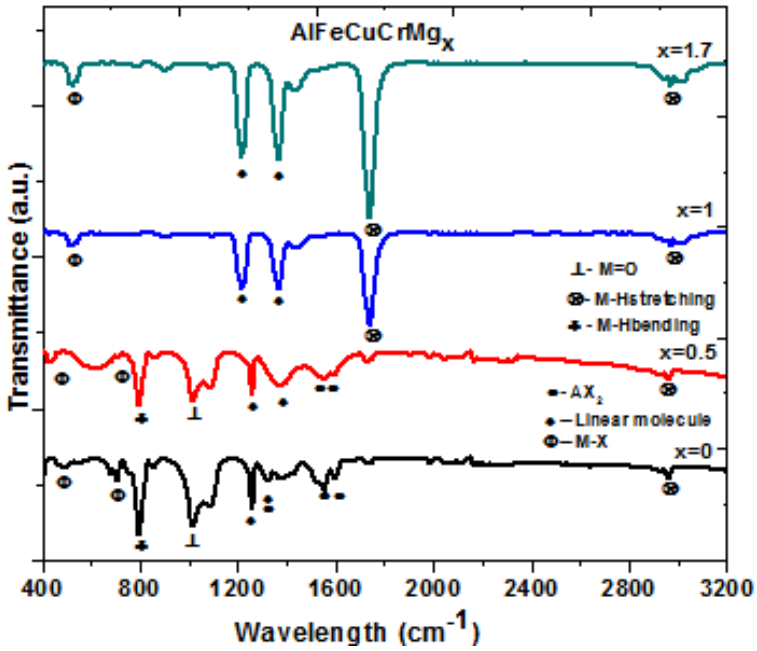

Figure 5.16 IR spectrum after polarization measurement of SPSed $AlFeCuCrMg_x$ HEAs

With increase in the Mg content (x = 1) the bands due to M = O stretching and M-H bending disappears and predominately the M-X stretching which may be due to formation of Mg and Cu chlorides, linear molecule stretching like $AlCl_2$ and $FeCl_2$and M-H stretching bands due to MgH_2, $Mg(OH)_2$, and $FeH_2$are present [116]. Similar types of corrosion product have been formed in the case of $AlFeCuCrMg_{1.7}$ alloy. It is to be noted that in the case of $AlFeCuCrMg_x$ (x = 1, 1.7) alloys i.e. higher Mg content HEAs lead to form $MgCl_2$, MgH_2 along with diatomic MgCl compounds which results in predominantly M-X stretching and M-H stretching bands in the IR spectrum.

5.2 Thermodynamic parameters and Structure-Property Correlation

In this section, the phase evolution in these alloys has been considered using thermodynamic parameters, and the structure-property relationship has also been proposed by conventional strengthening mechanisms.

5.2.1 Thermodynamic considerations in phase formation

The microstructural evolution for $AlFeCuCrMg_x$ (x = 0, 0.5, 1, 1.7) HEAs can also be explainedon the basis of thermodynamics properties. The enthalpy of mixing (ΔH_{mix}) of binary alloy systems of the constituent elements is presented in Table. 4.4. Due to the negative enthalpy of mixing between binary elements such as Mg-Cu (-3 kJ/mol) and Al-Fe (-11 kJ/mol) [104] the formation of compounds between these elements is thermodynamically more favourable. Thus, major fraction of the microstructure consists of Cu_2Mg and AlFe ordered phase (Fig 5.3 (b), (c) and (d)) in $AlFeCuCrMg_x$ (x = 0.5, 1, 1.7) HEAs. In addition to that Table. 4.4 shows that $AlFeCuCrMg_x$ HEAs do not satisfy the Zhang's [10] criterion for the formation of simple solid solution; -10 kJ/mol < ΔH_{mix} < 5 kJ/mol, and δ < 4%. Thus, positive enthalpy of mixing and the large atomic size difference (δ) leads to solid solution plus intermetallic microstructure in $AlFeCuCrMg_x$ (x = 0, 0.5, 1, 1.7) HEAs (Table 4.4).

Parameters α_1 and α_2 were proposed in [43] that considered the effect of atomic size and lattice distortion on the ability of HEAs to form solid solution phases. α_1& $\alpha_2$are calculated using Eq. 2.11 & 2.12 resp.(Chapter 2).

Table.5.4 summarizes the value of parameter α_1 and α_2(see Eq. 2.11, 2.12, Section 2.3) with respect to Mg content for alloys in the present study. For AlFeCuCr and $AlFeCuCrMg_x$ (x = 0.5, 1, 1.7) HEAs, the values of α_1 and $\alpha_2$fall in the solid solution region according to [43]. However, it has been shown that these SPS alloys contain multiple BCC phases and numerous intermetallic phases. Hence, it can be concluded that α_1 and α_2 do not explain the evolution of microstructure in case of $AlFeCuCrMg_x$ HEAs. These parameters appear more useful in differentiating between a solid solution and metallic glass HEA.

Electronegativity is a tendency of an atom to attract an electron and according to the Hume-Rothery rules high electronegativity of a solute tends to form intermetallic compounds. In HEAs, the electronegativity difference is calculated by the composition of the HEA and not by lattice type (Eq. 2.9)

The role of electronegativity on the phase stability of HEAs was described by Dong et al. [43] showing that a topologically closed packed (TCP) structure is stable in HEAs where $\Delta X > 0.133$.

Table 5.4 α_1, α_2, $\overline{Md}$, in AlFeCuCrMg$_x$ HEAs

Composition	α_1	α_2	$\overline{Md}$
AlFeCuCr	0.04372	0.01092	1.1287
AlFeCuCrMg$_{0.5}$	0.06922	0.01649	1.3263
AlFeCuCrMg	0.08337	0.01993	1.4866
AlFeCuCrMg$_{1.7}$	0.09269	0.01977	1.6626

Table. 4.4 summarize the values of ΔX for alloys in this study, with only AlFeCuCr alloy having a ΔX less than 0.133. However, this and all alloys in this study contained TCP phases. Hence it appears TCP phase stability is inconclusive between $\Delta X = 0.1176$ to 0.133, as reported by [40]. Although, in AlFeCuCrMg$_x$ (x = 0, 0.5, 1. 1.7) HEAs the phase fraction of TCP increases with the increase in the electronegativity difference from 0.1186 to 0.2247. Thus, it is clear from the results that electronegativity difference plays an important role is stabilization of TCP phases. The values of $\overline{Md}$(see Eq. 2.10, Section 2.3) are shown in Table. 5.4. These values suggest that the formation of TCP are favourable in AlFeCuCrMg$_x$ (x = 0, 0.5, 1, 1.7) HEAs.

5.2.2 Microstructural evolution and properties correlation

As-milled AlFeCuCr HEA powder contains BCC phase with a relatively small fraction of FCC. After sintering the small volume fraction of FCC phase was completely transformed and two BCC phases have evolved. It is due to supersaturation of all the elements in the single BCC phase in mechanically alloyed powder which had led to the

formation of another BCC (BCC 2) phase while sintering. It is interesting to note that AlFeCuCr alloy forms a nanocrystalline bulk product due to a high heating rate of 100^{o}C/min inherent in the SPS process. The high heating rate does prevent grain coarsening while achieving high densification. The powder is further consolidated when kept at the desired sintering temperature by a formation of necks between two particles [64].

High hardness value (650 HVN) of AlFeCuCr HEA may be attributed to three factors (i) Grain size strengthening, (ii) Solid solution strengthening and (iii) brittle σ- type tetragonal phase. Grain size strengthening can be calculated by the Hall-Petch relationship given by Eq 5.3 [74]

$$\sigma_P = \sum_{i=1}^{5} \sigma_{0,i}\, C_{iP} + \sum_{i=1}^{5} k_i\, C_{iP} d^{-1/2} \qquad (5.3)$$

Where C_i is the composition of i^{th} element in a particular phase, σ_o and k are materials constants for friction stress for dislocation movement and strengthening coefficient respectively, σ_P is the yield strength of a particular phase, and d is the crystallite size (determined by XRD). Accordingly, for the AlFeCuCr alloy, the contribution to hardness of grain size strengthening is 14 % (yield strength, σ_y ~ 290 MPa). The contribution of solid solution strengthening can be determined by the relationship between yield strength and solid solution effects given by Eq. 5.4 [119]

$$\sigma_y = \frac{3.1\varepsilon G c^{1/2}}{700} \qquad (5.4)$$

where, ε is an experimental constant, G is the shear modulus of the matrix and c is the concentration of solute in atomic %. Eq. 5.4 is applicable to conventional alloy systems, however is less applicable to equiatomic or near equiatomic concentration HEAs. Thus, for HEAs the yield strength may be related to the solid solution effect Eq. 5.5

$$\sigma_y = \frac{3.1\varepsilon G \sum_{i=1}^{5} c_i^{1/2}}{700} \qquad (5.5)$$

where shear modulus, G for the HEAs is calculated by Voigt-Reuss-Hill bound formula, ε is the lattice strain of the phase (determined from XRD analysis), atomic concentration, c_i is the fraction of elements in i^{th} phase (determined from EDS analysis). Hence, the contribution of solid solution strengthening on hardness is found to be 15% (Yield strength, σ_y ~ 297 MPa). The total effect of grain size strengthening and solid solution strengthening on hardness is 30% (σ_y ~ 587MPa). It is to be noted that, phase fraction of WC contamination is found to be 0.08% (ImageJ) for AlFeCuCr alloy. Thus, the contribution of WC (Hardenss ~ 2400 HVN [17]) contamination was found to be 2.9% (σ_y ~ 57.6 MPa). Remaining contribution to hardness is due to brittle σ phase and presence of some contamination in AlFeCuCr alloy.

As-milled powder of $AlFeCuCrMg_{0.5}$ HEA alloy was composed of Cr type BCC phase with a small fraction of FCC. New phases evolved during sintering producing a nanostructured material with 11.5 nm (Fig. 5.6(c)) Cr-rich σ type phase in a Cu_2Mg type phase. The evolution of these precipitates is postulated to be via Cr rejection from the as milled BCC lattice after sintering. This rejection of Cr occurs due to high positive heat of mixing between Cr-Mg. The grain size effect calculated by Eq. 5.3 contributes approximately 15% (σ_y ~ 285 MPa) to the hardness. The contribution due to solid solution strengthening (Eq. 5.5) and intermetallic phase are determined to be 55% (σ_y ~ 1407 MPa).

The atomic misfit (ϵ) between a particle and a constituent phase along the c axis can be calculated using Eq. 5.6 [120].

$$\epsilon = \frac{2}{3}\frac{|a_p - a_m|}{a_m} \qquad (5.6)$$

where, a_m is the lattice parameter of the constituent phase, and a_p is the lattice parameter of the precipitate phase. Large strain misfit (ϵ = 0.159) suggests incoherency between the precipitate and the constituent phase [120]. Also, it was suggested by Holzwarth et al. [121] that in general, the critical radius of a precipitate required for a transition from coherency strengthening to the Orowan process is 5.37 nm. Kendig et al. [119] illustrated

the role of precipitation strengthening of Al-Mg-Sc-Zr alloy by both anti-phase boundary (APB) and Orowan particle strengthening models given by Eqs. 5.7 and 5.8.

$$\sigma_{APB} = (3.1)\frac{\gamma^{3/2}}{b^2}\left(\frac{rf}{G}\right)^{1/2} \quad (5.7)$$

$$\sigma_{orowan} = (3.1)(0.84)\frac{Gb}{\lambda} \quad (5.8)$$

Where γ is the energy required to form APB, b is the Burger vector for moving dislocation, r is the radius of the particles being cut, f is the volume fraction of particles, λ is inter-particle distance. APB strengthening mechanism is described for small precipitate size (< 20 nm) by the cutting of a precipitate by a moving dislocation (APB). With an increase in the particle size (> 20 nm) the cutting becomes difficult and strengthening in a solid is due to bowing of the dislocations (Orowans mechanism). In the case of $AlFeCuCrMg_{0.5}$ alloys both APB as well as Orowans mechanism is applicable due to small precipitate diameter. Contribution in hardness due to precipitates hardening is found out to be 26% (σ_y ~ 664MPa). Phase fraction of WC contamination is found to be 0.1% for x=0.5 alloy. Thus, contribution of WC contamination in this alloy is 2.8% (σ_y ~ 72 MPa). Overall estimated hardness 804 HVN (σ_y ~ 2428 MPa) falls below the experimental hardness value (853 ± 31.59 HVN) which may be due to some contamination or errors in the approximation in the microstructure.

As-milled AlFeCuCrMg and $AlFeCuCrMg_{1.7}$HEAs exhibit a structure composed of two supersaturated Cr type and Fe type BCC phases. After sintering an ordered AlFe type phase and Cr-rich precipitates are observed in a Cu_2Mg type phase, and the size of Cr-rich precipitates are larger (~ 150 nm) than the $AlFeCuCrMg_{0.5}$ HEA. When these HEAs are sintered at highertemperature, the negative enthalpy of mixing between Mg and Cu aids the formation of Cu_2Mg and Mg_2Cu type compounds, and excess of Cr may be rejected from the lattice. Formation of precipitates in the Cu_2Mg phase may be because of the combined effects of long range diffusion of Cr atoms and sluggish diffusion of Cr through the Cu_2Mg type phase (Ostwald ripening) [75].

There seems a relationship between the concentration of Mg in these x = 1, 1.7 HEAs and the size of precipitates formed. As the concentration increases the size of Cr-rich precipitates increases (20-150 nm for x = 1, 50-250 nm for x = 1.7). This phenomenon may be attributed to a greater amount of Cr rejection from the non-equilibrium as milled phase with high Mg content because of high positive enthalpy of mixing between Mg and Cr (24 kJ/mol [104]). Contribution of grain size strengthening, solid solution strengthening, precipitation strengthening and WC contamination (phase fraction ~ 0.03%) in AlFeCuCrMg alloy on hardness is determined to be 18% (σ_y ~ 399 MPa), 15% (σy ~ 339 MPa), 50% (1104 MPa) and 0.09% (21.6 MPa) respectively. On the other hand, $AlFeCuCrMg_{1.7}$ alloy is not havingnanocrystalline microstructure which may be due to higher phase fraction of Cu_2Mg. Thus, grain size and solid solution contributions are not calculated due to absence of the crystallite size and lattice strain values respectively. Although the contribution of hardening due to precipitates by orowans mechanism is determined to be 7% (σ_y~129 MPa). It is to be noted that precipitation hardening due to APB is not included because of larger precipitate size (~ 50 nm). Thus, the effect of precipitation hardening in x = 1.7 is only due to orowan mechanism resulting lower hardness in x =1.7 alloy.

Table 5.5 shows the hardness comparison of $AlFeCuCrMg_x$ (x = 0, 0.5, 1, 1.7) HEAs with commercially used Al,Titanium alloys and other HEAs. It can be observed that $AlFeCuCrMg_x$ (x = 0, 0.5, 1, 1.7) alloys have better hardness and specific strength thus could be considered as a potential candidate for transport applications. Further, studies on effect of heat treatment and contamination content will provide a complete view of the potential application of these HEAs.

Thus, to summarize microstructure of bulk sintered AlFeCuCr consisted of two BCC phases and a small quantity of σ-phase. As the Mg content increased from x = 0.5 mol to x = 1.7 mol, the microstructure was composed of predominately AlFe type ordered structure, BCC phase, and Cu_2Mg laves phase, with metastable Cr-rich σ-phase precipitates.

Table.5.5 Comparison of hardness, density and specific strength of $AlFeCuCrMg_x$ (x = 0, 0.5, 1, 1.7) HEAs with other alloys [122, 123, 124].

Alloys	Experimental Condition	Hardness (HVN)	Density (g/cm^3)	Specific strength (MPa)	Reference
$AlFeCuCrMg_x$ (x=0, 0.5, 1, 1.7)	MA followed by SPS	533-853	6.09-4.91	325-442	Present Study
Al-7075	Casting	175[122]	2.8	187.5	[122]
Ti-6Al-4V	Casting	175-341[123]	4.42	118-231	[123]
Ti-15V-3Cr-3Sn-3Al	Casting	262-400[124]	4.76	165-252	[124]
$NbVZrTiAl_x$ (x=1, 1.5)	Casting	540-620	5.50-4.23	294-439	[92]
$Mg_{50}(MnAlZnCu)_{50}$	Casting	173	2.20	235	[84]
$Al_{20}Li_{20}Mg_{10}Sc_{20}Ti_{30}$	MA + Sintering	499	2.67	560	[89]
$Al_{26.6}Nb_{23.8}Ti_{25.1}V_{24.5}$	Casting	448	5.59	240.2	[90]

The formation and growth of Cr-rich precipitates in Cu_2Mg phase in case of $AlFeCuCrMg_x$ (x = 0.5, 1, 1.7) HEA is reasoned to be the effect of high positive enthalpy between the binary elements.

A peak hardness value has been achieved for the $AlFeCuCrMg_{0.5}$ HEA due to a combined effect of solid solution hardening, grain boundary hardening, and the precipitation hardening. Fig.. 5.17 shows that the $AlFeCuCrMg_x$ alloys have the strengths comparable to high-density HEAs.

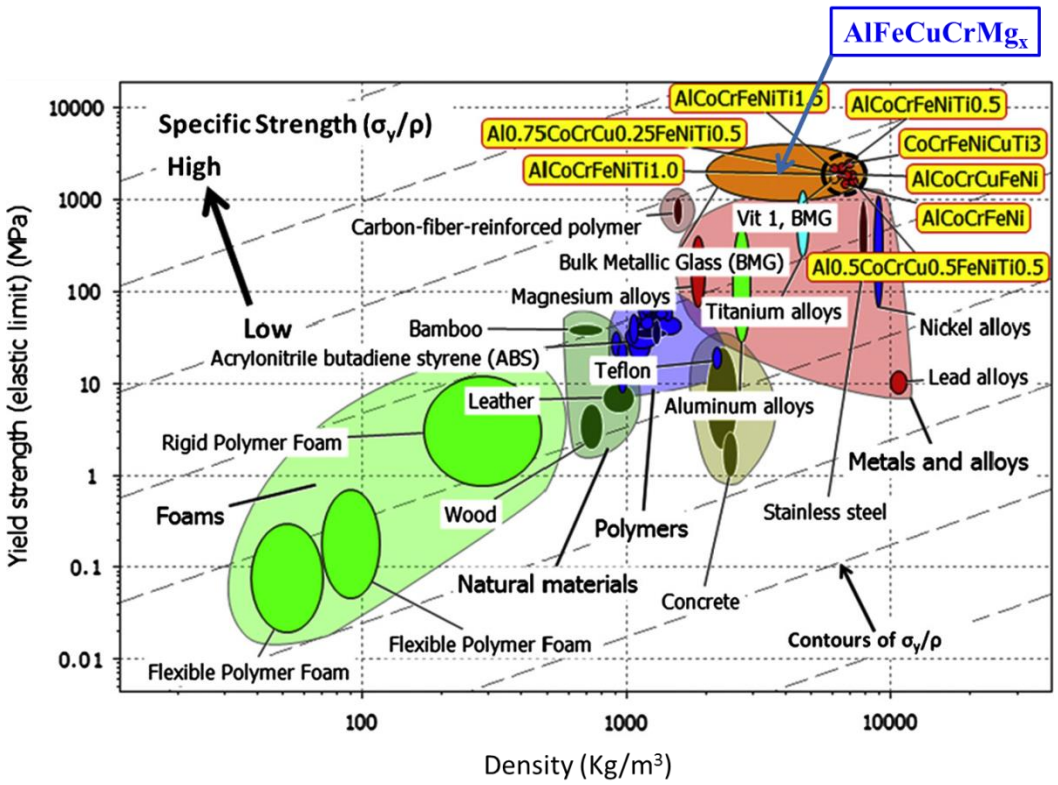

Figure 5.17 Yield strength versus density diagram [125]

Thus, the detailed study of $AlFeCuCrMg_x$ alloys showing high hardness hadbeen achieved over the density range 6.09-4.91 g/cm^3. In order to further reduce the density and synthesize a light weight alloy system some Ca, and Mg containing HEAs were also synthesized which will be discussed in the next chapter.

Chapter 6
Synthesis and characterization of Mg, Ca containing HEAs

Three Mg, Ca and Al containing HEAs namely AlMgCaNiCu, $(AlMgCa)_{1.33}(NiCu)_{0.5}$ and AlMgCaFeCr HEAs were synthesized by MA followed by spark plasma sintering (SPS). Thermodynamic parameters were conferred with the known criteria for the formation of solid solution in HEAs. The phase evolution of these HEAs after mechanical alloying (MA) followed by SPS has been reported here.

6.1 Thermodynamic parameters of the HEAs

Thermodynamic parameters such as ΔS_{conf}, ΔH_{mix}, atomic size mismatch δ, Valence electron configuration (VEC) and electronegativity (ΔX) are shown in Table. 6.1.It can be observed that the calculated value of ΔH_{mix} for both AlMgCaNiCu, and $(AlMgCa)_{1.33}(NiCu)_{0.5}$ alloys follows the Guo's criterion for formation of solid solution (as discussed in Section 2.3) due to the negative enthalpy of mixing between binary elements such as Ca-Ni, Ca-Cu, and Ca-Mg [95].

Table 6.1 Thermodynamic Parameters of AlMgCaNiCu, $(AlMgCa)_{1.33}(NiCu)_{0.5}$ and AlMgCaFeCralloys

Composition	ΔS_{config} (J/mol.K)	ΔH_{mix} (kJ/mol)	Delta % (δ)	ΔX	VEC
AlMgCaNiCu	13.38	-11.84	17.75	0.350	5.6
$(AlMgCa)_{1.33}(NiCu)_{0.5}$	12.61	-11.10	16.41	0.328	4.0
AlMgCaFeCr	13.38	8.8	17.64	0.293	4.2

On the other hand, δ parameter has ahigher value due to the large variation in atomic radius of individual elements and does not follow the Guo's criterion. On the other hand, ΔH_{mix}, and δ in case of equimolar AlMgCaFeCr alloy are not following the criterion for formation of solid solution due to high positive enthalpy between Mg-Fe, Mg-Cr, Ca-Fe, Ca-Cr [95] and large variation of atomic radius between the individual elements.

Studies suggest that there can be anomalies related with the criterions for formation of solid solutions in HEAs [101]. Valence electron configuration (VEC) [48] of these HEAs

suggests the formation of BCC structure. Calculated value of electronegativity (ΔX) favours the formation of topologically closed packed structure (TCP) for these HEAs [40]. Further, phase evolution in the case of all the three alloys has been studied and correlated with their respective thermodynamic parameters in the next section.

6.2 Phase Evolution after MA

XRD of as milled AlMgCaNiCu HEAs, shown in Fig. 6.1(a) suggests the formation of major ordered B2 (Lattice parameter, 287.07 pm) phase. Deconvolution of the peaks revealed the existence of two minor FCC phases (FCC1 and FCC2) with the lattice parameter of 359.46 pm & 353.45 pm respectively. Crystallite size for B2, FCC1, FCC2 phases is calculated to be 34.6 nm, 6.8 nm, 21.2 nm respectively. Lattice strain was determined to be 0.309%, 1.507%, and 0.546% respectively.

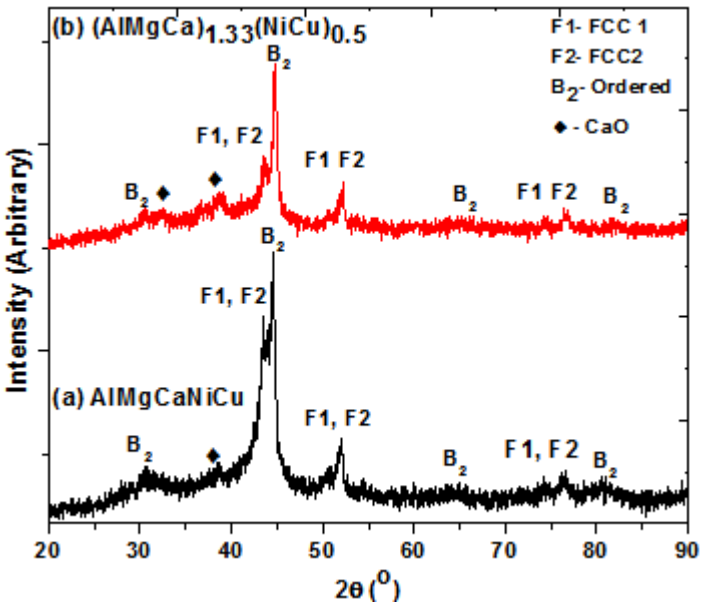

Figure 6.1 XRD pattern of 20hrs mechanically alloyed (a) AlMgCaNiCu (b) $(AlMgCa)_{1.33}(NiCu)_{0.5}$ HEAs

Further, XRD also reveals the formation of CaO and $Ca(OH)_2$ in the as-milled powder suggesting the presence of contaminants after MA which is due to the high reactivity of Calcium with grinding media and environment [62]. A similar phases are obtained from as milled $(AlMgCa)_{1.33}(NiCu)_{0.5}$ HEA (Fig 6.1(b)) with ordered B2 (lattice parameter,

286.51 pm), FCC1 (lattice parameter, 359.00 pm), FCC2 (lattice parameter, 351.21 pm) microstructure and smaller fraction of CaO, $Ca(OH)_2$. Crystallite size of ordered, FCC1, and FCC2 phase is found to be 31.0 nm, 7.00 nm, and 28.8 nm respectively. Lattice strain of ordered, FCC1 and FCC2 phase are found to be 0.399%, 1.463%, and 0.424% respectively. It is interesting to note that the lattice parameter obtained for FCC1 and FCC2 in AlMgCaNiCu and $(AlMgCa)_{1.33}(NiCu)_{0.5}$ HEAs are closely matching to the lattice parameters of Cu (361.1 pm) and Ni (352.3 pm) suggesting that two FCC phase (FCC1 & FCC2) formed are Cu type and Ni type.

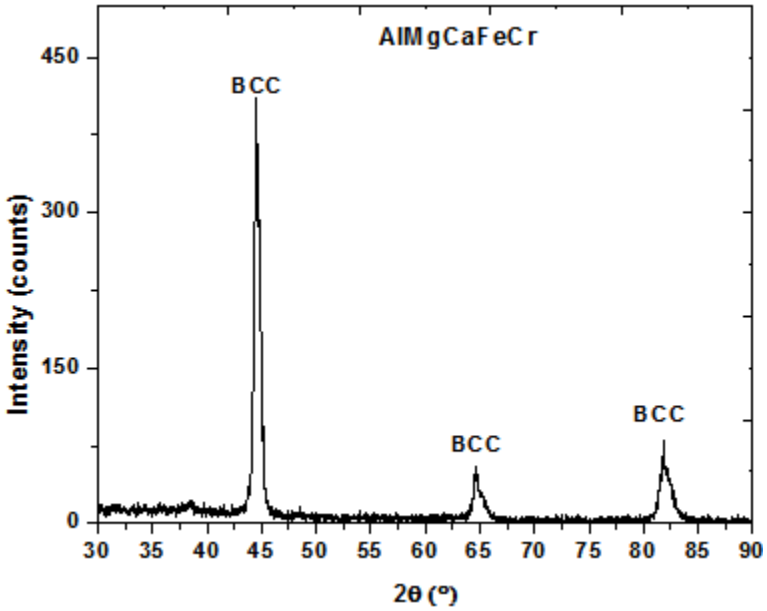

Figure 6.2 XRD pattern of 20 hrs mechanically alloyed AlMgCaFeCr HEA

XRD pattern of AlMgCaFeCr alloy (Fig 6.2) shows the formation of single phase BCC structure (lattice parameter, 287.6 pm). Crystallite size and lattice strain of BCC phase is found to be 20.6 nm, and 0.556 respectively. A small fraction of CaO phase is also present in the as milled AlMgCaFeCr alloy. In case of AlMgCaFeCr alloys the lattice parameters obtained for both the phases formed in AlMgCaFeCr alloy are closely matching to the lattice parameter of Cr (288.3 pm) suggesting Cr type of BCC lattice.

6.3 Structural evolution after sintering

SPS of AlMgCaNiCu, $(AlMgCa)_{1.33}(NiCu)_{0.5}$ and AlMgCaFeCr alloys was performed at 700^{o}C, 600^{o}C and 700^{o}C respectively based on theoretical melting point assumptions [92]. It was interesting to note that HEAs are physically disintegrated into powder form just after removing the graphite cover from the sintered alloy. The images of the sintered HEAs are shown in Fig. 6.3. Phase analysis of disintegrated samples was carried out by XRD which is shown in Fig. 6.4. XRD shows the formation of majorly ordered B2 phase (lattice parameter, 287.7 pm) with several minor phases such as Cu_2Mg, CaO, $Ca(OH)_2$, and orthorhombic phase (corresponding to complex CaCuMg oxide; JCPDS: 01-075-2858).

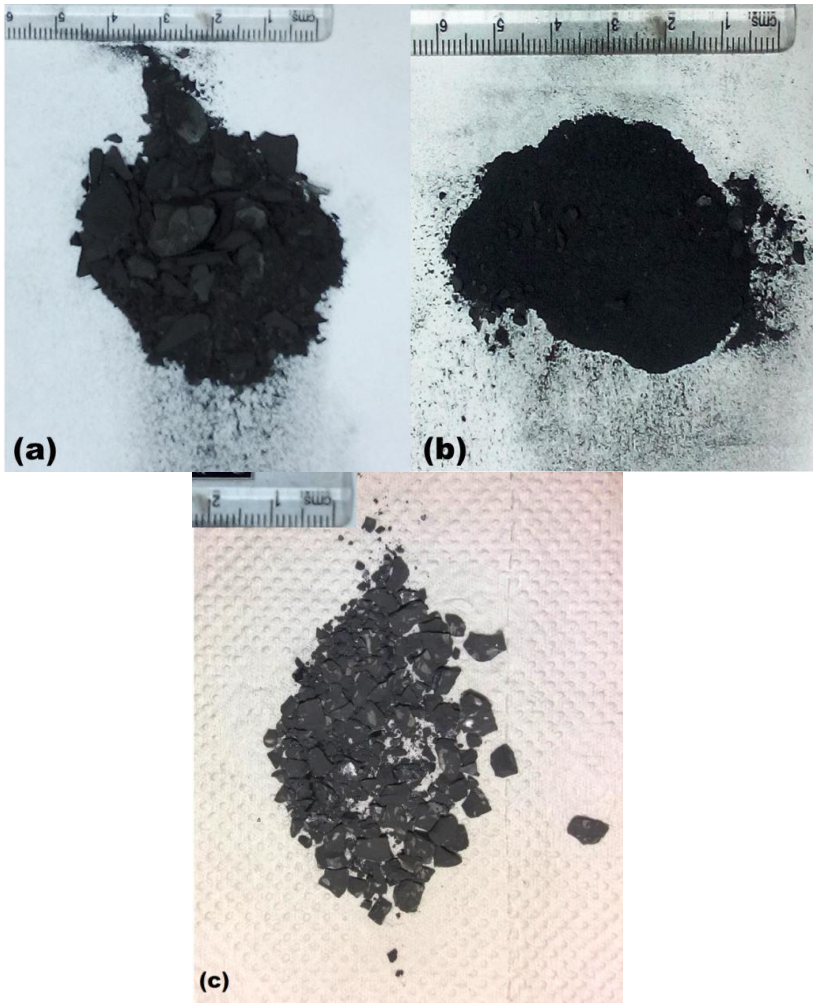

Figure 6.3 Micrograph showing the disintegration of sintered (a) AlMgCaNiCu (b) $(AlMgCa)_{1.33}(NiCu)_{0.5}$ (c) AlMgCaFeCr HEAs.

Similarly Fig. 6.3(b) suggests the formation of major B2 phase (lattice parameter, 285.6 pm) and minor FCC, Cu_2Mg, CaO, $Ca(OH)_2$ and orthorhombic phases. In case of AlMgCaFeCr alloy (Fig. 6.5) majorly BCC phase (lattice parameter, 287.4 pm) has evolved after SPS. Several minor phases such as FCC, CaO, $Ca(OH)_2$, and orthorhombic phase (corresponding to complex oxide; JCPDS: 01-075-2858) had also evolved after sintering in AlMgCaFeCr alloy.

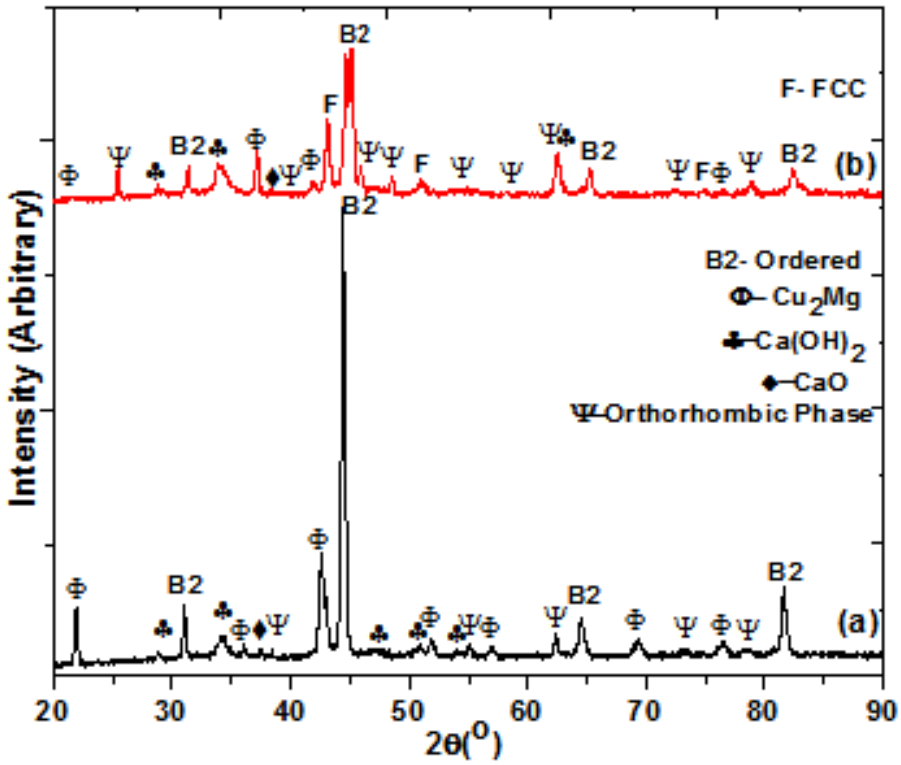

Figure 6.4 XRD pattern of SPSed (a) AlMgCaNiCu (b) $(AlMgCa)_{1.33}(NiCu)_{0.5}$ HEAs

In all cases phase evolution in these AlMgCaNiCu, $(AlMgCa)_{1.33}(NiCu)_{0.5}$ and AlMgCaFeCr alloys cannot be conferred with the thermodynamic parameters due to the separation of Ca element as $Ca(OH)_2$ and CaO from the major microstructure in as milled and sintered product.

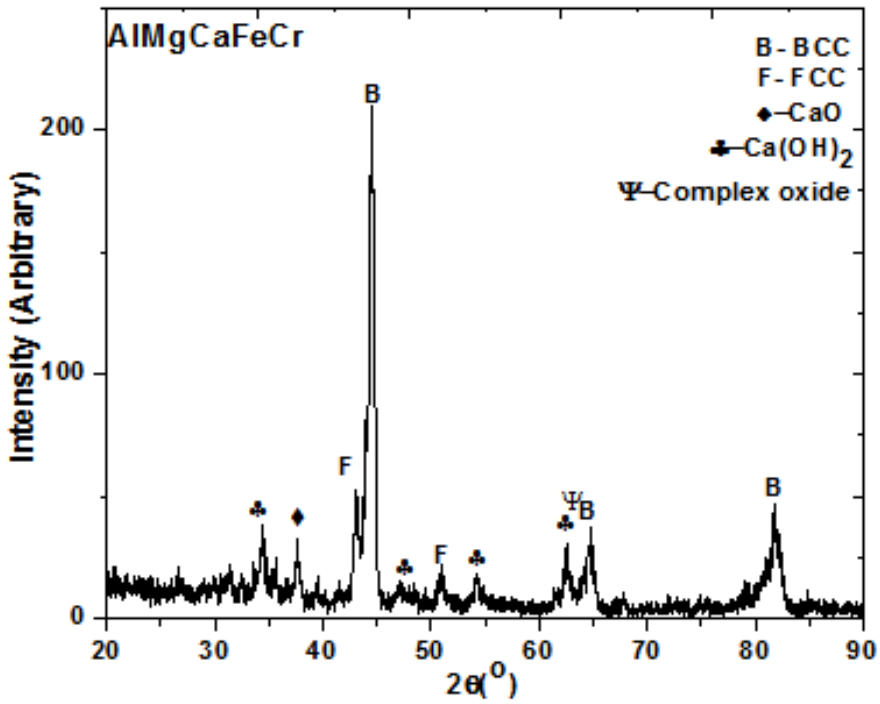

Figure 6.5 XRD pattern of SPSed AlMgCaFeCr HEA.

6.4 Microstructure Evolution in Ca containing HEAs

The disintegration in case of SPSed AlMgCaNiCu, $(AlMgCa)_{1.33}(NiCu)_{0.5}$ and AlMgCaFeCr alloys (see Fig. 6.3) may be due to the high reactivity of Ca elements with the environment. The disintegration of the sintered compact can be understood mainly in two steps firstly decomposition of $Ca(OH)_2$ and secondly vaporization of H_2O followed by diffusion of oxygen in milled powder.$Ca(OH)_2$is known to decompose and form CaO and H_2O at 580^oC [126]. Thus, sintering HEAs at a higher temperature ($\geq$ 600^oC) leads $Ca(OH)_2$ in the as milled alloys to decompose to form byproducts CaO and H_2O. CaO being a high melting temperature (~ 2613^oC) material does not allow individual particle of alloy powder to bind with each other at low temperature (in this case ~ 600^oC). On the other hand, other byproduct H_2O is vaporized while sintering to form complex CaCuMg oxide (JCPDS: 01-075-2858) which further does not allows these HEAs to compact while sintering. Due to a higher concentration of Ca metal in AlMgCaNiCu & $(AlMgCa)_{1.33}(NiCu)_{0.5}$ HEAs these effects are predominant and result in the physical disintegration of sintered alloy. Thus, this study suggests that Ca containing HEAs are difficult to synthesize due to the reactive behavior of Ca. Also, further studies on the

optimization of process parameters of MA like milling media, selection of PCA are needed to be done to fully understand and control structural evolution of these alloys.

It can be concluded that an attempt has been made to synthesize Ca containing lighter HEA system such as AlMgCaNiCu, $(AlMgCa)_{1.33}(NiCu)_{0.5}$ and AlMgCaFeCr by MA and SPS.XRD analysis indicated the formation of major ordered B2 phase and two FCC phases (FCC1, FCC2) in AlMgCaNiCu, $(AlMgCa)_{1.33}(NiCu)_{0.5}$ and major BCC phase in AlMgCaFeCr HEAs. Also, there was presence of a minor fraction of $Ca(OH)_2$ and CaO phases. Sintered compacts are physically disintegrated into a powder form. Phase characterization suggests disintegration is mainly because of $Ca(OH)_2$ and CaO phases during MA and sintering. It may also interpreted from the results that we may get rid of these unwanted species, such as $Ca(OH)_2$ and CaO, by performing mechanical alloying in a controlled atmosphere or using a powder of Ca based alloy/compound in place of elemental Ca powder.

Thus above described results have shifted the focus again to the $AlFeCuCrMg_x$ alloys, and further conventional sintering was performed on $AlFeCuCrMg_x$ alloys to establish the Materials-Structure-Process-Properties correlation of $AlFeCuCrMg_x$ HEAs.

Chapter 7

Structural Evolution in Conventionally Sintered $AlFeCuCrMg_x$ (x = 0, 0.5, 1, 1.7) HEAs

In this chapter as milled AlFeCuCr and $AlFeCuCrMg_x$ (x = 0.5, 1, 1.7) HEAs were conventionally sintered (based on melting point assumptions as discussed in section 3.1.4) at 900^{o}C and 800^{o}C respectively using electrical resistance furnace at air atmosphere. The sintered samples were characterized using XRD, SEM, and TEM techniques. The effect of conventional sintering on Mg-containing HEAs has been reported in this chapter.

7.1. Characterization of Bulk $AlFeCuCrMg_x$ HEAs

7.1.1 Bulk Density Measurement

The theoretical densities and the experimental bulk density are shown in Table 7.1. Theoretical density has been calculated using the rule of the mixture and the bulk density is calculated by Archimedes's principle. Experimental densities are in good agreement with the theoretical densities, as indicated by the relative density of 93 % to 100%. Also, relative density based on image analysis is determined for conventionally sintered $AlFeCuCrMg_x$ (x = 0, 0.5, 1, 1.7) HEAs using ImageJ software. Results indicate that minimum 72 % density has been achieved for AlFeCuCr alloy and maximum 98% density has been achieved for $AlFeCuCrMg_{1.7}$ alloy after sintering.

Table 7.1 Experimental bulk density and calculated relative density of $AlFeCuCrMg_x$ (x = 0, 0.5, 1, 1.7) HEAs

Composition	Theoretical Density (g/cm^3)	Bulk Density (g/cm^3)	Relative density w.r.t. Theoretical density (%)	Relative Density By Image analysis (%)
AlFeCuCr	6.28	4.534	72.1	72.8
$AlFeCuCrMg_{0.5}$	5.46	5.117	93.7	96.1
AlFeCuCrMg	4.54	4.369	96.2	96.2
$AlFeCuCrMg_{1.7}$	4.12	4.12	100	98.4

7.1.2 Phase analysis of AlFeCuCrMg$_x$ HEAs

The phase evolved after conventional sintering of AlFeCuCrMg$_x$ (x = 0, 0.5, 1, 1.7) alloys has been characterized by XRD and as shown in Fig 7.1.

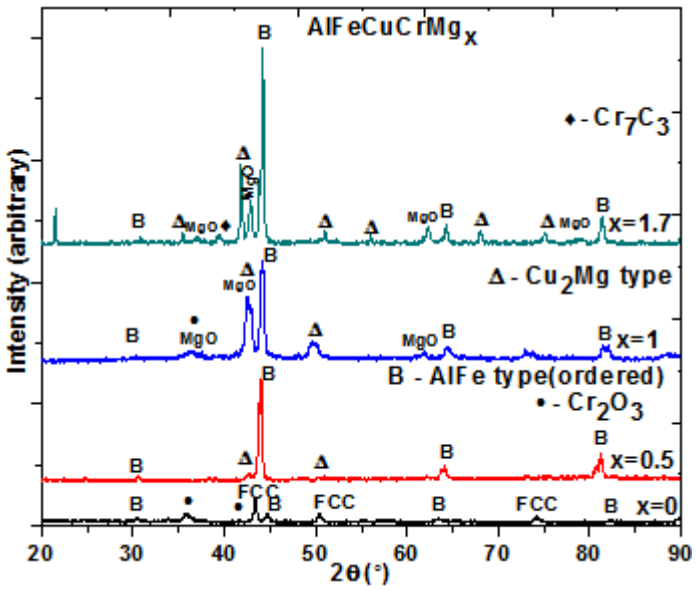

Figure 7.1 XRD patterns of AlFeCuCrMg$_x$ (x = 0, 0.5, 1, 1.7) HEAs after conventional sintering.

The XRD pattern of AlFeCuCr HEA (x = 0) (Fig 7.1) sintered at 800^{o}C shows the formation of majorly FCC phase with a lattice parameter of 360.8 pm. In addition to that minor ordered AlFe type phase is also present in the AlFeCuCr HEA having a lattice parameter of 286.5 pm. Also, it has been observed from the XRD pattern (Fig. 7.1) that several minor peaks of the oxide phases Cr_2O_3 (JCPDS: 00-006-0504) having a rhombohedral structure and lattice parameters a = 495.8 pm and c = 1359.3 pm are present. Magnified XRD patterns revealed that there are several other small peaks resembling some other oxide phases such as Al_2O_3 (JCPDS: 01-070-5679), Fe_2O_3 (JCPDS: 00-033-0664) both having a rhombohedral structure (Fig. 7.2).

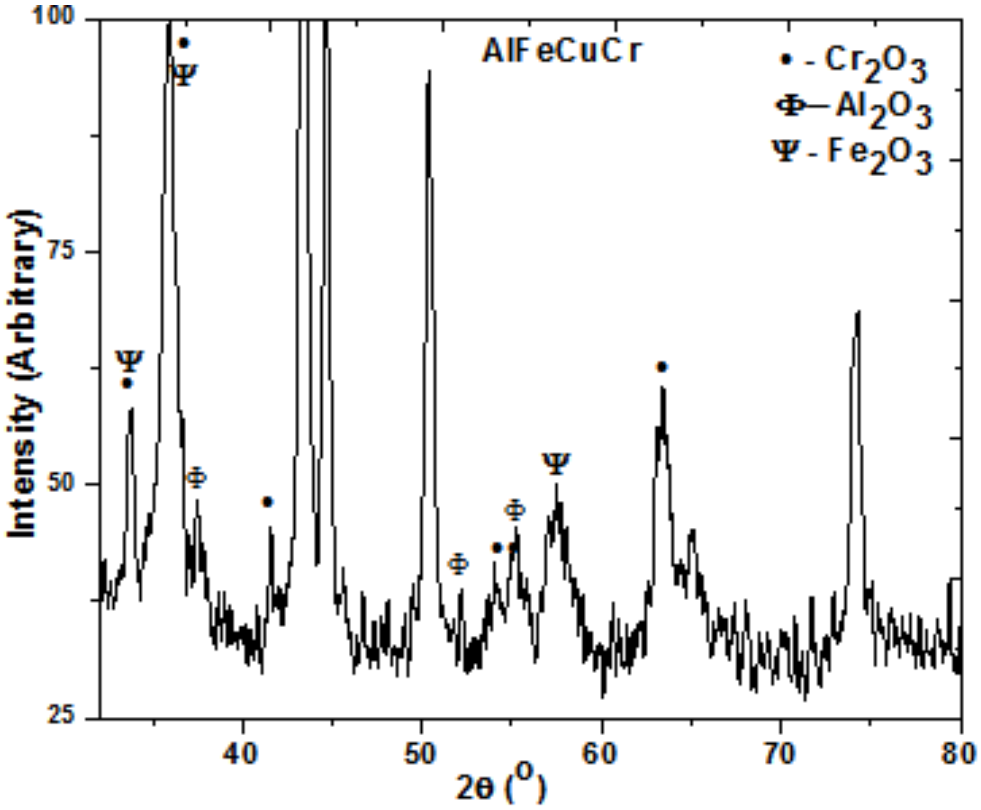

Figure 7.2 Oxide phases in conventionally sintered AlFeCuCr alloy

The XRD spectra of $AlFeCuCrMg_{0.5}$ HEA (x = 0.5) sintered at 800°C (Fig. 7.1) shows the formation of an ordered AlFe-type phase (JCPDS: 00-033-0020, lattice parameter, 292.3 pm) and minor Cu_2Mg type intermetallic (JCPDS: 00-058-0360, lattice parameter 704.0 pm). Detailed analysis and deconvolution of the major peak of $AlFeCuCrMg_{0.5}$ HEA revealed the formation of disordered BCC phase (Fig. 7.3) along with the ordered phase. The lattice parameter of disordered BCC phase is found to be 292.4 pm and a phase fraction is determined to be 0.393.

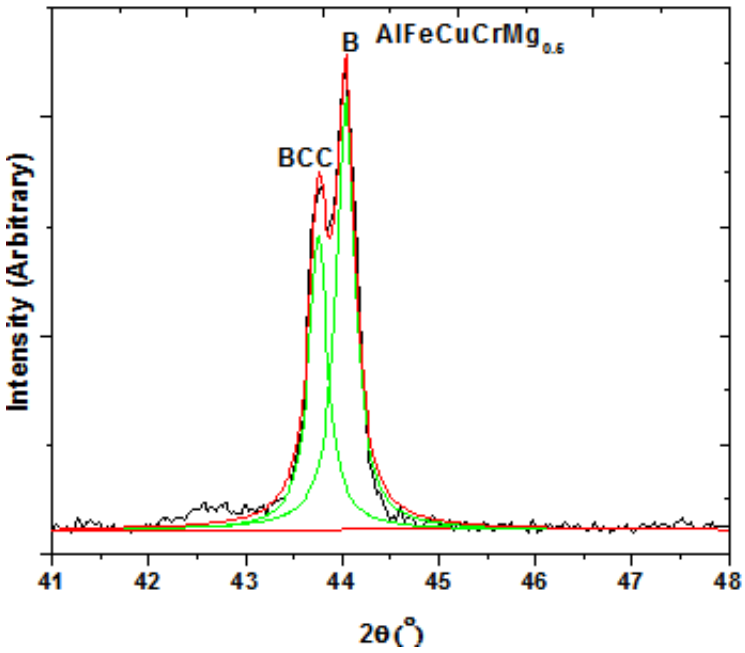

Figure 7.3 Deconvoluted XRD pattern of conventionally sintered $AlFeCuCrMg_{0.5}$ (x = 0.5) HEA

XRD pattern of AlFeCuCrMg HEA (x = 1) sintered at 800°C (Fig. 7.1) shows the formation of multi-phases such as majorly ordered AlFe type phase, Cu_2Mg and MgO phase. The ordered phase and Cu_2Mg have a lattice parameter 290.3 pm and 704.77pm respectively. Detailed analysis of the XRD curve (Fig. 7.4(a)) shows that BCC phase is present in the AlFeCuCrMg HEA. Lattice parameter of disordered BCC phase found out to be 288.7 pm. The fraction of BCC phase in x = 1 HEA is found out to be approx. 0.255. It is interesting to note that the fraction of BCC phase is increasing with increase in Mg content with respect to ordered phase.

Phase evolution of $AlFeCuCrMg_{1.7}$ HEA (x = 1.7) sintered at 800°C (Fig. 7.1) reveals the formation of ordered AlFe phase, Cu_2Mg lave phase, and MgO phase. The lattice parameters of ordered phase and Cu_2Mg is calculated to be 289.46 pm and 715.68 pm respectively. Fig.7.4 (b) shows detailed analysis of $AlFeCuCrMg_{1.7}$ alloy. It can be noted that disordered BCC phase has formed with lattice parameter 291.99 pm. Also, similar to the SPSed $AlFeCuCrMg_{1.7}$ alloy (see Table 5.2), in this case the fraction of disordered BCC phase is low (0.128). As explained earlier in chapter 5this is due to the higher Mg concentration that increases the intermediate phases resulting in the decrease in the disordered BCC phase.

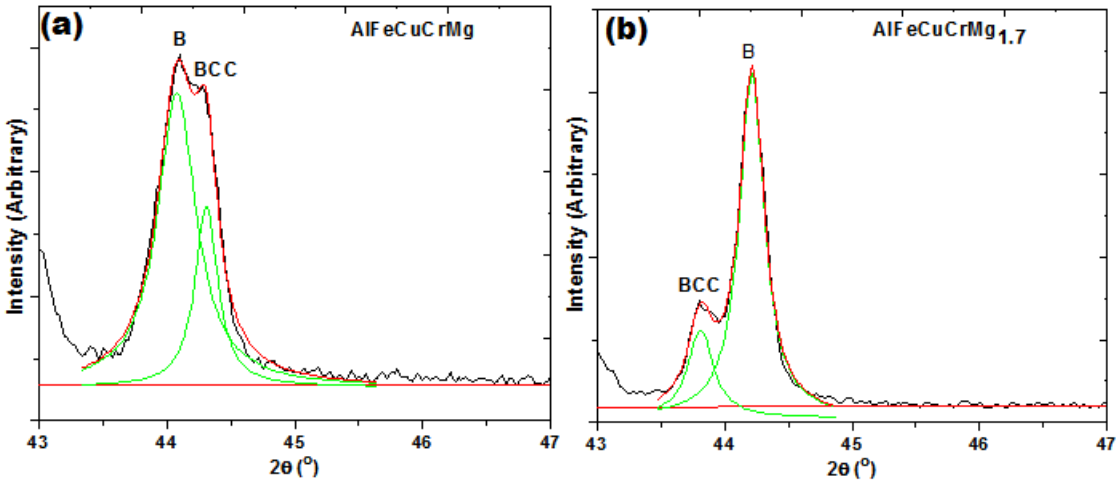

Figure 7.4 Deconvoluted XRD pattern of conventionally sintered (a) AlFeCuCrMg and (b) $AlFeCuCrMg_{1.7}$HEAs

Table 7.2 shows the phase fraction of constituent phases, lattice parameter, crystallite size and lattice strain in the conventionally sintered $AlFeCuCrMg_x$ (x = 0, 0.5, 1, 1.7) HEAs. Table 7.2depicts that in case of conventionally sintered alloys there is a relationship between the Mg content and lattice parameter of Cu_2Mg type phase in $AlFeCuCrMg_x$ (x = 0.5, 1, 1.7) HEAs. Mg content increases the lattice parameter of Cu_2Mg phase continuously shifts towards higher value which suggests the presence of sufficient amount of dissolved Mg in Cu_2Mg type phase. Although it can be observed that lattice parameter value of ordered phase first increases for Mg fraction 0.5 then decreases for x=1 and again increase for x = 1.7 on the other hand for BCC phase lattice parameter value for $AlFeCuCrMg_x$ (x = 0.5, 1, 1.7) first decreases upto the alloy having Mg mole fraction 1 and then increases for x = 1.7 alloy.This may be due to the fact that in case of conventionally sintered alloys as the Mg concentration increases up to x = 1 there occur structural relaxation/decomposition as well as elimination of defects in the crystal lattice [127, 128] but in case of x = 1.7 alloy, higher Mg content leads to the high lattice distortion.

Table 7.2 Phase fraction, Lattice parameter, Crystalline size and lattice strain of conventionally sintered $AlFeCuCrMg_x$ (x=0, 0.5, 1, 1.7) HEAs.

Composition	Phases	Phase Fraction	Lattice parameter (pm)	Crystallite Size (nm)	Lattice strain
AlFeCuCr	FCC	0.724	360.8	42.3	0.326
	Ordered phase	0.270	286.5	35.1	0.364
$AlFeCuCrMg_{0.5}$	BCC	0.393	292.43	72.5	0.223
	Ordered phase	0.581	290.55	73.2	0.220
	Cu_2Mg	0.025	704.06	23.4	0.526
AlFeCuCrMg	BCC	0.255	290.30	91.3	0.189
	Ordered phase	0.351	288.86	34.4	0.375
	Cu_2Mg	0.251	704.77	68.0	0.232
$AlFeCuCrMg_{1.7}$	BCC	0.128	291.99	72.7	0.220
	Ordered phase	0.551	289.46	72.7	0.220
	Cu_2Mg	0.215	715.68	39.0	0.290

7.1.3 Microstructure Characterization of $AlFeCuCrMg_x$ (x = 0, 0.5, 1, 1.7 mol) HEAs by SEM

Fig. 7.5 shows the back scattered electron (BSE) image of AlFeCuCr HEA along with the EDS analysis of the phases.

Fig. 7.5 confirms that there are two phases present in AlFeCuCr HEA. EDS analysis shows that white phase has the high Cu content. So, this phase can be implied as Cu type FCC structure, and the gray phase is AlFe type ordered structure. At lower magnification, white particles were dispersed uniformly in AlFeCuCr HEA. EDS results show that these white particles are WC, which results from the contamination from ball mill.

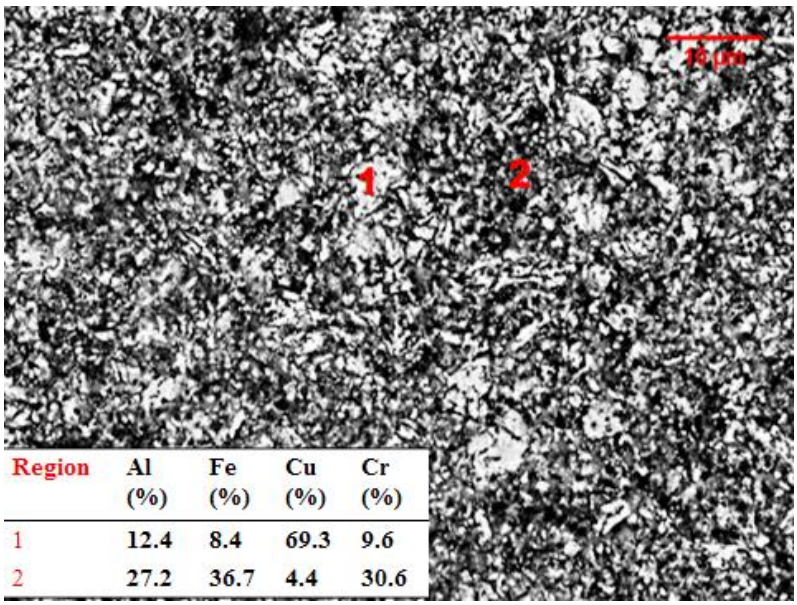

Figure 7.5 BSE micrograph and EDS analysis (inset) of conventionally sintered AlFeCuCr (x = 0) HEA

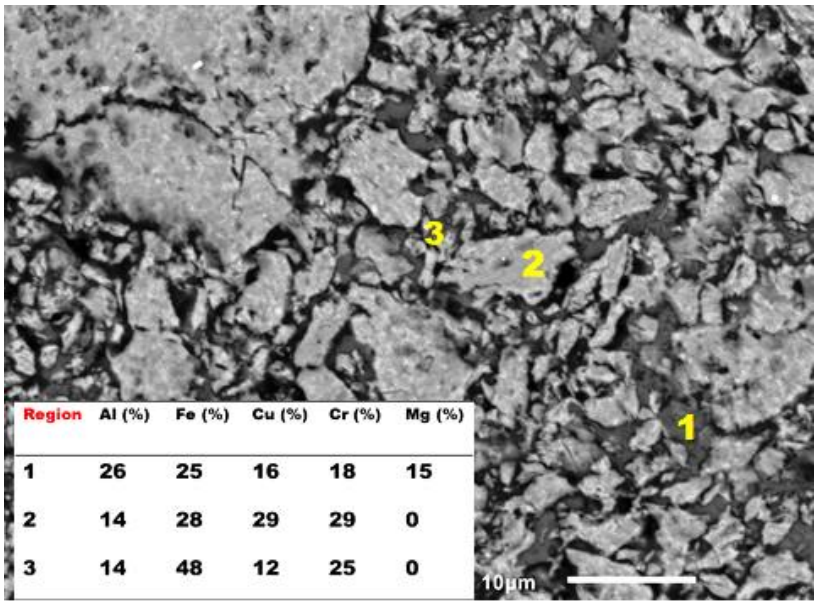

Figure 7.6 BSE micrograph and EDS analysis (inset) of conventionally sintered $AlFeCuCrMg_{0.5}$ HEA

Fig 7.6 shows the BSE image and EDS analysis of $AlFeCuCrMg_{0.5}$ HEA. It can be seen that the microstructure of $AlFeCuCrMg_{0.5}$HEA mainly contains three regions. The dark grey region (Fig 7.6, region '1') which constitutes of ordered phase as well as Cu_2Mg phase and coarse grains corresponding to the Fe, Cr, and Cu-rich phase (Fig 7.6 , region '2'). In the third region, Fe-rich smaller grains are being observed in $AlFeCuCrMg_{0.5}$

HEA, which may correspond to BCC phase and a small amount of σ phase as observed in XRD. It is to be noted that some white particles dispersed in the microstructure of $AlFeCuCrMg_{0.5}$ HEA are observed in this case also. The EDS analysis suggests that these white particles are due to WC contamination as the mechanical alloying has been done in tungsten carbide vials.

Fig. 7.7 shows the BSE mode microstructure and EDS analysis of AlFeCuCrMg HEA. As in the case of $AlFeCuCrMg_{0.5}$ HEA, there are two types of region present in x = 1 HEA. Region '1' i.e. coarse grains and region '3' corresponds to the Fe-rich region thus might have BCC crystal structure. Region '2' forms a network-like structure and constitutes of higher Al and Mg contents and has ordered type as well as Cu_2Mg type crystal structure.

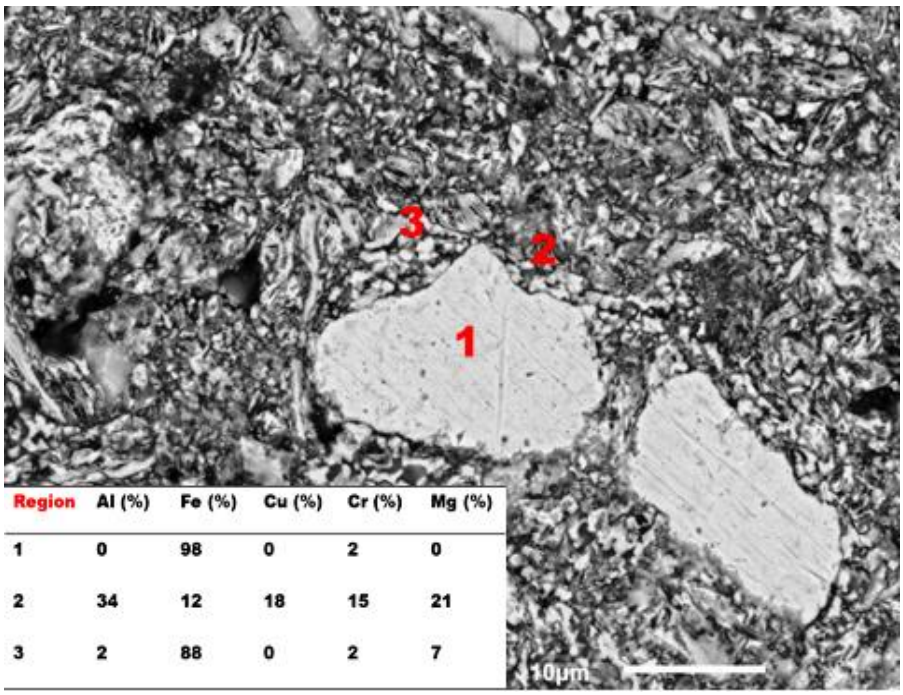

Region	Al (%)	Fe (%)	Cu (%)	Cr (%)	Mg (%)
1	0	98	0	2	0
2	34	12	18	15	21
3	2	88	0	2	7

Figure 7.7 BSE micrograph and EDS analysis (inset) of conventionally sintered AlFeCuCrMg HEA

It is interesting to note that the increase in the Mg content causes the more phase decomposition (see region '1', Fig. 7.8) which can be understood because of a high miscibility gap.

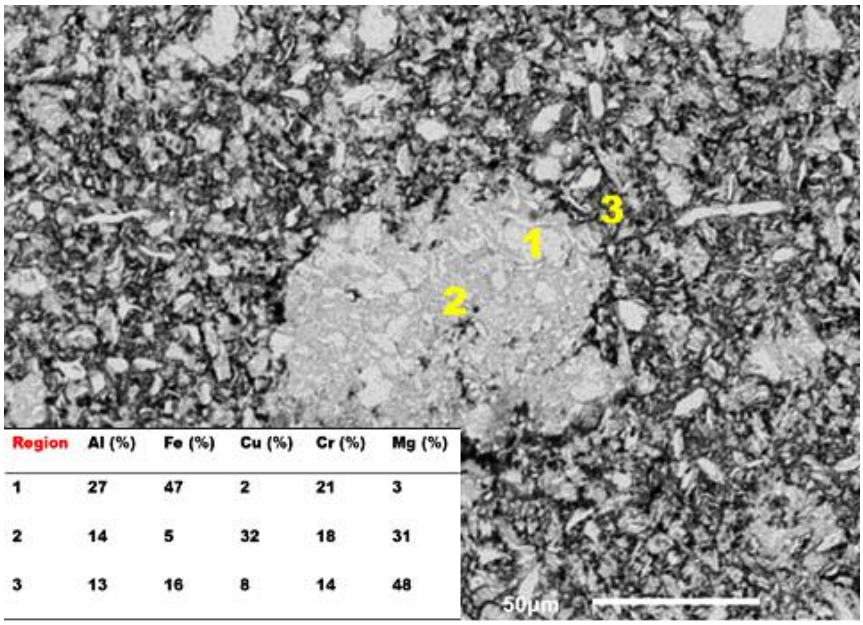

Region	Al (%)	Fe (%)	Cu (%)	Cr (%)	Mg (%)
1	27	47	2	21	3
2	14	5	32	18	31
3	13	16	8	14	48

Figure 7.8 BSE micrograph and EDS analysis (inset) of conventionally sintered AlFeCuCrMg$_{1.7}$ HEA

Fig 7.8 shows the BSE-SEM image of AlFeCuCrMg$_{1.7}$ HEA. The microstructure of high Mg content HEA can be described as coarse grains surrounded by a network of another phase. EDS analysis (Fig 7.8) reveals that coarse grain region in the microstructure is divided into two parts i.e. region '1' and region '2'. Region '1' corresponds to the ordered type and BCC structure and in region '2' mainly Cu_2Mg type of crystal structure is present. Surrounding these grains is the network of Mg-rich region in AlFeCuCrMg$_{1.7}$ HEA.

7.1.4 Microstructure Characterization of AlFeCuCrMg$_x$ HEAs by TEM

The sub-micron characterization of AlFeCuCr alloy by TEM could not performed due to the higher porosity fraction (see Table 7.1) and the presence of high amount of oxide phases. Nevertheless, the present study is focused to observe the behavior of Mg concentration on the sub-micron structure in these alloys.

Fig. 7.9(a), (b), (c) shows the TEM bright field, SAED pattern and dark field image for AlFeCuCrMg$_{0.5}$ HEA.

The bright field image (Fig. 7.9 (a)) of AlFeCuCrMg$_{0.5}$ HEA reveals the formation of the nanocrystalline microstructure of ordered phase, Cu_2Mg phase, and disordered BCC phase. SAED pattern (Fig. 7.9 (b)) reveals the formation of ordered AlFe type structure,

disordered BCC phase; Cu_2Mg laves phase and MgO phase. Bright field image also reveals the presence of spinodal decomposition in the microstructure (see inset Fig 7.9(a)).

Dark field image (Fig .7.9 (c)) was obtained by moving the aperture to the ordered phase ring and the crystallite size distribution was analyzed by image j. The average crystallite size obtained is found to be 38 nm.

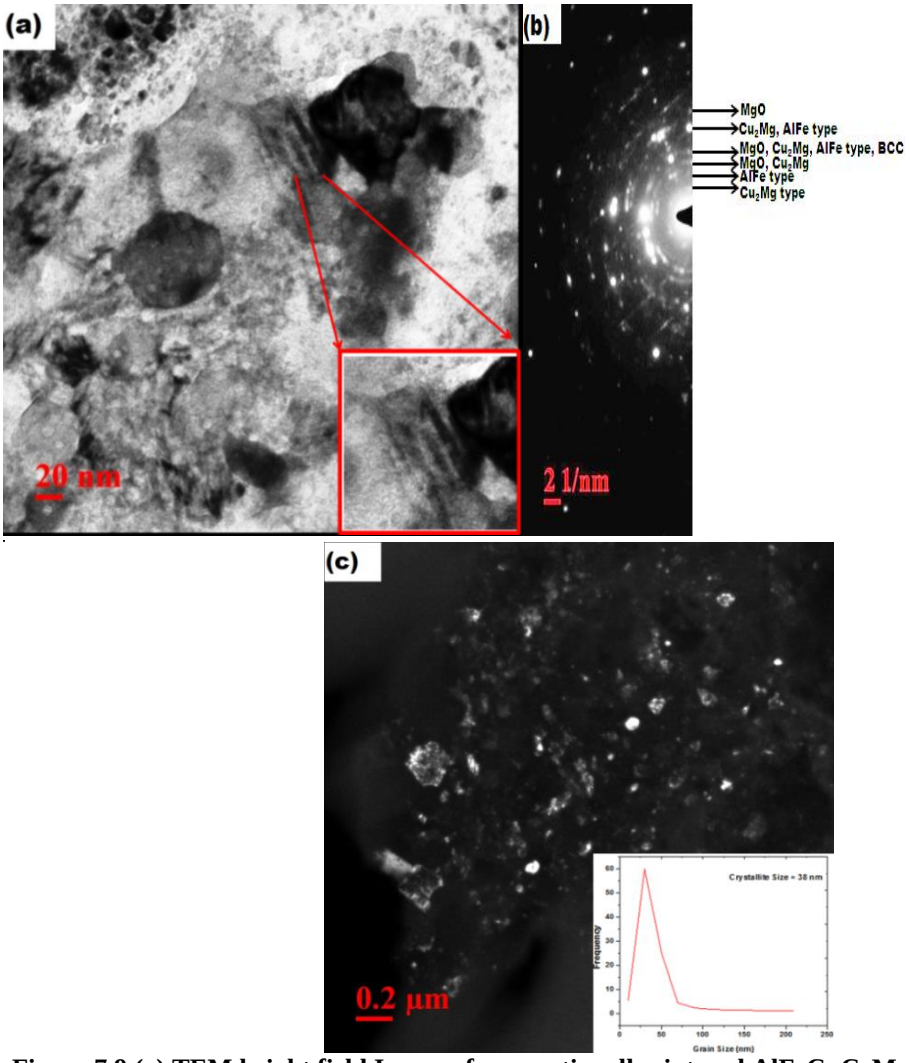

Figure 7.9 (a) TEM bright field Image of conventionally sintered $AlFeCuCrMg_{0.5}$ (x = 0.5) HEA and spinodal decomposition (inset), (b) SAED pattern corresponding to the bright field image ,(c) TEM dark field image of $AlFeCuCrMg_{0.5}$ (x = 0.5) HEA.

Multipoint EDS analysis of $AlFeCuCrMg_{0.5}$ HEA was obtained by transforming the bright field image to the STEM mode. Fig 7.10 shows the composition of different phases present in $AlFeCuCrMg_{0.5}$ alloy.

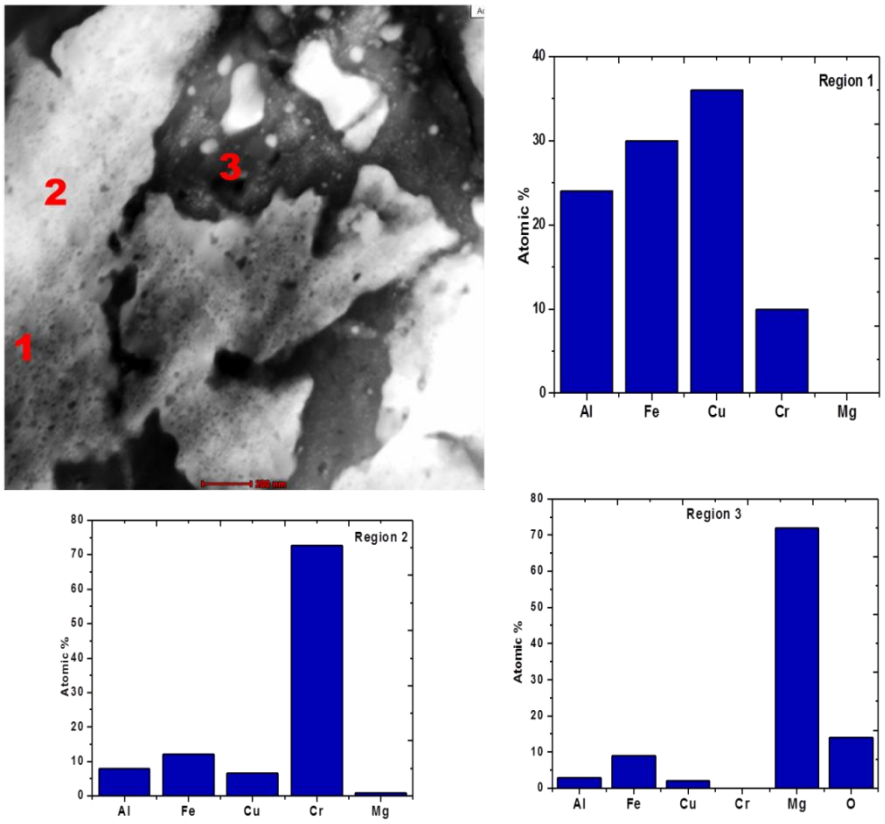

Figure 7.10 STEM image and multipoint EDS analysis of conventionally sintered $AlFeCuCrMg_{0.5}$ (x = 0.5) HEA

Fig. 7.11 shows the bright field image and SAED pattern for AlFeCuCrMg HEA. In case of AlFeCuCrMg HEA bright field image (Fig. 7.11) depicts the formation of nanocrystalline microstructure as well as micron size grains. Fig. 7.11(a) shows the SAED pattern for region 1 which corresponds to the cubic Cu_2Mg structure and MgO phase.

Fig. 7.11 shows that the region 2 corresponds to the BCC structure (Fig. 7.11(c)). Fig. 7.12 shows the dark field image of the precipitate phase which suggests that the range of precipitate sizes is from 10 nm to 130 nm.

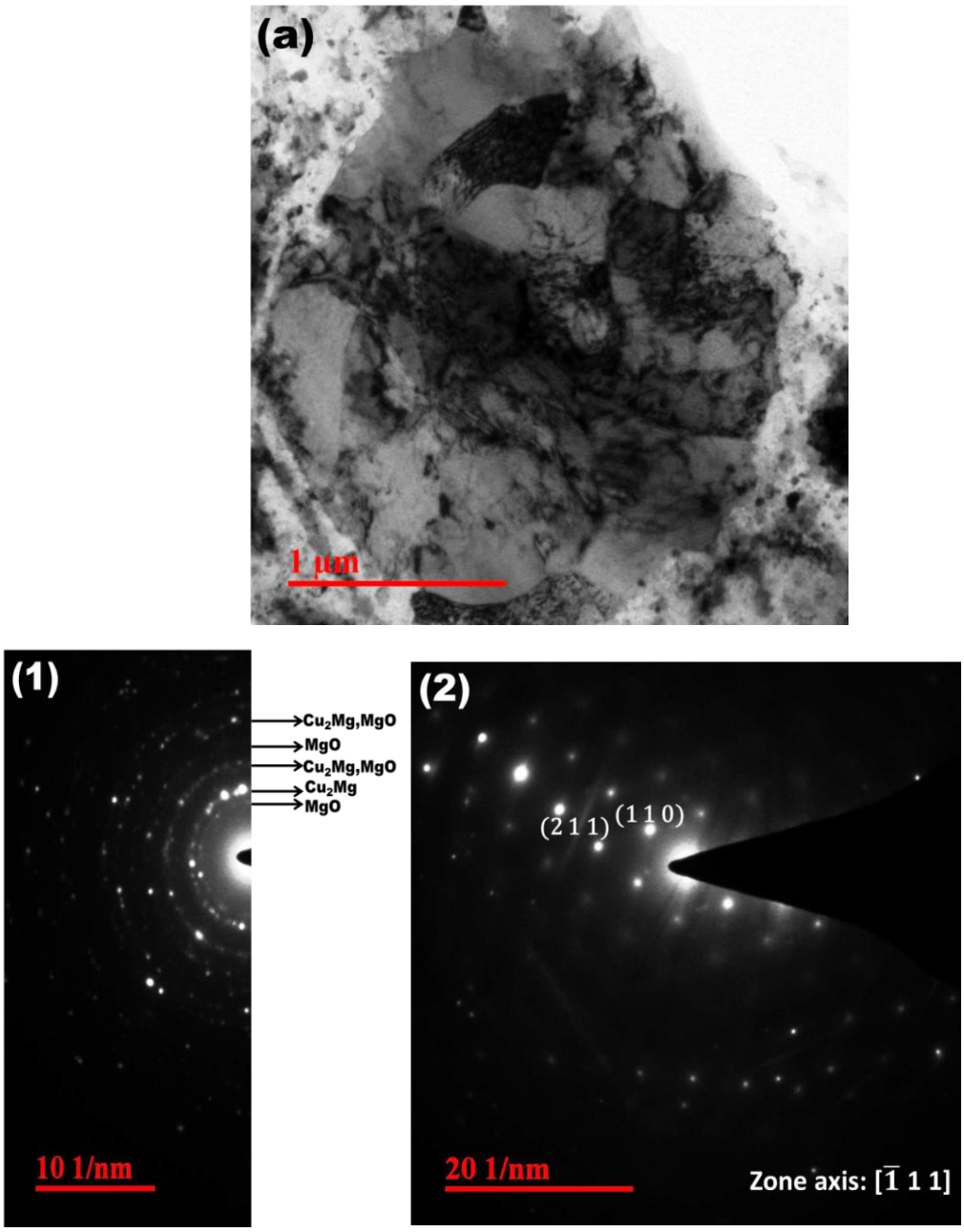

Figure 7.11 (a) TEM bright field image showing different morphology and SAED pattern corresponding to region 1 (Cu_2Mg and MgO) and region 2 (BCC phase) in conventionally sintered AlFeCuCrMg HEA.

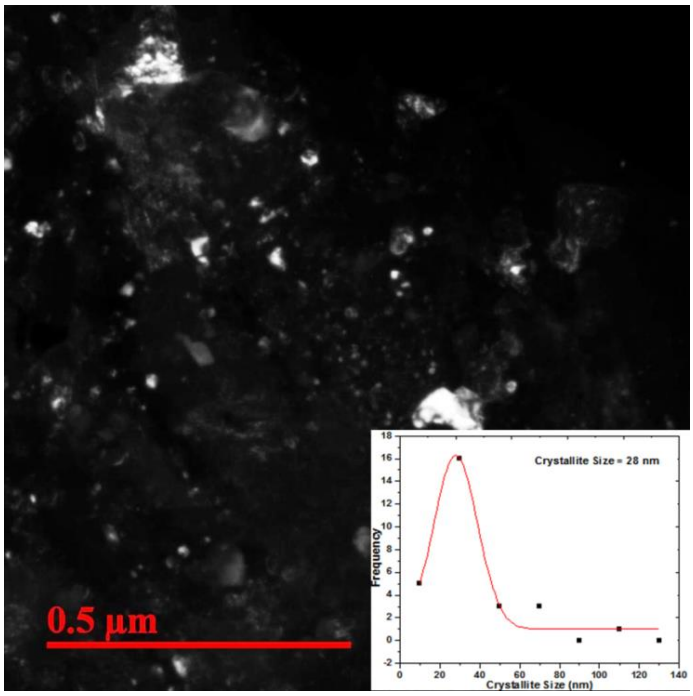

Figure 7.12 TEM dark field image of conventionally sintered AlFeCuCrMg (x = 1) HEA.

Fig. 7.13 shows the STEM image and multipoint EDS analysis of the precipitates. Results confirm the formation of BCC phase mainly constituting Fe element, and Cu_2Mg laves phase.

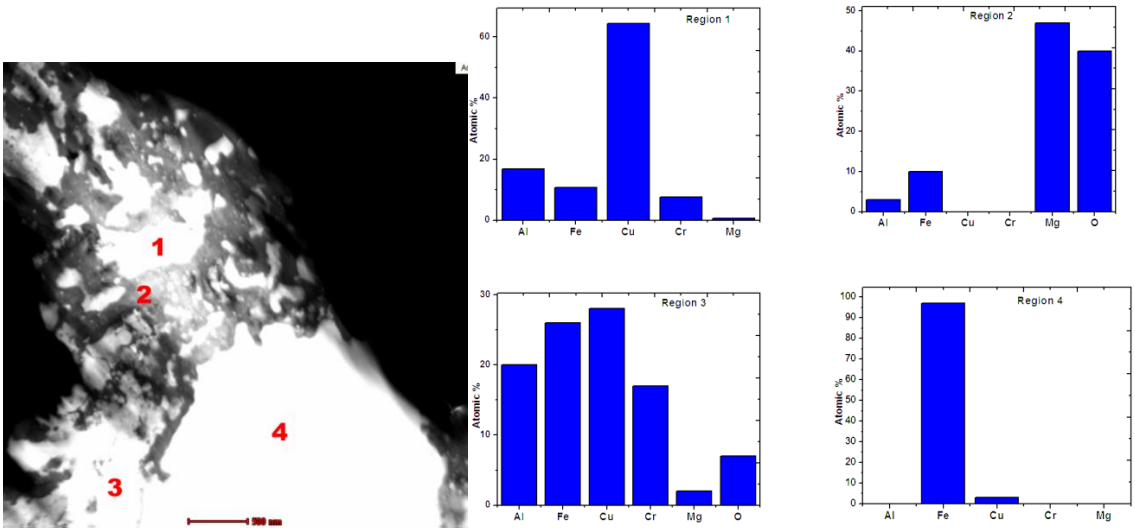

Figure 7.13 STEM image and multipoint EDS analysis of region 1, 2, 3 and 4in conventionally sintered AlFeCuCrMg (x = 1) HEA.

Fig.7.14 shows the bright field image and SAED patterns for $AlFeCuCrMg_{1.7}$ alloy which are characterized by irregularly shaped orthorhombic Cr_7C_3phase precipitates, in a cubic Cu_2Mg type phase (SAED, Fig. 7.14(1-2)). In this case, much of the carbon impurity

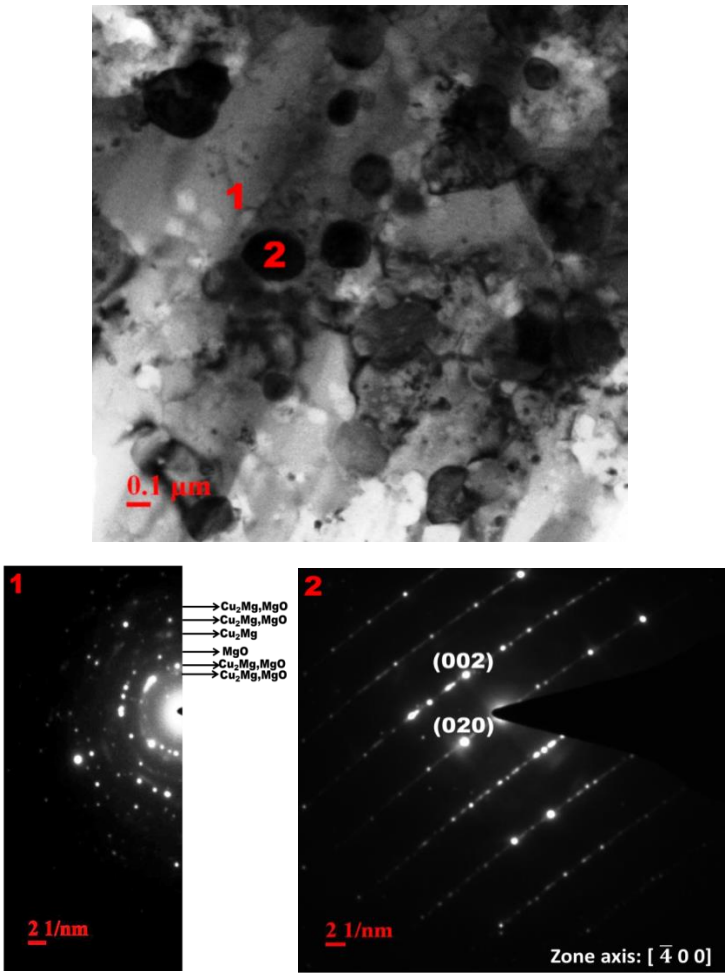

Figure 7.14 TEM bright field image showing different morphology and SAED pattern corresponding to region 1 (Cu_2Mg, MgO) and region 2 (Cr_7C_3) in TEM image in conventionally sintered $AlFeCuCrMg_{1.7}$ HEA

uptake might have occurred from the atmosphere during sintering. An absence of an orientation relationship between the Cu_2Mg phase and precipitates indicates that the precipitates are incoherent in nature.

Fig. 7.15 shows the dark field image of the precipitate phase, which suggests the size range of 10 nm to 150 nm.

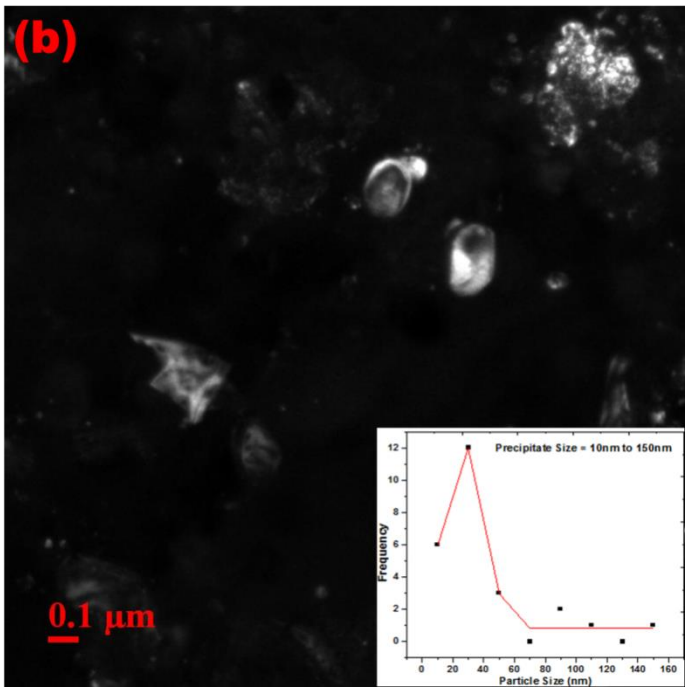

Figure 7.15 TEM dark field image of conventionally sintered $AlFeCuCrMg_{1.7}$ (x = 1.7) HEA.

Fig 7.16 shows the STEM image and multipoint EDS analysis, which confirm the formation of orthorhombic Cr_7C_3 precipitates and Cu_2Mg type phase.

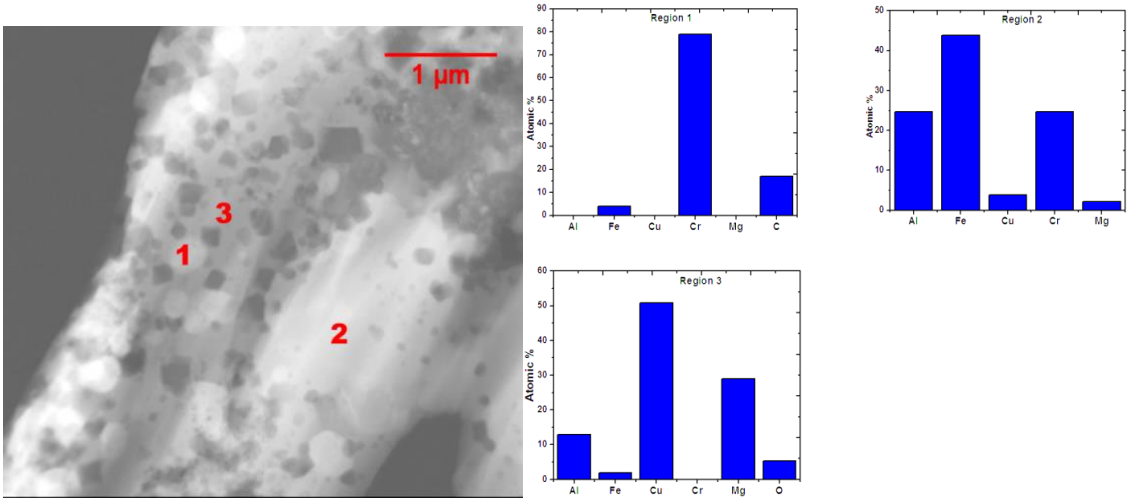

Figure 7.16 STEM image and multipoint EDS analysis of conventionally sintered $AlFeCuCrMg_{1.7}$ (x = 1.7) HEA.

It is to be noted that carbide phase (Cr_7C_3) is present in $AlFeCuCrMg_{1.7}$ which is attributed to the presence of Cr rich precipitates which pickup carbon very rapidly from the atmosphere or contaminations while sintering [129] and forming chromium carbide phase.

7.1.5 Hardness Measurement

Vickers hardness measurements carried out on $AlFeCuCrMg_x$ (x = 0, 0.5, 1, 1.7) HEAs plotted in Fig. 7.17

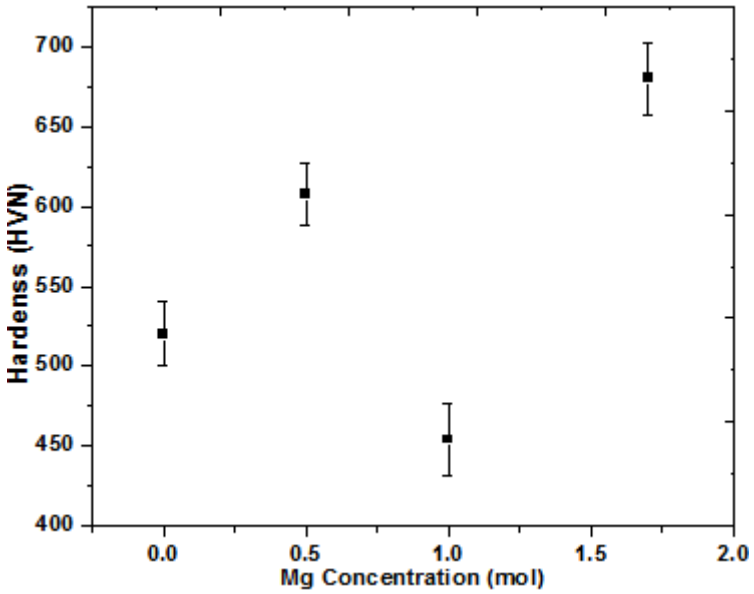

Figure 7.17 Microhardness of conventionally sintered $AlFeCuCrMg_x$ (x = 0, 0.5, 1, 1.7) HEAs.

Vickers hardness of $AlFeCuCrMg_x$ (x = 0.5, 1, 1.7) HEAs shows maximum hardness of 678 ± 22.5 HVN attained by $AlFeCuCrMg_{1.7}$ alloy. AlFeCuCrMg alloy had the lowest hardness value of 454 ± 22.6 HVN.

The yield strength from the Eq. 5.1 is determined to be 1560 MPa, 1809 MPa, 1362 MPa, and 2034 MPa for $AlFeCuCrMg_x$ (x = 0, 0.5, 1 and 1.7) respectively.

7.2 Microstructural Evolution and Structure-Processing-Property correlation

As-milled AlFeCuCr HEA powder contains BCC phase with a relatively small fraction of FCC. After conventional sintering, primarily FCC phase and minor ordered AlFe type phases have evolved. This maybe explained due to fact that supersaturated BCC structure evolved after MA is decomposed to thermodynamically more stable FCC type and ordered phases. It was seen that in these alloy substantial amount of oxide phases has also been formed, which is due to the air atmosphere while sintering and high affinity of oxygen with Al, Cr, and Fe elements. The hardness value of AlFeCuCr alloy may be attributed to three factors i.e. grain size strengthening, solid solution strengthening and the oxide phases formed while sintering.

In case of $AlFeCuCrMg_{0.5}$ alloys mainly constitute of ordered AlFe type phase and the BCC phase. The ordered phases have been evolved due to more negative heat of mixing between Al-Fe. Diffraction data suggests that there is a formation of MgO phase in the microstructure of $AlFeCuCrMg_{0.5}$ alloys due to oxygen uptake during sintering. It is interesting to note that positive heat of mixing and a miscibility gap between elements in these alloys have resulted in the small fraction of decomposition of different Cu, and Cr-rich regions in the microstructure. This canbe understood by the mechanism of spinodal decomposition which may be explained as an atomic level mechanism by which a metastable single solid solution phase of different elements can be made thermodynamically more stable by phase segregation [130]. The necessary condition for the stability of dissimilar mixture is that the curvature of Gibbs free energy, G, of a phase must increase with respect to the concentration thus implying that $\partial^2 G/\partial x^2 > 0$, at a given temperature. If this condition is not seen then the mixture will decompose. Thus, a metastability limit can be defined as a spinodal, where $\partial^2 G/\partial x^2 = 0$ [130, 131]. Spinodal decomposition involves compositional modulations of the local composition of the phase with wavelength, λ, in the range $2 \leq \lambda \leq 5$ nm [132].

Thus, microstructural studies suggest that hardness value of $AlFeCuCrMg_{0.5}$alloy can be mainly attributed to three factors (i) grain size strengthening, (ii) solid solution strengthening and (iii) spinodal hardening [119].

Grain size strengthening can be calculated by the Hall-Petch relationship as shown in Eq. 5.3. The effect of grain size strengthening cannot be calculatedwith respect to the phase formed due to the phase decomposition of Cu, Mg, and Cr elements. Thus, in this case, the contribution of grain size strengthening is being calculated by considering the total concentration of the solute phase in $AlFeCuCrMg_{0.5}$ alloy. Accordingly, for the $AlFeCuCrMg_{0.5}$ alloy, the contribution to the hardness of grain size strengthening is 8% (yield strength, $\sigma_y \sim 135$ MPa).

The contribution of solid solution strengthening (Eq. 5.5) on hardness of $AlFeCuCrMg_{0.5}$ alloy was calculated to be 5.8 % (Yield strength, $\sigma_y \sim 105$ MPa). Spinodal hardening also has a contribution in the hardness in $AlFeCuCrMg_{0.5}$ alloys. Several models have been proposed for explaining the yield strength in the alloys, which mostly suggest the dependencies on compositional fluctuation, A and wavelength of compositional fluctuation, λ [133, 134]. It has been proposed that not all spinodal alloys show crystallographic alignment due to lower elastic strain [131].In the case of $AlFeCuCrMg_{0.5}$ alloy, although the microstructure does not show any crystallographic alignment the strengthening due to the Orowan looping mechanism seems to be more favourable due to the small segregations of Cr, Cu-rich regions. Cahn et al. [135] determined that in the case of strengthening by Orowan mechanismthe yield strength is proportional to $(A/\lambda^2)^{1/3}$. Also, presence of contamination and MgO phase plays a major part in the strengthening in $AlFeCuCrMg_{0.5}$ alloy.

As-milled AlFeCuCrMg HEA exhibits a structure composed of two supersaturated Cr type and Fe type BCC phases. After sintering primarily an ordered AlFe type phase, disordered BCC phase and Cu_2Mg phase were observed. TEM studies revealed that there are some regions in the microstructure where there is decomposition of Fe, Cr, and Cu-rich phases (see Fig. 7.12). These observations suggest that as in the case of $AlFeCuCrMg_{0.5}$ alloy this alloy too shows the spinodal decomposition mechanism in the microstructure. However, in AlFeCuCrMg alloy there is much higher miscibility gap compared to $AlFeCuCrMg_{0.5}$ alloy due to the increase in Mg concentration, which results in larger scale of decomposition of the Fe, Cr and Cu regions. Also, there is a formation

of MgO phase due to the uptake of oxygen while conventional sintering. For AlFeCuCrMg alloy, the grain size effect contributes approximately8% (σ_y ~ 121 MPa) to the hardness. The contribution due to solid solution strengthening (Eq. 5.5) and intermetallic phase are determined to be 5% (σ_y ~ 68 MPa). Rest of the strengthening is due to the combined effect of spinodal hardening, contamination, and MgO phases.

Apart from $AlFeCuCrMg_x$ (x = 0.5, 1) alloys it is interesting to note that in the case of conventionally sintered $AlFeCuCrMg_{1.7}$ alloy precipitation takes place instead of decomposition. Primarily ordered AlFe type phase, Cu_2Mg phase and disordered BCC phase and MgO phase have evolved after sintering. It is to be noted that Cr_7C_3 precipitates are observed in a Cu_2Mg type phase in this alloy. It can be explained due to negative enthalpy of mixing between Mg and Cu, which aids the formation of Cu_2Mg compounds, and excess of Cr may be rejected from the lattice. C and O uptake may have occurred from the atmosphere and contaminations present while sintering. The precipitate size was found to be in the range from 20 nm to 150 nm. Contribution of grain size strengthening, solid solution strengthening, and precipitation strengthening in $AlFeCuCrMg_{1.7}$ alloy on hardness is determined to be 8% (σ_y ~ 161 MPa), 62 % (σy ~ 1270 MPa), and 5 % (100 MPa) respectively. It is to be noted that in this case Orowan particle strengthening is considered due to larger precipitate size. Remaining strengthening in $AlFeCuCrMg_{1.7}$ alloy may be due to the contamination and formation of MgO phase.

The formation of precipitates in higher Mg concentration (x = 1.7) compared to lower Mg concentration may be explained on the basis of diffusion mechanism. As SPSed x = 1.7 alloy, in case of conventionally sintered $AlFeCuCrMg_{1.7}$ alloy due to higher phase fraction of Cu_2Mg formation of precipitates is due to the combined effects of long range diffusion of Cr_7C_3 precipitates and sluggish diffusion of Cr_7C_3through the Cu_2Mg type phase (Ostwald ripening). Although in the case of $AlFeCuCrMg_x$ (x = 0.5, 1) alloys due to lower concentration of Mg and lower fraction of Cu_2Mg phase suppress the effect of Ostwald ripening and decomposition is favored due to miscibility gap.

It is interesting to note that the hardness values in case of conventionally sintered $AlFeCuCrMg_x$ (x = 0, 0.5, 1) alloys is lower than the hardness obtained after SPSed $AlFeCuCrMg_x$ (x = 0, 0.5, 1) which may be attributed to the spinodal decomposition [133]. This result in reduced severe lattice distortion effect in the HEAs which in turn leads to the inferior properties of the conventionally sintered alloys compared to SPSed alloys [9]. The decomposition of the phase is due to two primary reasons after conventional sintering i.e. longer time period given to sintering which enables the elemental atoms to segregate and result in high immiscibility gap between elements. On the other hand, in SPS the sintering time is substantially lower, which results in nanocrystallinity of the alloys and severe lattice distortion in the phases formed [66]. In case of $AlFeCuCrMg_{1.7}$ alloys the higher hardness value (678 ± 22.5 HVN) compared to the SPSed $AlFeCuCrMg_{1.7}$ alloys (533 ± 17.4 HVN) may be explained on the basis of precipitation hardening and higher contamination of O and C in the lattice structure.

Therefore, this part of studies concludes that the phase evolved after conventional sintering of AlFeCuCr consists of majorly FCC phase with minor fraction of ordered AlFe type phase, Al_2O_3, Cr_2O_3 and Fe_2O_3 phase. As the Mg content increased from x = 0.5 mol to x = 1.7mol, the microstructure was primarily composed of AlFe type ordered structure, BCC phase, and Cu_2Mg lavesphase and MgO phase. Sub-micron characterization of $AlFeCuCrMg_x$ (x = 0.5, 1) alloys shows the presence of spinodal decomposition in the microstructure. However, in case of $AlFeCuCrMg_{1.7}$ alloys, the microstructure characterization shows that Cr_7C_3 precipitates have evolved in a Cu_2Mg phase and the microstructure does not constitute of spinodal decomposition. Except for $AlFeCuCrMg_{1.7}$ alloy the microhardness values in case of $AlFeCuCrMg_x$ (x = 0, 0.5, 1) alloys is being lower compared to hardness achieved after SPSed alloys. Thus, further heat treatment of SPSed samples have been carried to see the effect of temperature in $AlFeCuCrMg_x$ (x = 0, 0.5, 1, 1.7) alloys

Chapter 8

Heat Treatment of Spark Plasma Sintered AlFeCuCrMg$_x$ HEAs

In this chapter, the heat treatment of SPSed bulk AlFeCuCrMg$_x$ (x = 0, 0.5, 1, 1.7) alloys was carried out at 470^{o}C, 600^{o}C and 820^{o}C for 4 hrs in an argon atmosphere to study phase stability of alloys with respect to temperature. The heat treated alloys were characterized by using XRD, SEM, and TEM techniques. Hardness testing of the sintered samples was performed using micro hardness tester.

8.1 Phase Evolution

8.1.1 Phase Evolution after Heat Treatment of AlFeCuCrMg$_x$ HEAs

The phase evolved after heat treatment at 470^{o}C for AlFeCuCrMg$_x$ (x = 0, 0.5, 1, 1.7) has been characterized by XRD and is shown in Fig 8.1

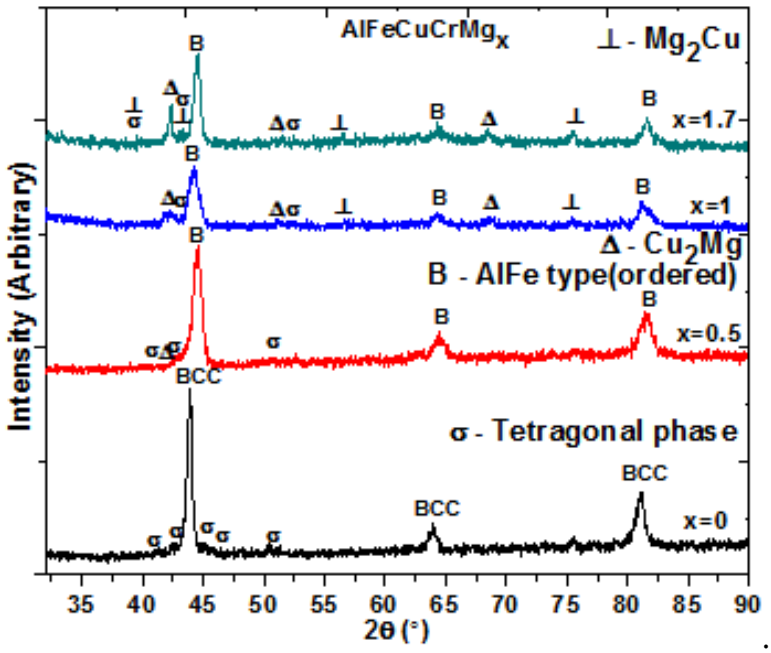

Figure 8.1 XRD patterns of AlFeCuCrMg$_x$ (x = 0, 0.5, 1, 1.7) HEAs after heat treatment at 470^{o}C.

As in case of spark plasma sintered alloy the phase evolution after heat treatment at 470^{o}C in Ar atmosphere for 4 hrs shows the formation of BCC phase with a lattice parameter of 290.14 pm and several minor peaks indicative of σ phase (JCPDS: 01-071-

7530) having a tetragonal structure (lattice parameters such as a = 879.66 pm and c = 455.82 pm). The major peak at 43.95^{o} (see Fig.5.2 (a)) displayed asymmetry and upon deconvolution revealed a second BCC phase (BCC 2) having a lattice parameter 290.9 pm and FCC phase with the lattice parameter 358.0 pm has evolved. The phase fraction for BCC 2, BCC 1 and FCC phase is calculated to be 47%, 17%, and 34% respectively. Similarly, in the case of $AlFeCuCrMg_{0.5}$ alloy, the major phases present are ordered AlFe type phase, and Cu_2Mg type disordered BCC phase and σ phase. Also, a detailed analysis suggests that there is a small fraction of FCC (lattice parameter, 358.3 pm) present after heat treatment at 470^{o}C.

For Mg-containing alloys i.e. $AlFeCuCrMg_x$ (x = 1, 1.7), the phase evolved after heat treatment was found to be similar to the phases formed after SPS (Chapter 5). Multi-phase microstructure in the alloys constitutes of ordered AlFe type phase as the major phase, Cu_2Mg type, Mg_2Cu,disordered BCC phase (lattice parameter 290.74 pm, approximate phase fraction 0.503), and σ phase. It is to be noted that as Mg content increases the phase fraction of Cu_2Mg laves phase also increases.

Table 8.1 summarizes XRD analysis conducted including the lattice parameter and phase fraction of constituent phases, crystallite size and lattice strain in the sintered $AlFeCuCrMg_x$ (x = 0, 0.5, 1, 1.7) HEAs. Instrumental broadening was corrected using a single crystalline Si substrate. Lattice strain, ε, was determined by the Eq. 4.2.

It is interesting to note that the nanocrystalline structure of the alloys is intact even after the heat treatment for 4 hours suggesting that SPS is effective technique to synthesizenanocrystalline materials. As compared to the SPSed alloys the lattice parameters of Cu_2Mgphase is decreased after heat treatment which may be due to relaxation of the internal stresses present in the lattice after SPS. In this case too there is no relationship between the lattice parameter and phase fraction of the BCC phase in comparison to the SPSed alloys which suggests that BCC phase is not containing Mg element.

Table 8.1 Phase fraction, Lattice parameter, Crystallite size and lattice strain of heat treated $AlFeCuCrMg_x$ (x = 0, 0.5, 1, 1.7) HEAs.

Composition	Phases	Phase Fraction	Lattice parameter (pm)	Crystallite Size (nm)	Lattice Strain
AlFeCuCr	BCC 2	0.34	292.6	38.4	0.346
	BCC 1	0.47	290.9	53.9	0.270
	FCC	0.17	358.0	26.6	0.461
$AlFeCuCrMg_{0.5}$	BCC	0.44	288.6	18.9	0.598
	Ordered phase	0.47	286.6	21.5	0.536
	Cu_2Mg	0.03	698.3	15.4-	0.737
AlFeCuCrMg	BCC	0.29	291.5	24.6	0.488
	Ordered phase	0.58	288.6	13.8	0.786
	Cu_2Mg	0.12	706.1	9.7-	1.116-
$AlFeCuCrMg_{1.7}$	BCC	0.37	287.7	-	-
	Ordered phase	0.40	286.7	51.7	0.274
	Cu_2Mg	0.22	707.40	90.6	0.198-

The phase evolved after heat treatment at 600^{o}C for 4 hours in Ar atmosphere is shown in Fig. 8.2

It can be observed that the phase evolution after heat treating $AlFeCuCrMg_x$ (x = 0, 0.5, 1, 1.7) alloys is same as in case when heat treated at 470^{o}C. XRD have confirmed the formation of two BCC (BCC 1 and BCC 2) type and FCC type structure in AlFeCuCr alloys. For $AlFeCuCrMg_{0.5}$ alloy, ordered AlFe type phase as the major phase, and Cu_2Mg type, disordered BCC phase, σ phase and FCC phase (lattice parameter, 356.7 pm) have evolved. On the other hand, ordered AlFe type phase as the major phase, and Cu_2Mg type, Mg_2Cu, disordered BCC phase, σ phase are formed in case of $AlFeCuCrMg_x$ (x =.0.5, 1, 1.7) alloys.

Table 8.2 summarizes XRD analysis conducted including the lattice parameter and phase fraction of constituent phases, crystallite size and lattice strain in the sintered $AlFeCuCrMg_x$ (x = 0, 0.5, 1, 1.7) HEA.

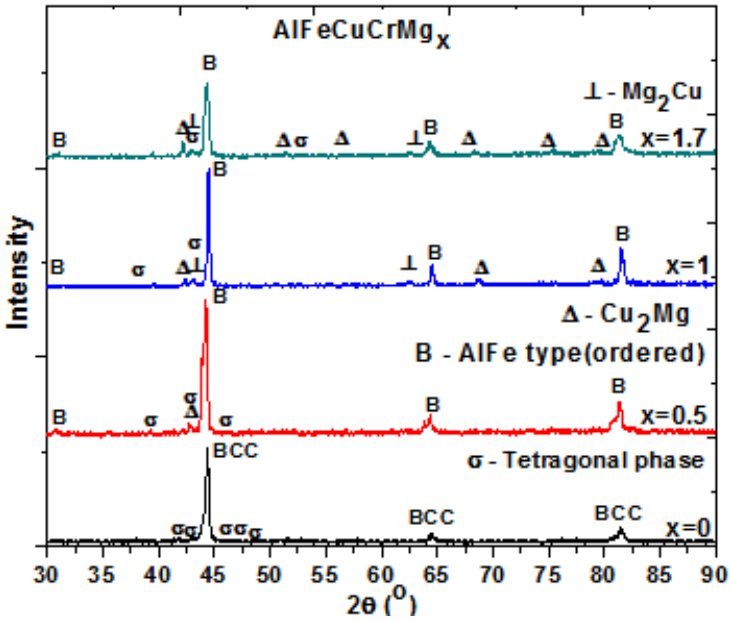

Figure 8.2 XRD patterns of AlFeCuCrMg$_x$ (x = 0, 0.5, 1, 1.7) HEAs after heat treatment at 600°C.

Table 8.2 Phase fraction, Lattice parameter, Crystalline size and lattice strain of AlFeCuCrMg$_x$ (x = 0, 0.5, 1, 1.7) HEAs after 600°C.

Composition	Phases	Phase Fraction	Lattice parameter (pm)	Crystallite Size (nm)	Lattice Strain
AlFeCuCr	BCC 2	0.34	288.9	84.1	0.199
	BCC 1	0.55	288.1	84.1	0.198
	FCC	0.10	356.4	25.3	0.476
AlFeCuCrMg$_{0.5}$	BCC	0.23	291.4	81.6	0.205
	Ordered phase	0.71	289.3	71.5	0.222
	Cu$_2$Mg	0.05	701.4	32.2	0.407
AlFeCuCrMg	BCC	0.25	287.3	318.0	0.488
	Ordered phase	0.70	287.9	134.1	0.786
	Cu$_2$Mg	0.06	706.1	152.0	0.145
AlFeCuCrMg$_{1.7}$	BCC	0.21	289.7	173.0	0.127
	Ordered phase	0.66	289.7	39.9	0.333
	Cu$_2$Mg	0.21	709.7	258.0	0.107-

Fig 8.3 shows the phase evolved after heat treatment at 800^{o}C in Ar atmosphere for 4 hours in AlFeCuCrMg$_x$ (x = 0, 0.5, 1, 1.7) alloys.

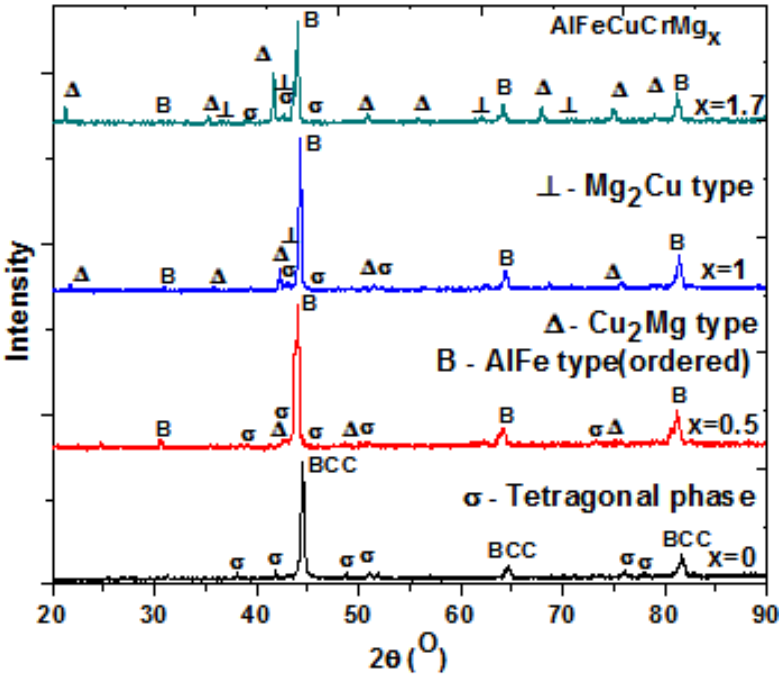

Figure 8.3 XRD patterns of AlFeCuCrMg$_x$ (x = 0, 0.5, 1, 1.7) HEAs after heat treatment at 820^{o}C.

It can be observed that the microstructure after heat treatment is similar to the microstructure evolved after heat treatment at 470^{o}C and 600^{o}C.

Table 8.3 summarizes XRD analysis conducted including the lattice parameter and phase fraction of constituent phases, crystallite size and lattice strain in the sintered AlFeCuCrMg$_x$ (x = 0, 0.5, 1, 1.7) HEA.

Table 8.3 Phase fraction, Lattice parameter, Crystallite size and lattice strain of $AlFeCuCrMg_x$ (x = 0, 0.5, 1, 1.7) HEAs after heat treatment at 820°C.

Composition	Phases	Phase Fraction	Lattice parameter (pm)	Crystallite Size (nm)	Lattice Strain
AlFeCuCr	BCC 2	0.31	288.1	45.4	0.303
	BCC 1	0.65	287.3	72.8	0.218
	FCC	0.02	355.6	-	-
$AlFeCuCrMg_{0.5}$	BCC	0.38	292.3	67.9	0.232
	Ordered phase	0.57	290.7	97.4	0.182
	Cu_2Mg	0.03	704.0	198.3	0.123
AlFeCuCrMg	BCC	0.31	288.6	318.0	0.488
	Ordered phase	0.56	289.1	134.1	0.786
	Cu_2Mg	0.11	709.1	103.9	0.182
$AlFeCuCrMg_{1.7}$	BCC	0.10	293.1	109.7	0.171
	Ordered phase	0.70	290.8	79.3	0.208
	Cu_2Mg	0.22	719.1	154.5	0.145

It is to be noted that in all the heat treatment cycles the nanocrystallinity of the SPSed samples are retained. In spite of this incase of alloys heat treated at 820°C the crystallite size is higher compared to that of alloys heat treated at 470°C and 600°C. This may be due to high supersaturated phases which had been evovlved after SPS, which possesses positive Gibbs free energy. The tendency of a system to lower its Gibbs free energy is driving the processes for an increase in the crystallite size of the phases. The relation between Gibbs free energy change per unit volume, ΔGv, and supersaturation is given by the Eq 8.1[136]

$$\Delta Gv = -[\, kT\, \Omega\,]\ln(C\text{-}Co\,) = -[\, kT\, \Omega\,]\ln(1+\sigma) \qquad (8.1)$$

where C is the concentration of the solute, Co is the equilibrium concentration or solubility, k is the Boltzmann constant, T is the temperature, Ω is the atomic volume and σ is the supersaturation defined by (C − Co)/Co. It can be seen from the relation that Gibbs free energy and supersaturation is dependent on temperature as well as the rate of reaction. The higher temperature leads to the increase in a solubility of the elements and hence lower supersaturation. Also, in all cases of heat treatment of $AlFeCuCrMg_x$ (x = 0, 0.5, 1, 1.7) alloy the lattice parameter of Cu_2Mg phase is constantly shifting towards lower angle side suggesting the compressive stresses present in the lattice due varying atomic radii of each elements [137].

8.1.2 Microstructure of the heat treated $AlFeCuCrMg_x$ HEAs

Fig. 8.4 shows the back scattered electron (BSE) image and chemical composition (inset) of $AlFeCuCrMg_x$ (x = 0, 0.5, 1, 1.7) HEA. In case of AlFeCuCr alloys BSE contrast

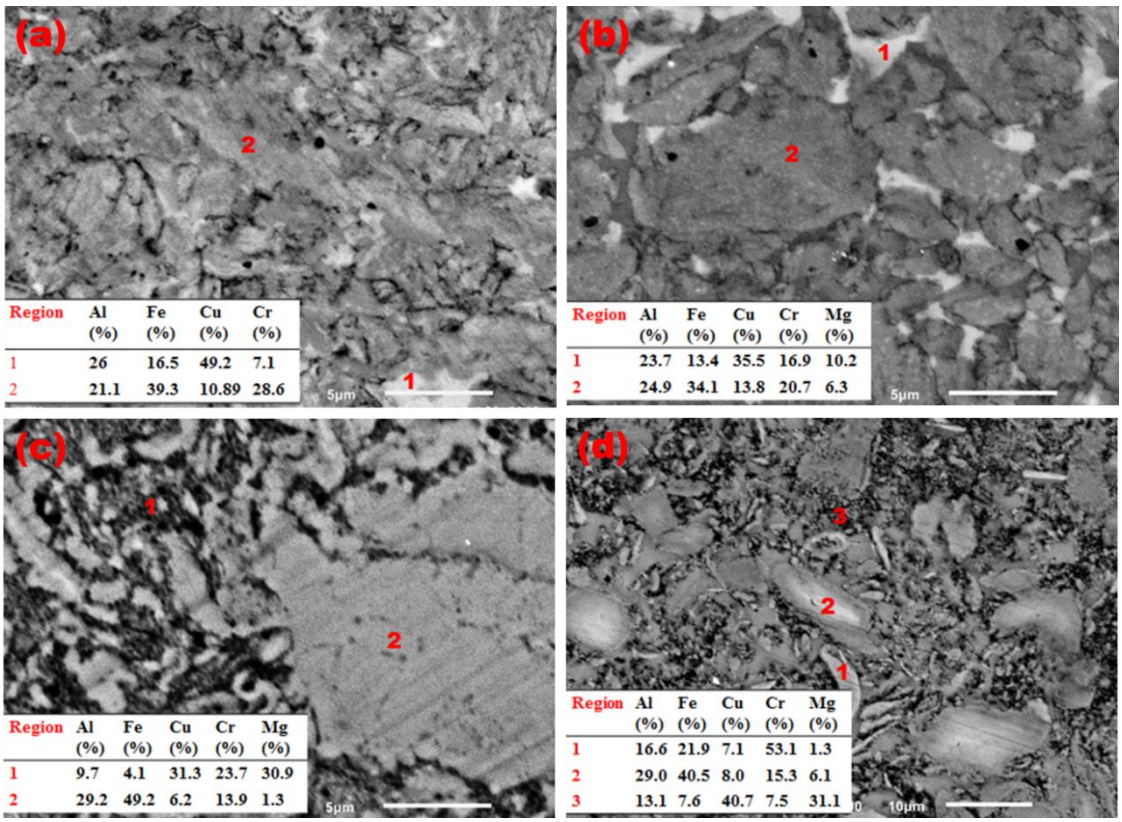

Figure 8.4 BSE micrograph and EDS analysis (inset) of (a) AlFeCuCr (x = 0), (b) $AlFeCuCrMg_{0.5}$ (x = 0.5), (c) AlFeCuCrMg (x = 1), (d) $AlFeCuCrMg_{1.7}$ (x = 1.7) HEAs heat treated at 470°C.

revealed the presence of two phases. EDS results reveal that light grey phase (region '1') is generally richer in Cu and correspond to FCC structure. At lower magnification, white particles were dispersed uniformly in AlFeCuCr HEA. EDS results show that these white particles are WC, which result from the contamination from ball mill. Similarly, in case of $AlFeCuCrMg_{0.5}$ alloy the microstructure constitutes of mainly two regions. Light grey (region '1') corresponds to the Cu rich phase (FCC). The dark grey region (region '2') corresponds to the ordered phase as well as disordered BCC phase. In case of $AlFeCuCrMg_x$ (x = 1, 1.7) alloys the microstructure is similar to that obtained after SPS. The Cu_2Mg and Mg_2Cu form a network like structure and coarse grains correspond to the ordered and BCC structure.

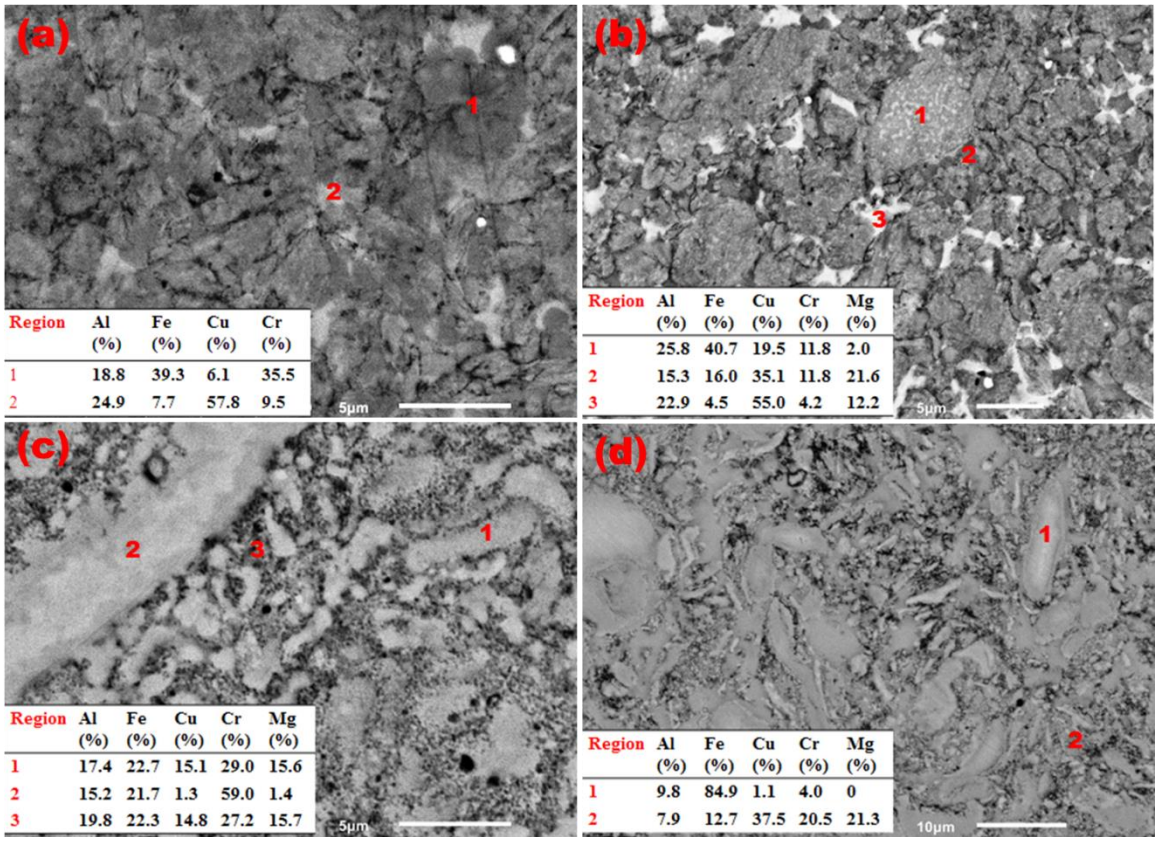

Figure 8.5 BSE micrograph and EDS analysis (inset) of (a) AlFeCuCr (x = 0), (b) $AlFeCuCrMg_{0.5}$ (x = 0.5), (c) AlFeCuCrMg (x = 1), (d) $AlFeCuCrMg_{1.7}$ (x = 1.7) HEAs heat treated at 600°C.

In case of heat treated $AlFeCuCrMg_x$ (x = 0, 0.5, 1, 1.7) alloys at 600°C the microstructures evolved have been observed similar to the microstructure obtained when

heat treated at 470^{o}C (see Fig 8.5). The white particles observed are dispersed in a microstructure, which are the WC contamination due to the milling conditions.

Similar microstructure has been observed after heat treatment at 820^{o}C for 4 hours (Fig. 8.6). In case of AlFeCuCrMg$_x$ (x = 0, 0.5) alloys having two phase structure region '1' is ordered as well as BCC phase and region '2' having a Cu rich FCC type structure.

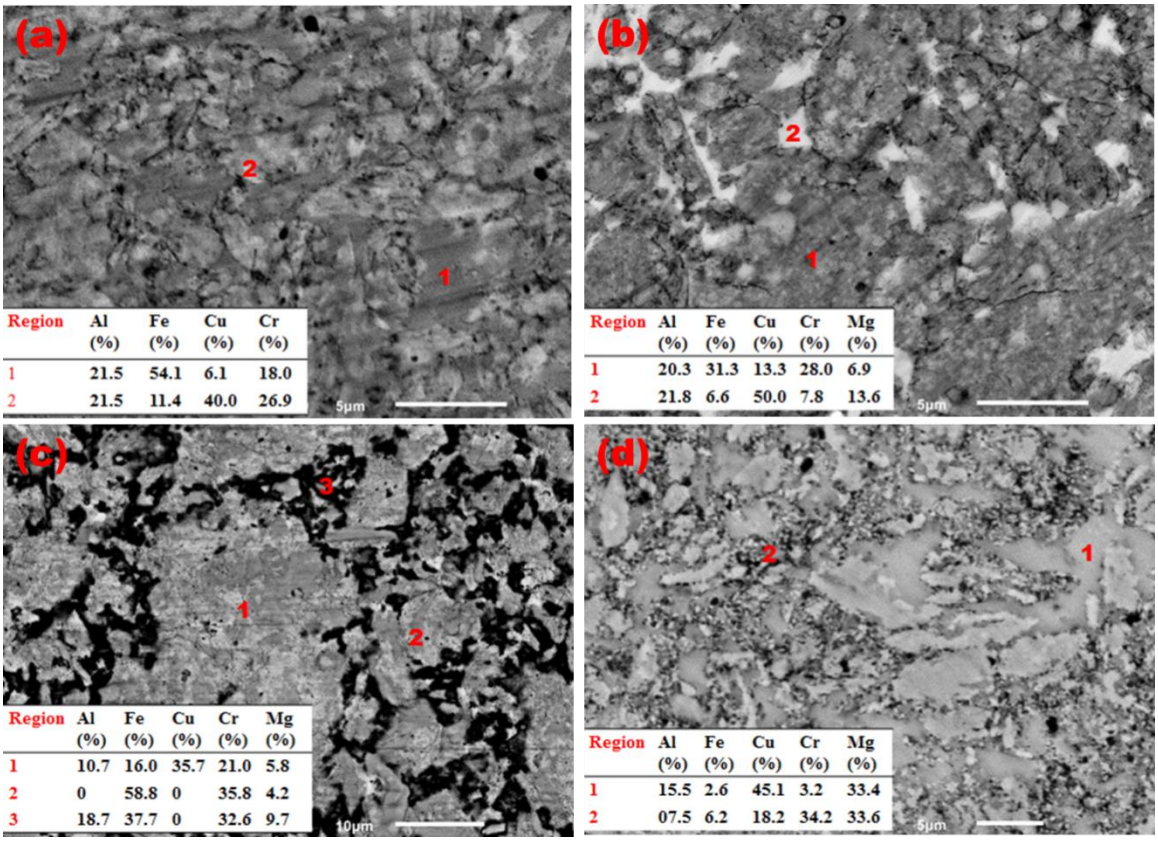

Figure 8.6 BSE micrograph and EDS analysis (inset) of (a) AlFeCuCr (x = 0), (b) AlFeCuCrMg$_{0.5}$ (x = 0.5), (c) AlFeCuCrMg (x = 1), (d) AlFeCuCrMg$_{1.7}$ (x = 1.7) HEAs heat treated at 820^{o}C.

On the other hand AlFeCuCrMg$_x$ (x = 1, 1.7) alloys have coarse grains having ordered as well as BCC structure and the network like structure constituting of Cu_2Mg phase.

It is to be noted that the decomposition temperature of Fe-Cr σ phase is at 820^{o}C. In order to determine the effect of high temperature (820^{o}C) on the precipitates TEM is performed on equiatomic AlFeCuCrMg alloy.

8.1.3 Transmission Electron Microscopy

The sub-micron characterization of AlFeCuCrMg alloy by TEM was performed to observe the effect of high temperature heat treatment on the microstructure and tetragonal precipitates in case of AlFeCuCrMg (see Fig 8.7) alloys.

The bright field image (Fig 8.7(a)) of AlFeCuCrMg HEA reveals the formation of grains of ordered phase, and disordered BCC phase having the grain size of 700 nm.

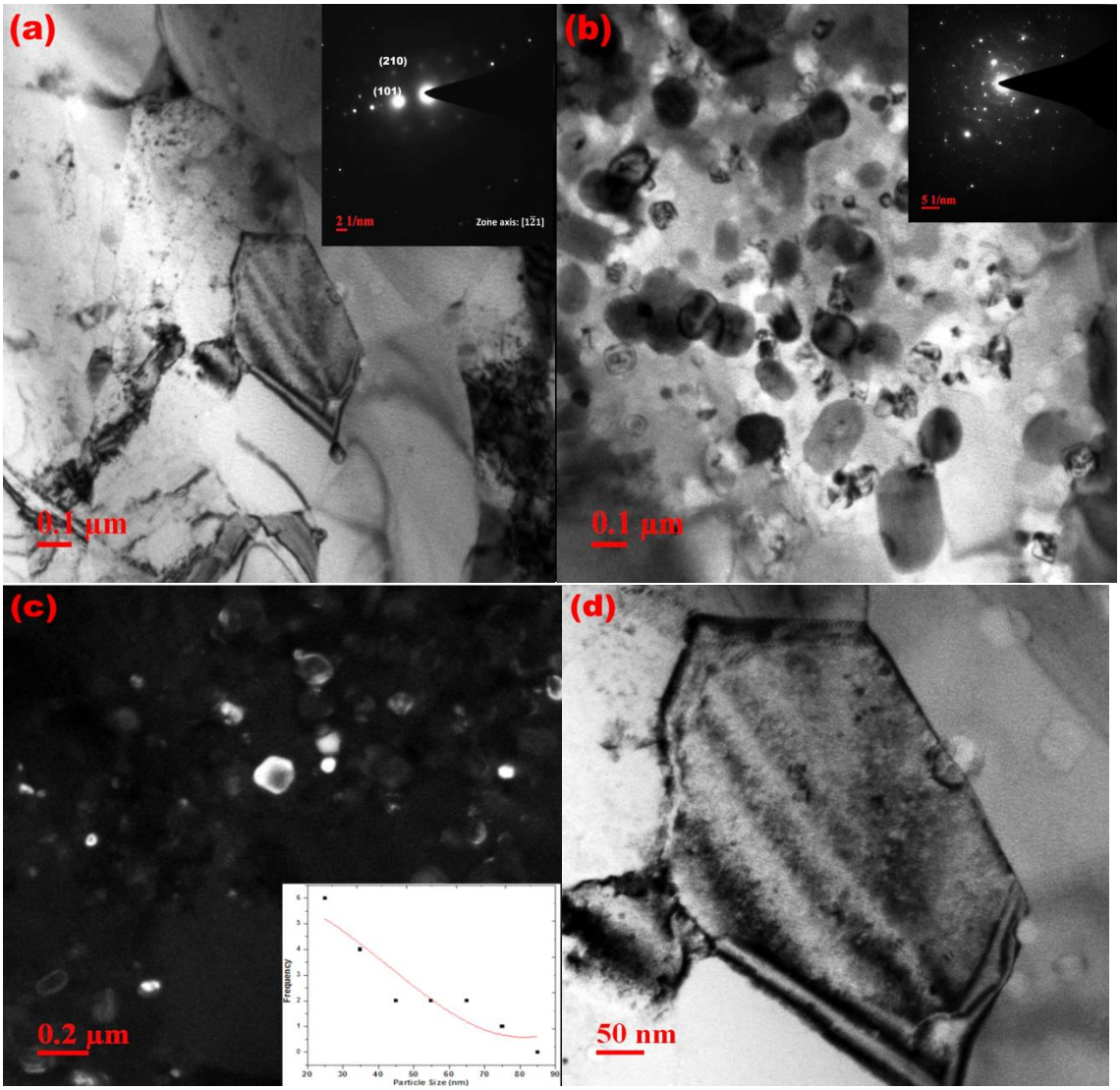

Figure 8.7 TEM image of heat treated (820°C) AlFeCuCrMg alloy, (a) Bright field image and SAED pattern (inset), (b) Bright field image and SAED pattern (inset) corresponding to Cu_2Mg phase (c) TEM dark field (d) spinodal decomposition image of AlFeCuCr Mg HEAs

Bright field image (Fig. 8.7(b)) shows that Cr rich tetragonal phase precipitates; a cubic Cu_2Mg type phase is retained after the heat treatment. Fig. 8.7(c) shows the dark field

image of the precipitate phase, which suggests a size of 25 nm to 90 nm and average precipitate size of 25 nm. Fig. 8.7(d) shows the presence of probable spinodal decomposition in the BCC phase

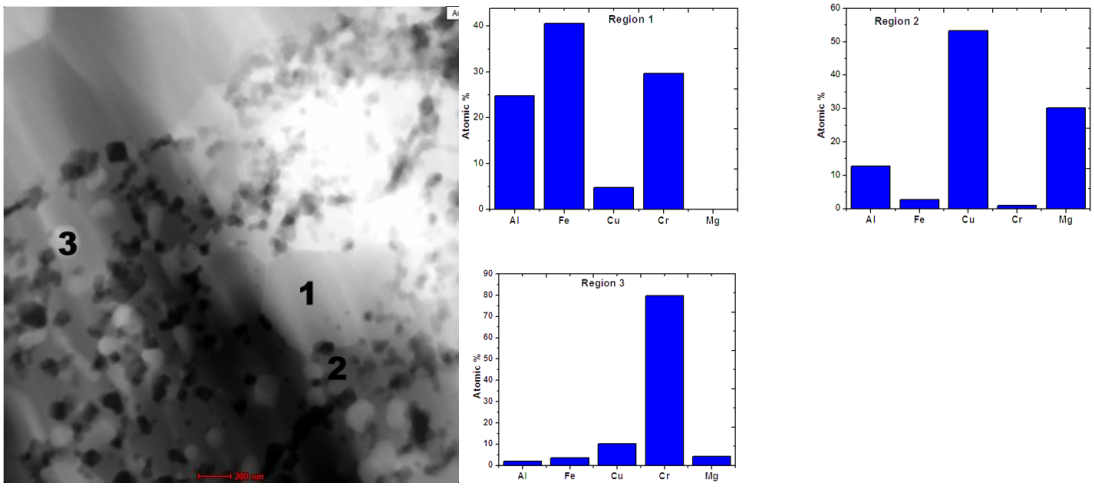

Figure 8.8 STEM image of heat treated AlFeCuCrMg alloy and corresponding EDS point analysis of corresponding regions

Fig 8.8 shows STEM image and the corresponding EDS mapping of AlFeCuCrMg alloy. The map shows smaller precipitates are Cr rich and the grains are rich in Fe, Cr and Al. The regions surrounding the precipitates are rich in Cu and Mg suggesting that the Cr rich precipitates are nucleated in the Cu_2Mg phase.

8.1.4 Density Measurement

The experimental bulk density after the SPS and heat treatment is shown in Table 8.4. The bulk density after the heat treatment is calculated by Archimedes's principle.

For the alloys heat treated at 470^{o}C for 4 hours a slight increase in density is observed for $AlFeCuCrMg_x$ (x = 0, 0.5, 1) alloys compared to the SPSed alloys (see Table 8.4). However, the density of $AlFeCuCrMg_{1.7}$ alloys decreases when it is heat treated at 470^{o}C.

Table 8.4 Experimental bulk density before and after heat treatment in $AlFeCuCrMg_x$ (x = 0, 0.5, 1, 1.7) HEAs

Composition	After SPS (g/cm^3)	HT at 470°C (g/cm^3)	HT at 600°C (g/cm^3)	HT at 820°C (g/cm^3)
AlFeCuCr	6.091	6.215	6.211	6.212
$AlFeCuCrMg_{0.5}$	5.790	6.016	5.944	5.862
AlFeCuCrMg	5.367	5.474	5.470	5.468
$AlFeCuCrMg_{1.7}$	4.910	4.857	4.751	4.731

The increase in the density for $AlFeCuCrMg_x$ (x = 0, 0.5, 1) alloys may be attributed to the removal of defects in the alloys at 470°C, and thus increasing the mass of the alloys and higher density [138]. Although in case of $AlFeCuCrMg_{1.7}$ alloys the decrease in the density may be due to the melting of small fraction of Mg_2Cu phase present in these alloys.

For heat treatment at higher temperatures i.e. 600°C and 820°C it can be observed that density of AlFeCuCr is same as when heat treated at 470°C. Although, small decrease in the density in Mg containing $AlFeCuCrMg_x$ (x = 0.5, 1) alloys is seen. This may be due to the thermal expansion in the crystal lattice and the release of the internal stresses [126] in the lattice which increases volume of the cell and thus the density decreases. In case of $AlFeCuCrMg_{1.7}$ alloys there is a substantial decrease in the density (approx. 3% of the density after SPS) which is due to the melting of higher fraction Mg_2Cu phase.

8.1.5 Hardness Measurement

Vickers hardness measurements were performed on $AlFeCuCrMg_x$ (x = 0, 0.5, 1, 1.7) HEAs with load of 200 gf and dwell time at 15 sec. The results are plotted against Mg content in Fig 8.9.

Maximum hardness of 1000 ± 30.2 HVN was attained by $AlFeCuCrMg_{0.5}$ alloy heat treated at 470°C. It is to be noted that for AlFeCuCr alloy the hardness is almost same for whole temperature range which can be correlated to the similar density obtained for these alloys with respect to different heat treatment temperatures. Moreover, for $AlFeCuCrMg_x$

(x = 0.5, 1) alloys the hardness decreases as the heat treatment temperature increases from 470°C to 820°C.

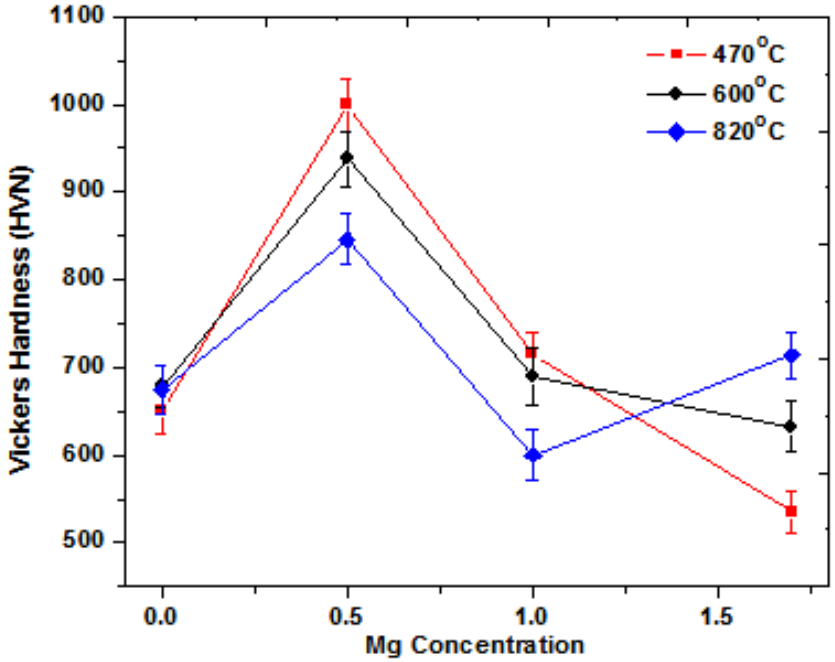

Figure 8.9 Hardness of AlFeCuCrMgx (x = 0, 0.5, 1, 1.7) HEAs after heat treatment at 470°C, 600°C, and 820°C.

This may be attributed to the increase in the removal of internal stresses and the decrease in the dislocation density. It is interesting to note that for $AlFeCuCrMg_{1.7}$ alloys the hardness increases from 535 ± 25.3 HVN to 714 ± 27.8 HVN. This is due to the melting of Mg_2Cu phase which further increases the phase fraction of harder phase such as ordered and brittle σ phases.

8.2 Materials-Structure-Processing-Property correlation after heat treatment

The phase evolved after heat treatment of AlFeCuCr alloys at 470°C, 600°C and 820°C suggests that along with the two BCC phases (BCC 1 and BCC 2, see chapter 2) evolved after SPS the heat treatment of these alloys leads to the nucleation and growth of a Cu rich FCC phase. The decomposition of the Cu rich phase may be thermodynamically explained due to the high positive enthalpy between Fe-Cu and Cr-Cu. High positive enthalpy drives the Cu atoms to diffuse and nucleate on the grain boundaries of the BCC 1 and BCC 2 phases. Further, grain growth of the nucleated particle follows the power

law relationship showing the kinetics for normal grain growth and is as given by Eq. 8.1[139]

$$D^n - D_o^n = Kt \qquad (8.1)$$

where D is a grain diameter at time t, D_o is the grain diameter at time t= 0, K is the grain growth constant, and n is the grain growth exponent. The diffusion kinetics may be driven by primarily due to the intergranular diffusion of the Cu particles on the boundary and then different particles connecting to a grain boundary network (Fig 8.10)

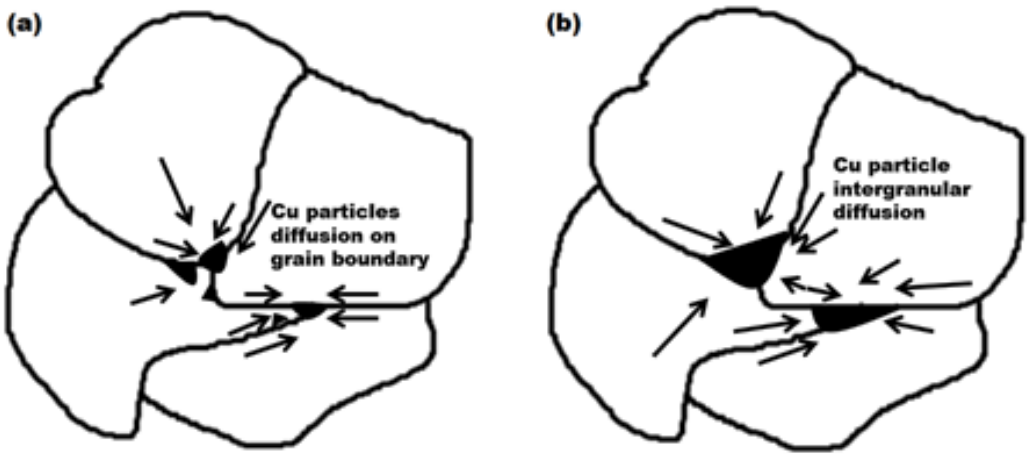

Figure 8.10 Schematic of (a) Ostwald ripening process in alloys(b) coalescence

Similarly in case of $AlFeCuCrMg_{0.5}$ alloys the Cu rich FCC grains along with small fraction of Cu_2Mg has been formed. The phase fraction of FCC phase in these alloys are calculated by ImageJ software and is found to be 3.3 %, 6.1 % and 9.6 % for heat treatment cycles 470^{o}C, 600^{o}C and 820^{o}C respectively. It is interesting to note that as the heat treatment temperature increases the fraction of FCC phases in these alloys increases, which may be attributed to the higher positive enthalpy of mixing (4.04 kJ/mol) compared to AlFeCuCr (0.50 kJ/mol), which drives the more Cu atoms to diffuse through the BCC phase and decompose at the grain boundary.

In case of $AlFeCuCrMg_x$ (x = 1, 1.7) alloys the FCC phase has not been found. Instead the microstructure is similar to that obtained after SPS. This may be explained due to the higher Mg content which favors the formation of Cu_2Mg phase rather than FCC Cu rich phase. The Cu_2Mg phase in the microstructure forms the network like structure while coarse grains constitute of ordered as well as BCC structure.

The TEM analysis of equiatomic AlFeCuCrMg alloys heat treated at 820^{o}C reveals that there is small fraction of spinodal decomposition (Fig. 8.7(d)) in the grains corresponding to the BCC phases which may be due to the miscibility gap formed between the elements. Previous studies suggested that on FeCr alloys the spinodal decomposition is predominant on aging at higher temperatures [139]. The mechanism of decomposition can be explained as compositional fluctuation wavelength, λ, and regions of different composition concentration forms which is derived by the miscibility gap and also the rate of these decomposition is very slow [140]. Also, similar to the SPSed alloys in this case also precipitation of Cr-rich precipitates are formed in the Cu_2Mg due to high positive heat of formation between Mg-Cr and Cu-Cr.

Except for $AlFeCuCrMg_{1.7}$ alloy hardness values for heat treated $AlFeCuCrMg_x$ (x = 0, 0.5, 1) alloys follows the same pattern as that in SPSed samples. Thus, it can be predicted that in these alloys the primary strengthening is due to the combined effects of grain size strengthening, solid solution hardening, and precipitation hardening. Further, these alloys show that in all cases the hardness value of $AlFeCuCrMg_{0.5}$ is the highest. In the case of $AlFeCuCrMg_{1.7}$alloy, the higher hardness is due to the melting of Mg_2Cu phase leading to the increase in the fraction of brittle phases.

To conclude the results, heat treatment of $AlFeCuCrMg_x$ (x = 0, 0.5, 1, 1.7) alloys are performed at 470^{o}C, 600^{o}C and 820^{o}C for 4 hours in Ar atmosphere. The phase evolution shows the formation of additional minor FCC phase present in $AlFeCuCrMg_x$ (x = 0, 0.5) alloys. On the other hand, the $AlFeCuCrMg_x$ (x = 1, 1.7) alloys have a similar microstructure as of SPSed alloys. The hardness of the $AlFeCuCrMg_x$ (x = 0, 0.5, 1) alloys decreases with the increase in the heat treatment temperature due to the thermal expansion of the crystal lattice and removal of internal stresses. For $AlFeCuCrMg_{1.7}$ alloys the hardness value increases due to removal of Mg_2Cu phase and increase in the fraction of brittle phases.

Chapter 9

Conclusions and Suggestions for Future Work

The research work on synthesis and characterization of light weight HEAs has been carried out. Based on the finding from density, phase evolution, phase stability with respect to temperature and hardness, the following conclusions can be made.

- Novel $AlFeCuCrMg_x$ (x = 0, 0.5, 1, 1.7 moles) HEAs were prepared by solid state processing route.
- Phase analysis of as milled $AlFeCuCrMg_x$ alloys indicates the formation of major BCC phase with minor FCC fraction in case of AlFeCuCr and $AlFeCuCrMg_{0.5}$ HEAs. AlFeCuCrMg and $AlFeCuCrMg_{1.7}$ alloy powders have two BCC phases i.e. BCC 1 and BCC 2. Phase fraction of BCC 2 is found out to be 27.45% and 34.06% for AlFeCuCrMg and $AlFeCuCrMg_{1.7}$ respectively.
- Even with a high enthalpy of mixing (ΔH_{mix}), the formation of solid solution is being observed due to the combined effect of severe plastic deformation during the mechanical alloying and sluggish diffusion. Moreover, calculated thermodynamic parameters suggest that $AlFeCuCrMg_x$ alloys powders synthesized by MA do not follow criteria given for the formation of a single phase solid solution.
- From the phase analysis, it can be concluded that the addition of Mg enhances the probability of formation of BCC structure.
- Local atomic environment study of as-milled $AlFeCuCrMg_x$ alloy powder shows that bond length distribution in Fe and Cr K-edge EXAFS measurements is in favor of the formation of majorly BCC phase however although Cu K-edge data have shown formation of some copper oxide (CuO) phases in $AlFeCuCrMg_x$ alloys. Also with increase in the Mg content, the fraction of CuO phase decreases.
- As-milled $AlFeCuCrMg_x$ (x = 0.0, 0.5, 1, 1.7) alloy powders have been compacted successfully by spark plasma sintering.
- The microstructure of bulk-sintered AlFeCuCr consisted of two BCC phases and a small quantity of σ-phase. As the Mg content increased from x = 0.5 to x = 1.7, the microstructure was composed of predominately AlFe-type ordered structure, BCC phase,

and Cu_2Mg laves phase, with metastable Cr-rich σ-phase precipitates. The formation and growth of Cr-rich precipitates in Cu_2Mg phase in case of $AlFeCuCrMg_x$ (x = 0.5, 1, 1.7) HEA is reasoned to be the effect of high positive enthalpy between the binary elements.

- A peak hardness value has been achieved for the $AlFeCuCrMg_{0.5}$ HEA due to a combined effect of solid solution hardening, grain boundary hardening, and the precipitation
- Phase evolved after sintering, in addition to that based on the criterions for formation of solid solution in HEAs suggests that addition of Mg in HEAs leads to the formation of intermetallic compounds. Also, the fraction of intermetallic compounds increases with the increase in the Mg concentration. The strength in these alloys has been found to mainly due to grain size effect, solid solution strengthening, and precipitation hardening.
- Mg was found to decrease the phase stability from above 1000^oC for the AlFeCuCr alloy to 800^oC for $AlFeCuCrMg_x$ (x = 0, 0.5, 1) and 450^oC for $AlFeCuCrMg_{1.7}$.
- An attempt has been made to synthesize AlMgCaNiCu & $(AlMgCa)_{1.33}(NiCu)_{0.5}$ HEAs by MA and SPS which were physically disintegrated mainly because of the formation of $Ca(OH)_2$ and CaO phases during MA and sintering.
- Conventional Sintering of $AlFeCuCrMg_x$ (x = 0.5, 1) alloys shows the evolutionof multi-phase microstructure having AlFe-type ordered structure, BCC phase, and Cu_2Mg laves phase and MgO.
- Sub-micron characterization of $AlFeCuCrMg_x$ (x = 0.5, 1) alloys shows the presence of spinodal decomposition in the microstructure. However, for $AlFeCuCrMg_{1.7}$ alloys the sub-micron characterization shows the formation of Cr_7C_3 precipitates in Cu_2Mg phase and the microstructure does not constitute the spinodal decomposition.
- A peak hardness value has been achieved for the $AlFeCuCrMg_{1.7}$ HEA due to a combined effect of solid solution hardening, grain boundary hardening, and the precipitation hardening.
- Heat treatment of $AlFeCuCrMg_x$ (x = 0, 0.5, 1, 1.7) alloys are performed at 470^oC, 600^oC and 820^oC for 4 hours in Ar atmosphere. The phase evolution shows the formation of additional minor FCC phase present in $AlFeCuCrMg_x$ (x=0, 0.5) alloys. On the other hand, the $AlFeCuCrMg_x$ (x = 1, 1.7) alloys have a similar microstructure as of SPSed alloys.

- The hardness of the $AlFeCuCrMg_x$ (x = 0.5, 1) alloys decreases after heat treatment at 820^oC due to the thermal expansion of the crystal lattice and removal of internal stresses. For $AlFeCuCrMg_{1.7}$ alloys the hardness value increases due to melting and removal of Mg_2Cu phase and an increase in the fraction of brittle phases.
- The present studies suggest that these alloys may have a potential usage in high temperature application and application requiring high wear resistance. However, further studies on the mechanical properties can give a better idea on the applications of these alloys.

Suggestions for Future Work

Thus based on the conclusion following work on $AlFeCuCrMg_x$ and Ca containing alloys can be done in the future.

- Some computational work is required to design and develop a Cu free light weight HEAs.
- EXAFS studies on the Al K-edge and Mg K-edge can be studied to get more detailed information about the crystal structure of as milled $AlFeCuCrMg_x$ HEAs.
- More studies on the contamination content in the bulk alloys will provide the potential application of these HEAs.
- More studies on the milling and sintering parameters to successfully synthesize Ca based HEAs would be required.
- Detailed studies on the segregation and spinodal decomposition of conventionally sintered $AlFeCuCrMg_x$ HEAs would be useful.
- Detailed TEM studies of the heat treated $AlFeCuCrMg_x$ alloys to understand the diffusion kinetics in $AlFeCuCrMg_x$ HEAs can be important.
- Studies on the mechanical properties such as tensile strength, compressive strength, wear and fracture behavior of $AlFeCuCrMg_x$ HEAs can be taken up.
- Suitable coating method may be selected to coat these alloys on various substrates.
- Oxidation study of the proposed HEAs may be performed to suggest its high temperature application as a coating material.
- Extensive corrosion study may also be performed with varying chloride concentration.

References

[1] F.C. Campbell, Lightweight Materials: Understanding the Basics,ASM International, Materials Park, OH, 2012

[2] V. Kumar, Govind, R. Shekhar, R. Balasubramaniam, K. Balani, Microstructure evolution and texture development in thermomechanically processed Mg–Li–Al-basedalloys, Mater. Sci. Eng. A, Vol. 547, 2012, 38-50

[3] V. Kumar, A. Gupta, D. Lahiri, K. Balani, Serrated yielding during nanoindentation of thermo mechanically processed novel Mg–9Li–7Al–1Sn and Mg–9Li–5Al–3Sn–1Zn alloys, J. Phys. D: Appl. Phys., Vol. 46, 2013, 145304-1-145304-8.

[4] I. J. Polmear, Light alloys: Metallurgy of the light metals (Metallurgy and materials science), ASM International, Materials Park, OH, 1982.

[5] M. M. Avedesian, Hugh Baker, Magnesium and Magnesium Alloys, ASM International,Materials Park, OH, 1999.

[6] A.H. Musfirah, A.G. Jaharah, Magnesium and Aluminum Alloys in Automotive Industry, J. Appl. Sci. Res., Vol. 8(9), 2012, 4865-4875.

[7] J. W. Yeh, S. K. Chen, S. J. Lin, J. Y. Gan, T. S. Chin, T. T. Shun, C. H. Tsau, S. Y. Chang, Nanostructured high-entropy alloys with multiple principal elements: novel alloy design concepts and outcomes, Adv. Eng. Mater.,Vol. 6, 2004, 299–303.

[8] P. Wang, H. Cai, X. Cheng, Effect of Ni/Cr ratio on phase, microstructure and mechanicalproperties of $Ni_xCoCuFeCr_{2x}$ (x = 1.0, 1.2, 1.5, 1.8 mol) high entropy alloys, J.Alloy. Comp.,Vol. 662, 2016, 20-31

[9] B. S. Murty, J. W. Yeh, S. Ranganathan, High-Entropy Alloy, Elsevier Inc., London, 2014.

[10] Y. Zhang, T. T. Zuo, Z. Tang, M. C. Gao, K. A. Dahmen, P. K. Liaw, Z. P. Lu, Microstructure and properties of high-entropy alloy, Prog. Mater. Sci., Vol. 61, 2014, 1-93.

[11] J. Joseph, T. Jarvis, X. Wu, N. Stanford, P. Hodgson, D. M. Fabijanic, Comparative study of the microstructures and mechanical properties of direct laser fabricated and arc-melted $Al_xCoCrFeNi$ high entropy alloys, Mater. Sci. Eng. A, Vol. 633, 2015, 184-193.

[12] E. Ma, Dissolving Equilibrium-Immiscible Elements via Severe Plastic Deformation, Mater. Trans., Vol. 47, 2006, 1269-1274.

[13] A.C. Reardon, Metallurgy for the Non-Metallurgist, 2nd Edition, ASM International, 2011

[14] M. H. Tsai, J. W. Yeh, High-Entropy Alloys: A Critical Review, Mater. Res. Lett., Vol. 2, 2014, 107-123.

[15] B. Cantor, I. T. H. Chang, P. Knight, A. J. B. Vincent, Microstructural development in equiatomic multicomponent alloys, Mater. Sci. Eng. A, Vol. 375-377, 2004, 213-218.

[16] S. Guo, C. T. Liu, Phase stability in high entropy alloys: formation of solid solution phase and amorphous phase, Prog. Nat. Sci.: Mater. Int., Vol.211 (21), 2015, 433–446.

[17] C. J. Tong, M. R. Chen, J. W. Yeh, S. J. Lin, S. K. Chen, T. T. Shun, S. Y. Chang, Mechanical performance of the Al_xCoCrCuFeNi high-entropy alloy system with multiprincipal elements, Metall. Mater. Trans. A, Vol. 36 (5), 2005, 1263-1271.

[18] F. Otto, A. Dlouhy, Ch. Somsen, H. Bei, G. Eggeler, E. P. George, The influences of temperature and microstructure on the tensile properties of a CoCrFeMnNi high-entropy alloy, Acta Mater., Vol. 61 (15), 2013, 5743-5755.

[19] J. W. Yeh, Recent progress in high entropy alloy, Ann. Chim. Sci. Mat., Vol. 31 (6), 2006, 633-648.

[20] K.B. Zhang, Z.Y. Fu, J.Y. Zhang, J. Shi, W.M.Wang, H. Wang, Y.C.Wang, Q.J. Zhang, Nanocrystalline CoCrFeNiCuAl high-entropy solid solution synthesized by mechanical alloying, J. Alloys Comp., Vol. 485, 2009, L31–L34.

[21] H. P. Chou, Y. S. Chang, S. K. Chen, J. W. Yeh, Microstructure, thermophysical and electrical properties in Al_xCoCrFeNi ($0 \leq x \leq 2$) high-entropy alloys, Mater. Sci. and Eng. B, Vol. 163, 2009, 184–189.

[22] F. Otto, Y. Yang, H. Bei, E. P. George, Relative effects of enthalpy and entropy on the phase stability of equiatomic high-entropy alloys, Acta Mater. Vol. 61(7), 2013, 2628–2638.

[23] D. B. Miracle, O. N. Senkov, A critical review of high entropy alloys and related concepts, Acta Mater., 2016, 1-64, *In Press*

[24] J. W. Yeh, Alloy design strategies and future trends in high-entropy alloys, J. Met., Vol. 65, 2013, 1759-1771.

[25] B. Gludovatz, A. Hohenwarter, K. V. S. Thurston, H. Bei, Z. Wu, E. P. George, R. O. Ritchie, Exceptional damage-tolerence of a medium-entropy alloy CrCoNi at cryogenic temperatures, Nat. Comm., Vol. 7, 2015, 1-8.

[26] A. Gali, E. P. George, Tensile properties of high- and medium- entropy alloys, Intermetallics, Vol. 39, 2013, 74-78.

[27] J. W. Yeh, Y. L. Chen, S. J. Lin, S. K. Chen, High-entropy alloys – A new era of exploitation, Mater. Sci. Forum Vol. 560, 2007, 1-9.

[28] J. W. Yeh et al., Formation of simple crystal structures in Cu–Co–Ni–Cr–Al–Fe–Ti–V alloys with multiprincipal metallic elements, Metall. Mater. Trans. A, Vol. 35 (8), 2004, 2533–2536.

[29] J. W. Yeh, S. Y. Chang, Y. D. Hong, S. K. Chen, S. J. Lin, Anomalous decrease in X-ray diffraction intensities of Cu-Ni-Al-Co-Cr-Fe-Si alloy systems with multi-principal elements, Mater. Chem. Phys., Vol. 103, 2007, 41-46.

[30] K.Y. Tsai, M. H. Tsai, J. W. Yeh, Sluggish diffusion in Co-Cr-Fe-Mn-Ni high entropy alloys. Acta Mater., Vol. 61, 2013, 4887-4897.

[31] K. Kulkarni, G. P. S. Chauhan, Investigation of quaternary interdiffusion in a constituent system of high entropy alloys, AIP Adv., Vol. 5, 2015, 097162 1-7

[32] S. Ranganathan, Alloyed pleasures: multimetallic cocktails, Curr. Sci., Vol. 85, 2003, 1404-1406.

[33] C. J. Tong et al., Microstructure characterization of Al_xFeCuCrCoNi high entropy alloy system with multiprincipal elements, Metall. Mater. Trans. A, Vol. 36, 2005, 881-893.

[34] Y. F. Kao, T. J. Chen, S. K. Chen, J. W. Yeh, Microstructure and mechanical property of As-cast, homogenized, and deformed Al_xCoCrFeNi ($0 \leq x \leq 2$) high-entropy alloys, J. Alloy. Compd., Vol. 488, 2009, 57–64.

[35] Y. Zhang, Y. J. Zhou, J. P. Lin, G. L. Chen, P. K. Liaw, Solid-solution phase formation rules for multi-component alloys, Adv. Eng. Mater., Vol. 10(6), 2008, 534–538.

[36] S. Guo, Q. Hu, C. Ng, C. T. Liu, More than entropy in high-entropy alloys: forming solid solutions or amorphous phase, Intermetallics, Vol. 41, 2013, 96-103.

[37] K. B. Zhang, Z. Fu, Effects of annealing treatment on phase composition and microstructure of $CoCrFeNiTiAl_x$ high-entropy alloys, Intermetallics, Vol. 22, 2012, 24–32.

[38] X. Yang, Y. Zhang, Prediction of high-entropy stabilized solid-solution in multicomponent alloys, Mater. Chem. Phys., Vol. 132, 2012, 233-238.

[39] Y. Zhang, X. Yang, P. K. Liaw, Alloy design and properties optimization of high entropy alloys, JOM, Vol. 64, 2012, 830-838.

[40] Y. Dong, Y. Lu, L. Jiang, T. Wang, T. Li, Effects of electronegativity on the stability of topologically closed packed phase in high entropy alloy, Intermetallics, Vol. 52, 2014, 105-109.

[41] Y. Lu, Y. Dong, L. Jiang, T. Wang, T. Li, Y. Zhang, A criterion for topological closed-packed phase formation in high entropy alloys, Entropy, Vol. 17, 2015, 2355-2366.

[42] M. Morinaga, N. Yukawa, H. Adachi, Superalloys. New PHACOMP and its application to alloy design, Proceedings of the Fifth International Symposium Superalloys (1984), Seven Springs, PA, USA, 7–11 October 1984.

[43] Z.J. Wang, W.F. Qiu, Y. Yang, C.T. Liu, Atomic-size effects in crystalline lattices with multiple principal elements, Intermetallics, Vol. 64, 2015, 63-69.

[44] O.N. Senkov, D.B. Miracle, A New Thermodynamic Parameter to Predict Formation of Solid Solution or Intermetallic Phases in High Entropy Alloys, J. Alloy Compd.,Vol. 658, 2015, 603-607.

[45] Y.F. Ye, Q. Wang, J. Lu, C. T. Liu, Y. Yang, Design of high entropy alloys: A single-parameter thermodynamic rule, Scripta Mater., Vol. 104, 2015, 53–55.

[46] I. Toda-Caraballo, J. S. Wrobel, S. L. Dudarev, D. Nguyen-Manh, P. E. J. Rivera-Diaz-del-Castillo, Interatomic spacing distribution in multicomponent alloys, Acta Mater., Vol. 97, 2015, 156–169.

[47] I. Toda-Caraballo, P. E. J. Rivera-Díaz-del-Castillo, A criterion for the formation of high entropy alloys based on lattice distortion, Intermetallics , Vol. 71, 2016, 76-87.

[48] S. Guo, C. Ng, J. Lu, C. T. Liu, Effect of valence electron concentration on stability of fcc and bcc phases in high entropy alloy, J. Appl. Phys., 2011, Vol. 109, 103505-1-103505-2.

[49] M. H. Tsai, K.Y. Tsai, C. W. Tsai, C. Lee, C. C. Juan, J. W. Yeh, Criterion for sigma phase formation in Cr- and V- containing high-entropy alloys, Mater. Res. Lett., Vol. 1, 2013, 207-212.

[50]M. G. Poletti, L. Battezzati, Electronic and thermodynamic criteria for the occurrence of high entropy alloys in metallic systems, Acta. Mater., 2014,Vol. 75, 297-306.

[51] M. Laurent-Brocq, L. Perriere, R, Pir`es, Y. Champion, From high entropy alloys to diluted multi-component alloys: Range of existence of a solid-solution, Mater. Design, Vol. 103, 2016, 84-89.

[52] A. Takeuchi, K. A. Amiya, T. Wada, K. Yubuta,Alloy design for high-entropy alloys based on Pettifor map for binary compounds with 1:1 stoichiometry, Intermetallics, Vol. 66, 2015, 56-66.

[53] J. Hafner, The Structures of Binary Compounds, North-Holland Sole Distributors for the USA and Canada, Elsevier Science Pub. Co., 1989.

[54] S. Singh, N. Wanderka, B. S. Murty, U. Glatzel, J. Banhart, Decomposition in multi-component AlCoCrCuFeNi high-entropy alloy, Acta Mater., Vol. 59, 2011, 182–190.

[55] O. N. Senkov,G. B. Wilks, D. B. Miracle, C. P. Chuang, P. K . Liaw, Refractory high-entropy alloys, Intermetallics, Vol. 18(9), 2010, 1758–65.

[56] C. Li, J. C. Li, M. Zhao, Q. Jiang, Effect of alloying elements on microstructure and properties of multiprincipal elements high entropy alloys, J. Alloy Compd., Vol. 475, 2009, 752–757.

[57] H. Cui, H. Wang, J. Wang., H. Fu, 2011a. Microstructure and micro segregation in directionally solidified FeCoNiCrAl high entropy alloy. Adv. Mater. Res., Vol. 189-193, 2011, 3840-3843.

[58] S. G. Ma, S. F. Zhang, M. C. Gao, P. K. Liaw, Y. Zhang, A successful synthesis of the $CoCrFeNiAl_{0.3}$ single-crystal, high-entropy alloy by Bridgman solidification, JOM,Vol. 65, 2013, 1751-1758.

[59] B. A. Welk, R. E. A. Williams, G. B. Viswanathan, M. A. Gibson, P. K. Liaw, H. L. Fraser, Nature of the interfaces between the constituent phases in the high entropy alloy CoCrCuFeNiAl, Ultramicroscopy, Vol. 134, 2013, 193-199.

[60] V. Ocelik, N. Janssen, S. N. Smith, J. Th. M. De Hosson, Additive Manufacturing og high entropy alloys by laser processing, JOM, Vol. 68(7), 2016, 1810-1818.

[61] S. Chen, X. Chen, L. Wang, J. Liang, C. Liu, Laser cladding FeCrCoNiTiAl highentropy alloys coating reinforced with self-generated TiC particles, J. Laser Appl., Vol. 29 (1), 2016, 012004-1-8.

[62] C. Suryanarayan, Mechanical alloying and milling, Prog. Mater. Sci., Vol. 46, 2001, 1-184.

[63] S. Varalakshmi, M. Kamaraj, B. S. Murty, Synthesis and characterization of nanocrystalline AlFeTiCrZnCu high entropy solid solution by mechanical alloying. J. Alloy Compd., Vol. 460, 2008, 253-257.

[64] M. Omori, Sintering, consolidation, reaction and crystal growth by the spark plasma system (SPS), Mater. Sci. Eng. A 287 (2000) 183-188.

[65] N. Saheb, Z. Iqbal, A. Khalil, A.S. Hakeem, N.A. Aqeeli, T. Laoui, A.A. Qutub, R. Kirchner, Spark plasma sintering of metals and metal matrix nanocomposites: A Review, J. Nano, Vol. 983470, 2012, 1-13.

[66] Z. A. Munir, U. Anselmi, The effect of electric field and pressure on the synthesis and consolidation of materials: A review of the spark plasma sintering method, J. Mater. Sci., Vol. 41, 2006, 763 –777.

[67] S. Chakraborty, P. K. Das, D. Ghosh, Spark Plasma Sintering and Structural Properties of ZrB_2 Based Ceramics: A Review, Rev. Adv. Mater. Sci., Vol. 44, 2016, 182-193.

[68] P.J. Kelly, R.D. Arnell, Magnetron sputtering: a review of recent developments and applications, Vacuum, Vol 56, 2000, 159-172.

[69] Z. An, H. Jia, Y. Wu, P. D. Rack, A. D. Patchen, Y. Liu, Y. Ren, N. Li, P. K. Liaw, Solid-Solution CrCoCuFeNi High-Entropy Alloy Thin Films Synthesized by Sputter Deposition, Mater. Res. Lett., Vol. 3(4), 2014, 203–209.

[70] T. Yang, S. Xia, S. Liu, C. Wang, S. Liu, Y. Zhang, J. Xue, S. Yan, Y. Wang, Effects of Al addition on microstructure and mechanical properties of Al*x*CoCrFeNi High entropy alloy, Mater. Sci. Eng. A, Vol. 648, 2015, 15-22.

[71] A. Munitz, S. Salhov, S. Hayun, N. Frage, Heat treatment impacts the micro-structure and mechanical properties of AlCoCrFeNi high entropy alloy, J. Alloy Compd., Vol. 683, 2016, 221-230.

[72] A. Zhang, J. Han, J. Meng, B. Su, P. Li, Rapid preparation of AlCoCrFeNi high entropy alloy by spark plasma sintering from elemental powder mixture, Mater. Lett., Vol. 181, 2016, 82-85.

[73] R. Sriharitha, B. S. Murty, R. S. Kottada, Phase formation in mechanically alloyed AlxCoCrCuFeNi (x = 0.45, 1, 2.5, 5 mol) high entropy alloys, Intermetallics, Vol. 32, 2013, 119-126.

[74] R. Sriharitha, B. S. Murty, R. S. Kottada, Alloying, thermal stability and strengthening in spark plasma sintered $Al_xCoCrCuFeNi$ high entropy alloys, J. Alloys Compd., Vol. 583, 2014, 419-426.

[75] S. Praveen, J. Basu, S. Kashyap, R. S. Kottada, Exceptional resistance to grain growth in nanocrystalline CoCrFeNi high entropy alloy at high homologous temperatures, J. Alloys Compd., Vol. 662, 2016, 361-367.

[76] B. Liu, J. Wang, Y. Liu, Q. Fang, Y. Wu, S. Chen, C. T. Liu, Microstructure and mechanical properties of equimolar FeCoCrNi high entropy alloy prepared via powder extrusion, Intermetallics, Vol. 75, 2016, 25-30.

[77] C. F. Lee, T. T. Shun, Effect of Fe content on microstructure and mechanical properties of $Al_{0.5}CoCrFe_xNiTi_{0.5}$ high-entropy alloys, Mater Charac., Vol. 114, 2016, 179-184.

[78] C. Y. Hsu, C. C. Juan, W. R. Wang, T. S. Sheu, J. W. Yeh,, S. K. Chen, On the superior hot hardness and softening resistance of $AlCoCr_xFeMo_{0.5}Ni$ high-entropy alloys, Mater. Sci. Engg. A, Vol. 528, 2011, 3581-3588.

[79] Y. J. Hsu, W. C. Chiang, J. K. Wu, Corrosion behavior of $FeCoNiCrCu_x$high-entropy alloys in 3.5% sodium chloride solution, Mater. Chem. Phy., 2005, Vol. 92, 112-117.

[80] H. F. Sun, C. M. Wang, X. Zhang, R. Z. Li, L. Y. Ruan, Study of microstructure and performance of high entropy alloys $Al_xFeCuCoNiCrTi$, Mater. Res, Innov., Vol. 19, 2015, 89-93.

[81] A. Takeuchi, K. Amiya, T. Wada, K. Yubuta, W. Zhang, High-Entropy Alloys with a Hexagonal Close-Packed Structure Designed by Equi-Atomic Alloy Strategy and Binary Phase Diagrams, JOM, Vol. 66 (10), 2014, 1984-1992.

[82] A. Takeuchi, K. Amiya, T. Wada, K. Yubuta, Dual HCP structures formed in senary ScYLaTiZrHf multi-principal element alloy, Intermetallics, Vol. 69, 2016, 103-109.

[83] Y.J. Zhao, J.W. Qiao, S.G. Ma, M.C. Gao, H.J. Yang, M.W. Chen, Y. Zhang, A hexagonal close-packed high-entropy alloy: The effect of entropy, Mater. Des., Vol. 96, 2016, 10-15.

[84] R. Li, J. Gao, K. Fan, Study to microstructure and mechanical properties of Mg Containing High Entropy Alloys, Mater. Sci. Forum, Vol. 650, 2010, 265-271.

[85] R. Li, J. Gao, K. Fan. Microstructure and mechanical properties of MgMnAlZnCu high entropy alloy cooling in three conditions, Mater. Sci. Forum, Vol. 686, 2011, 235-241.

[86] Y. L. Chen, C. W. Tsai, C. C. Jaun, M.H. Chuang, J. W. Yeh, T.S. Chin, S.K. Chen, Amorphization of equimolar alloys with HCP elements during mechanical alloying, J. Alloys Comp., Vol. 506, 2010, 210-215.

[87] X. Q. Gao, K. Zhao, H. B. Ke, D. W. Ding, W. H. Wang, H. Y. Bai, High mixing entropy bulk metallic glasses, J. Non Crys. Sol., Vol. 357, 2011, 3557-3560.

[88] X. Yang, S. Y. Chen, J. D. Cotton, Y. Zhang, Phase stability of low-density, multiprincipal component alloys containing Aluminum, Magnesium, and Lithium, JOM, Vol. 66, 2014, 2009-2020.

[89] K. M. Youssef, A. J. Zaddach, C. Niu, D. L. Irving, C. C. Koch, A novel low density, high hardness, high entropy alloy with close packed single phase, Mater. Res. Lett., Vol. 3, 2015, 95-99.

[90] N.D. Stepanov, D.G. Shaysultanov, G. A. Salishchev, M.A. Tikhonovsky, Structure and mechanical properties of a light-weight AlNbTiV high entropy alloy, Mater. Lett., 2015, 142, 153-155.

[91] R. Feng, M. C. Gao, C. Lee, M. Mathes, T. Zuo, S. Chen, J. A. Hawk, Y. Zhang, P. K. Liaw, Design of Light-Weight High-Entropy Alloys, Entropy, Vol. 18, 2016, 1-21.

[92] N. D. Stepanov, N.Y. Yurchenko, D. G. Shaysutanov, G. A. Salishchev, M. A. Tikhonovsky, Effect of Al on structure and mechanical properties of $Al_xNbTiVZr$ (x = 0, 0.5, 1, 1.5) high entropy alloys, Mater. Sci. Technol. 2015, Vol. 31, 1184–1193.

[93] A Novel Light High-Entropy Alloy $Al_{20}Be_{20}Fe_{10}Si_{15}Ti_{35}$. Available online: http://www.science24.com/paper/19071 (accessed on 25 August 2016).

[94] A. Kumar, M. Gupta, An Insight into Evolution of Light Weight High Entropy Alloys: A Review, Metals, 2016, Vol. 6, 1-19, DOI:10. 3390/met6090199

[95] P. C. Sharma, Production Technology (Manufacturing Processes): Manufacturing Processes, S. Chand Publisher, 2008.

[96] S. Basu, C. Nayak, A. K. Yadav, A. Agrawal, A. K. Poswal, D. Bhattacharyya, S. N. Jha, N. K. Sahoo,A comprehensive facility for EXAFS measurements at the INDUS-2 synchrotron source at RRCAT, Indore, India, J. Phys. Conf. Ser., 2014, Vol. 493, 012032-1-012032-4.

[97] A. K. Poswal, A. Agrawal, A. K. Yadav, C. Nayak, S. Basu, S. R. Kane, C. K. Garg, D. Bhattachryya, S. N. Jha, N. K. Sahoo, Commissioning and first results of scanning type EXAFS beamline (BL-09) at INDUS-2 synchrotron source, AIP Conf Proc., 2014, Vol. 1591,649-651.

[98] Y. L. Chen, Y. H. Hu, C. A. Hsieh, J. W. Yeh, S. K. Chen, Competition between elements during mechanical alloying in an octonary multi principal element alloy system, J. Alloys Comp. 2009, Vol. 481, 768-775.

[99] S. Guo, C. Ng, Z. Wang, C. T. Liu, Solid solutioning in equiatomic alloys: Limit set by topological instability, J. Alloys Comp., 2014, Vol. 583, 410-413.

[100] F. Tian, L. Delezeg, N. Chen, L. K. Varga, J. Shen, L. Vitos, Structural stability of NiCoFeCrAlx high entropy alloy from ab initio theory, Phys. Rev., Vol.81, 2013, 085128-1- 085128-5.

[101] S. Praveen, B. S. Murty, R. S. Kottada, Alloying behaviour in multi component AlCoCrCuFe and NiCoCrCuFe high entropy alloy, Mater Sci Engg A,Vol. 534, 2012, 83-89.

[102] S. Kumari, D. K. Singh, P. K. Giri, Strain Anisotropy in freestanding germanium nanoparticles synthesized by ball milling, J. Nanosci. Nanotechnol., 2009, Vol. 9, 1-6.

[103] H. A. Baghbaderani, S. Sharafi, M. D. Chermahini, Investigation of nanostructure formation mechanism and magnetic properties in $Fe_{45}Co_{45}Ni_{10}$ system synthesized by mechanical alloying, Powder Tech., 2012,Vol. 230, 241-246.

[104] A. Takeuchi, A. Inoue, Classification of Bulk Metallic Glasses by Atomic Size Difference, Heat of Mixing and Period of Constituent Elements and Its Application to Characterization of Main Alloying Element, Mater. Trans., 2005, Vol. 46, 2817-2829.

[105] http://www.camd.lsu.edu/beamline_info/XrayInfo/Reference_X-Ray_Spectra_for_Metal_Foils.pdf

[106] D. C. Konigsberger, R. Prince, 1988, X-Ray Absorption: Principles, Applications, Techniques of EXAFS, SEXAFS and XANES, Wiley, New York.

[107] S. D. Kelly, D. Hesterberg, B. Ravel, 2008, Analysis of soils and minerals using X-ray absorption spectroscopy, in Methods of Soil Analysis, Part 5–Mineralogical methods; (A.L.Ulery, L.R. Drees, Eds.); Soil Science Society of America: Madison, WI, USA, 367-464.

[108] M. Newville, B. Ravel, D. Haskel, J. J. Rehr, E. A. Stern, Y. Yacoby,Analysis of multiple-scattering XAFS data using theoretical standards, Physica B, 1995, Vol. 208, 154-156.

[109] https://www.fiz-karlsruhe.de/icsd.html.

[110] E. Clementi, D. L. Raimondi, W.P. Reinhardt, Atomic Screening Constants from SCF functions. II. Atoms with 37 to 86 Electrons, J. Chem. Phys., 1967, Vol. 47, 1300-1307.

[111] ASM Handbook, Volume 3, ASM International.

[112] F. Khodabakhshi, M. Haghshenas, H. Eskandari, B. Koohbor, Hardness-strength relationships in fine and ultra-fine grained metals processed through constrained groove pressing, Mater. Sci. Eng. A, Vol. 636, 2015, 331-339.

[113] ASTM Standard G31-72, ASTM, PA, 2003.

[114] X. W. Qiu, Y. P. Zhang, L. Hea, C. Liu, Microstructure and corrosion resistance of AlCrFeCuCo high entropy alloy, J. Alloys Compd., 2013, Vol. 549, 195-199.

[115] J. R. Davis, Corrosion: Understanding and Basics, ASM International, Materials Park, Ohio, 2000

[116] file:///G:/ftir/interpretation/Infrared_%20Interpretation%20

[117] E. M. Sahrif, Corrosion Behavior of Magnesium in Naturally Aerated Stagnant Seawater and 3.5% Sodium Chloride Solution, Int. J. Electrochem. Sci., 2012, Vol. 7, 4235-4249.

[118] M. K.Abbass, K.S. Hassan, A. S Alwan, Study of Corrosion Resistance of Aluminum Alloy 6061/SiC Composites in 3.5% NaCl Solution, Int. J. Mater. Mech. Manuf, 2015, Vol. 3(1), 31-35.

[119] K.L. Kendig, D.B. Miracle, Strengthening mechanisms of an Al-Mg-Sc-Zr alloy, Acta Mater., 2002, Vol. 50, 4165–4175.

[120] S. Mohanty, N.P. Gurao, K. Biswas, Sinter ageing of equiatomic $Al_{20}Co_{20}Cu_{20}Zn_{20}Ni_{20}$ high entropy alloy via mechanical alloying, Mater. Sci. Eng. A, 2014, Vol. 617, 211-218.

[121] U. Holzwarth, H. Stamm, The precipitation behaviour of ITER-grade Cu-Cr-Zr alloy after simulating the thermal cycle of hot isostatic pressing, J. Nuclear Mater. 279 (2000) 31-45.

[122] http://asm.matweb.com/search/SpecificMaterial.asp?bassnum=MA7075T6

[123] N. Poondla, T.S. Srivatsan, A. Patnaik, M. Petraroli, A study of the microstructure and hardness of two titanium alloys: Commercially pure and Ti–6Al–4V, J. Alloys Comp. 486 (2009) 162–167.

[124] H.C. Lin, L.M. Wang, Improved mechanical properties of Ti–15V–3Cr–3Sn–3Al alloy by electron beam welding process plus heat treatments and its microstructure evolution, Mater Chem. and Phy. 126 (2011) 891–897.

[125] http://www.grantadesign.com/download/pdf/teaching_resource_books/2-Materials-Charts-2010.pdf

[126] R.S. Mikhail, S. Brunauer, L.E. Copeland, Kinetics of the thermal decomposition of calcium hydroxide, J. Coll. Inter. Sci., 1966, Vol. 21, 394-404.

[127] B. D. Cullity, Elements of X-Ray Diffraction, Addison-Wesley Publicating Company, Massachusetts, 1956.

[128] http://nptel.ac.in/courses/113101003/downloads/partV/module1.pdf

[129] http://www.msm.cam.ac.uk/phase-trans/2004/z/3750-003.pdf

[130] http://li.mit.edu/Stuff/PM/Termpaper/LaurenAyers22-71.pdf

[131] S. S. Brenner, M. K. Miller, W.A. Soffa, Spinodal Decomposition of Iron-32 at.% Chromium at 470°C, Scripta Metall., 1982, Vol. 16, 831-836.

[132] J. Androulakis et al., Spinodal decomposition and nucleation and growth as a means to bulk nanostructured thermoelectrics: enhanced performance in $Pb_{1-x}Sn_xTe$-PbS, J. Am. Chem. Soc., 2007, Vol.129, 9780-9788.

[133] I. Baker et al., Microstructural evolution of spinodally formed $Fe_{35}Ni_{15}Mn_{25}Al_{25}$, Intermetallics, 2009, 886-893.

[134] J. W. Cahn, Hardening by spinodal decomposition, Acta Metall., 1963, Vol. 11, 1275–85.

[135] V. Raghavan, Materials Science and Engineering, Fifth Ed., PHI Learning, 2004.

[136] P. Hidnert, Thermal expansion and effects of heat treatments on the growth, density, and structure of some heat resisting alloys, J. Res. Nat. Bur. Stand., 1938, Vol. 20, 809-823.

[137] https://en.wikipedia.org/wiki/Grain_growth

[138] K .B. Alexander, P. F. Becher, S.B. Waters, and A. Bleier, Grain Growth Kinetics in Alumina-Zirconia (CeZTA) Composites, J Am. Ceram. Soc., 1994, Vol.77(4),939-946.

[139] T. De Nys, P. M. Gielen, Spinodal Decomposition in the Fe-Cr System, Metall. Trans., 1971, Vol. 2, 1423-1428.

[140] M. K. Miller et al., Spinodal decomposition in Fe-Cr alloys: Experimantal study at the atomic level and comparison with computer models-I. Inroduction and methodology, Acta Metall. Mater., Vol. 43(9), 3385-3401.

List of Publication from this Research work

- Ornov Maulik, N. Patra, D. Bhattacharyya, S.N. Jha, and Vinod Kumar, "Local atomic structure investigation of $AlFeCuCrMg_x$ (0.5, 1, 1.7)High Entropy Alloys: X-ray Absorption Spectroscopy study", Solid State Communications, 2017 (Accepted).
- Ornov Maulik, Devesh Kumar, Saurav Kumar, Daniel M. Fabijanic, and Vinod Kumar, "Structural evolution of spark plasma sintered $AlFeCuCrMg_x$ (x = 0, 0.5, 1, 1.7) high entropy alloys", Intermetallics, 2016, 77, 46-56.
- Ornov Maulik, and Vinod Kumar, "Synthesis of $AlFeCuCrMg_x$ (x = 0, 0.5, 1, 1.7) alloy powders by mechanical alloying", Materials Characterization, 2015, 110, 116-125.
- Ornov Maulik, andVinod Kumar, "Effect of Conventional sintering on Mg containing $AlFeCuCrMg_x$ (x = 0.5, 1, 1.7) alloys" (Under preparation).
- Ornov Maulik, and Vinod Kumar, "Heat treatment of spark plasma sintered $AlFeCuCrMg_x$ (x = 0, 0.5, 1,1.7) alloys" (Under Preparation).

Other Publications

- Devesh Kumar, Ornov Maulik, Atul Singh Bagri, Y.V.S.S. Prasad, and Vinod Kumar,"Microstructure and characterization of mechanically alloyed equiatomic AlCuCrFeMnW high entropy alloy", Materials Today: Proceeding, (2016) Accepted.
- Heena Khanchandani, Priyanka Sharma, Rupesh Kumar, Ornov Maulik,and Vinod Kumar, "Effect of sintering on phase evolution in $AlMgFeCuCrNi_{4.75}$ high entropy alloy", Advanced Powder Technology, 27 (2016) 289-294.
- Rajat Goel, Mahesh Upadhayay, Ornov Maulik, Y.V.S.S. Prasad, and Vinod Kumar, "Effect of Magnesium on strain hardening response of Al-Mg-Mn based alloys", Procedia Materials Science, 5 (2014) 1241-1247.